The effects of inoxydable steel in reinforced concrete structural elements

Sophia C. Alih

UNIVERSITE de LORRAINE
ECOLE DOCTORALE « EMMA »

2012

THÈSE

Présentée pour obtenir le grade de

DOCTEUR DE L'UNIVERSITE DE LORRAINE
Spécialité : Sciences des Matériaux

Par

Sophia C. ALIH

Sujet :

EFFET DES ACIERS INOX SUR LE COMPORTEMENT STRUCTURAL DES ÉLÉMENTS EN BÉTON ARMÉ

Directeur de thèse : A. KHELIL

Soutenue le 24 septembre 2012 devant la commission d"examen:

Rapporteurs : H. TOUTANJI, Professor
A. BOUCHAIR, Professeur

Examinateurs : M. Ph. Phong LUONG, Directeur de Recherche CNRS
T. SOURISSEAU, Ingénieur de Recherche
A. LECOMTE, Professeur

"Dedicated with love and honor to

my Ayah & Ina,

Abang Bik & Abang King,

and my six sisters

whose support and trust has made this long battle victorious"

Acknowledgements

This thesis is conducted in the *Institute Jean Lamour,* IJL UMR 7198 CNRS*, Équipe* 207 under the supervision of Professor KHELIL, in the Université de Lorraine.

I would like to express my sincere gratitude to Professor KHELIL for his dedication and support during the whole duration of my work. The objectives of this thesis can never be achieved without his intellectual advices, moral support, and guidance.

My appreciation goes to Professor Houssam TOUTANJI, Chair, Department of Civil & Environmental Engineering in the University of Alabama in Huntsville, USA, for his willingness to be the evaluator of my work despite of his tight schedule and other responsibilities.

Special thanks to Professor Abdelhamid BOUCHAIR, from the Department of Civil Engineering Université Blaise Pascal, Polytech Clermont-Ferrand, Aubière Cédex for his acceptance to evaluate this thesis.

This acknowledgement also addresses to Minh Phong LUONG, Research Director CNRS in the Laboratoire de Mécanique des Solides Ecole Polytechnique Palaiseau for his willingness to be the examiner of my work.

I would also like to thank Thomas SOURISSEAU, Research & Development Engineer in the Center of Research UGITECH Ugine for his interest in this thesis and effort to examine my work.

My thanks also go to Professor André LECOMTE, in the Université de Lorraine, for the willingness to examine my thesis despite of his other commitments.

I dedicate my deep appreciation to all members of the Civil Engineering Department in the IUT Nancy-Brabois for their help and support in my work. First and foremost M. Paul-Glez, technician in the department, for his direct involvement in all stages of my laboratory works. A special thanks also goes to Hanaa FARES, Firas MAHMOUD, Foudil MOHRI, Joelle PASSARD, Rémi BOISSIERRE, and Laurent ROUGE, Maitre de Conference and technician in the department for their support. My acknowledgement goes to Mr. ROY, Chair of Civil Engineering Department, for his interests in this study and research activities in the department.

Last not least, I would like to express my gratitude to the person close to me; Damien, Tuti, Ali, Abid, Naja, Sherry, Ezatul, Andrew, and other friends for their full support and understanding especially during the difficult phases of my study. Special thanks to the Ministry of Higher Education of Malaysia, and the Universiti Teknologi Malaysia, Skudai for offering me scholarship and full time study leave.

Summary

RE. Résumé Étendu

RE1. Introduction

L'acier inoxydable ou Inox est une famille d'aciers résistant à la corrosion et à la chaleur contenant au moins 10,5% de chrome [1]. Ce chrome est destiné à la formation d'une couche superficielle de protection dite « couche passive ». Cette couche est un film très mince de quelques nanomètres, invisible à l'œil et composée d'oxydes de chrome, qui protège le métal de l'environnement extérieur et qui fait partie intégrante du métal. Il existe une large gamme d'aciers au carbone répondant à des exigences différentes de résistance, soudabilité et de ténacité. On trouve donc un large éventail d'acier inoxydable avec des niveaux plus ou moins élevés de résistance à la corrosion et aux déformations. Les résultats de l'addition contrôlée d'éléments d'alliage, offrent des attributs spécifiques en termes de résistance ultime et de capacité de résister à des environnements différents. Ces aciers sont classés par famille de type austénitique, ferritique, austénitique-ferritique ou duplex, et martensitique [2]. La classification est basée sur la composition chimique et le traitement thermique. Chaque famille partage le même comportement de base.

L'utilisation de l'acier inoxydable pour des applications structurales en génie civil est relativement limitée. On l'utilise en général pour les éléments secondaires [3]. Sa ductilité élevée est avantageuse en termes de redistribution des efforts avant la ruine et de dissipation d'énergie dans le cas d'un chargement cyclique. Son excellente résistance à la corrosion augmente la durabilité des structures exposées à un environnement agressif [4] - [6]. Le béton armé connait, au cours du temps, une dégradation de sa structure dans certains conditions d'emploi ; on estime qu'environ 70% des pathologies du béton sont liées à la corrosion des armatures en acier ordinaire. Il existe des solutions éprouvées pour éviter ou amoindrir l'effet de ces pathologies : la protection cathodique, l'augmentation de l'enrobage, les inhibiteurs de corrosion etc. … Mais aujourd'hui, l'armature en acier inoxydable constitue aussi, pour certaines applications, une solution à prendre en considération, en particulier quand il y'a des difficultés de maintenance [5]. L'acier inoxydable dispose également d'une bonne esthétique et d'une bonne résistance au feu [7].

Une partie de ce travail est consacrée à l'étude du comportement des aciers inoxydables afin d'évaluer leurs performances lorsqu'ils sont utilisés comme éléments structuraux en béton (poutres, poteaux). Deux types sont considérés : austénitique à chaud, AH (Type 304LN) et austénitique-froid, AC (type 4362). Des échantillons sont testés pour caractériser les propriétés mécaniques. Les résultats sont ensuite utilisés pour élaborer une loi de comportement représentative pour les deux types d'austénitique.

Le type « AH » est étudié en détail pour déterminer son comportement en tant que armature de poutres en béton armé. L'étude est concentrée sur le comportement de l'interaction avec le béton (phénomène de raidissement en traction). Un modèle de raidissement en traction du béton est développé pour modéliser cette interaction en se basant sur l'essai de flexion au lieu de l'essai de traction utilisé par de nombreux chercheurs [8]-[12]. Ce modèle est intégré dans l'analyse globale d'une poutre en béton armé avec des aciers inoxydable. Une méthode inverse basée sur la combinaison de résultats expérimentaux et numériques obtenus à partir d'une analyse non-linéaire (NNA) est développée pour déterminer les paramètres du modèle.

Les lois de comportements obtenues ainsi que les propriétés de raidissement sont implémentées dans un code de calcul par éléments finis (FEM) pour simuler le comportement réel des poutres.

Enfin, l'effet de l'inox dans l'élément structural; poutres et colonnes est également étudié. Différentes poutres renforcées par des armatures inoxydables et des aciers au carbone standard sont réalisées et testées en flexion cyclique jusqu'à la rupture. Les paramètres mécaniques (résistance à la traction, ductilité) sont comparés à ceux de l'acier au carbone. L'effet de l'acier inox sur les réponses structurales sous actions sismiques est également présenté. Trois modèles sont conçus et analysés vis-à-vis de la capacité sismique en tenant compte de la ductilité structurale apportée par les armatures inox.

RE1.1 Objectifs

Cette étude a pour objectifs :

- Etudes des propriétés de l'acier inoxydable avec la mise en évidence de l'interaction avec le béton (transfert des efforts de traction)
- Etude du comportement de l'acier inoxydable dans un élément « poutre BA » approches expérimentale et numérique (Analyse non linéaire).
- Modélisation d'une structure BA sous actions sismiques (effet de l'acier inox sur le facteur de comportement). Evaluation de la capacité sismique en tenant compte de la ductilité structurale apportée par les armatures inox.

RE1.2 Motivation de l'étude

Malgré les avantages que procure l'acier inoxydable dans la construction, les recherches sur ce type d'armatures sont encore limitées par rapport à l'acier au carbone [13]. Leur coût élevé est souvent un obstacle à la construction ordinaire. Il est donc réservé uniquement dans les structures plus vulnérables aux agents agressifs. L'acier inoxydable est principalement utilisé dans les éléments secondaires et leur utilisation sous forme de barres d'armature dans le béton armé n'a pas été suffisamment explorée. Pourtant, les armatures inox sont une solution pertinente pour une multitude d'ouvrages et parties d'ouvrages coulés en place ou préfabriqués, soumis à des contraintes environnementales pouvant générer des risques de corrosion.

Un nouveau type d'acier austénitique a été étudié dans ce travail. Ce nouvel acier possède des propriétés mécaniques améliorées : résistance élevée et une grande capacité de déformation plastique avant la rupture.

RE1.3 Méthodologies

Ce travail est mené en plusieurs étapes pour atteindre les objectifs (Figure RE1). Pour réaliser le premier objectif, une recherche bibliographique est menée pour caractériser l'acier inoxydable. Les essais de laboratoire sont ensuite effectués pour déterminer les propriétés mécaniques des éprouvettes inox prélevées dans les armatures. Les résultats sont ensuite analysés et utilisés pour établir les lois de comportement spécifiques pour ces aciers.

Le second objectif concerne les propriétés d'interaction entre les armatures inox et le béton**.** Des travaux de laboratoire et de modélisation numériques par éléments finis sont réalisés. Différents types de poutre en béton armé sont équipées de jauges de déformations fixées sur les barres et la surface de béton. Ces échantillons sont testés en flexion afin de vérifier les propriétés d'interaction entre l'inox et béton pour chaque incrément de charge. Les résultats des travaux de laboratoire sont combinés avec l'analyse numérique non linéaire (ANN) des sections de poutres afin de développer un modèle d'interaction. La procédure de calcul de ce modèle d'interaction est développée sous Matlab. Ce modèle d'interaction ainsi que la loi comportement de l'inox sont ensuite implémentés dans le code de calcul par éléments finis Abaqus. Ce code de calcul permet de prendre en compte les non-linéarités géométriques et matérielles avec le contrôle de la convergence en force ou en déplacement.

Enfin, l'objectif trois traduit l'effet de l'acier inoxydable sur le comportement structural à travers plusieurs essais expérimentaux et numériques. Plusieurs poutres en béton armé avec différents types d'armatures inox sont fabriquées puis testées sous chargement cyclique jusqu'à la rupture. La réponse en termes de force-déplacement est analysée puis comparée aux mêmes éléments renforcés avec de l'acier au carbone standard. Enfin, l'effet de l'acier inox sur les réponses structurales sous actions sismiques est présenté. Trois modèles sont conçus et analysés vis-à-vis de la capacité sismique en tenant compte de la ductilité structurale apportée par les armatures inox.

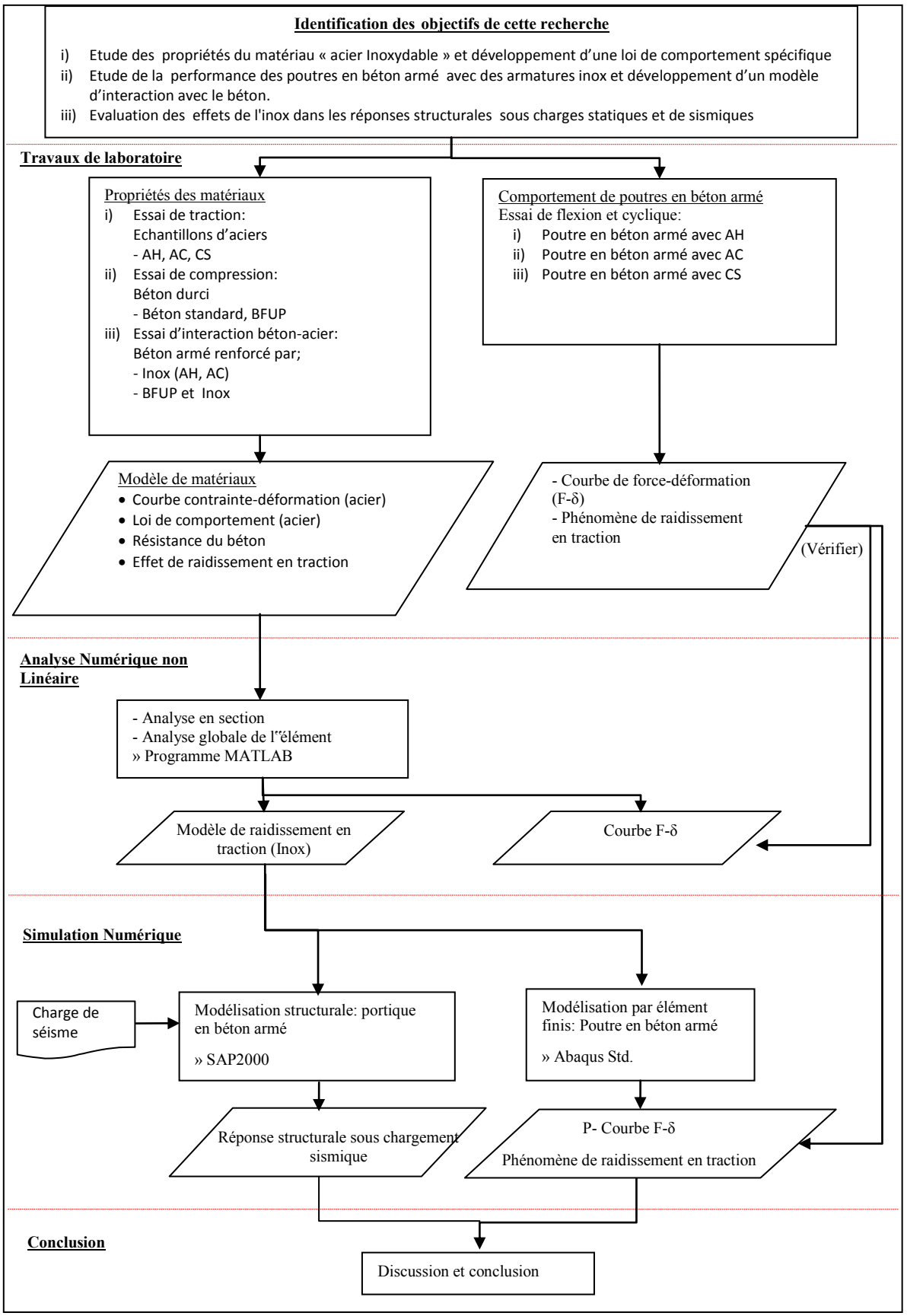

Fig. RE1 Principes et protocoles utilisés

RE1.4 Contenu sommaire

Ce mémoire est composé de quatre chapitres.

i) Chapitre 1: Introduction

Ce chapitre présente brièvement le contexte général de cette étude ainsi que les objectifs recherchés.

ii) Chapitre 2: Bibliographie

Ce chapitre présente les travaux existants ainsi que les approches théoriques de modélisation.

iii) Chapitre 3: Modèles de comportement des matériaux

Ce chapitre traite le comportement de l'acier inoxydable utilisé comme armature en béton armé :

- Développement d'une nouvelle loi de comportement.
- Modélisation de l'interaction acier-béton (objectifs 1 et 2).

iv) Chapitre 4: Acier Inoxydable dans l'analyse structurale

Ce chapitre traite les effets de l'acier inoxydable dans les éléments structuraux (objectif 3) :

- Réponse sous chargement cyclique.
- Réponse sous charge sismique.

RE2. Comportement des barres d'armature en acier inoxydable

En métallurgie, les aciers sont répertoriés sous différentes appellations suivant leur composition chimique ; il est courant de parler des aciers inoxydables sous l'appellation générique « inox », les aciers non alliés étant communément appelés« aciers doux » ou « aciers au carbone. L'inox est un alliage résultant de la fusion, à très haute température (plus de 1500 °C), de différents constituants, principalement le fer, le carbone et le chrome. Pour que l'acier soit appelé « inoxydable », ces éléments doivent obéir à la composition suivante:

– Chrome: plus de 10,5 % en poids ;
– Carbone : moins de 1,2 % en poids ;
– Fer : le complément.

Les aciers inox sont classés dans quatre groupes principaux selon leur structure métallurgique : austénitique, ferritique, austéno-ferritique ou duplex, martensitique. Chaque famille partage le même comportement de base. Parmi ces familles d'inox, l'inox austénitique représente 70% de l'acier inoxydable sur le marché, suivi de l'inox ferritique 29%. Les deux autres familles représentent seulement 1% du marché.

Les aciers austénitiques sont caractérisés par leur haute résistance à la corrosion et leur très bonne dureté. Dans l'industrie du bâtiment, le type austénitique est largement répandu comparativement aux autres familles d'inox. Les aciers ferritiques sont aussi caractérisés par leurs bonnes propriétés de corrosion, mais avec une dureté modérée. Les aciers duplex modernes ont la même résistance à la corrosion que les aciers austénitiques. Ce type d'inox est caractérisé par sa dureté et sa haute résistance à la fatigue [16]. Les inox austénitiques et austéno-ferritiques ont des coefficients de dilatation supérieurs aux aciers carbones. La conductivité thermique des inox austénitiques et austéno-ferritiques est inférieure à celle des inox ferritiques et des aciers [18].

L'acier inox offre également une meilleure conservation de ses caractéristiques mécaniques aux températures élevées [19]. La résistance à la corrosion de tout matériau utilisé pour la réalisation d'un bâtiment ou d'un ouvrage de génie civil est une propriété nécessaire mais qui peut cependant être perturbée, dans certaines conditions, par des agressions environnementales. Il peut donc survenir des phénomènes de corrosion dans les bétons armés. La bonne résistance à la corrosion de l'inox permet de s'affranchir de ces phénomènes.

RE2.1 Propriétés mécaniques

Afin de déterminer les paramètres mécaniques et d'étudier les relations contrainte-déformation, des essais de traction sont effectués sur éprouvettes en acier inoxydable et en acier carbone. La méthodologie d'essai est basée sur le document normatif British Standard [48]. La Figure RE2 montre les dimensions des éprouvettes. Deux types d'acier inoxydable austénitique sont examinés ; austénitique-chaud (AH) et austénitique-froid (AC) ainsi que l'acier au carbone. La figure RE3 donne les diagrammes contrainte-déformation pour ces trois types d'acier.

Pour un acier dur, il est difficile de déterminer l'effort qui correspond parfaitement à la limite d'élasticité [1]. Les inox austénitiques ne présentent pas de limite apparente d'élasticité (appelée également limite d'écoulement) très nette. De ce fait, par convention, la norme définit une charge unitaire à la limite conventionnelle d'élasticité, appelée RP0,2. Elle correspond à l'effort tel, qu'après suppression de cet effort, le métal garde un allongement permanent donné de 0,2 % [1]. Le module d'élasticité trouvé est respectivement de 177300 MPa et 199000 MPa pour l'austénitique chaud et l'austénitique froid. Ces valeurs sont inférieures à celles de l'acier au carbone (204,000 MPa). Cependant, plusieurs recherches ont montré que l'acier inoxydable austénitique a une résistance à la traction finale plus élevée; 773 MPa pour l'austénitique-chaud et 911 MPa pour l'austénitique-froid. Ceci prouve que la limite d'élasticité pour l'austénitique est relativement basse comparée à sa résistance ultime. Quant au rapport de ductilité ($\varepsilon_u/\varepsilon_y$), les deux l'acier inoxydable austénitique donnent des valeurs plus élevées (de 48.5 à 36.6) par rapport l'acier standard (23.9).

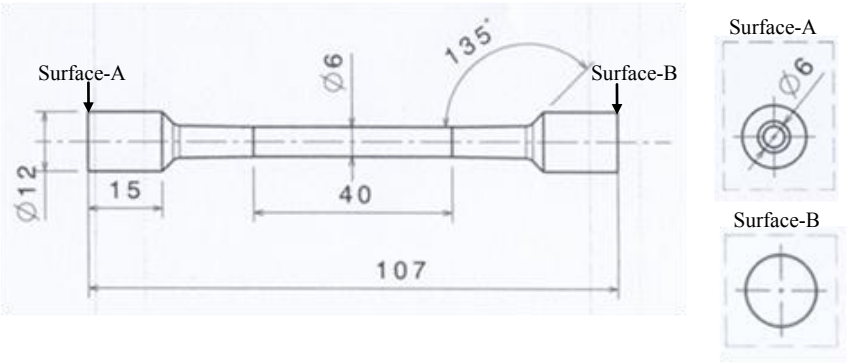

Fig. RE2 Dimensions en mm des échantillons d'acier inoxydable utilisés dans l'essai de tension

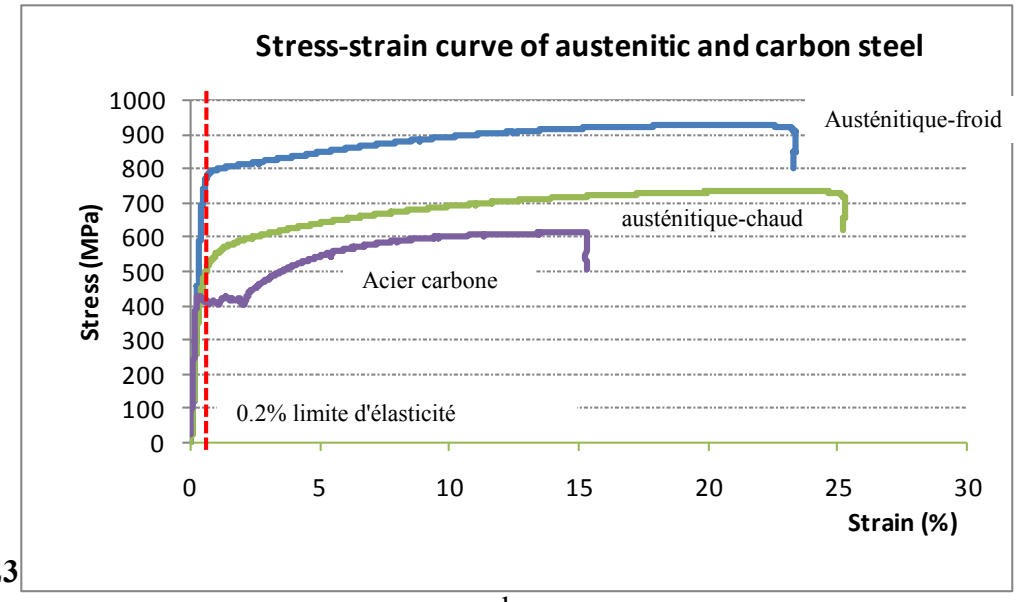

Fig. RE3 l'acier au carbone.

RE2.2 Loi de Comportement de l'acier Inox

À partir des résultats expérimentaux obtenus pour les nuances d'aciers citées ci-dessous une étude numérique a été effectuée afin d'établir un modèle mathématique décrivant les relations contrainte-déformation de l'acier inoxydable à température ambiante. Le modèle mathématique largement utilisé est la relation de Ramberg-Osgood [41] :

$$\varepsilon = \varepsilon e + \varepsilon p = \frac{\sigma}{E_0} + p\left(\frac{\sigma}{\sigma_p}\right)^n \qquad \text{(Eq. RE1)}$$

ε est la déformation totale de l'acier inoxydable (εe élastique plus εp plastique) ;

D'où E_0 = Module de Young

σ_p = limite d'élasticité

p = déformation plastique correspondante

n = paramètre qui caractérise la non linéarité de la courbe

On peut voir sur la figure. RE4(i) que ce modèle donne une relation implicite entre contrainte et déformation qui ne couvre pas les résultats d'essais. Par conséquent, un autre modèle mathématique est proposé sur la base de la partie expérimentale pour l'acier l'austénitique- chaud et l'austénitique- froid. La signification et la définition des différents paramètres sont indiquées en détail dans la partie 3.2.1 (chapitre en anglais).

L'équation proposée pour l'austénitique- chaud est :

$$\varepsilon = \frac{\sigma}{177\,305} + 0.002\left(\frac{\sigma}{480}\right)^{5.56} \quad \text{pour } \sigma \leq \sigma_{0.2} \qquad \text{(Eq. RE2)}$$

$$\varepsilon = \frac{\sigma-480}{34\,724} + 0.38\left(\frac{\sigma-480}{293}\right)^{3.17} + 0.0047 \quad \text{pour } \sigma > \sigma_{0.2} \qquad \text{(Eq. RE3)}$$

Et pour austénitique-froid l'équation suivante :

$$\varepsilon = \frac{\sigma}{198\,810} + 0.002\left(\frac{\sigma}{780}\right)^{11.42} \quad \text{pour } \sigma \leq \sigma_{0.2} \qquad \text{(Eq. RE4)}$$

$$\varepsilon = \frac{\sigma-780}{29\,148} + 0.14\left(\frac{\sigma-780}{131}\right)^{4.0} + 0.0059 \quad \text{pour } \sigma > \sigma_{0.2} \qquad \text{(Eq. RE5)}$$

On peut observer sur les courbes de la figure RE4(ii) une bonne corrélation entre les résultats expérimentaux et ceux données par les lois de comportement proposées. Ces équations sont implémentées dans le code Abaqus pour l'analyse par éléments finis des poutres en béton armés avec des armatures en inox.

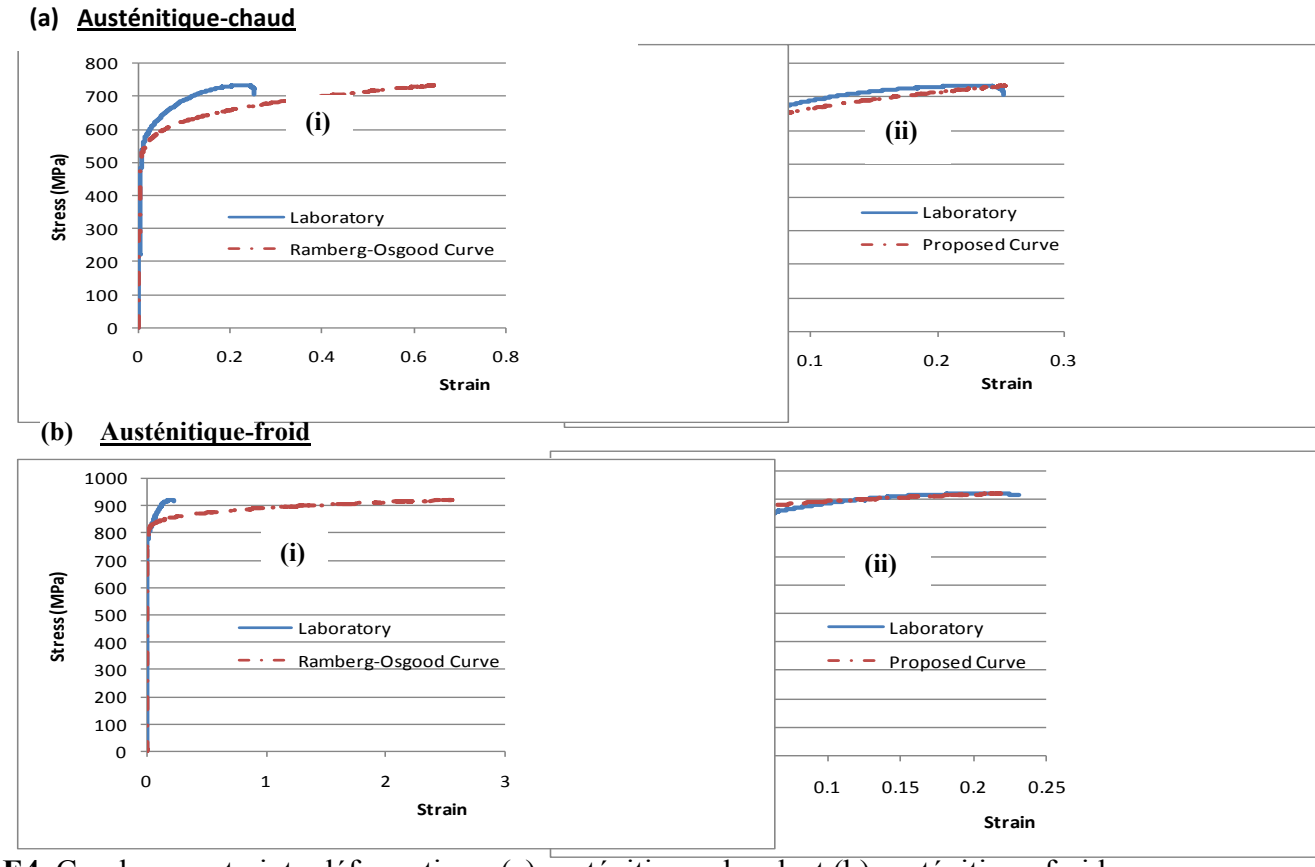

Fig. RE4 Courbes contrainte-déformation - (a) austénitique-chaud, et (b) austénitique-froid

RE4. Raidissement en traction

Le phénomène de raidissement en traction a été observé expérimentalement par de nombreux chercheurs à partir des essais de traction directe [9]-[12]. La majorité de ces travaux se rapportent à l'étude du béton renforcé avec de l'acier standard ou par des matériaux polymères (FRP). Toutefois, les résultats obtenus avec cet équipement sont très variables.

Dans cette étude, le phénomène de raidissement en traction dans une poutre en béton est évalué à partir des essais de flexion quatre points. Une série de jauges de déformation uni-axiales est fixée sur les barres d'acier austénitique dans la zone de traction pour mesurer l'évolution de l'effort de traction en fonction du chargement appliqué. Cette variation d'effort de traction est analysée en particulier durant la phase de fissuration. Des capteurs de type LVDT sont placés au milieu du dispositif pour mesurer les déplacements à mi-travée.

RE4.1 Échantillons et configurations

La figure RE5 montre les dimensions des poutres en béton armé utilisées pour ces essais. Deux barres d'acier austénitiques de 20mm de diamètre sont introduites comme armatures dans la zone de traction et des barres d'acier au carbone de 8mm de diamètre sont disposées dans la zone de compression. Pour ces tests, deux type de poutres sont réalisés ; une avec de l'acier austénitique-chaud et une autre avec de l'acier austénitique-froid. Les cadres destinés à reprendre les efforts de cisaillement sont formés par des barres d'acier doux de 6mm.

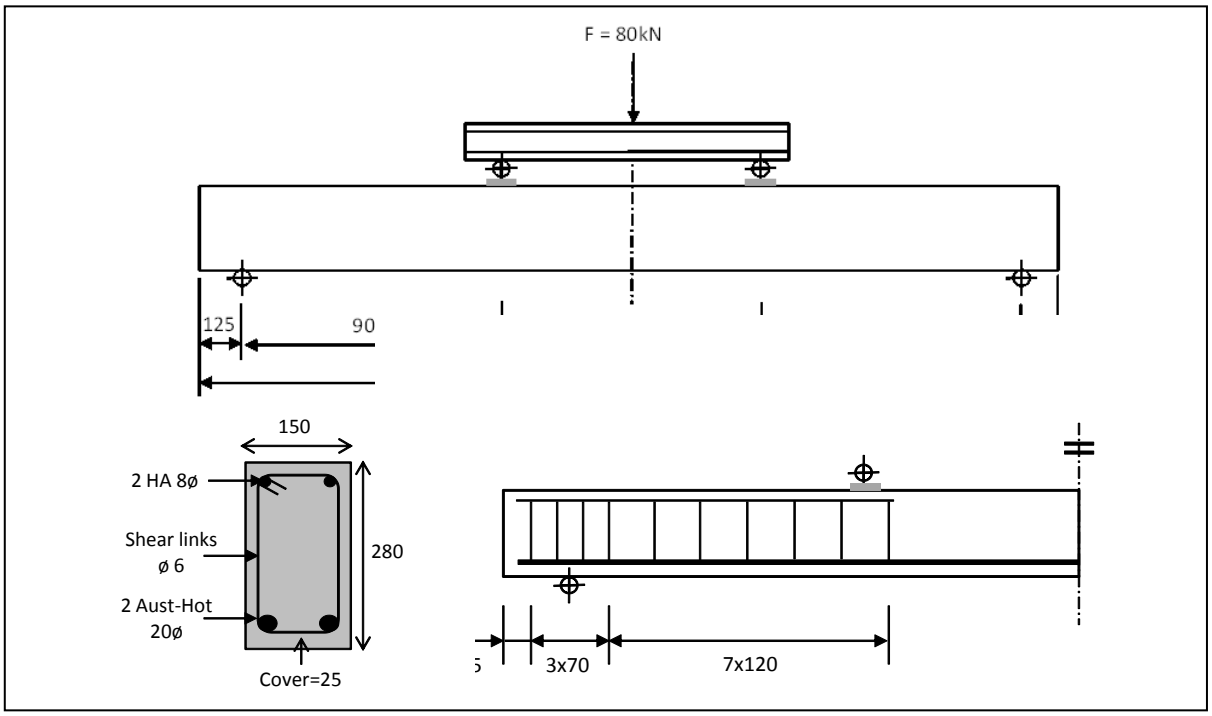

Fig. RE5 Dimension en mm des poutres en béton armé

Le nombre de jauges fixées sur les barres est optimisé de façon (figure RE6) à réduire au minimum les perturbations de l'adhérence entre l'acier et béton. La figure RE7(b) montre la disposition jauges (J1 à J6). Elles sont placées en quinconce entre les deux barres (figure RE7(a)). Les jauges J2, J4, et J6 sont placées le long de la barre 1 et les jauges J1, J3, et J5 sont placées le long de la barre 2 (figure RE8).

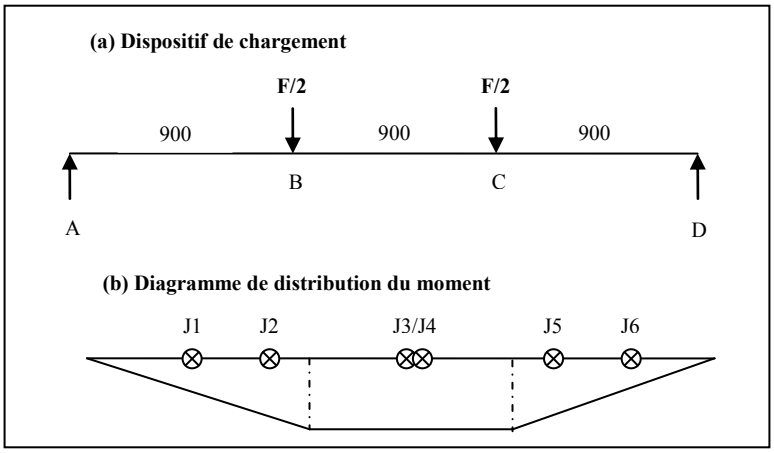

Fig. RE6 Position de jauges. (a) dispositif de chargement, (b) diagramme théorique du moment fléchissant

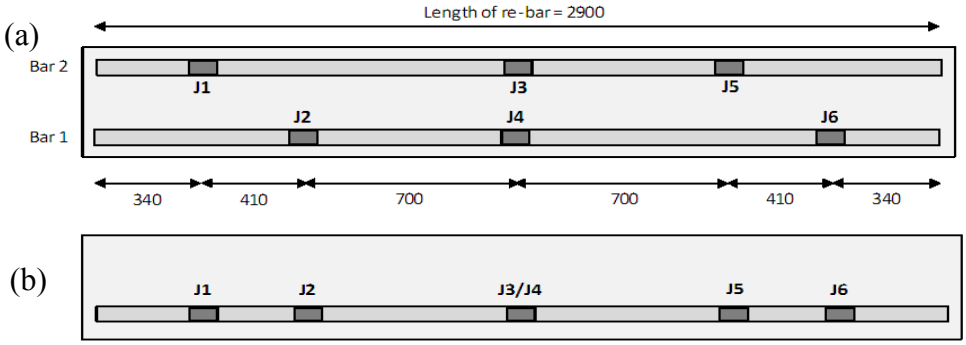

Fig. RE7 Position détaillée des jauges le long des barres: (a) vue en plan (b) vue de côté

Fig. RE8 Jauges sur les armatures

RE4.2 Phénomène de raidissement en traction

Avant chaque essai, des chargements préliminaires sont appliqués afin de tester la réponse des instruments de mesures (calibration des jauges et des capteurs LVDT). Un chargement monotone croissant est appliqué symétriquement jusqu'à 80kN; Le déplacement est enregistré au centre de la poutre en utilisant des capteurs de déplacement LVDT. La figure RE9 montre la courbe force-déplacement obtenue. Le déplacement à mi-travée est de 6.9 mm pour une charge totale de 80kN. Trois lignes sont tracées sur cette courbe (figure. RE9(a)) pour distinguer les trois zones de fissuration figure RE9(b); pré-fissuration, étape de développement de la fissuration, et post- fissuration. Le début de la fissuration correspond à un effort de 27.5kN. Durant l'essai, les fissures sont visibles à partir du chargement appliqué de 31kN.

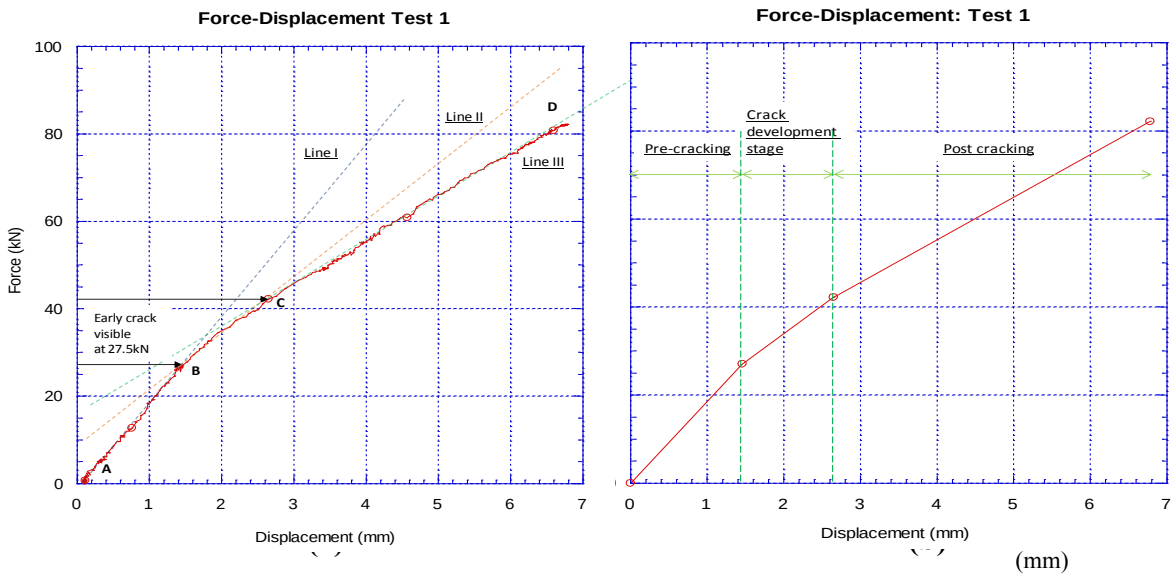

Fig. RE9 Courbes force-déplacement

Le phénomène de raidissement en traction est observé avec l'augmentation de la contrainte enregistrée le long des barres d'acier juste au début de la fissuration du béton. La figure RE10 montre l'évolution des contraintes dans les barres en fonction de l'effort appliqué. Pour chacune des six jauges, une augmentation significative des contraintes est enregistrée entre 27 et 44 kN de chargement appliqué. Cet incrément peut être visualisé en deux phases comme le montre la figure RE10. Prenant l'exemple de la jauge J4 ; une augmentation linéaire est enregistrée entre 0 kN et kN 27, suivi d'une augmentation plus élevée entre 27 et 80 kN. Cette augmentation soudaine de déformation et donc de contrainte, montre le phénomène de raidissement en traction comme pour un essai de traction simple. Toutes les jauges montrent la même configuration pour le même intervalle de charge. Cet intervalle de charge correspond exactement au début de la fissuration.

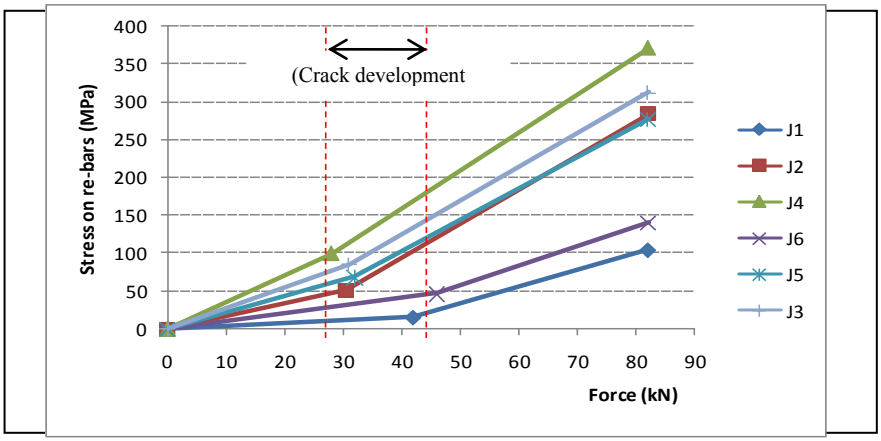

Fig. RE10 Contraintes dans des jauges en fonction de l'effort appliqué

La figure RE11 montre l'évolution des déformations le long des deux barres pour différents niveaux de chargement. Quand la charge de 30 kN est appliquée, l'augmentation de la déformation est plus importante. Les déformations élevées sont enregistrées au niveau de la position des premières fissures. Cette observation est par ailleurs constatée par d'autres chercheurs ayant effectué des essais de traction simple [9].

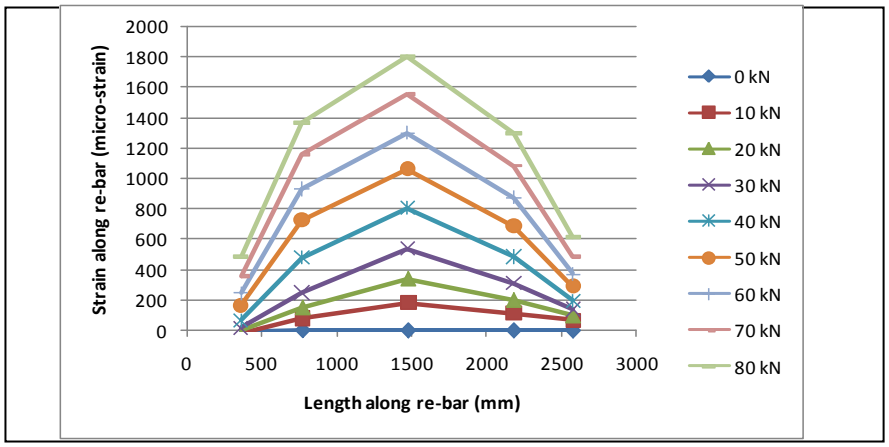

Fig. RE11 Déformation le long des armatures.

RE5. Analyse Numérique Non-linéaire

Cette section présente les propriétés d'interaction entre l'acier inoxydable et le béton. Un modèle de raidissement en traction du béton est développé pour modéliser cette interaction. Ce modèle est intégré dans l'analyse globale d'une poutre en béton armé avec des aciers inoxydables. Une méthode inverse basée sur la combinaison de résultats expérimentaux et numériques obtenus à partir d'une analyse non-linéaire (NNA) est développée pour déterminer les paramètres du modèle. L'effet de raidissement développé pour l'acier inox est comparée à celui l'acier carbone standard. Les résultats obtenus montrent que l'effet de raidissement du béton avec de l'acier inoxydable est plus important durant la phase de fissuration que celui du béton avec de l'acier standard.

Pour cette étude, nous avons adapté le modèle de comportement proposé par Nayal et Rasheed, 2006 [30] pour représenter les propriétés d'interaction entre les armatures en acier inoxydable et le béton (figure RE12). Quatre paramètres C_d, C_b, C_p, et C_s sont nécessaires pour caractériser complètement ce modèle. Les caractéristiques mécaniques du béton dans la phase de traction sont f'$_t$ and ε_{cr};

$$f'_t = 0.3 f_{ck}^{\left(\frac{2}{3}\right)} \quad \text{(Eq. RE6)}$$

$$\varepsilon_{cr} = \frac{f'_t}{E} \quad \text{(Eq. RE7)}$$

f_{ck} la résistance à la compression du béton et E le module d'élasticité

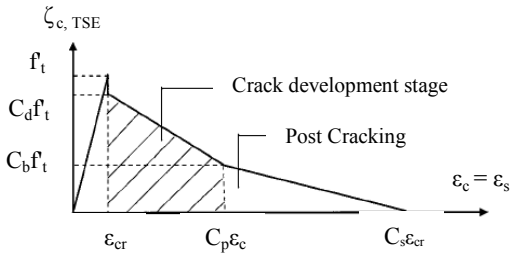

Fig. RE12 Modèle de raidissement en traction [30]

La prise en compte de l'effet raidissant du béton permet une modélisation plus rigoureuse du comportement mécanique du béton tendu. L'étude porte sur des éléments en béton armé avec des armatures inox de type austénitique (haute adhérences (HA).

RE5.1 Méthode et approche

Afin de déterminer les quatre paramètres caractérisant le modèle de raidissement en traction, une analyse numérique non linéaire (NNA) du comportement d'une section fléchie est développée. Ce calcul est basé l'analyse de la courbe force – déplacement et du comportement d'une section fléchie. La procédure de calcul est représentée sur la figure. RE13. Au début de l'analyse des valeurs initiales des paramètres de raidissement ainsi que les autres propriétés mécaniques de l'élément en béton sont introduites. Dans la première itération, le comportement en section puis de l'élément fléchi est analysé. L'analyse en section fournit le détail des propriétés pour une fibre donnée pour chaque incrément de charge. Ces propriétés sont utilisées dans l'analyse globale de l'élément fléchi afin de déterminer la courbe de force-déplacement à mi-travée. La courbe force-déplacement obtenue à partir de ce calcul est ensuite comparée à celle obtenue à partir des essais de flexion 4 points d'une poutre. Le modèle de raidissement en traction appliqué dans l'analyse de la section est alors corrigé en changeant les valeurs des quatre paramètres C_d, C_b, C_p, C_s ainsi que les valeurs de la courbe force-déplacement issues du calcul jusqu'à ce que les résultats convergent vers ceux issues des mesures. L'ensemble de paramètres qui donnent la meilleure approximation des valeurs expérimentales sont adoptés comme valeurs de référence pour le raidissement en traction du béton armé avec des armatures inoxydables.

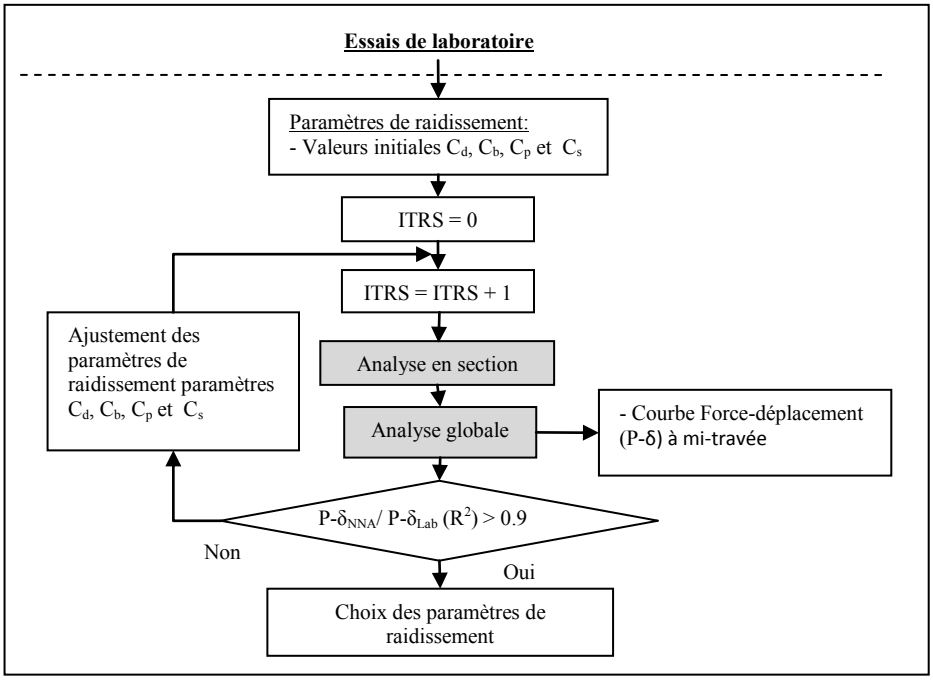

Fig. RE13 Étapes de calcul dans l'analyse non-linéaire

L'erreur entre les deux courbes expérimentale et numérique est calculée à partir du coefficient R^2 défini dans la figure RE13. Les valeurs des coefficients C_d, C_b, C_p et C_s qui minimisent cette erreur sont considérés comme les paramètres du modèle.

RE5.2 Modèles de comportement des matériaux

Dans la zone comprimée du béton nous considérons le polynôme de degré 4 pour représenter la loi de comportement du béton [50];

$$\sigma_c = a_0 + a_1\varepsilon_c + a_2{\varepsilon_c}^2 + a_3{\varepsilon_c}^3 + a_4{\varepsilon_c}^4 \qquad \text{(Eq. RE8)}$$

Cette représentation polynômiale a été choisie du faite que les coefficients peuvent être déterminés par identification avec la courbe expérimentale.

$$\begin{Bmatrix} a_0 \\ a_1 \\ a_2 \\ a_3 \\ a_4 \end{Bmatrix} = \begin{bmatrix} 1 & 0 & 0 & 0 & 0 \\ 0 & 1 & 0 & 0 & 0 \\ 1 & \varepsilon_m & \varepsilon_m^2 & \varepsilon_m^3 & \varepsilon_m^4 \\ 0 & 1 & 2\varepsilon_m & 3\varepsilon_m^2 & 4\varepsilon_m^3 \\ 1 & 1 & 2C_u\varepsilon_m & 3(C_u\varepsilon_m)^2 & 4(C_u\varepsilon_m)^3 \end{bmatrix}^{-1} \begin{Bmatrix} 0 \\ E_{ci} \\ f_m \\ 0 \\ E_{cf} \end{Bmatrix} \qquad \text{(Eq. RE9)}$$

où, $f_m = k_c.f_c'$, $k_c = 1.0$. E_{ci} est le module initial du béton, E_{cf} est le module d'élasticité à l'état limite ultime, $C_u = 1.5$ et ε_m est la déformation maximale.

En ce qui concerne le béton tendu, on utilise la relation de contrainte-déformation représentée sur la figure RE12 ainsi que les paramètres de raidissement en traction décrits ci-dessus.

Les aciers inoxydables austénitiques présentent une excellente résistance à la corrosion. Ces aciers riches en chrome sont ductiles et ont une résistance mécanique élevée. Ils sont amagnétiques et sont formables et soudables. L'élément étudié est composé d'une section d'acier inoxydable (austénitique) disposée dans la zone tendue. Une loi de comportement spécifique pour cet acier a été développée (Eq. RE2, et Eq. RE3).

RE5.3 Analyse en Section

Le modèle de simulation développé repose en premier lieu sur le comportement de la section en intégrant les lois contrainte-déformation du béton et des armatures. Pour cela, on subdivise la section en plusieurs couches (figure. RE14). Le diagramme des déformations axiales est considéré linéaire, seuls deux paramètres sont nécessaires pour le définir à chacune des couches ; la courbure ϕ et la profondeur de l'axe neutre inélastique Y_c. Cette approche de discrétisation horizontale de la section associée à l'intégration sur toute la longueur de la poutre qui est divisée en plusieurs sections (295 sections de 10 mm de longueur) permet de représenter le plus justement possible le comportement structural.

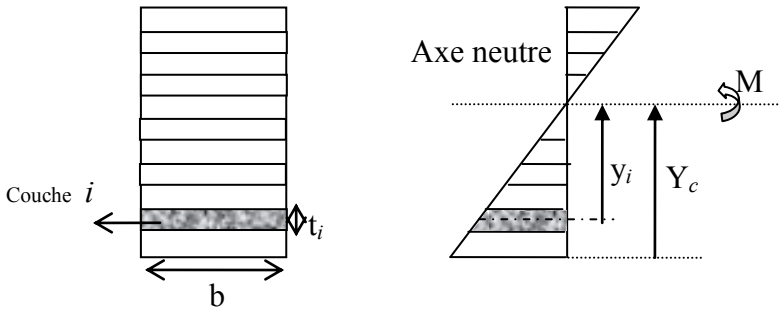

Fig. RE14 Analyse de la section

La procédure de calcul repose sur le calcul de la rigidité axiale et flexionnelle non linéaire autour de l'axe y. La rigidité axiale d'une section située à la fibre Y est donnée par l'intégrale suivante:

$$EA_s = \int_{Y_N}^{H+Y_N} E(Y).B.dY + \sum_{i=1}^{N}(E_{sti} - E_{cti})\,A_{sti} + \sum_{j=1}^{M}(E_{sbj} - E_{cbj})A_{sbj} \quad \text{(Eq. RE10)}$$

$$\boldsymbol{E(Y)} = \frac{\boldsymbol{\sigma(Y)}}{\boldsymbol{\varepsilon(Y)}} \quad \text{(Eq. RE11)}$$

$$E_{sti} = \frac{\sigma_{sti}}{\varepsilon_{sti}} \quad \text{(Eq. RE12)}$$

$$E_{sbj} = \frac{\sigma_{sbj}}{\varepsilon_{sbj}} \quad \text{(Eq. RE13)}$$

N, M sont respectivement le nombre de couche de renforcement (section d'acier) respectivement sur la partie supérieure et inférieure.
La rigidité flexionnelle (EI_s) est donnée par l'intégrale suivante:

$$EI_s = \int_{Y_N}^{H+Y_N} E(Y).B.(Y-Y_o)^2 \ .dY + \sum_{i=1}^{N}(E_{sti} - E_{cti})\, A_{sti}(H + Y_N - Y_{sti} - Y_o)^2 + \sum_{j=1}^{M}\left(E_{sbj} - E_{cbj}\right) A_{sbj}\left(Y_N - Y_{sbj} - Y_o\right)^2 \quad \text{(Eq. RE14)}$$

I_s est l'inertie de flexion par rapport au centre inélastique de flexion Y_c.

Les efforts internes moment (M_{int}) et effort axial F_x s'expriment de la façon suivante :

$$F_x = \int_{Y_N}^{H+Y_N} \sigma(Y).B.dY + \sum_{i=1}^{N}(E_{sti} - E_{cti})\, \varepsilon_{sti} A_{sti} + \sum_{j=1}^{M}\left(E_{sbj} - E_{cbj}\right) \varepsilon_{sbj} A_{sbj} \quad \text{(Eq. RE15)}$$

$$M_{int} = \int_{Y_N}^{H+Y_N} \sigma(Y).B.(Y-Y_o)^2 \ .dY + \sum_{i=1}^{N}(E_{sti} - E_{cti})\, \varepsilon_{sti} A_{sti}(H + Y_N - Y_{sti} - Y_o) + \sum_{j=1}^{M}\left(E_{sbj} - E_{cbj}\right) \varepsilon_{sbj} A_{sbj}\left(Y_N - Y_{sbj} - Y_o\right) \quad \text{(Eq. RE16)}$$

Les lois de comportement sont intégrées par zone de sollicitation de part et d'autre de l'axe neutre. Les formes explicites des rigidités ainsi que les efforts internes sont déterminés pour toutes les couches en effectuant des intégrations analytiques.

$$EA_s = \sum_{i=1}^{2}\sum_{j=1}^{NRi} EA_{ij} \quad \text{(Eq. RE17)}$$
$$F_x = \sum_{i=1}^{2}\sum_{j=1}^{NRi} F_{x_{ij}} \quad \text{(Eq. RE18)}$$
$$EI_s = \sum_{i=1}^{2}\sum_{j=1}^{NRi} EI_{ij} \quad \text{(Eq. RE19)}$$
$$M_{int} = \sum_{i=1}^{2}\sum_{j=1}^{NRi} M_{c_{ij}} \quad \text{(Eq. RE20)}$$

NRi est le nombre de couche par zone

Les propriétés effectives de la section correspondantes à chaque incrément de charge sont évaluées comme suit (figure RE15):

1. La courbure instantanée est déterminée en divisant le moment appliqué par la valeur la de la rigidité flexionnelle de la section :
$$\phi = \frac{M}{EI_s} \quad \text{(Eq. RE21)}$$
2. Les hauteurs des zones tendue et comprimées sont définies en utilisant le dernier calcul de la position de l'axe neutre inélastique Y_c et la hauteur totale de la section H: $Y_{N1} = H - Y_c$ and $Y_{N2} = Y_c$
3. Les rigidités (EA_s, EI_s), les efforts internes (F_x) et (M_{int}) sont calculées pour la déformation axiale moyenne sur chacune des couches à partir des équations (Eq. RE17 – Eq. RE20).
4. A cette étape de calcul, la position de l'axe neutre est analysée en utilisant le critère de convergence suivant :

$$\frac{ES}{EA_s x Y_c} \leq 5\text{x}10 - 7 \quad \text{(Eq. RE22)}$$

Avec $ES = \frac{F_x}{\phi}$ (Eq. RE23)

5. Si l'équation RE22 est satisfaite, l'équilibre entre les efforts externes et internes est atteint, la position de l'axe neutre ainsi que les caractéristiques correspondantes de la section sont retenues. Si non, on répète les étapes de calcul de 1 à 4 en utilisant *la position de Yc* corrigé jusqu'à ce que le critère de convergence soit satisfait.

$$Y_{c(corrig\ )} = Y_{c(actuel)} + \frac{ES}{EA_s} \qquad \text{(Eq. RE24)}$$

6. L'arrêt du processus de calcul est gouverné par l'atteinte des critères de rupture implémentés à savoir l'écrasement du béton ou l'atteinte de la déformation ultime de l'acier. Une valeur cible de rupture du béton est fixée égale à 0.003 fois sa résistance en compression.

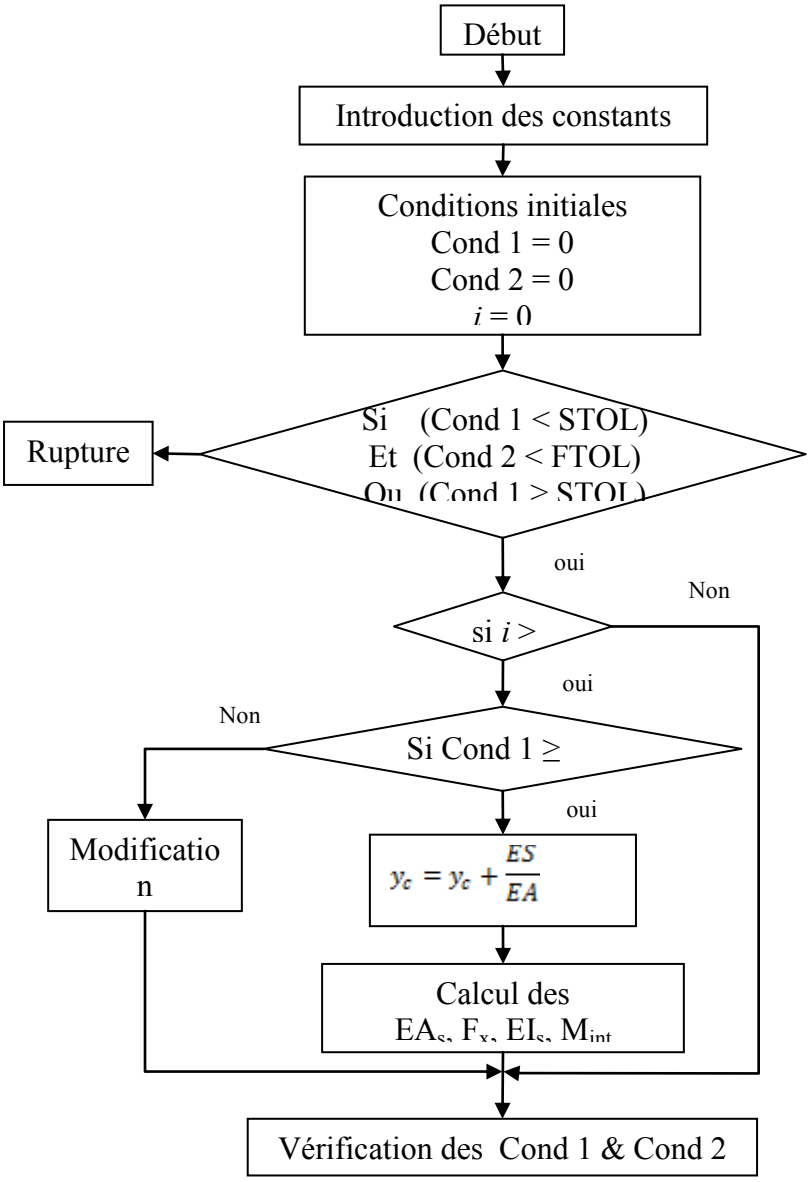

Fig. RE15 Organigramme du calcul numérique développé sous MATLAB

RE5.4 Analyse globale de l'élément

Le comportement global de l'élément est réalisé en utilisant une discrétisation verticale en se basant sur la variation du moment fléchissant le long de la poutre. L'effet de raidissement du béton en traction (tension stiffening), considéré pour une prédiction réaliste du comportement global permet le calcul d'une nouvelle relation moment-courbure. Le profil de courbure le long de la poutre associé à une certaine distribution du moment de fléchissant est alors estimé. La procédure développée pour l'analyse de la section est reprise pour calculer les courbures associées à un moment appliqué à chaque section (la poutre étant divisée en plusieurs sections droites). La rotation aux points de calcul le long de la poutre est obtenue en intégrant numériquement les courbures obtenues par l'analyse en section. L'effet cumulatif des rotations le long de la demi-travée est considéré pour une seconde intégration numérique qui permet alors d'obtenir le profil de la déformée de la poutre. Pour la flexion 4 points, cette intégration s'exprime par :

$$\Delta_{midspan} = \int_0^{L/2} x\varphi(x)dx \quad = \sum_{i=1}^{N_s} \frac{P}{2EI_{si}} \left[\frac{X_{i+0.5}^3 - X_{i-0.5}^3}{3}\right] + \frac{PL_a}{2EI_{si}} \frac{\left[\left(\frac{L}{2}\right)^2 - (L_a)^2\right]}{2} \qquad \text{(Eq. RE25)}$$

N_s est le nombre de segment le long de la poutre, *P est la force totale* ; $X_{i-0.5}$ est la distance de l'appui à l'origine du segment i; $X_{i+0.5}$ est la distance de l'appui à l'extrémité du segment i; L_a= distance entre l'appui et le point d'application de la force (figure RE16), and EI_{si}= rigidité flexionnelle du segment i. La figure RE17 montre la comparaison entre de la flèche mi-travée calculée et celle obtenue expérimentalement.

Le modèle de raidissement en traction appliqué dans l'analyse en section est alors corrigée en changeant les valeurs des quatre paramètres ; Cd, Cb, CP, Cs ainsi les valeurs de la courbe de force-déplacement issue du calcul numérique jusqu'à concordance des résultats numériques et expérimentaux. Les paramètres qui donnent la meilleure approximation sont adoptés comme valeur de référence définissant ce raidissement pour l'élément en béton avec de l'acier inox. Ces valeurs estimées par la méthode inverse donnent une représentation plus fiable des propriétés d'interaction entre l'acier inox et le béton.

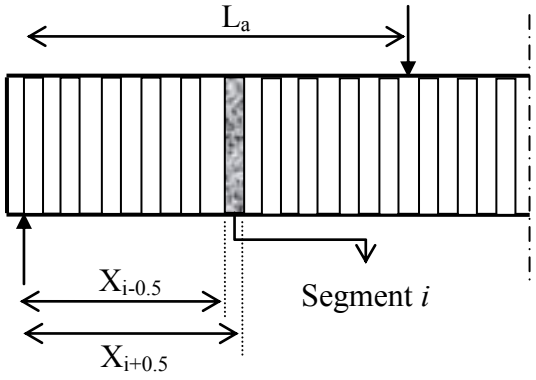

Fig. RE16 Discrétisation vertical de la poutre

RE5.5 Détermination des paramètres du modèle de raidissement en traction du béton

Les résultats obtenus à partir du calcul non linéaire sont comparés aux résultats expérimentaux afin de déterminer le modèle de raidissement en traction. Pour cela une poutre en béton avec des armatures inox est réalisée. Les corps d'éprouves choisis sont des poutres de section rectangulaires. Les caractéristiques géométriques et le schéma de ferraillage sont représentés sur la figure RE5. Les poutres sont placées dans un bâti approprié pour réaliser l'essai de flexion 4 points. Le dispositif d'essai est constitué d'un vérin équipé d'un chevêtre assurant la répartition de l'effort total appliqué en deux points de chargement symétrique par rapport à l'axe de la poutre. La poutre repose sur deux appuis simples pour éviter la mise en jeu d'un effort normal parasite dès que les flèches atteignent des valeurs significatives. La charge est appliquée de façon monotone croissante jusqu'à la rupture de l'élément. Le pilotage du vérin est réalisé par régulation en force. Cette flexion 4 points génère une zone de moment constant sur 0.9 m permettant d'obtenir un réseau de fissuration significatif en partie médiane de la poutre. La résistance en compression du béton est égale à 50 Mpa et le module instantané est égal à 37.5 MPa.

Le Tableau RE1 montre les quatre séries de valeurs testées des paramètres du C_d, le C_b, C_P, C_s. Basé sur les propriétés obtenues à partir de l'analyse en section (analyse non linéaire) et de l'analyse globale de l'élément, la comparaison avec des résultats expérimentaux donne les valeurs suivantes : $C_d = 0.9$; $C_b = 0.5$; $C_P = 5$ et $C_s = 13$.

En implémentant ces paramètres dans l'analyse non linéaire La courbe force déplacement obtenue est comparée avec celle déduite de l'expérimentation (figure. RE17). On constate une bonne concordance des résultats numériques et expérimentaux. La figure. RE18 montre que le modèle de raidissement en traction développé pour le comportement global d'un élément en béton armé avec des armatures inox de type austénitique. Ce modèle est implémenté dans le code de calcul par élément finis Abaqus.

Table RE1: Paramètres de raidissement en traction

Paramètres	Valeurs sélectionnées de C_d	Valeurs sélectionnées de C_b	Valeurs sélectionnées de C_p	Valeurs sélectionnées de C_s	Paramètres sélectionnés
C_d	0.8, **0.9**, 1	1.5	1.5	1.5	0.9
C_b	0.5	0.45, **0.5**, 1	0.8	0.8	0.5
C_p	4	4	4, **5**, 6	4	5
C_s	40	40	40	5, 10, **13**, 20	13

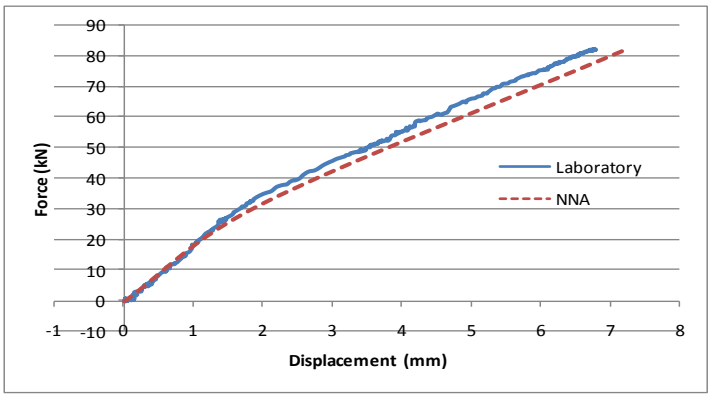

Fig. RE17 Courbes force-déplacement

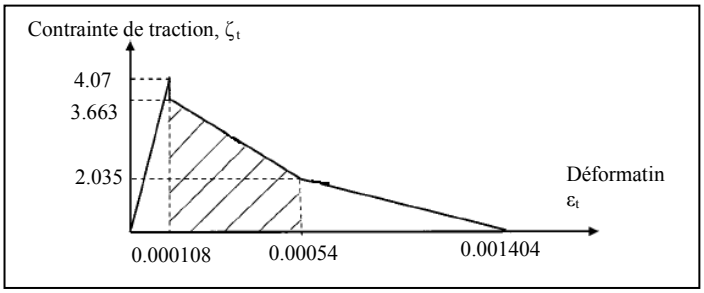

Fig. RE18 Modèle de raidissement en traction pour une poutre en béton armé avec des armatures inoxydable

Selon une étude entreprise par Nayal et Rasheed, 2006 [30], les valeurs choisies pour les paramètres de raidissement en traction pour une poutre en béton armé avec de l'acier carbone sont :Cd = 0.8, Cb= 0.45, CP = 4, et Cs = 10. La figure RE19 montre la comparaison entre les deux modèles pour l'acier inox et l'acier carbone.

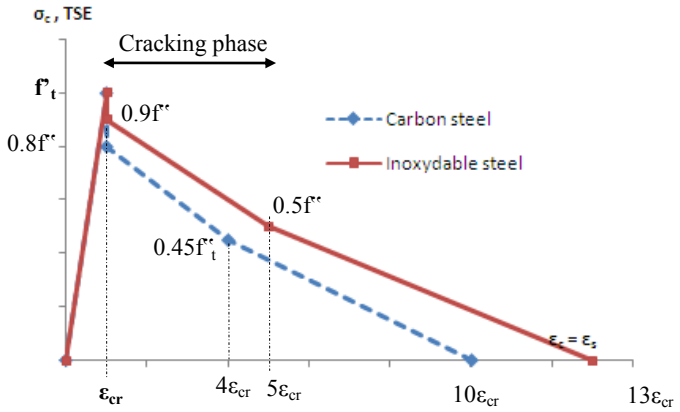

Fig. RE19 Comparaison des modèles de raidissement en traction du béton avec des armatures en acier inox et en acier standard.

On constate que l'effet de raidissement en traction provoqué par l'acier inoxydable est plus élevé que celui induit par l'acier standard utilisé en béton armé. Dans la phase de rupture, le raidissement avec de l'acier inoxydable augmente de 50 pour cent par rapport à l'acier standard.

RE6. Etude numérique par élément finis.

Un modèle éléments finis est développé avec le logiciel Abaqus (version 6.4). Ce logiciel permet de prendre en compte les non-linéarités géométriques et matérielles. L'interaction entre l'acier de renforcement et béton est également considérée. Pour la résolution des problèmes non linéaires, il y a deux méthodes de calcul; la méthode traditionnelle de Newton-Raphson (général statique), et la méthode de longueur d'arc de Riks (Riks statique). La première méthode est appliquée dans cette étude pour simuler le comportement des poutres en béton armé avec des armatures inox.

RE6.1 Stratégie de modélisation

Le béton est modélisé en utilisant des éléments 3-D à 8 nœuds. Les armatures sont modélisées en utilisant la formulation de type barre à 2 nœuds. Les barres sont traitées en tant que parties intégrantes de l'élément en béton en vue de simuler le transfert des efforts entre l‟acier et le béton.

Les charges sont appliquées à travers des plaques très rigides pour éviter les phénomènes locaux de concentration des déformations (figure. RE20(a)). La figure. RE20(b) montre la position de la cage d‟armatures. Les positions des jauges; J1, J2, J3, J4, J5, et J6 sont marquées avec précision le long de chaque barre comme le modèle expérimental (figure RE7).

Afin de développer un modèle fiable, nous avons fait varier le nombre d‟éléments du maillage entre 60 et 400. L'effet de la taille d'élément est vérifié en comparant le déplacement vertical obtenu à partir du calcul élément finis et celui mesuré au laboratoire (figure. RE21(a)). Le maillage à 396 éléments comme le montre la figure. RE21(b) donne des résultats concordants avec les essais. La figure RE22 montre les courbes force-déplacement numériques et expérimentales. On observe que le modèle MEF décrit de manière réaliste le comportement des poutres en béton.

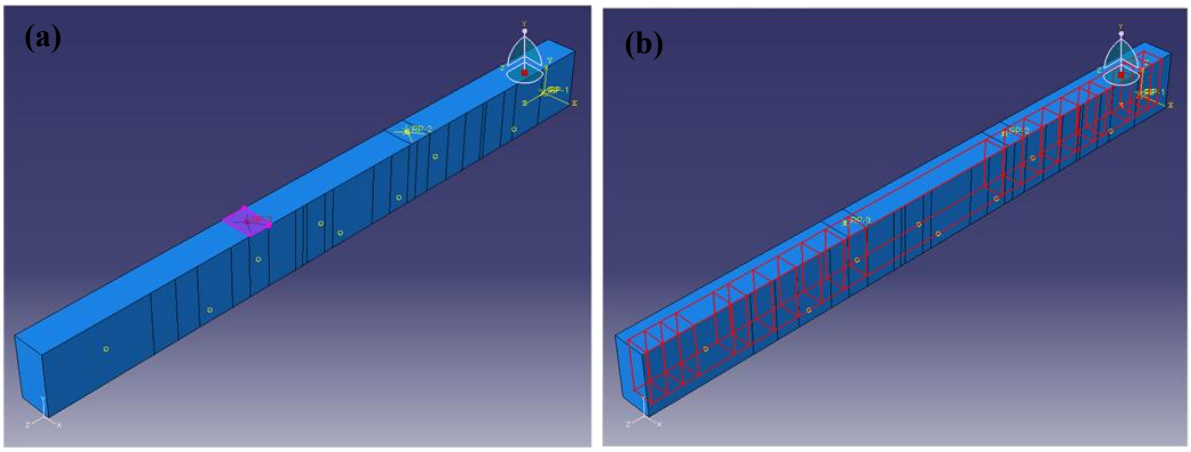

Fig. RE20 Modélisation de la poutre en béton armé (a) Force appliquée à travers une plaque rigide, (b) modèle de cage d‟armatures

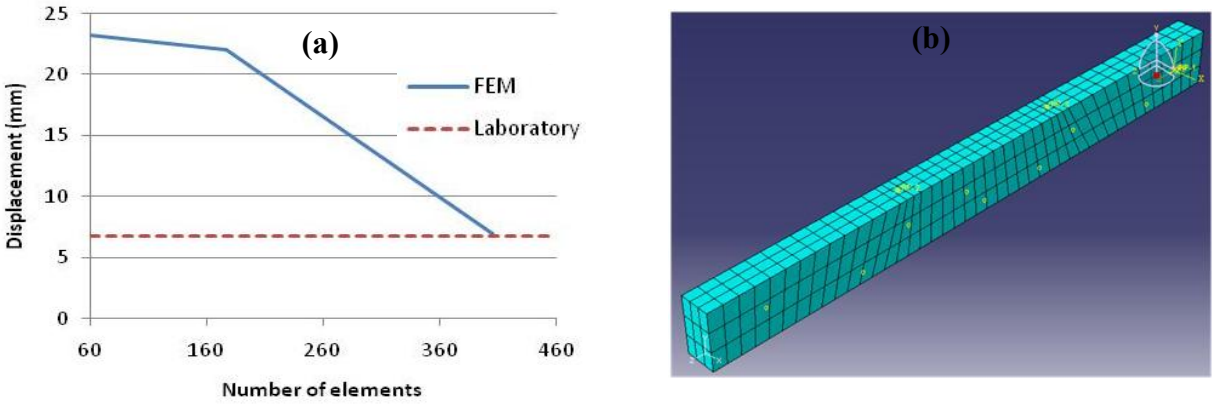

Fig. RE21 Exemple de maillage

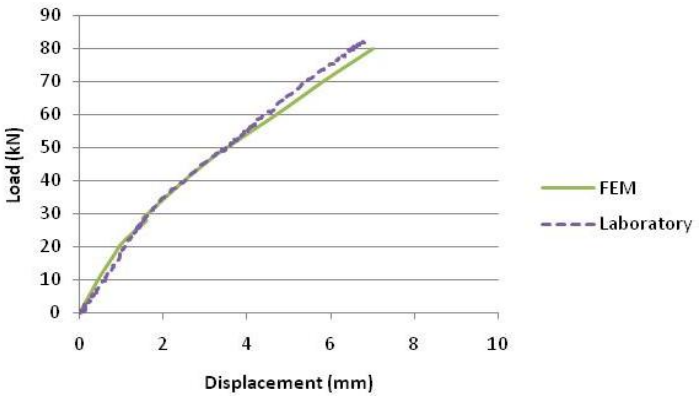

Fig. RE22 Courbes force – déplacement

L'effet d'adhérence entre béton et l'acier est modélisé en implémentant dans Abaqus le modèle de raidissement en traction développé ci-dessus.

RE6.3 Comparaison des résultats expérimentaux et numériques

La figure RE24 montre l'évolution des contraintes au niveau des positions des jauges J1 à J6 simulées dans le modèle (figure RE23). L'augmentation soudaine de contrainte simulant le phénomène de raidissement en traction est obtenu à 22kN de chargement. Les positions J3 et J4 montrent des valeurs de contraintes plus élevées durant tout le processus de chargement (figure RE25). Ceci est dû à leur position au centre de la poutre où le déplacement est maximal.

La figure RE26 montre la comparaison des courbes contrainte-effort dans les barres d'acier. Ces résultats font apparaître des écarts faibles par rapport à ceux issus des essais de laboratoire.

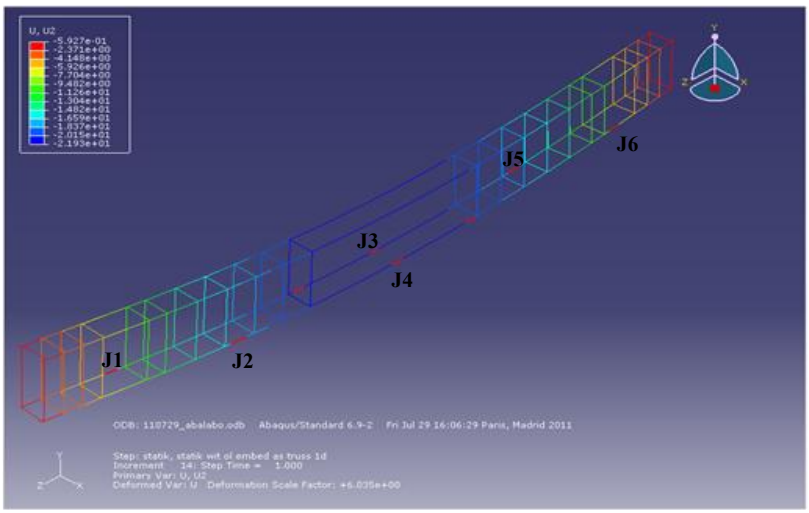

Fig. RE23 Résultats pour chaque position des jauges J1 à J6.

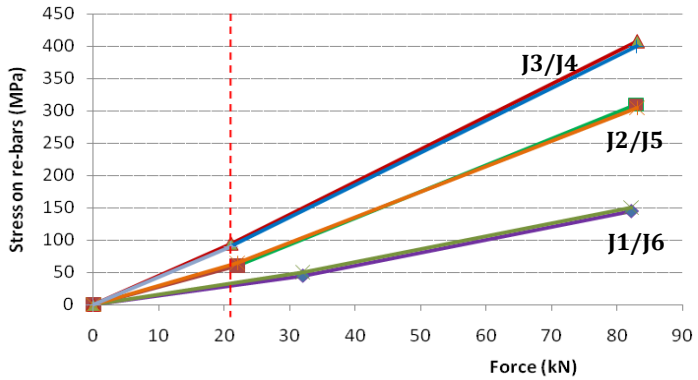

Fig. RE24 Contraintes calculées au niveau de la position des jauges en fonction de l‟effort appliqué

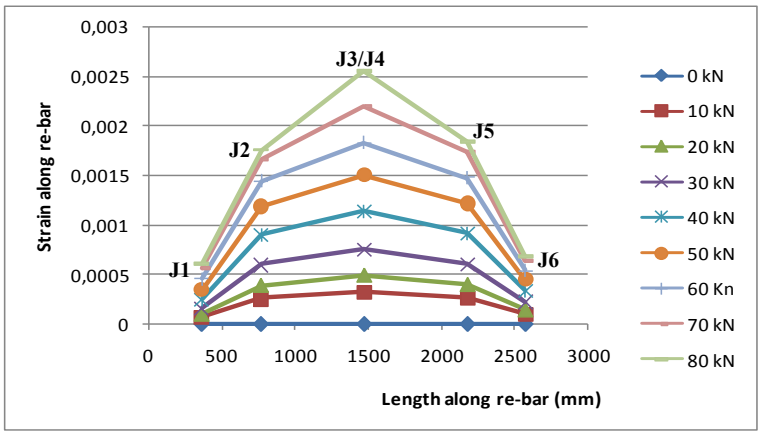

Fig. RE25 Déformations calculées le long de la barre

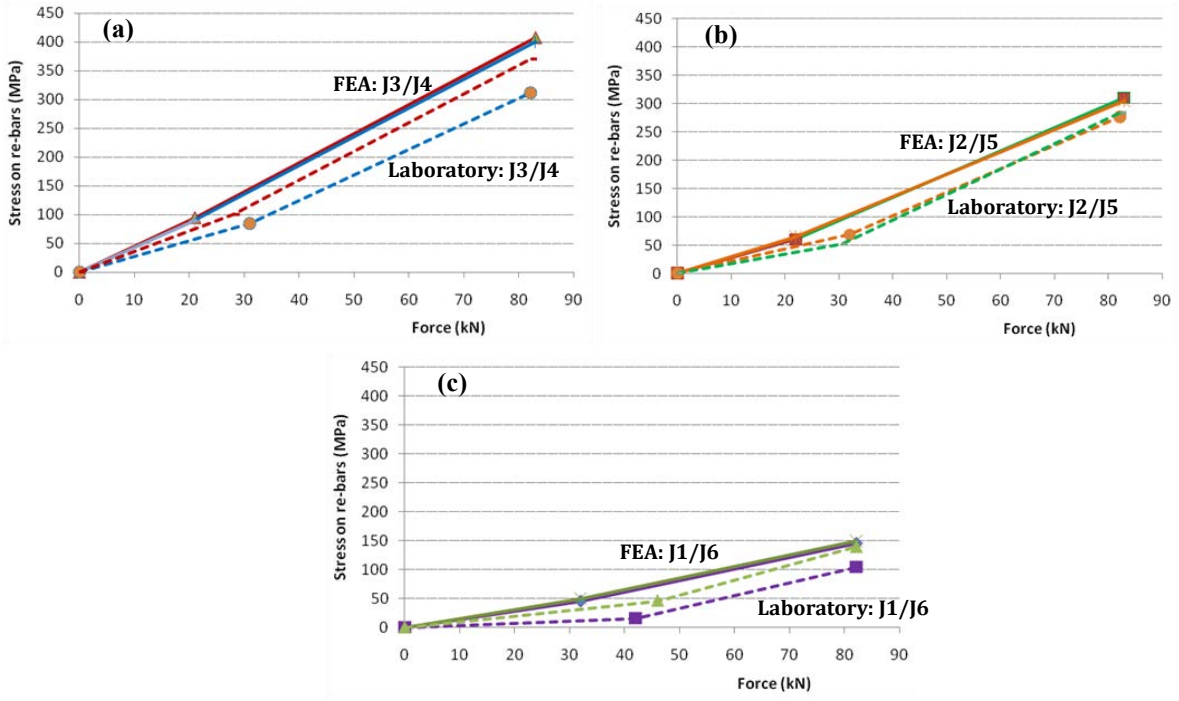

Fig. RE26 Contraintes dans les jauges: comparaison des résultats numériques et expérimentaux.

RE 7. Contributions originales :

- Développement d‟une nouvelle loi de comportement pour les aciers inox utilisés comme armatures dans le béton.
- Développement d‟un outil de modélisation du comportement d‟éléments en béton armé avec de l‟inox selon une discrétisation par couches horizontales pour la section et une discrétisation verticale pour l‟élément. En flexion, la modélisation repose sur la capacité de prédire d‟une part, le comportement d‟une section fissurée en intégrant l‟effet de raidissement et d‟autre part, le comportement global d‟une poutre fléchie.
- Implémentation du modèle de raidissement en traction du béton développé pour l‟acier inox dans le logiciel Abaqus. La comparaison entre les résultats expérimentaux et la prédiction du modèle démontre une très bonne concordance
- Etude de l‟effet de l‟acier inox sur les réponses structurales sous actions sismiques. Trois modèles sont conçus et analysés vis-à-vis de la capacité sismique en tenant compte de la ductilité structurale apportée par les armatures inox.

La suite de la thèse est écrite en anglais.

Chapter 1

1. Introduction

Inoxydable steel or Inox is a family of steels with corrosion and heat resistant containing a minimum of 10.5% chromium [1]. It is also widely known as stainless steel. Just as there is a wide range of structural and engineering carbon steels meeting different requirement of strength, weldability and toughness, so there is a wide range of inoxydable steel with progressively higher levels of corrosion resistance and strength. Results from the controlled addition of alloying elements, offer specific attributes with respect to strength and ability to resist different environments. Inoxydable steel or in short; inox, can be classified into families of austenitic, ferritic, austenitic-ferritic or duplex, and martensitic [2]. The classification is based on the chemical composition and thermal treatment. Each family shares the same basic behavior.

The use of inoxydable steel for structural applications in civil engineering is relatively limited. In construction, stainless steel is commonly used for secondary elements [3]. Stainless steel is used in construction for multiple reasons. Its high ductility is advantageous with respect to energy dissipation in the case of cyclic loading. This property enables loads to be redistributed before failure. It has excellent resistance to corrosion and can effectively be used to increase durability of reinforced structures exposed to aggressive environment [4]-[6]. This is one of the main advantages of inoxydable steel since corrosion in concrete leads to cracking, reduction of bond strength, reduction of steel cross section and loss of serviceability. Reinforced concrete undergoing corrosion does not only give the appearance of poor performance, but can in extreme cases, lose its structural integrity. Strength of a corroding reinforced concrete structure is reduced by both the loss in the area of steel and the loss in the bond between the corroding steel and the surrounding concrete. Low corrosion level decreased the fatigue bond strength by about 30% [5]. Inoxydable steel has also good aesthetic appeal, good resistance to fire and strong strain hardening characteristics [7].

The purpose of this study is to investigate the behavior of inoxydable steel, their performance when used in structural concrete elements such as beam and columns, and the effects of using this type of steel in structural frames. The austenitic type is chosen to be studied further because of their wide application in construction in annealed or cold worked states. In this study both types are studied and being referred as austenitic-hot, AH (type 304LN) and austenitic-cold, AC (type 4362), respectively. Detail investigation is conducted to determine the behavior of these steels as bare steel bar compare to carbon steel, CS (Grade 460). Samples are tested tension to determine the difference in their mechanical properties. The results are also used to develop a specific constitutive law targeted to the two types of austenitic.

The AH is studied further to determine their behavior as reinforcement bar in composite concrete beams. Focus is made on the interaction behavior with concrete and the tension stiffening phenomenon. This study highlighted an approach to observe this interaction behavior in bending test instead of direct tension as per reported in many references [8]-[12]. The approach and strategies proposed has been easier to set up. Their possibility to observe the tension stiffening behavior in composite concrete beams is then determined. Finally, the constitutive law developed and the tension stiffening properties are applied to numerical finite element analysis (FEA) to verify their correlation with actual behavior. FEA is conducted using ABAQUS software. Modeling strategies to simulate the actual condition of laboratory work is also elaborated. The constitutive laws, experimental work concept, and the FEA strategies used in this study could benefit future research in inoxydable steel and composite concrete.

Apart from developing the constitutive laws and material models of inoxydable steel in composite concrete, the effect of inox in structural element; beams and columns are also investigated. Different beam samples reinforced with inoxydable steels and standard carbon steel are constructed in laboratory and tested under bending for cyclic load case up to rupture. The high tensile strength and ductility of inox as per tested in the tensile test are compared with the carbon steel when they are applied in structural element. Different model of structural frames are also developed and simulated using seismic load in a computer program to determine the different performance between inox and standard carbon steel in resisting dynamic excitation. These analyses will be able to give an insight to the performance capacity and potential of inox to be used in structural element.

1. 1 Objectives

This study is conducted to have better understanding of inoxydable steel and their potential to be used in structural elements. It is based on three main objectives;

i) To study the behavior of inoxydable steel as reinforcing bars and develop a constitutive law to represent their nonlinear behavior

ii) To study the application of inoxydable steel in reinforced concrete composite and study the bonding behavior between inox and the surrounding concrete

iii) To determine the effect of inoxydable steel in structural elements and study the performance of the structure system as a whole when subjected to bending and seismic load.

1. 2 Significance of the Study

Despite the advantages of inoxydable steel and their potential application in construction, research on this type of steel is still limited as compared to carbon steel [13]. Their high cost often makes it a barrier to ordinary construction and used only in critical structure especially when longer lifetime is required. Inoxydable steel is mainly used in secondary elements and their utilization as reinforcement bars in composite concrete has not yet being explored in detail.

A new type of austenitic steel was chosen for further study. This new steel shown improved mechanical properties. Apart from conceiving the main advantages of austenitic family; high ductility and high corrosion resistance, its high strength could lower the overall cost by using smaller section as equivalent to bigger one with lower strength. Due to these benefits, this type of inox has the potential to be used further in construction and therefore studies on their behavior would become handy in the future. The constitutive law developed could represent the nonlinear behavior of this type of inox in any computer modeling works. The understanding of their interaction properties with concrete is advantageous if this type of

inox is to be used as reinforcing bars in composite concrete structural elements like beams and columns.

Inoxydable steel has been utilized in construction mainly to increase the lifetime of a structure due to its high resistance to contaminated atmosphere and corrosion. It has also been used as retrofit approach to repair existing structures. By determining the effects of inoxydable steel as reinforcing bars in structural elements of building, this study will provide an insight to extend the utilization of inox in construction works by means of providing higher strength and ductility, while maintaining the high resistance significant to the inox steel. This study also looked into the possibility of maximizing the benefits of inox by determining their optimal quantity and position in structural elements to increase the overall performance. If this could be achieved, not only will the structure have high resistance to different environmental conditions, but the higher strength and ductility could resist better load as well. In other words, not only does the maintenance cost could be lowered, the optimization on the structural design could reduce the construction cost too.

1. 3 Methodologies

This study is conducted in different stages to achieve the objectives (Fig. 1.1). To achieve the first objective, bibliography research is conducted to study the background of inoxydable steel. Laboratory work is then conducted to determine mechanical properties of inox sample from austenitic type, together with the ordinary construction steel bar. A series of tensile test is carried out on these types of steel in the form of whole reinforcing bar, and small sample. Results are then analyzed and used to develop the constitutive laws.

Major work is conducted to study the application of inoxydable steel in reinforced concrete composite and their interaction properties (Objective 2). This involved laboratory work, nonlinear numerical analysis, and finite element modeling. Composite concrete beams reinforced with different types of inoxydable steel and carbon steel are prepared with strain gauges attached along the reinforcement bars and concrete surface. These samples are tested under bending to verify the interaction properties between inox and concrete for each load increment. Results from laboratory work are combined with nonlinear numerical analysis

(NNA) of the beam sections to develop the interaction model. Programming language Matlab is used to run the NNA. The interaction model and constitutive law of inox are then applied to finite element modeling to verify the proposed model with the laboratory results. ABAQUS software is used for the solid modeling of the beam sample.

In order to determine the effects of inoxydable steel in structural elements and to the overall performance of the structure (Objective 3), laboratory work and finite element modeling are conducted. Concrete beam reinforced with different types of inoxydable steel is prepared and tested under cyclic loading, until rupture. Load-deflection response for these structural elements is analyzed and compared to the same concrete model reinforced with standard carbon steel. The behavior of inoxydable steel in reinforced concrete frame is also investigated. Simulation is conducted using SAP2000 software. The analysis involved similar material properties of the beam element. The beam, column, and building frame are also subjected to earthquake load and analyzed through free vibration analysis, time history analysis, and push-over analysis. The effect of using inoxydable steel in the structural elements when it is subjected to earthquake load are then analyzed. The effect of using inoxydable steel in certain location in the beam and column for the development of plastic hinge in the structure, damage position, and failure is discussed. Improvement in the overall performance of the structure by maximizing the benefits of inox will then be verified.

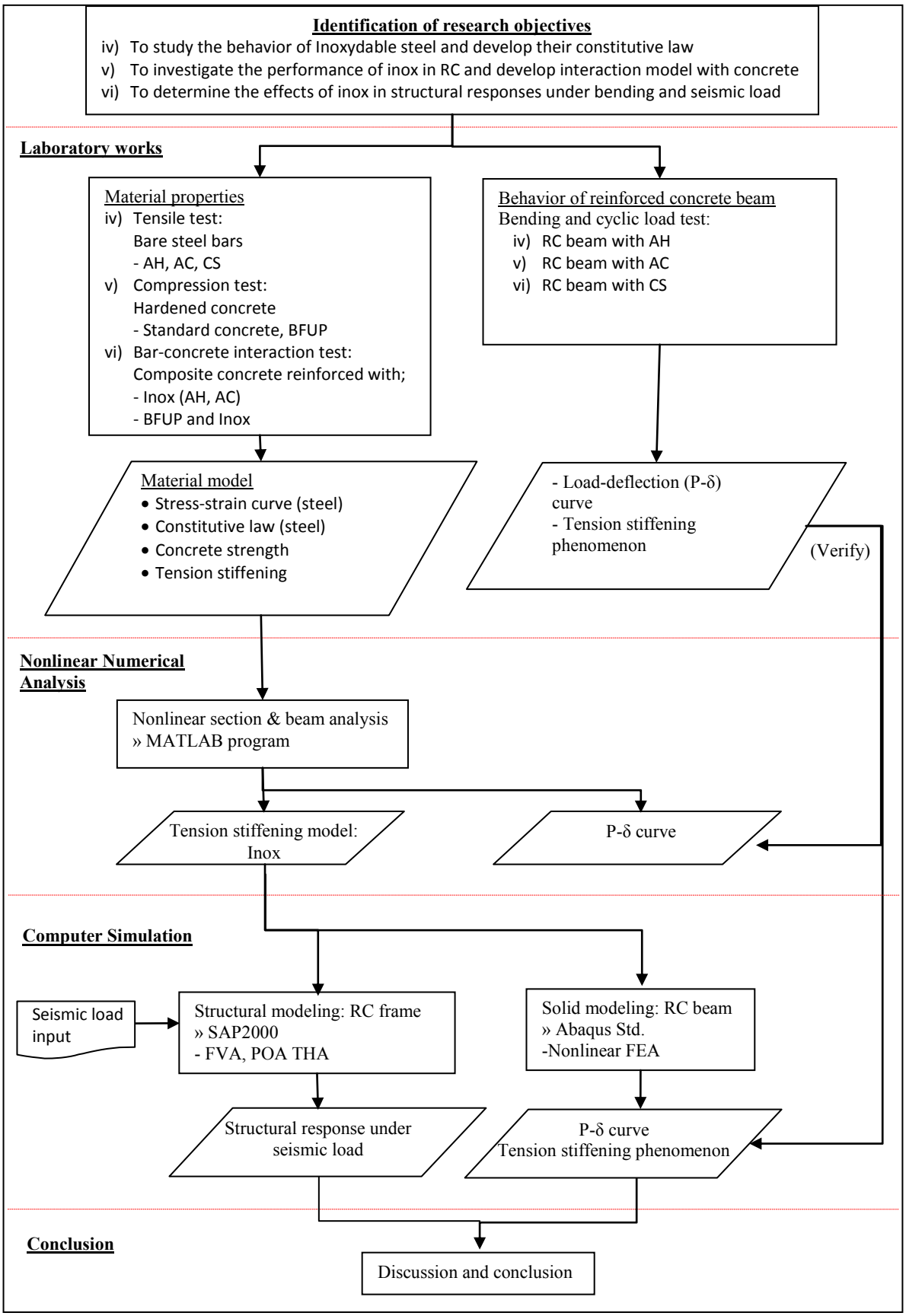

Fig. 1. 1 Summarization of methodologies involved

1. 4 Arrangement of Thesis

This thesis consists of four main chapters. The arrangement is as follows;

v) Chapter 1: Introduction

- This chapter briefly introduces the overall background of this study; the objectives, significance of the topic chosen, and work flow involved.

vi) Chapter 2: Bibliography

- This chapter focuses on literature review and general theoretical background of topics involved in the study.
- Inoxydable steel background, their application in construction industry are discuss followed by their material properties as bare steel bars, and the interaction properties when used as reinforcing bars in composite concrete.
- Analysis to verify the structural responses is discuss in the end of the chapter.

vii) Chapter 3: Material Models

- This chapter focuses on the behavior of inoxydable steel and the material model when it is used in composite concrete beams.
- New constitutive law is developed for inox.
- Interaction properties with surrounding concrete are discussed.
- This chapter covers Objective 1 and Objective 2.

viii) Chapter 4: Inoxydable Steel in Structural Elements

- This chapter discusses the effects of inoxydable steel in structural elements and building frames. Discussion is made on the plastic hinge development, yield and damages, energy dissipation, and maximization of overall structural performance.
- Findings are compared with carbon steel
- This chapter covers Objective 3.

Chapter 2

2. Bibliography

Iron and the most common iron alloy, steel, from a corrosion viewpoint, are poor materials since they rust in air, corrode in acids and scale in furnace atmospheres. In spite of this, there is a group of iron-base alloys, the iron-chromium-nickel alloys known as inoxydable steel, that do not rust in sea water, resistant concentrated acids and do not scale at temperatures up to 1100°C [14]. This is largely a unique universal usefulness, in combination with good mechanical properties and manufacturing characteristics, which gives the inoxydable steel their advantages and makes them an indispensable tool for designers. The usage of inoxydable steel is small compared with that of carbon steels but exhibits a steady growth, in contrast to the constructional steels. Inoxydable steels as a group is perhaps more heterogeneous than the constructional steels, and their properties are in many cases relatively unfamiliar to the designer. In some ways inoxydable steels are an unexplored world but to take advantage of these materials will require an increased understanding of their basic properties. The following chapters aim to give an overall picture of the "inoxydable world" and what it can offer from the construction point of view.

2. 1 Types of Inoxydable Steel

There are different types of inoxydable steel for which it is classified based on the chemical composition and thermal treatment. They can be classified into four main groups according to their metallurgical structure; austenitic, ferritic, austenitic-ferritic or duplex, martensitic. Each family shares the same basic behavior. Among these families of inox, austenitic is the most utilized and represents 70% of the inoxydable steel in the market. This is followed by ferritic; 29%. The other two families only represent 1% from the total market. The demand and utilization of inox is based on their behaviors that suit the purpose of the project. Behavior of each group will be discussed briefly.

i) Austenitic

The austenitic steels are characterized by very good corrosion resistance, very good toughness and very good weldability. The austenitic steels are used in almost all types of applications and industries. Typical areas of use include piping systems, heat exchangers, tanks and process vessels for the food, chemical, pharmaceutical, pulp and paper and other process industries. Austenitic steels are often used in applications requiring non-magnetic materials since they are the only non-magnetic steels [15]. In construction industry, austenitic type of inoxydable steel is widely used compared to the other inox families.

Austenitic can be divided in three groups based on the alloying composition; low-carbon grades, high-alloyed, and high-alloyed heat resistance. The low-carbon grades exhibit good resistance to intergranular corrosion. The high alloyed steels; high carbon grades (AISI 304H) and stabilized steels (AISI 321, 347 and 316Ti) or nitrogen-alloyed steels (AISI 304LN and 316LN) are used at elevated and moderately high temperatures depending on the service temperature and environment. The high alloyed heat resistant grades, such as „353MA", are used in aggressive high temperature environments (above about 750 °C), such as those encountered in waste incineration.

ii) Ferritic

The ferritic steels are characterized by good corrosion properties, very good resistance to stress corrosion cracking and moderate toughness. The toughness of ferritic stainless steels is generally not particularly high. Lower carbon and nitrogen levels, as in AISI 444, give a considerable improvement in both toughness and weldability, although toughness is limited for thicker dimensions. Use of ferritic includes piping, heat exchanger tubes, vessels and tanks in the food, chemical and paper industries. It can also be used in water with moderately high level of chlorides in applications where there is a danger of stress corrosion cracking. Low alloyed ferritic stainless steels are also used in mild environments where freedom from maintenance is sought or where a „non-rusting" material is required.

iii) Duplex

The modern duplex steels have the same wide range of corrosion resistance as the austenitic steels. This type of inox is characterized by high strength, good toughness, very good corrosion resistance in general and excellent resistance to stress corrosion cracking and corrosion fatigue in particular [16]. An increased level of chromium, molybdenum and nitrogen increases corrosion resistance, while the higher nitrogen level also contributes to a further increase in strength above that associated with the duplex structure.

Applications of duplex steels are typically those requiring high strength, good corrosion resistance and low susceptibility to stress corrosion cracking or combinations of these properties. Some examples of such applications are: hot water tanks in the breweries, pulp storage towers in the pulp and paper industry, tanks for storage of chemical in the chemical process industry and tank farms in tank terminals in the transportation industry. It is also used in piping systems, heat exchangers, tanks and vessels for chloride-containing media in the chemical industry, in piping and process equipment for the oil and gas industry, in cargo tanks in ships for transport of chemicals, and in shafts, fans and other equipment which require resistance to corrosion fatigue. It is used in offshore industry (oil and gas) and in equipment for environments containing high chloride concentrations, such as sea water.

iv) Martensitic

The steels in this group are characterized by high strength and limited corrosion resistance [17]. An increased carbon content increases strength, but at the expense of lower toughness and considerable degradation of weldability. The martensitic stainless steels are resistant to damp air, steam, freshwater, alkaline solutions (hydroxides) and dilute solutions of organic and oxidizing inorganic acids. The areas of use of martensitic steels are naturally those in which the high strength is an advantage and the corrosion requirements are relatively small. The martensitic steels with low carbon are often used as stainless constructional materials. The martensitic steels with high carbon content are used for springs, surgical instruments and for sharp-edged tools such as knives and scissors.

2. 2 Application of Inoxydable Steel in Construction

The physical characteristics of inoxydable steel makes it well suited to use in construction; it possesses high strength and stiffness (comparable with carbon steel), very high ductility (approximately two times that of carbon steel), and excellent corrosion resistance, which means, suitably specified that it requires no protective coatings [18]. Inoxydable steel also offers better retention of strength and stiffness than carbon steel at elevated temperatures [19]. The principal disincentive for the application of stainless steel in construction is the initial material cost, though considered on a whole life basis, cost comparisons with carbon steel become more favorable.

The use of inoxydable steel for structural applications in civil engineering is relatively limited despite of their benefits (Fig. 2.1). In construction, inoxydable steel is commonly used for secondary elements [3]. It is also applied in structural element as reinforcement bars in composite concrete and as rehabilitation materials. They can be joined to the ribbed carbon steel that reinforces structures using traditional un-welded laps, mechanical couplers or welding. The last joining technique is especially interesting when stainless steel reinforcements are used to restore structures that already exhibit serious corrosion damage, because it can reduce the amount of concrete that must be removed during the process [20].

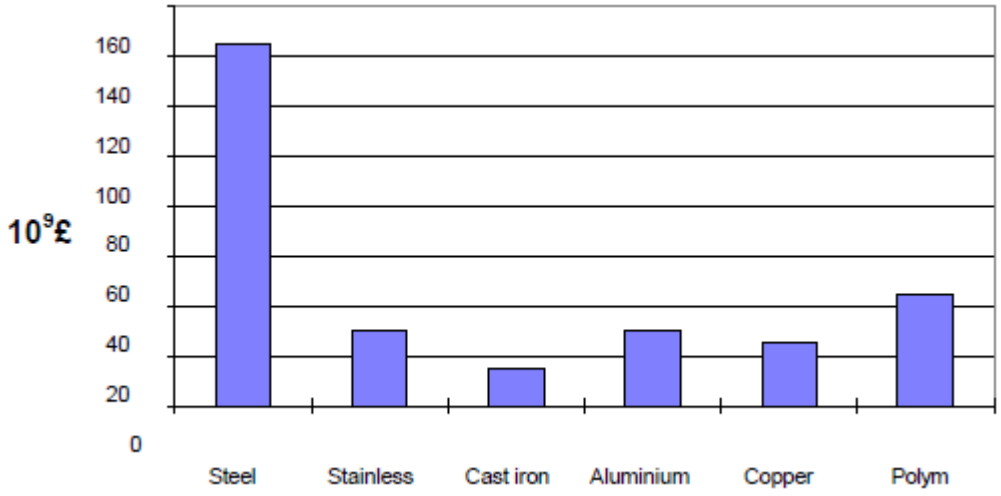

Fig. 2. 1 World consumption various materials in the middle of 1980"s [3]

Despite of their limited application in construction as compared to the standard carbon steel, inoxydable steel has their own advantages and potential. With improving design guidance, wider product availability and a greater emphasis now being placed on the whole life performance of structures, the use of inoxydable steel in structural applications is increasing [21]. This type of steel is used in construction for multiple reasons including;

i) Corrosion resistance

- It has excellent resistance to corrosion and can effectively be used to increase durability of reinforced structures exposed to aggressive environment [22].
- Study conducted by Gu, P., et. al. [23] shows that the corrosion rate of stainless steel reinforcement is at least 50 times lower than that of black steel in chloride contaminated concrete. This is one of the main advantages of inoxydable steel since corrosion in concrete leads to cracking, reduction of bond strength, reduction of steel cross section and loss of serviceability.
- Reinforced concrete undergoing corrosion does not only give the appearance of poor performance, but can in extreme cases, lose its structural integrity.
- Strength of a corroding reinforced concrete structure is reduced by both the loss in the area of steel and the loss in the bond between the corroding steel and the surrounding concrete.
- Low corrosion level decreased the fatigue bond strength by about 30% [5].

ii) Controllable mechanical properties

- Strength of each inoxydable steel is adjustable based on the composition of alloy used in the manufacturing process.
- Figure 2.2 shows the variety of strength level for the inox families.
- Martensitic steels have high yield and tensile strength but low ductility due to the increase in carbon, while austenitic grades have low yield strength and excellent ductility due to the amount of nickel. Ferritic-austenitic or duplex and ferritic steels both lie somewhere between these two extremes.
- The ferritic steels generally have somewhat higher yield strength than the austenitic steels, while the ferritic austenitic steels have appreciably higher yield strength than both austenitic and ferritic steels. The ductility of the

ferritic and ferritic-austenitic steels is of the same order of magnitude, even if the latter are somewhat superior in this respect.

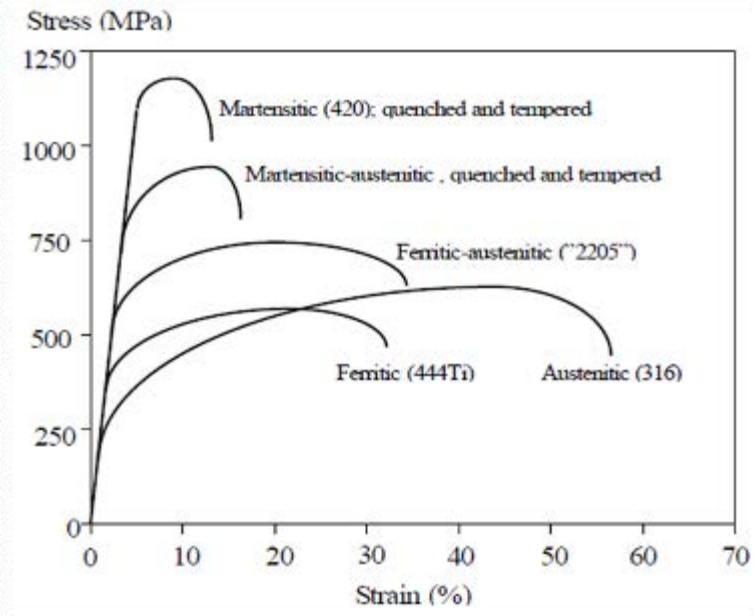

Fig. 2. 2 Different strength level for the inoxydable steel families [1]

iii) High ductility and deformation capacity

- Compared to the ordinary carbon steel, inoxydable steels have high ductility.
- This is advantageous with respect to energy dissipation in the case of cyclic loading and enables loads to be redistributed before failure.
- It is also related to the behavior factor of the overall structure.
- Study conducted by Choi, J.H. [24] shows a significant improvement in flexural strength and ductility can be achieved using inoxydable steels.

Inoxydable steels have also good aesthetic appeal, good resistance to fire and strong strain hardening characteristics.

The utilization of inoxydable steel as reinforcement bars could extend the lifetimes of reinforced concrete structures. When it comes to building or repairing reinforced concrete structures so that life-cycle costs are minimized, many authorities are specifying the use of

inoxydable steel reinforcing bars instead of the traditional carbon steel re-bars. Inox containing molybdenum (Mo) are the alloys of choice when inoxydable rebar is specified. Molybdenum is added to several grades of inox to improve corrosion resistance, particularly pitting and crevice corrosion resistance in chloride-containing solutions. Commonly specified alloys for rebar are shown in Table 1.

Table 2. 1 Inoxydable steel commonly used for rebar (nominal compositions in weight %):

Grade	Types	Cr	Ni	Mo	N	C (max)	Resistance to chlorides
Type 316	Austenitic	17	12	2.5		0.08	Good
Type 316L	Austenitic	17	12	2.5		0.03	Better when welded
Type 316LN	Austenitic	17	12	2.5	0.13	0.03	Better when welded
Alloy 2205	Duplex	20	5	3.0	0.14	0.03	Best

These alloys can provide long-term corrosion resistance when concrete is exposed to chloride-containing environments, for example road salts and sea water. They have been used as rebar in highways bridges, ramps and barrier walls, parking garages, tunnels, sea walls and marine facilities, building foundations and restorations.

The US Federal Highway Administration (FHWA) organized extensive corrosion testing to find rebar materials that could extend the lifetime of reinforced concrete bridges to 75-100 years, when the concrete was contaminated to chlorides. Their 1998 report (FHWA-RD-98-153) concluded that Type 316 inoxydable steel rebars would be capable of providing that required lifetime.

In Europe, Mo-containing inoxydable steel rebars have been widely used since the mid-80s. in North America, their use in highway bridges has been steadily growing since the mid-90s, with many large bridges being constructed or extensively repaired. Listed in Table 2 are just a few examples of projects that have used inoxydable steel rebars.

Table 2. 2 Examples of projects using inoxydable steel rebar

Project	**Inoxydable Steel used**
Bridge on I 696, near Detroit, MI (1984)	Type 304 rebars
Underpass, near Newcastle, Tyneside, UK (1995)	Type 316 rebars
Bridge on Highway 407, near Toronto, Canada (1996)	Type 316LN rebars
Highway project near Ajax, Ontario, Canada (1998)	Type 316LN rebars
Ramp for Garden State Parkway, New Jersey (1998)	Alloy 2205 rebars
Smith River Bridge, Oregon (1998)	Type 316LN rebars
Haynes Inlet Slough Bridge, Oregon (2003)	Alloy 2205 rebars
Broadmeadows Bridge, Ireland (2003)	Type 316 rebars
French Creek, Chautauqua Co., NY (2003) (Fig. 2.4)	Type 316LN rebars
South Work St. Bridge, Falconer, NY (2004)	Alloy 2205 rebars
Bridge on I 29, Sioux Falls, South Dakota (2004)	Alloy 2205 rebars
Belt Parkway Bridge, Brooklyn, NY (2004)	Alloy 2205 rebars
Driscoll Bridge, NJ (2005)	Mostly Alloy 2205 rebars
Thorold Tunnel, Ontario, Canada	Type 316LN rebars
Woodrow Wilson Bridge linking Virginia and Maryland	Type 316LN rebars & Alloy 2205
Parking garage, Brighton, MA	Type 316LN rebars & Type 304L

Inoxydable steel rebar is substituted for carbon steel rebar only in critical parts of the structure that will experience corrosive conditions. For bridges, experience now indicates that the total project cost can increase by only 3% when using inoxydable steel rebars. The actual cost increase will, of course, depends on the size and complexity of the bridge.

The use of Mo-containing inoxydable steel rebars is expected to continue to increase as the authorities demand much lower maintenance costs, fewer disruptions and longer lifetimes for their bridges and other important concrete structures.

Fig. 2. 3 Inoxydable steel components for concrete reinforcing: rebar, U-bent rebar, threaded rebar, tie-wire and rebar coupler [2].

Fig. 2. 4 Installation of inoxydable steel rebar at the French Creek Bridge, Chautauqua Co., NY [22].

2. 3 Composition of Inoxydable Steel

The variety of mechanical properties in each of the inoxydable steel families depends on the type and composition of alloy used in the manufacturing process. Different grades in the same families of inox can have different properties due to the effects from alloying elements. These effects will be briefed in the following section. It should also be noted that

the effect of the alloying elements differs in some aspects between the hardenable and the non-hardenable inox. Hardenable means that it is possible to modify the properties of inox via heat treatment in the same way as for hardenable carbon steels. Martensitic is hardenable inoxydable steel. The other three categories; ferritic, ferritic-austenitic (duplex) and austenitic are not hardenable, but are basically used in the as received condition.

The alloying element used in the manufacturing of inoxydable steel and their effects are as follows [1]:

i) Chromium (Cr)

This is the most important alloying element in inoxydable steel. This element gives the inox their basic corrosion resistance. The corrosion resistance increases with increasing chromium content. It also increases the resistance to oxidation at high temperatures. Chromium promotes a ferritic structure.

ii) Nickel (Ni)

The main reason for the nickel addition is to promote an austenitic structure. Nickel generally increases ductility and toughness. It also reduces the corrosion rate and is thus advantageous in acid environments. In precipitation hardening steels nickel is also used to form the inter-metallic compounds that are used to increase the strength.

iii) Molybdenum (Mo)

Molybdenum substantially increases the resistance to both general and localized corrosion. It increases the mechanical strength somewhat and strongly promotes a ferritic structure. Molybdenum also promotes the formation secondary phases in ferritic, ferritic-austenitic and austenitic steels. In martensitic steels it will increase the hardness at higher temperatures due to its effect on the carbide precipitation.

iv) Copper (Cu)

Copper enhances the corrosion resistance in certain acids and promotes an austenitic structure. In precipitation hardening steels copper is used to form the inter-metallic compounds that are used to increase the strength.

v) Manganese (Mn)

Manganese is generally used in stainless steels in order to improve hot ductility. Its effect on the ferrite/austenite balance varies with temperature: at low temperature manganese is an austenite stabilizer but at high temperatures it will stabilize ferrite. Manganese increases the solubility of nitrogen and is used to obtain high nitrogen contents in austenitic steels.

vi) Silicon (Si)

Silicon increases the resistance to oxidation, both at high temperatures and in strongly oxidizing solutions at lower temperatures. It promotes a ferritic structure.

vii) Carbon (C)

Carbon is a strong austenite former and strongly promotes an austenitic structure. It also substantially increases the mechanical strength. Carbon reduces the resistance to inter-granular corrosion. In ferritic stainless steels carbon will strongly reduce both toughness and corrosion resistance. In the martensitic and martensitic-austenitic steels carbon increases hardness and strength. In the martensitic steels an increase in hardness and strength is generally accompanied by a decrease in toughness and in this way carbon reduces the toughness of these steels.

viii) Nitrogen (N)

Nitrogen is a very strong austenite former and strongly promotes an austenitic structure. It also substantially increases the mechanical strength. Nitrogen increases the resistance to localized corrosion, especially in combination with molybdenum. In ferritic stainless steels nitrogen will strongly reduce toughness and corrosion resistance. In the martensitic and martensitic-austenitic steels nitrogen increases both hardness and strength but reduces the toughness.

ix) Titanium (Ti)

Titanium is a strong ferrite former and a strong carbide former, thus lowering the effective carbon content and promoting a ferritic structure in two ways. In austenitic steels, it is added to increase the resistance to inter-granular corrosion but it also increases the mechanical properties at high temperatures. In ferritic

stainless steels, titanium is added to improve toughness and corrosion resistance by lowering the amount of interstitials in solid solution. In martensitic steels, titanium lowers the martensite hardness and increases the tempering resistance; a process of hardening or strengthening metal by application of heat or by heating and cooling. In precipitation hardening steels titanium is used to form the inter-metallic compounds that are used to increase the strength.

x) Niobium (Nb)

Niobium is both a strong ferrite and carbide former. As titanium it promotes a ferritic structure. In austenitic steels, it is added to improve the resistance to inter-granular corrosion but it also enhances mechanical properties at high temperatures. In martensitic steels niobium lowers the hardness and increases the tempering resistance. In U.S. it is also referred to as Columbium (Cb).

xi) Aluminium (Al)

Aluminium improves oxidation resistance, if added in substantial amounts. It is used in certain heat resistant alloys for this purpose.

xii) Cobalt (Co)

Cobalt only used as an alloying element in martensitic steels where it increases the hardness and tempering resistance, especially at higher temperatures.

xiii) Vanadium (V)

Vanadium increases the hardness of martensitic steels due to its effect on the type of carbide present. It also increases tempering resistance. Vanadium stabilizes ferrite and will, at high contents, promote ferrite in the structure. It is only used in hardenable stainless steels.

xiv) Sulphur (S)

Sulphur is added to certain stainless steels, the free-level machining grades, in order to increase the machinability. At the present in these grades sulphur will substantially reduce corrosion resistance, ductility and fabrication properties, such as weldability and formability.

xv) Cerium (Ce)

Cerium is one of the rare earth metals (REM) and is added in small amounts to certain heat resistant temperature steels and alloys in order to increase the resistance to oxidation and high temperature corrosion.

2. 4 Inoxydable Steel in Composite Concrete

In reinforced concrete structures, the presence of steel necessitates the consideration of bar-concrete interaction. The bond between concrete and reinforcing bars is one of the main of traits in reinforced concrete study [25]. The bar-concrete adherence allows the concrete located between cracks to resist tensile stresses, thereby reducing the average reinforcement stress level compared to its magnitude at the crack. This phenomenon results in a gain in rigidity, called tension stiffening.

Referring to Fig. 2.5(b), tension stiffening is described as the stress difference $\sigma_{S,TSE}$ between the steel stress σ_S of the reinforced concrete member and the stress $\sigma_{S,II}$ of bare steel at a given strain. The stress increase $\sigma_{S,TSE}$ can be replaced by an equivalent concrete stress $\sigma_{C,TSE}$ which can be determined as [8],

$$\sigma_{C,TSE} = \rho_{eff}\sigma_{S,TSE} \tag{2.1}$$

where, $\sigma_{S,TSE} = (\sigma_S - \sigma_{S,II})$ (2.2)

$$\rho_{eff} = A_s \,/\, A_{c,eff} \tag{2.3}$$

A_s = sectional area of the steel

$A_{c,eff}$ = effective zone of the concrete

ρ_{eff} is the effective reinforcement ratio, and $A_{c,eff}$ is the effective zone of concrete around the re-bars which can be determine according to Eurocode 2: Part 1-1 [26]; $A_{c,eff}$ is the effective zone of concrete around the rebars for the height of $h_{c,ef}$ as illustrated in Fig. 2.6, $h_{c,ef}$ is the smallest value between 2.5 $(h-d)$, $(h-x)/3$, and $^{h}/_{2}$.

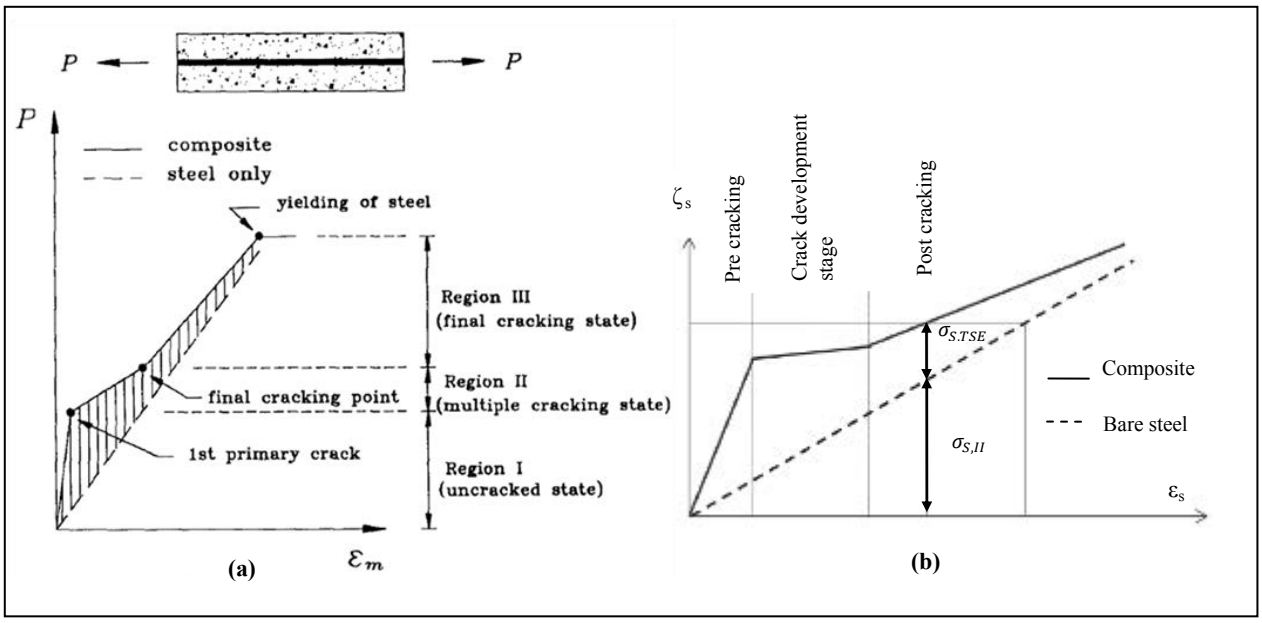

Fig. 2. 5 Phenomenon to account for tension stiffening effect in RC sample under uniaxial tension (a) load-average strain curve [27], (b) stress-strain relationship for a composite and embedded reinforcing bar [8], [9].

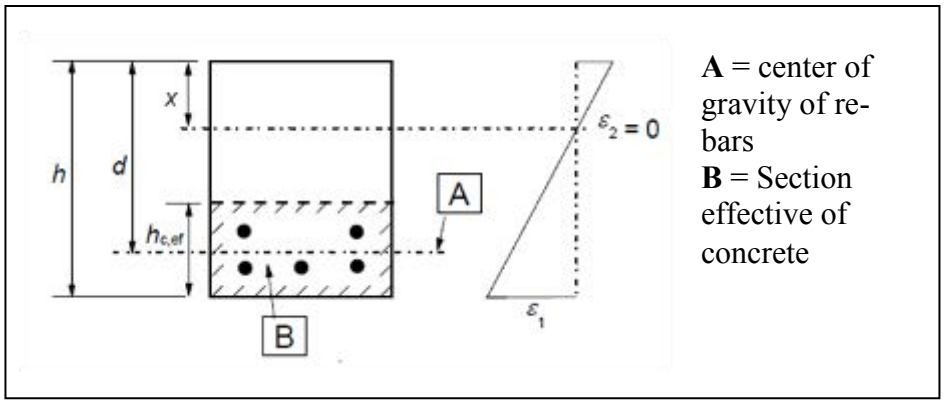

Fig. 2. 6 Determination of section effective of concrete around re-bars for beam as per recommended by Eurocode 2: Part 1-1 [26].

The stress-strain curve for reinforced concrete under uniaxial tension can be divided in three regions; pre cracking, crack development stage, and post cracking [9] as shown in Fig. 2.5. Before cracks start to form (pre cracking), concrete are able to resist tensile stress. These results in a higher stress level in concrete as shown in Fig. 2.8. When cracks start to form (crack development stage), concrete slowly looses their ability to resist tensile stress and so the stress level decreases. With the increase in formation of cracks (post cracking), stress in concrete decreases and more stresses will be carried by the reinforcement bars.

Reinforcement stress level increases evidently after the formation of cracks. The tensile capacity of concrete; tension stiffening effect, contribute to structural stiffness over the entire pre-cracking and post-cracking stage [28], [50].

2.4. 1 Tension Stiffening Model

A simple way to account for this local phenomenon is to integrate the bar-concrete interaction in a global dimension by modifying the stress-strain relationship of the material, either the reinforcing bar or the concrete [29]. When this effect is considered in concrete model, Eq. (2.1) is used. Several investigators have developed the tension stiffening model by modifying the concrete material model as shown in Fig. 2.5 [30]. Scanlon and Murray (1974) were the first to model tension stiffening in terms of the degraded concrete modulus as shown in Fig. 2.5. Lin and Scordelis (1975) considered another model having a polynomial branch in their study of concrete slabs and shells as shown in Fig. 2.8. Vebo and Ghali (1977) proposed a linear and a bilinear descending branch in their analysis of concrete slabs, showing the latter to correlate better with experimental results.

Gilbert and Warner (Fig. 2.7(d)) proposed two basically different approaches for taking tension stiffening into account in a layered finite-element analysis of reinforced concrete slabs. In the first approach, concrete post-cracking response in the tension zone was ignored while its effect was lumped at the steel reinforcement level. The second approach allowed for concrete post-peak softening. They examined the Scanlon and Murray stepped model, the Lin and Scordelis model, and a modified version of Vebo and Ghali‟s bilinear model, considering a discontinuity at initial cracking (Figs. 2.7 (a–d)). Gilbert and Warner assigned different model parameters to different tension layers, depending on their proximity to steel reinforcement. This consideration required an extra book-keeping effort in the numerical procedure. It is also expected to yield some discontinuity in the global response, as the same strains correspond to different tensile stresses at different layers.

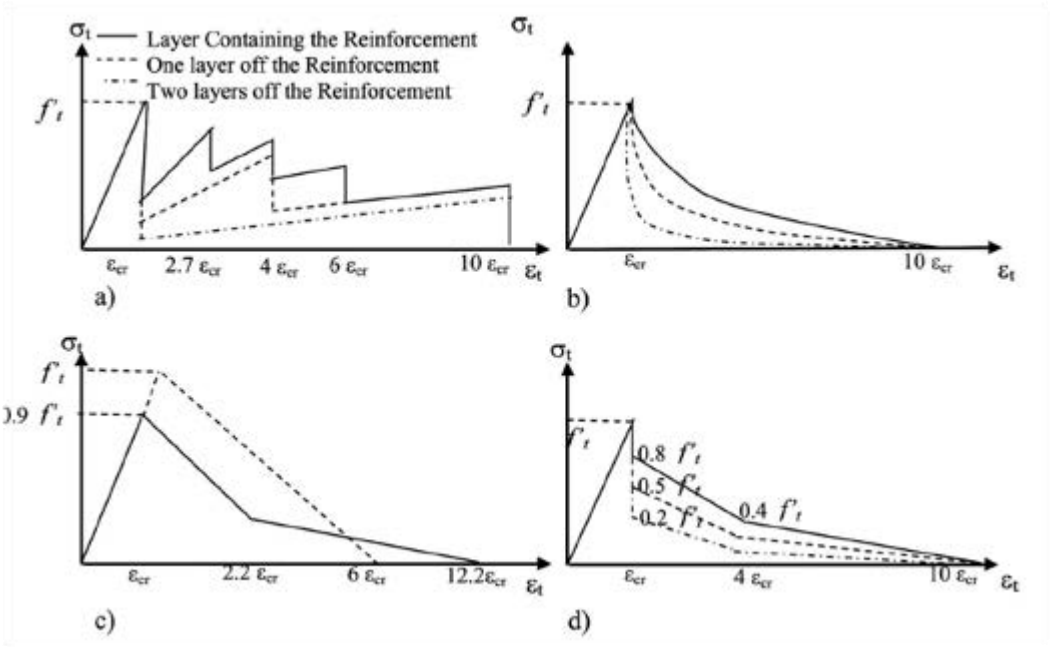

Fig. 2. 7 Different tension stiffening models: (a) Scalon-Murray model; (b) Lin and Scordelis model; (c) Vebo and Ghali model; and (d) Gilbert and Warner model [30]

The homogenized stress-strain relationship suggested by Gilbert and Warner is adopted in a study conducted by Nayal and Rasheed, 2006 [30] to simulate the post-cracking behavior. Fig. 2.5 shows this tensile stress-strain master curve, which depicts the main phenomena of primary and secondary cracking. In their study, a single set of stiffening parameters applicable to the entire tension zone at all steps of analysis is developed. This tension stiffening model is chosen to represent interaction model between concrete and Inoxydable steel.

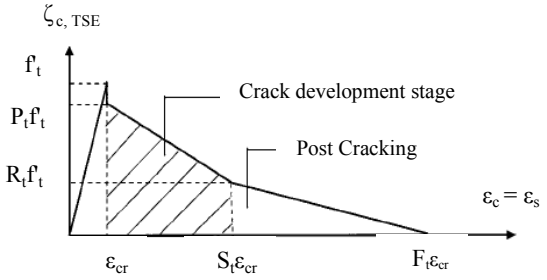

Fig. 2. 8 Tension stiffening model used by Nayal and Rasheed, 2006 [30]

2.4. 2 Investigation of Tension Stiffening

This tension stiffening phenomenon has been observed experimentally by numbers of researchers through a uniaxial tension test [9], [10], [11], and [12]. Most of these researches involved the study of concrete reinforced with construction steel and fiber-reinforced polymer (FRP) material. For these studies, the reinforced concrete specimen and the reinforcement bars are equipped with strain gauges and LVDT to record changes in stress before the specimen starts to crack until failure. Specific arrangements are also required to support the reinforced concrete sample while applying direct tension.

Sooriyaarachchi, 2005 [9] uses a specially manufactured FRP bar built with a series of strain gauges closely distances along the bar. The bar is cut longitudinally in half and strain gauges were placed at the centre of the bar to avoid interference between the bar surface and concrete since a number of strain gauges are used. Using test specimens ranges from 1.3 to 1.5 meter, the samples is subjected to uniaxial tension and tension stiffening parameter is verified on the area where crack is initially introduced. LVDT is fixed on the beam member to determined strain of the overall member. This type of setting has successfully observed and studied the tension stiffening in FRP bar when subjected to direct tension. Changes and increases in stress are observed along the reinforcement bar before and after the formation of cracks.

However, due to the difficulties of conducting the direct tension test, only limited and often conflicting results are available. Nayal and Rasheed, 2006 [30] has applied bending test results to study tension stiffening parameter in concrete beam reinforced with carbon steel. Through the combination of nonlinear numerical analysis, tension stiffening model are inversely estimated from the nonlinear analysis of beam section and the experimental results. The study however did not observe the tension stiffening phenomenon for concrete structure under bending; the changes in stress when load is applied as per observe in the direct tension test.

2. 5 Inoxydable Steel in Structural Elements

The behavior and effects of inoxydable steel in structural elements are analyzed and compared with construction steel bars based on three types of analysis;

i) Free vibration analysis

ii) Push-over analysis

iii) Time history analysis

Push-over is a static nonlinear analysis, and time history analysis is dynamic nonlinear.

2.5. 1 Free Vibration Analysis

Free vibration can be expressed by means of the motion of a structure without any dynamic excitation-external force or support motion. A structure is undergoing free vibration when it is disturbed from its static equilibrium position and then allowed to vibrate without any external dynamic excitation. An example of a pagola and water tank is depicted in Figure 2.9. Free vibration analysis is used to obtain natural frequencies, analytically, and damping ratio, experimentally.

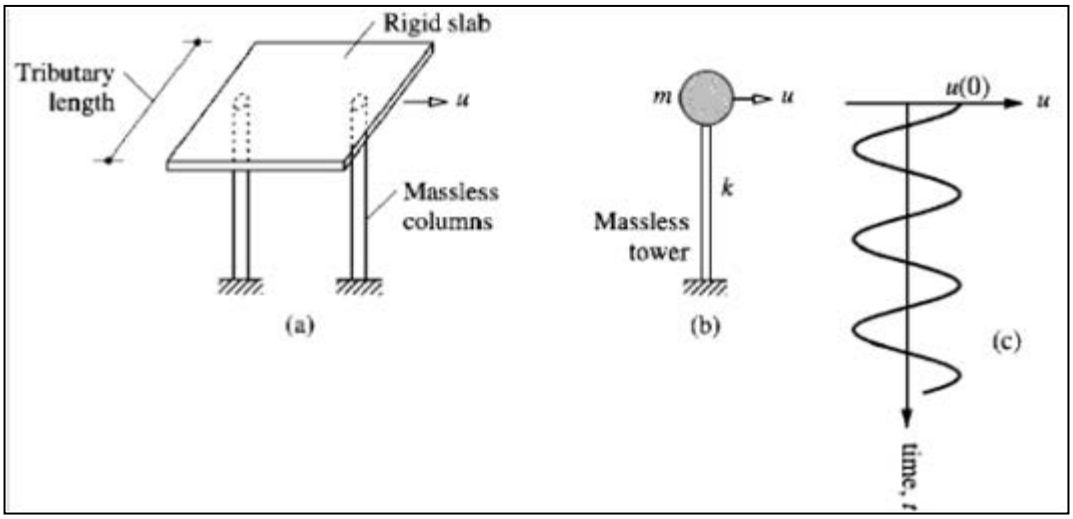

Fig. 2. 9 (a) idealized pergola; (b) Idealized water tank; (c) Free vibration due to initial displacement, Chopra, 2001 [31]

2.5. 2 Push-Over Analysis

The term “push-over analysis” describes a modern variation of the classical „collapse analysis“ method. It refers to an analysis procedure whereby an incremental-iterative solution of the static equilibrium equations carried out to obtain the response of a structure subjected to monotonically increasing lateral load patterns. This method has been extensively verified in many years for building assessment. But the application of push-over analysis for building assessment study has been a limited subject up till nowadays, Pinho et al, 2007 [32].

Push-over analysis which is also known as Nonlinear Static Procedure (NSP) is a performance-based analysis that refers to a methodology in which structural criteria are expressed in terms of achieving a performance objective for different damage states. A performance level described a limiting damage condition which may be considered satisfactory for a given structure and earthquake ground motion. The objective of the Push-over analysis is to calculate the building“s performance point which represents the building“s ultimate deformation under the design earthquake. The performance point can also be described as the intersection of building“s seismic capacity curve and seismic demand curve. The seismic capacity curve is derived from the base shear versus pier“s top displacement curve. This curve is generated by increasing forces imposed on the building“s nonlinear structural model, and updating element stiffness and redistributing seismic forces whenever yield or collapse of any structural elements are detected. The seismic demand curve is represented by plot of building“s spectral acceleration versus its spectral displacement, which could be derived from the design Response Spectrum. There are four standard performance levels expressed under push-over analysis; operational, immediate occupancy, life safety and collapse prevention (Figure 2.10).

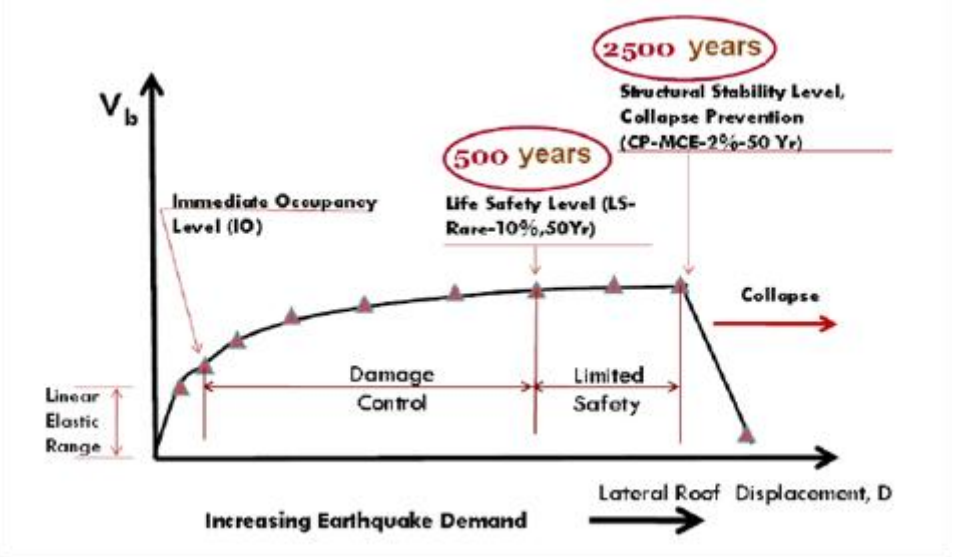

Fig. 2. 10 Performance and structural deformation for structures, Applied Technology Council 40, 1996 [33].

Push-over analysis can be used to determine the ultimate lateral load and deflection capability of a structure. Local nonlinear effects, such as flexural hinges at the member joints, are modeled and an increasing lateral load pushes the structure until a defined limit state is reached in the computer program. The process of flexural hinges can be seen in Figure 2.11. The procedure is fully specified in the U.S. documents FEMA-356 [34] and ATC-40 [33].

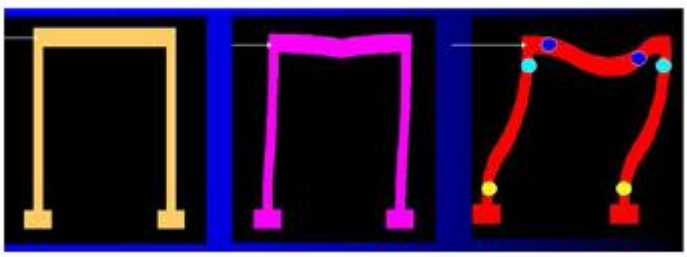

Fig. 2. 11 Hinge develops at structure component

Figure 2.12 below illustrates a global Push-over (capacity) curve and the three levels of earthquake demand: moderate event, major event, and severe event. The intersection of earthquake demand curve with the capacity curve indicates globally how far the building would be pushed and is defined as the performance point of the particular event. The damage levels are labeled by IO, LS, CP and C. This analysis is used to determine reliable

displacement capacities of a structure or frame as it reaches its limits of structural stability. It also provides a base shear versus top pier displacement relationship, which indicates the change in stiffness as well as lateral load capacity of structure. The changes in the slope of the base shear versus top pier curve suggest yielding of various structural elements.

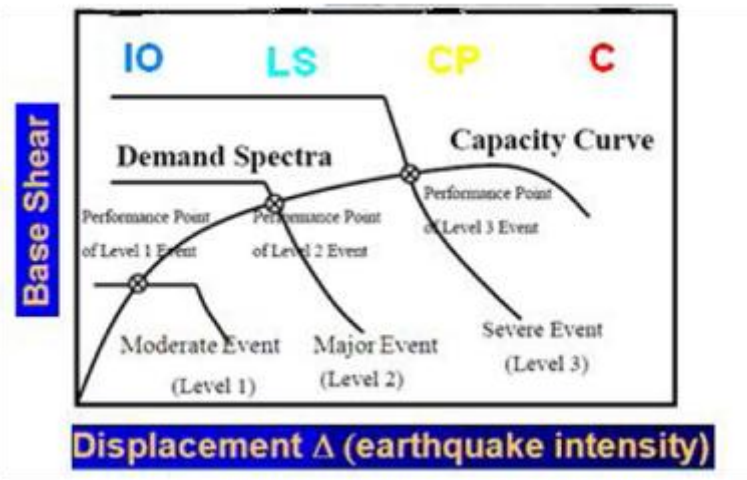

Fig. 2. 12 Base shear versus building displacement curve, Kawashima, 2006 [35] and ATC40, 1996 [33]

Five points labeled as A, B, C, D and E are used to define the force deformation behavior of the hinge (Figure 2.13). A is unloaded component (origin), B is effective yield point, C is ultimate capacity line, D is residual strength, and E is total failure. Line AB is linear response begins, BC is strain hardening, CD is strength degradation, and line DE is strength reduced. Three points labeled as IO, LS and CP are used to define the acceptance criteria for the hinge. IO is immediate occupancy, LS is life safety, while CP is collapse prevention.

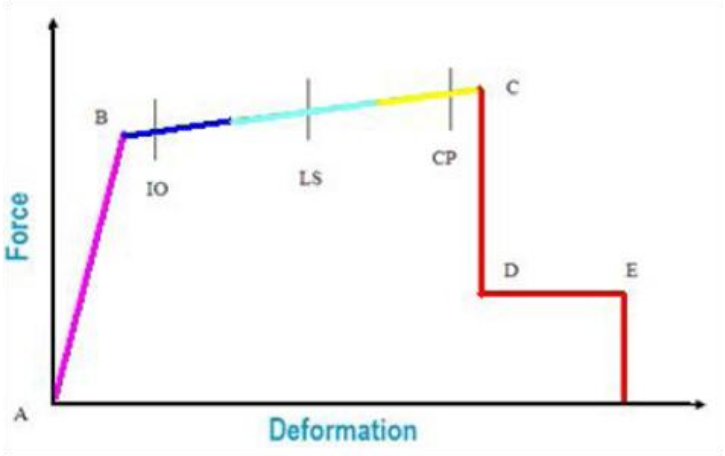

Fig. 2. 13 The force deformation criteria for hinges [34]

Section 2.4.2.1.of FEMA356 states that the Nonlinear Static Procedure (NSP) should not be used for structures in which higher mode effects are significant (usually building with height greater than 30 meters). To determine whether higher modes are significant, a modal Response Spectrum analysis shall be performed for the structure by using sufficient modes to capture 90% of mass participation. A second Response Spectrum analysis is also performed, considering only the first mode participation. Higher mode effects are considered significant if the shear in any story from the modal analysis is more than 90% of mass participation. This stipulation can also be implemented for building structure. The advantages of Push-over analysis are (1) it allows the designer to evaluate structural behavior and performance characteristics, (2) it enables the designer to investigate the sequential formation of plastic hinges in the individual structural elements constituting the entire structure, (3) it enables the designer to determine how the building works by identifying modes of failure and the potential for progressive collapse, and (4) when a structure is to be strengthened through a rehabilitation process, it allows the designer to reinforce only the required members, thereby it maximizes the cost efficiently.

Some factors are considered for modeling and analysis under Push-over analysis. They are (1) Model the building by using inelastic material response at the member joints. (2) Apply monotonically increasing lateral forces or displacements to a nonlinear mathematical model of a building until either the displacement of the control node exceeds a target displacement or the building collapses. (3) Use the idealized force versus deformation curve

to evaluate the performance of individual members once the displacement of the total structure is confirmed to exist within the range of the target performance.

Based on ATC-40, 1996 [33] Push-over analysis is a comparison between the "demand" of an earthquake that is placed on a structure and the "capacity" of the building to resist the load. In other words, a building must provide sufficient capacity to resist the demand of an earthquake. The nonlinear static procedure requires determination of three primary elements: performance point, capacity, and demand. The results of Push-over analysis are usually presented as a plot of base shear versus pier‟s top displacement. Since the demand curve is derived from the design Response Spectrum, which is plotted based on a single degree of freedom (SDOF) system, the base shear-pier‟s top displacement‟s plot needs to be transformed to acceleration versus displacement plot of the equivalent SDOF system in order to locate the performance point (Fig. 2.12). The transformation can be done as suggested in ATC-40 equations.

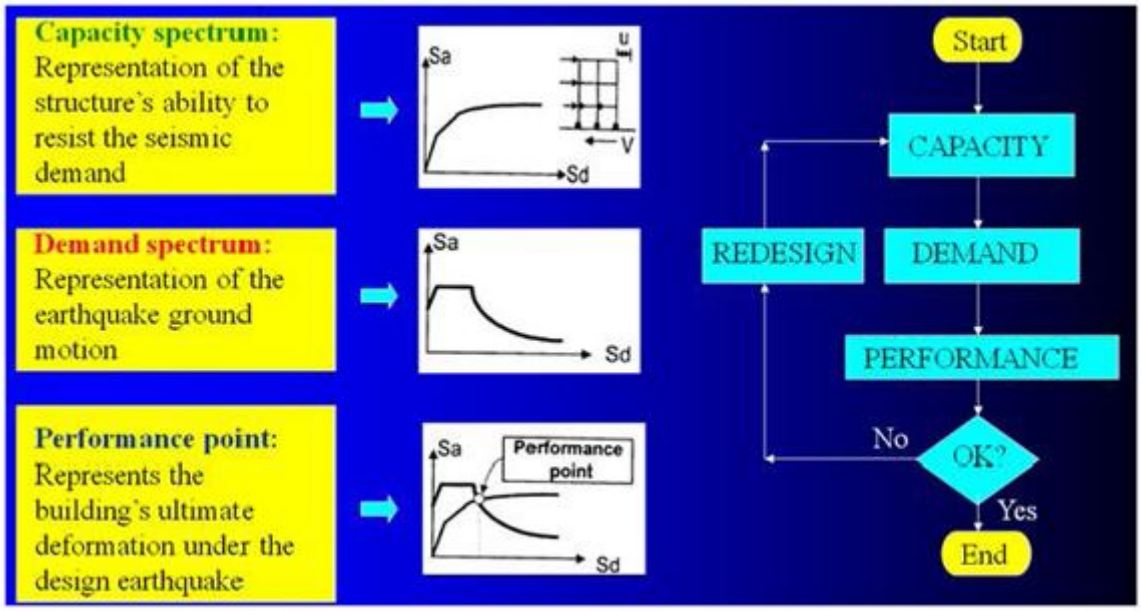

Fig. 2. 14 Simple Push-over method of evaluation [33]

Based on the stipulation by ATC-40, 1996 [33] for Performance Evaluation, engineers should check the responses of the building by using certain acceptability criteria based on performance point. The responses can be checked on two levels. First, there are global limits on building responses for each performance objective, like lateral load stability and drift limits. Secondly, the engineers should check local element or component responses against

acceptability limit, such as element strength and sectional inelastic rotation limits. The limit on inelastic rotation is recommended based on observation from tests and experience from the past earthquake. This stipulation can be implemented for building and building structure. When the responses of a structure do not meet the targeted performance level, the structure needs to be resized and the design process is repeated until a solution for the desired performance point is reached. In general, the determination of the satisfactory performance point that fulfils both system level responses and element responses requires a trial-and-error iterative design procedure with the aid of today‟s engineering software such as: SAP2000. Push-over analysis involves the application of a set of loads, or displacements that are applied incrementally in one direction until failure occurs. Push-over analysis can evaluate buildings loaded beyond the elastic range but is unable to fully capture the dynamics of response, especially higher mode effect. The procedure for nonlinear pushover analysis flowchart can be seen in Figure 2.15.

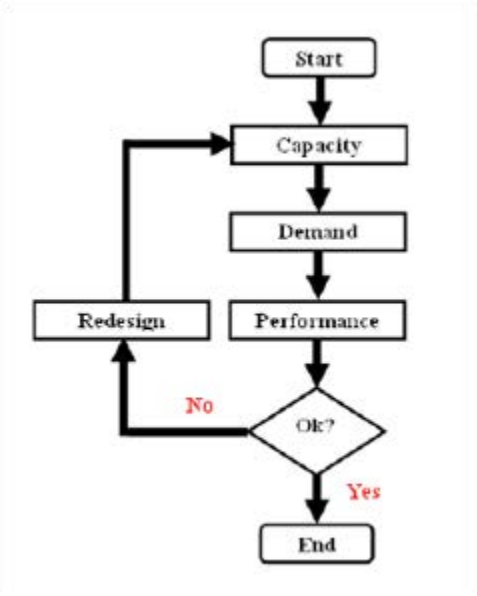

Fig. 2. 15 Static nonlinear push-over analysis procedures

2.5. 3 Time History Analysis

Inelastic time history is used to determine the reliable displacement capacities of a structure or frame as it reaches its limits of structural stability. Time history analysis

(sometimes called response history analysis or Transient Dynamic analysis) involves a time-step-by-step evaluation of building response. It is used to determine the dynamic response of a structure to arbitrary loading using the accelerogram at base motion input.

Time History analysis which is also known as Nonlinear Dynamic analysis is a performance based analysis that refers to a methodology in which criteria for structural damage (in terms of induced levels of ductility demand), and criteria for collapse prevention (in terms of inelastic drift index of structure) are expressed. This analysis involves a time-step-by-step evaluation of building response. It is used to determine the reliable displacement capacities of a structure or frame as it reaches its limits of structural stability. It is also used to determine the dynamic response of a structure to arbitrary loading by using the accelerogram at base motion input. There are two types of Time History analysis namely elastic linear time history analysis and inelastic nonlinear time history analysis. Elastic linear time history analysis is required when the results of Response Spectrum analysis indicate that the computed top of pier or deck‟s displacement exceeds the allowable values, or when special conditions exist. Elastic Linear analysis often underestimates certain behaviors, particularly behaviors that are related to the higher mode of vibration which will result to a high base shear. An Inelastic Nonlinear Time History analysis may be necessary when the results of an Elastic linear analysis show that the structure could suffer significant damage during a major earthquake. The calculated forces will be significantly greater than the section capacity over a large region and are repeated several times during the earthquake excitation.

Hence, severe cracking of the concrete, joint slippage, and yielding of reinforcements can be expected. Under these conditions, the dynamic behavior of the structure is drastically different from the linear response, and a valid estimate of the damage is only possible if a true nonlinear performance is incorporated in the analysis. Therefore, Inelastic Nonlinear Time History analysis is used to justify a structural design of a structure. It is also used when NL link elements are induced in the structural system.

Based on Parke and Hewson, 2008 [36], the Inelastic Nonlinear Time History analysis can be used to determine the non-linear behavior of plastic hinges. It is useful to study the sequence of development, the extent of inelastic behavior through the structure and to determine the force demands in non-ductile elements. In the regions of plastic hinges, the stress–strain diagrams for both concrete and reinforcement should show the post-yield

behavior, by taking into account the confinement of concrete when relevant, and strain hardening and local buckling effects for steel. The shape of hysteresis loops should be properly modeled. Strength and stiffness degradation and hysteretic pinching should be taken into account, if indicated by appropriate laboratory tests. For Time History analysis, the set of applied forces change continuously as the ground acceleration changes. If the building is being damaged, then the stiffness continuously changes as well. The response is calculated at each time step, typically every 1/100th of a second or less. At each step the loads are changed, so do the stiffness if necessary. For a typical building, this may require solving a set of several thousand simultaneous equations up to 3000 times. This is where computer speed becomes essential.

For earthquake time analysis, the set of applied forces changes continuously as the ground acceleration changes. If the building is damaged, the stiffness continuously changed as well. The response is calculated at each time step every 1/100th of a second or less. At each step the loads change, and the stiffness also changes if necessary. For a typical building, this may require a set of several thousand simultaneous equations up to 3000 times to be solved. This is where computer speed becomes essential.

Nonlinear time history analysis using the combination of ground motion records, with detailed structural model theoretically, is capable of producing results with relatively low uncertainty, compared to nonlinear push-over analysis. Based on FEMA 350 [37], the response quantities of time history analysis are computed as follows:

1. Each response quantity is taken as the maximum value if less than seven pairs of ground motion records are used to perform the analyses.
2. The median value of each of the response quantities computed from the suite of analyses may be used as the demand if seven or more pairs of ground motion records are used to perform the analyses.

There are some problems occur in Time History analysis. First, it is unknown whether the selected accelerogram is appropriate to use or not. Second, errors in damping value assumption and other quantities due to accumulation of large numbers of modes. Due to the problems occur in Time History analysis which is sensitive to ground motion assumptions and modeling, UBC code requires a minimum of three pairs of Time History components [38]. Those three pairs of Time History shall be scaled from selected strong earthquake

motions which is recorded at or near the site; or strong earthquake motions which is recorded at other sites with similar geological, topographic and seismotectonic characteristics. The maximum response from all parameters shall be used for design.

The purpose of this method is to ensure adequate coverage of the problems above. If seven or more pairs are selected and scaled, then the average value of the response parameter may be used for design. When appropriate recorded ground-motion Time History pairs are not available, appropriate simulated ground-motion Time History pairs may be used to make up the total number required. Synthetic accelerogram should be based on probabilistic methods.

The word pairs means that the instrumentation that recorded the earthquake acceleration captured the two horizontal components of ground motion and one vertical component of ground motion simultaneously e.g., the earthquake records of 1940 El-Centro site vertical. Although SAP2000 can apply acceleration recorded along the three axes of the model simultaneously, the procedure to date has not applied vertical acceleration concurrent with the horizontal acceleration. Therefore, a pair of two horizontal components of the earthquake record is applied simultaneously to the computer model history load case. The orientation of the applied loads is then varied to determine the worst-case direction.

Chapter 3

3. Material Models

This chapter will cover the first two main objectives; developing constitutive law for inoxydable steel bars, and developing material model for composite concrete when inoxydable steel is used as reinforcing bars, focusing on the interaction behavior between concrete and inox. For the first objective, method involved; laboratory and mathematical procedure, and data analysis will be discussed in detail. This will lead to the development of the new constitutive law proposed in this study. The accuracy of the equation developed is then verified with the actual behavior of inox. Apart from the equation, mechanical properties of inoxydable steel will also be discus focusing on to structural application in construction.

As for the second objective, methodologies involved; laboratory, nonlinear numerical analysis, and finite element modeling to determine the interaction properties will be presented. Results from laboratory works will be used as an input to the nonlinear numerical analysis in order to develop interaction model that corresponds with the actual behavior of inox as reinforcing bars in composite concrete structural element. Mathematical calculation, analysis flow chart, and computer program using Matlab are applied in the numerical analysis.

Finally, the interaction model and constitutive law developed are applied to finite element modeling to verify their correlation with laboratory results. Abaqus is used in the finite element analysis. Results will be analyzed to determine whether the material models can represent the actual behavior of inox as reinforcement bars in composite concrete structures. Methodologies applied and findings in this chapter are useful for future research on inoxydable steel in structural element modeling for it can represent the behavior of this type of steel.

3. 1 Mechanical Properties of Inoxydable Steel

Inoxydable steel are often selected for their corrosion resistance, but they are at the same time constructional materials. For structural application, mechanical properties such as strength, ductility and deformation are thus important. The difference in the mechanical properties between inoxydable steels and carbon steel can be seen most clearly in the stress-strain curves. Therefore in this study, tensile test is conducted on inoxydable steel sample and the ordinary carbon steel to investigate these differences closely between the selected steels.

3.1. 1 Laboratory Test Preparation

Tensile test is conducted on the austenitic stainless steel and carbon steel to study the stress-strain performance. Test procedure and sample preparation is based on BS EN 10002-1 [48]. Two types of austenitic stainless steel are tested (Fig. 3.1); austenitic-hot and austenitic-cold together with the carbon steel. Sample of each type of steel bar is prepared as shown in Fig. 3.2. Detailing of dimension for the samples is shown in Fig. 3.3. The inoxydable steel type used is summarized in Table 3.1.

Table 3.1: Samples of inoxydable steel used and tested

Family type	Grade	Manufactured	Abbreviation
Austenitic	304LN	Annealed	Austenitic-Hot (AH)
Austenitic	4362	Cold	Austenitic-Cold (AC)

a) Austenitic-hot

b) Austenitic-cold

Fig. 3.1. Inoxydable steel reinforcement bar used (a) Austenitic-hot, (b) Austenitic-cold

Fig. 3.2. Sample prepared for each of the inoxydable steel re-bar

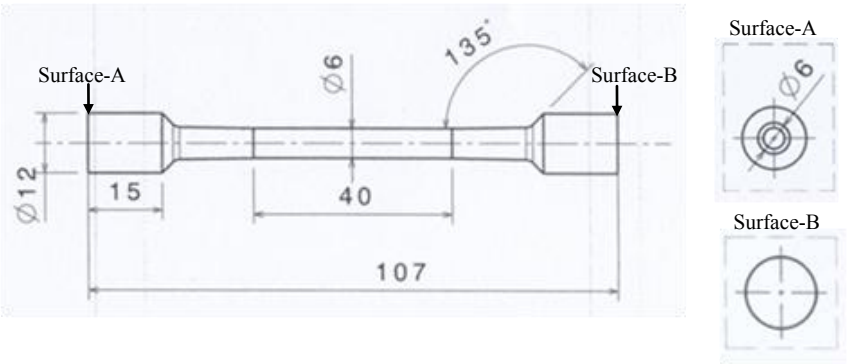

Fig. 3.3. Dimension of inoxydable steel samples used in tensile test (units are in millimeter)

3.1. 2 Tensile Test Results

Fig. 3.4 shows the stress-strain profile plotted for the three types of steel. The inoxydable steel stress–strain curve is different from that of carbon steel. Indeed, carbon steel exhibits linear elastic behavior followed by plastic deformation before strain-hardening, while stainless steel has a curve without a well-marked elastic limit.

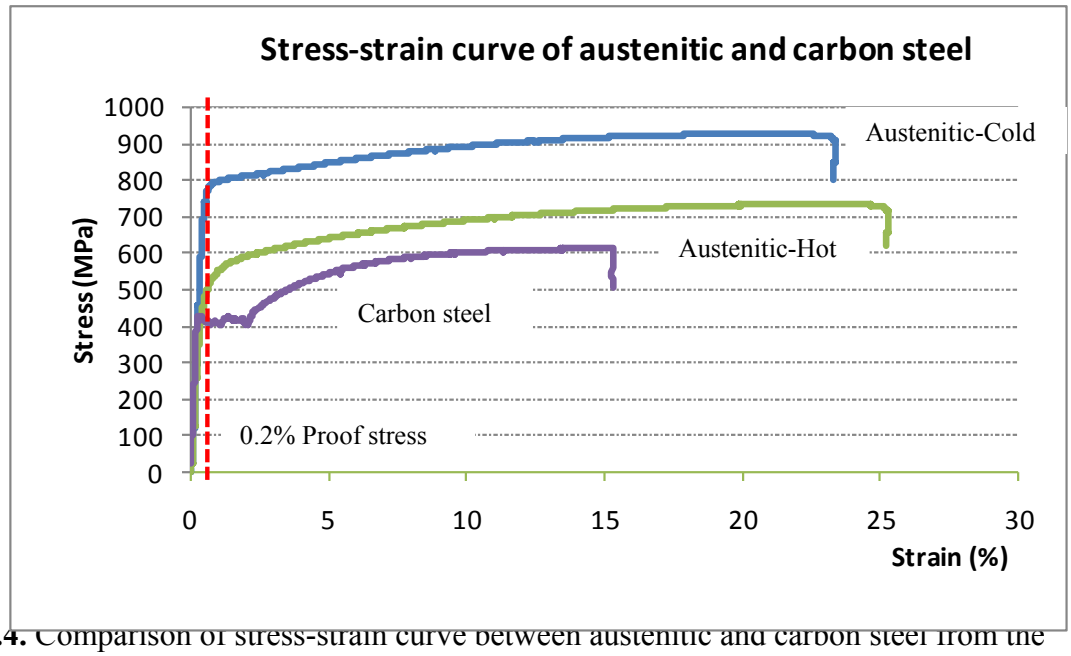

Fig. 3.4. Comparison of stress-strain curve between austenitic and carbon steel from the tensile test

Table 3.2: Tensile test results

Steel type	Modulus of Elasticity, E (MPa)	Yield strength, f_y (MPa)	Ultimate tensile strength, f_u (MPa)	Yield strain/ Ultimate strain, ($\varepsilon_u/\varepsilon_y$)
Austenitic – Hot	177,300	480	773	48.5
Austenitic – Cold	198,800	780	911	36.6
Carbon steel	204,000	430	600	23.9

When tests are made on harder steels, no defined yield-point is observed. For hardened steel, it is difficult to determine the stress which really corresponds to the elastic limit [1]. When determined through standard procedures, the elastic limit of these steels is exceedingly low as compared to the yield-point and the ultimate tensile strength [5]. In this study, standards recommendation of determining the elastic limit with 0.2% proof stress [1] is applied. It gives the modulus of elasticity of 177,300 MPa and 198,800 MPa for austenitic-hot and austenitic-cold respectively. These values are lower compared to that of carbon steel; which is 204,000 MPa.

However, as discussed by many researchers, the austenitic stainless steel shows higher ultimate tensile strength; 773 MPa for austenitic-hot and 911 MPa for austenitic-cold,

compared to carbon steel; 600 MPa. This shows that the elastic limit for austenitic is relatively low compared to its ultimate strength. It also has higher yield strength; 480 MPa for austenitic-hot and 780 MPa for austenitic-cold.

As for the ductility ratio (εu/εy), both austenitic inoxydable steel shows higher values compared to carbon steel; 48.5 and 36.6 for austenitic-hot (AH) and austenitic-cold (AC), respectively, two times of the carbon steel ductility ratio; 23.9. Comparing AH and AC samples, a general decrease in ductility ratio can be observed with an increase in proof stress. This finding correlates well with results obtained by Samuel K.G [39] on the relation between strength and ductility in austenitic steels.

3. 2 Constitutive Laws of Inoxydable Steel

Apart from determining the mechanical properties, developing constitutive law for inoxydable steel is the main objective of conducting the tensile test.

3.2. 1 Method of Ramberg-Osgood

A constitutive law for full range stress-strain curve of austenitic is developed based on the experimental work described above. Method applied by Rasmussen, 2001 [40] is being referred to in developing the stress-strain expression. This approach is based on the Ramberg-Osgood base formulation. Stress-strain relationship in steel has been developed by Ramberg and Osgood, 1943 [41] and cited by many researchers. This relationship however is not suitable for the design and numerical modeling of stainless steel members and elements which reach stresses beyond the 0.2% proof stress in their ultimate limit state. In this stress range, current stress-strain curve based on the Ramberg-Osgood expression become seriously inaccurate principally because they are extrapolation of curve fits to stresses lower than the 0.2% proof stress. In other words, the extrapolation becomes particularly inaccurate for alloys with pronounced strain hardening.

A study conducted by Rasmussen [40] has developed expressions for determining the ultimate tensile strength (σ_u) and strain (ε_u) for given values of the Ramberg-Osgood parameters ($E_0, \sigma_{0.2}, n$). Based on expressions for (σ_u) and (ε_u), the entire stress-strain curve is then constructed from the Ramberg-Osgood parameters ($E_0, \sigma_{0.2}, n$). This approach is applied as a base to develop the stress-strain relationship of austenitic steel using data obtained from experimental work. Comparison is made to verify the suitability of this relationship and amendments are suggested to achieve accurate constitutive law for austenitic steel as part of the inoxydable steel group.

Stress-strain curve in terms of the Ramberg-Osgood expression,

$$\varepsilon = \frac{\sigma}{E_0} + p\left(\frac{\sigma}{\sigma_p}\right)^n \tag{3.1}$$

Where E_0 = Young"s modulus

σ_p = proof stress

p = corresponding plastic strain

n = parameter which determines the sharpness of the curve

Proof stress is an approximation for the yield point or elastic limit for materials that don't have a definite one [51]. In order to get the approximation (as shown in Fig. 3.5(a)), a tangent is produced from the proportional limit; point where an increase in stress no longer has a linear relationship with an increase in strain. Sometimes this is known as the elastic limit. The point of intersection between the graph and the tangent defines the proof stress of the material. A 0.2% proof stress is illustrates in the figure where the tangent is produced from a point slightly (0.002) to the right of the proportional limit.

In this study, as the inoxydable steels sample does not have a significant yield point, 0.2% proof stress ($\sigma_{0.2}$) will be taken as the equivalent yield stress as recommended by Eurocode 3 [51];

$$\varepsilon = \frac{\sigma}{E_0} + 0.002\left(\frac{\sigma}{\sigma_{0.2}}\right)^n \tag{3.2}$$

Parameter n is determine using the 0.01% and 0.2% proof stresses which leads to the following expression;

$$n = \frac{\ln(20)}{\ln(\sigma_{0.2} / \sigma_{0.01})} \tag{3.3}$$

Equation (3.3) ensures that the Ramberg-Osgood approximation matches exactly the measured stress-strain curve at the 0.01% and 0.2% proof stresses. It generally provides close approximation to measured stress-strain curves for stresses up to the 0.2% proof stress. This approach is based on recommendation of standard such as; American (ASCE, 1991), Australian (AS/NZS 4673, 2001) and South African (SABS 1997) standards for stainless steel structures. Stress-strain curves obtained from the tensile test results are exploited to determine the values of 0.01% and 0.2% proof stresses which will be used in Eq. (3.3).

Equation (3.2) is chosen for the stress-strain curve stresses up to the 0.2% proof stress,

$$\varepsilon = \frac{\sigma}{E_0} + 0.002\left(\frac{\sigma}{\sigma_{0.2}}\right)^n \qquad \text{for } \sigma \leq \sigma_{0.2} \tag{3.4}$$

In developing a model for the part of the stress-strain curve between the 0.2% proof stress and the ultimate tensile strength (σ_u), linear transformation of the stress and strain will be used since it could be observed that the shape of curve between 0.2% proof stress and (σ_u) are similar with the curve up to the 0.2% proof stress, as shown in Fig. 3.5. This linear transformation is aimed to ensure simplicity in the stress-strain curve formulation. The stress-strain curve shall be defined in terms of a minimum of additional parameters. Equation (3.1) will be used in the form of,

$$\bar{\varepsilon} = \frac{\bar{\sigma}}{E_{0.2}} + \varepsilon_{u_p}\left(\frac{\bar{\sigma}}{\bar{\sigma}_u}\right)^m \qquad \text{for } \sigma > \sigma_{0.2} \tag{3.5}$$

Where $\bar{\varepsilon}$ and $\bar{\sigma}$ are the transformed strain and stress (see Fig. 3.5b), defined as

$$\bar{\varepsilon} = \varepsilon - \varepsilon_{0.2} \tag{3.6}$$

$$\bar{\sigma} = \sigma - \sigma_{0.2} \tag{3.7}$$

The initial modulus to the curve ($E_{0.2}$) is also the tangent modulus of the stress-strain curve at the 0.2% proof stress, as shown in Fig. 3.5. By requiring continuity in slope at $\sigma_{0.2}$, $E_{0.2}$ is

$$E_{0.2} = \frac{E_0}{1+0.002n\,/\,e} \tag{3.8}$$

where e is the non-dimensional proof stress; $e = \sigma_{0.2}/E_0$.

In adopting Eq. (3.1), the „proof stress" (ζ_p) is taken as the transformed ultimate tensile strength ($\bar{\sigma}_u$),

$$\bar{\sigma}_u = \sigma_u - \sigma_{0.2} \tag{3.9}$$

And accordingly, the plastic strain (p) is the transformed ultimate plastic strain ($\bar{\varepsilon}_{u_p}$),

$$\bar{\varepsilon}_{u_p} = \varepsilon_u - \varepsilon_{0.2} - \sigma_u / E_0 \tag{3.10}$$

Stainless steel is generally ductile and therefore negligible error is made through approximating the transformed ultimate plastic strain by the total ultimate strain,

$$\bar{\varepsilon}_{u_p} \approx \varepsilon_u \tag{3.11}$$

The exponent (m) is dependent on the ultimate tensile strength in relation to the 0.2% proof stress;

$$m = 1 + 3.5 \frac{\sigma_{0.2}}{\sigma_u} \tag{3.12}$$

Therefore, the full-range stress-strain curve can be written out in full as follows:

$$\varepsilon = \begin{cases} \frac{\sigma}{E_0} + 0.002 \left(\frac{\sigma}{\sigma_{0.2}}\right)^n & \text{for } \sigma \leq \sigma_{0.2} \\ \frac{\sigma - \sigma_{0.2}}{E_{0.2}} + \varepsilon_u \left(\frac{\sigma - \sigma_{0.2}}{\sigma_u - \sigma_{0.2}}\right)^m + \varepsilon_{0.2} & \text{for } \sigma > \sigma_{0.2} \end{cases} \tag{3.13}$$

From the above equations, for a complete range of stress-strain curve, five parameters are needed. Three parameters (E_0, n, $\sigma_{0.2}$) are needed for $\sigma \leq \sigma_{0.2}$ and another two additional parameters (ε_u, σ_u) are needed for $\sigma > \sigma_{0.2}$. In the study conducted by Rasmussen [40], expressions are proposed to determine (ε_u, σ_u) in terms of n and e for stainless steel and all alloys;

$$\frac{\sigma_{0.2}}{\sigma_u} = 0.2 + 185e \tag{3.14}$$

$$\varepsilon_u = 1 - \frac{\sigma_{0.2}}{\sigma_u} \tag{3.15}$$

Parameters $E_{0.2}$ and m are determine from Eq. (3.8) and Eq. (3.12), respectively.

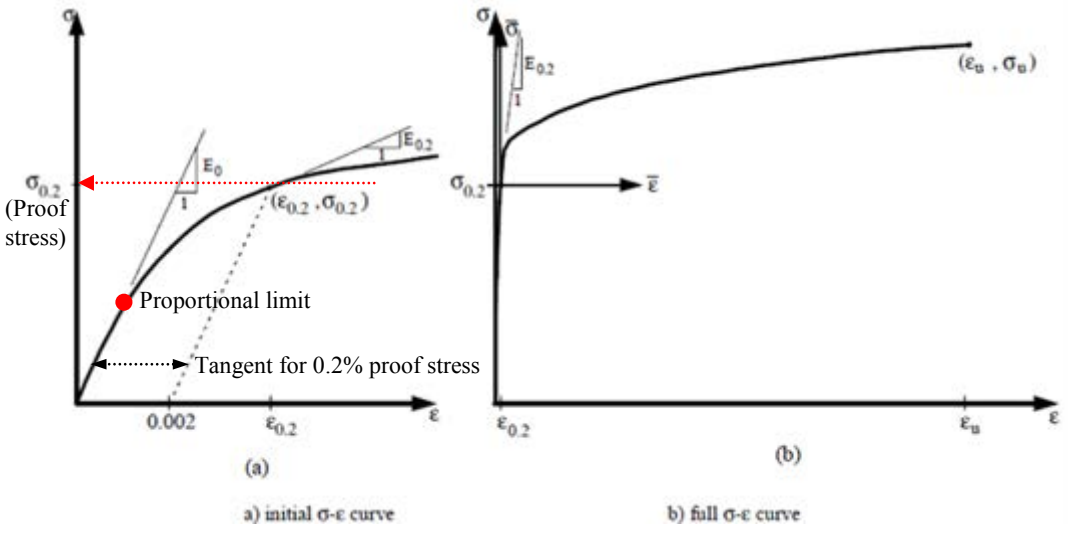

Fig. 3.5 Stress-strain curve (a) Initial curve and (b) full stress-strain curve [40]

3.2. 2 Application of Inoxydable Steel

For developing expressions for Inoxydable steel, the stress-strain curve is plotted in two phases: for stress less than 0.2% proof stress (Fig. 3.6), and stress between the 0.2% proof stress and the ultimate tensile strength, σ_u (Fig. 3.7). For austenitic steel, Eq. (3.14) that has been proposed to determine σ_u gives higher values of strain as compared to the laboratory results. This can be observed in Fig. 3.8(i), where the stress-strain values obtained from Eq. (3.14) are compared with the tensile test results. While the ultimate tensile stress predicted by the equation resembles the experimental results, the strain predicted is very high. The ultimate strain for austenitic-hot is 3 times higher than the experimental values, and it is 12 times higher for the austenitic-cold. This is shown in Fig. 3.8(a) and 6(b) respectively. A new expression is suggested to have the best fit curve for this type of steel;

$$\frac{\sigma_{0.2}}{\sigma_u} = 0.12 + 185e \tag{3.16}$$

It can be observed that the parameter 0.2 from Eq. (3.14) is replaced by 0.12. Referring to Eq. (3.14) and (3.16), for a given value of the non-dimensional proof stress; e, the new parameter indicates inoxydable steel has lower ratio of $\frac{\sigma_{0.2}}{\sigma_u}$. Parameter n (sharpness of the stress-strain curve) is lower. This shows that the studied steel have lower proportional limit, and extended strain hardening capability.

Optimization of parameter 0.2 to 0.12 as indicated in Eq. (3.14) and Eq. (3.16) is based on the best fit curve between experimental results and the developed equations. MATLAB program is used to calculate and minimize the error between the two equations; indicated by the coefficient of determination, R^2.

A new curve is plotted using Eq. (3.16) as shown in Fig. 3.8(ii). It can be observed that this new expression gives a better correlation for both austenitic-hot and austenitic-cold steels. It gives close resemblance between the equation and experimental results for both ultimate tensile stress values and strain values. This expression is then used further in this study.

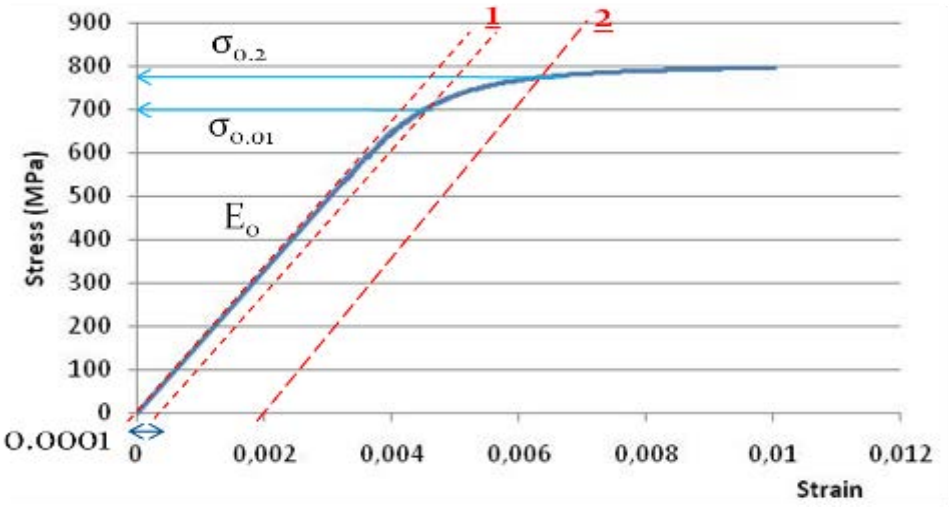

Fig. 3.6 Determination of sharpness of the curve (parameter *n*) for inoxydable steel

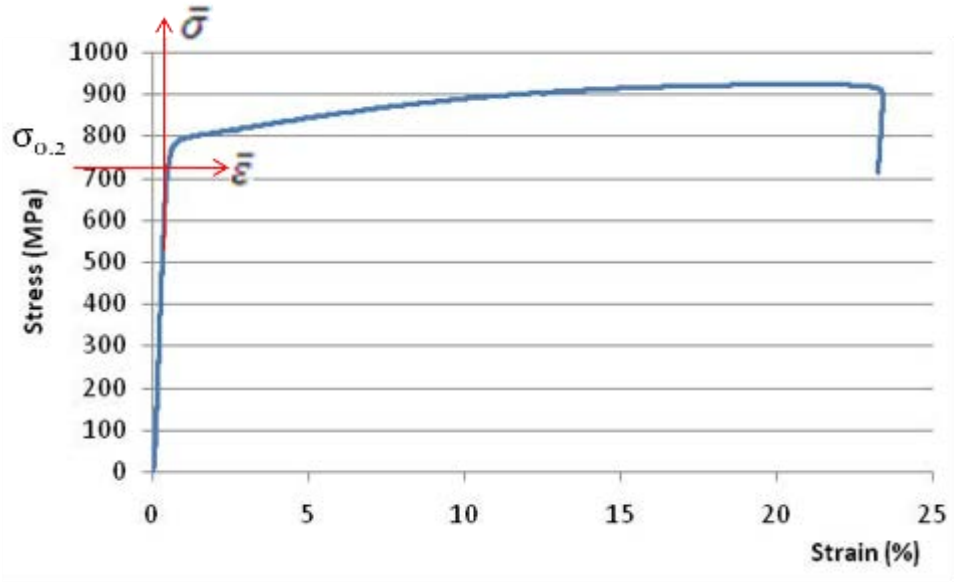

Fig. 3.7 Linear transformation of the curve for developing model between the 0.2% proof stress and the ultimate tensile strength (σ_u)

3.2. 3 The Developed Equations

Based on the method above, a stress-strain relation has been developed for austenitic-hot and austenitic-cold steels. For austenitic-hot, the proposed equation is:

$$\varepsilon = \frac{\sigma}{177\,305} + 0.002\left(\frac{\sigma}{480}\right)^{5.56} \qquad \text{for } \sigma \leq \sigma_{0.2} \qquad (3.17)$$

$$\varepsilon = \frac{\sigma-480}{34\,724} + 0.38\left(\frac{\sigma-480}{293}\right)^{3.17} + 0.0047 \quad \text{for } \sigma > \sigma_{0.2} \tag{3.18}$$

For austenitic-cold steel, the proposed stress-strain equation is as follows:

$$\varepsilon = \frac{\sigma}{198\,810} + 0.002\left(\frac{\sigma}{780}\right)^{11.42} \quad \text{for } \sigma \leq \sigma_{0.2} \tag{3.19}$$

$$\varepsilon = \frac{\sigma-780}{29\,148} + 0.14\left(\frac{\sigma-780}{131}\right)^{4.0} + 0.0059 \quad \text{for } \sigma > \sigma_{0.2} \tag{3.20}$$

The proposed constitutive laws; Equation (3.17)-(3.20) are useful for further study in inoxydable steel from austenitic type. Based on the comparison made between the proposed curve and laboratory results, a good correlation can be observed. These equations are then used further in this study in the finite element analysis to apply the material properties for the reinforcement bars.

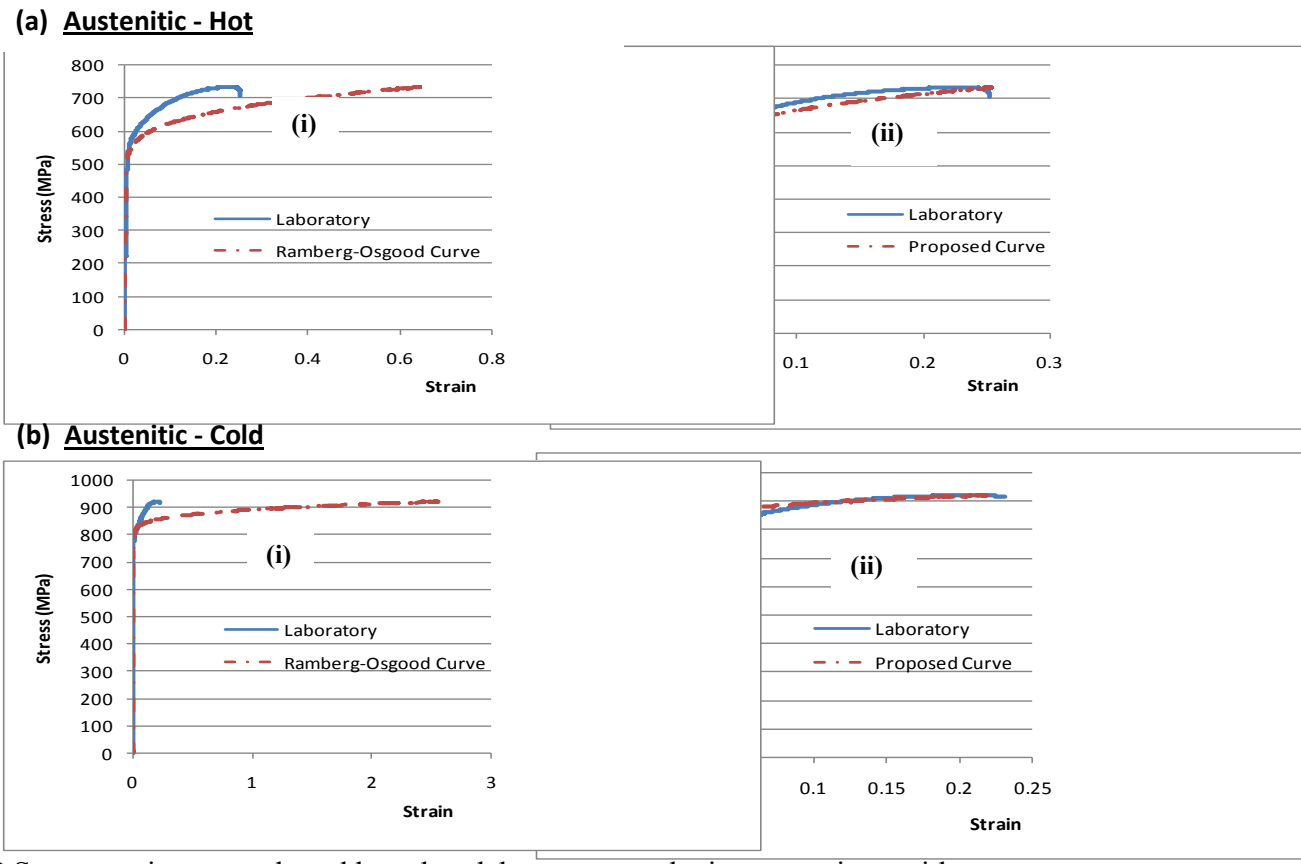

Fig. 3.8 Stress-strain curve plotted based on laboratory results in comparison with curve derived from Ramberg-Osgood method (i) and the proposed new parameter in this study (ii) for (a) austenitic-hot, and (b) austenitic-cold

3. 3 Mechanical Properties of Concrete

In this study there are two types of concrete used; standard concrete and *Béton Fibré à Ultra-hautes Performance*, BFUP (Ultra-high performance fibre-reinforced concrete, UHPFRC). This type of concrete belongs to the group of fiber reinforced concretes that exhibit strain-hardening under uniaxial tension force [82]. It has ultra-high performance; its resistance is 6-8 times that of a conventional concrete [83]. BFUP contains metal fibers (Fig. 3.11 (c)) which make it ductile and has 10 times more resistant to bending than conventional concrete [84]. Compressive strength of this type of concrete range from 150-200 MPa [82]-[84]. BFUP also characterized by a very high workability often giving them a self-compacting character.

Standard concrete is used in preparing reinforced concrete beams and columns samples. The BFUP is used to prepare samples to determine tension stiffening parameter that will be discussed further in Section 3.5. Here, only the mechanical properties of the two types of concrete will be studied.

3.3. 1 Standard Plain Concrete

Fig. 3.9(a) shows the dimension of plain concrete sample used to prepare structural RC elements; beam and column. Three cylinder samples are prepared for each mixture. These samples are tested at the age of 28 days. Extensometer is attached to the sample to determine stress-strain values when the samples are subjected to compressive load as shown in Fig. 3.9 (b). The stress-strain curve determine from the average of the samples test results is shown in Fig. 3.10. The samples have an average maximum compressive stress of 50 MPa. Modulus of elasticity is equal to 37,565 MPa. The stress-strain curve values are used further in the development of tension stiffening parameter through nonlinear numerical analysis which will be discussed further in Section 3.6.2.

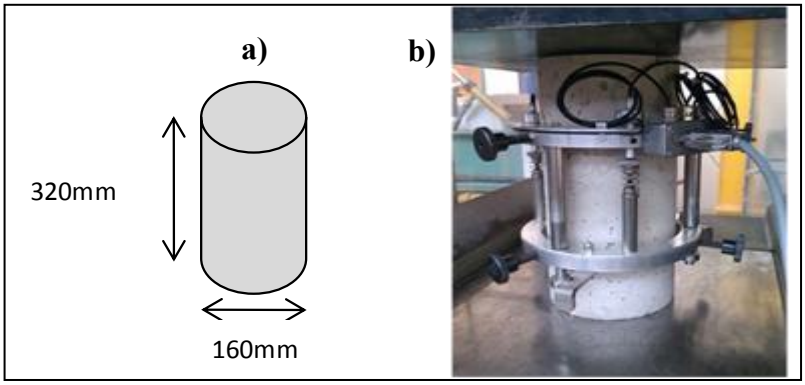

Fig. 3.9 Compression test on normal concrete; a) Dimension of sample, b) Extensometer used during test

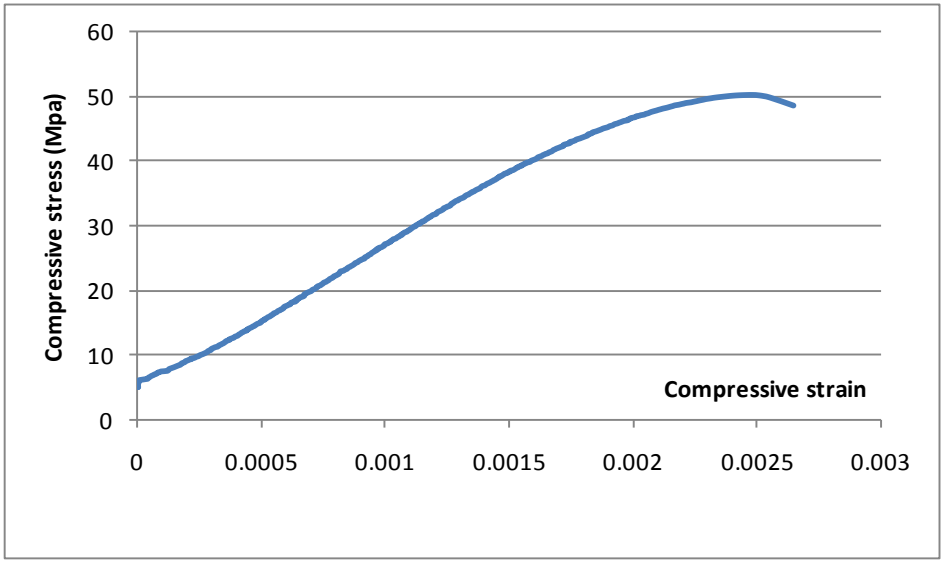

3.3. 2 Ultra-high Performance Fiber-reinforced Concrete (BFUP)

Figure 3.11(a) shows the dimension of BFUP sample used to determine the mechanical properties of this type of concrete. BFUP contains microfibers from metal with 0.16mm diameter and 13mm in length as shown in Fig. 3.11 (b). Smaller size samples are used to suit the capacity of compression test machine since the expected compressive strength of BFUP is six to 10 times higher than the standard concrete. Three cubical shape samples of 50x50x100 mm size are prepared. These samples are tested at the age of 28 days. A smaller size extensometer is attached to the sample to determine stress-strain values when the samples are subjected to compressive load as shown in Fig. 3.11 (c). The stress-strain curve determine from the average of the samples test results is shown in Fig. 3.12. It can be observed that the curve is different with the standard concrete. The BFUP has higher strain

hardening due to the metallic fiber in the mixture. The samples have an average maximum compressive stress of 183 MPa. Detail application of this type of concrete is discussed further in Section 3.8.

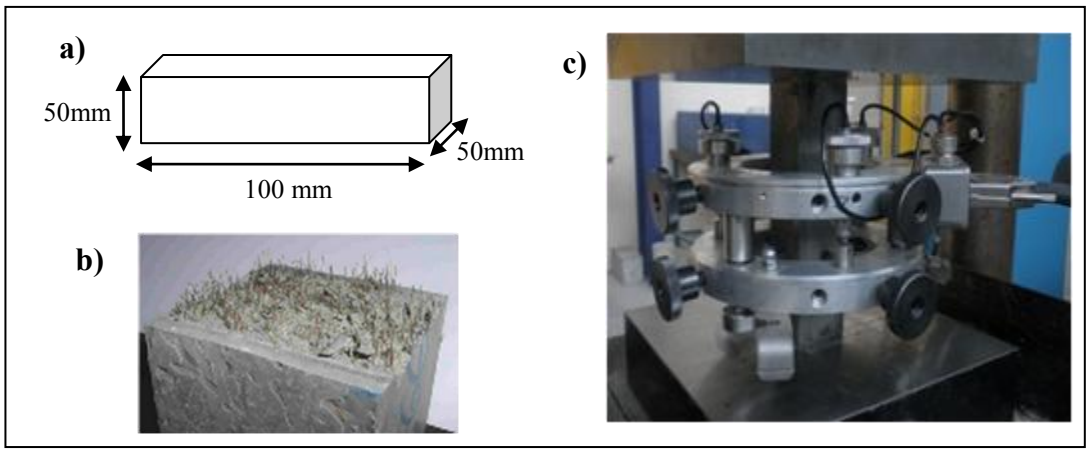

Fig. 3.11 Compression test on BFUP; a) Dimension of sample, b) metal fibers in BFUP c) Small size extensometer used during compression test

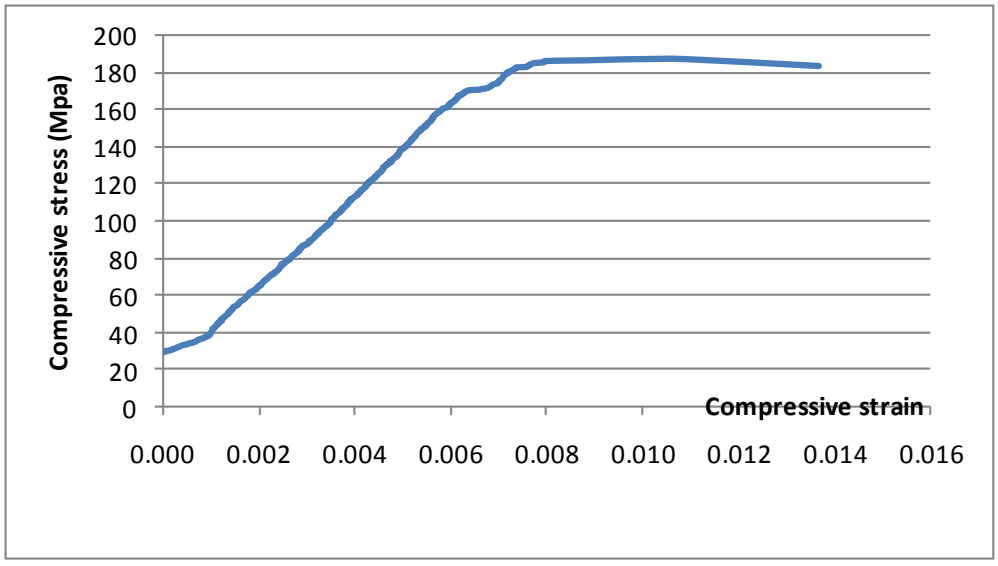

3. 4 Interaction Model in Composite Concrete

In the overall analysis of composite concrete element, the behavior of a steel bar alone is not the same with the one embedded in concrete. The bond between rebar allows the surrounding concrete to resists tensile forces, thereby reducing the average level of stress in

the steel. This results in a gain of rigidity; called the tension stiffening effect. The application of inoxydable steel in composite concrete as reinforcement bars is studied based on the bond properties between inox and concrete. This study focuses on the tension stiffening parameter to define the interaction (bond) parameter. In order to develop this interaction model, laboratory work is conducted along with nonlinear numerical analysis (NNA).

This tension stiffening phenomenon has been observed experimentally by numbers of researchers through a uniaxial tension test [9]-[12]. Most of these researches involved the study of concrete reinforced with construction steel and fiber-reinforced polymer (FRP) material. For these studies, the reinforced concrete specimen and the reinforcement bars are equipped with strain gauges and LVDT to record changes in stress before the specimen starts to crack until failure. Specific arrangements are also required to support the reinforced concrete sample while applying direct tension. However, due to the difficulties of conducting the direct tension test, only limited and often conflicting results are available.

In this study, the possibility of observing tension stiffening phenomenon in a concrete structure subjected to bending is being investigated. This study highlighted an approach to develop the tension stiffening model using an inverse approach by combining results from laboratory and NNA. Since tension stiffening models are adopted by the smeared crack approach to simulate global response, the present approach rationally develops those parameters through direct matching of detailed nonlinear beam analysis and experimental global response. By comparing the load-deflection values obtained from the NNA with the results from laboratory test, tension stiffening model is chosen based on the closest resemblance between results from these two methods. Finite element analysis, FEA is then conducted with the chosen tension stiffening model and constitutive law for inoxydable steel as been developed in previous sections. Results obtained are then compared with laboratory to verify the accuracy of the proposed method and material models to represent the nonlinear behavior of inoxydable steel in composite concrete structure. Fig. 3.13 shows the overall process of determining the interaction model for inoxydable steel.

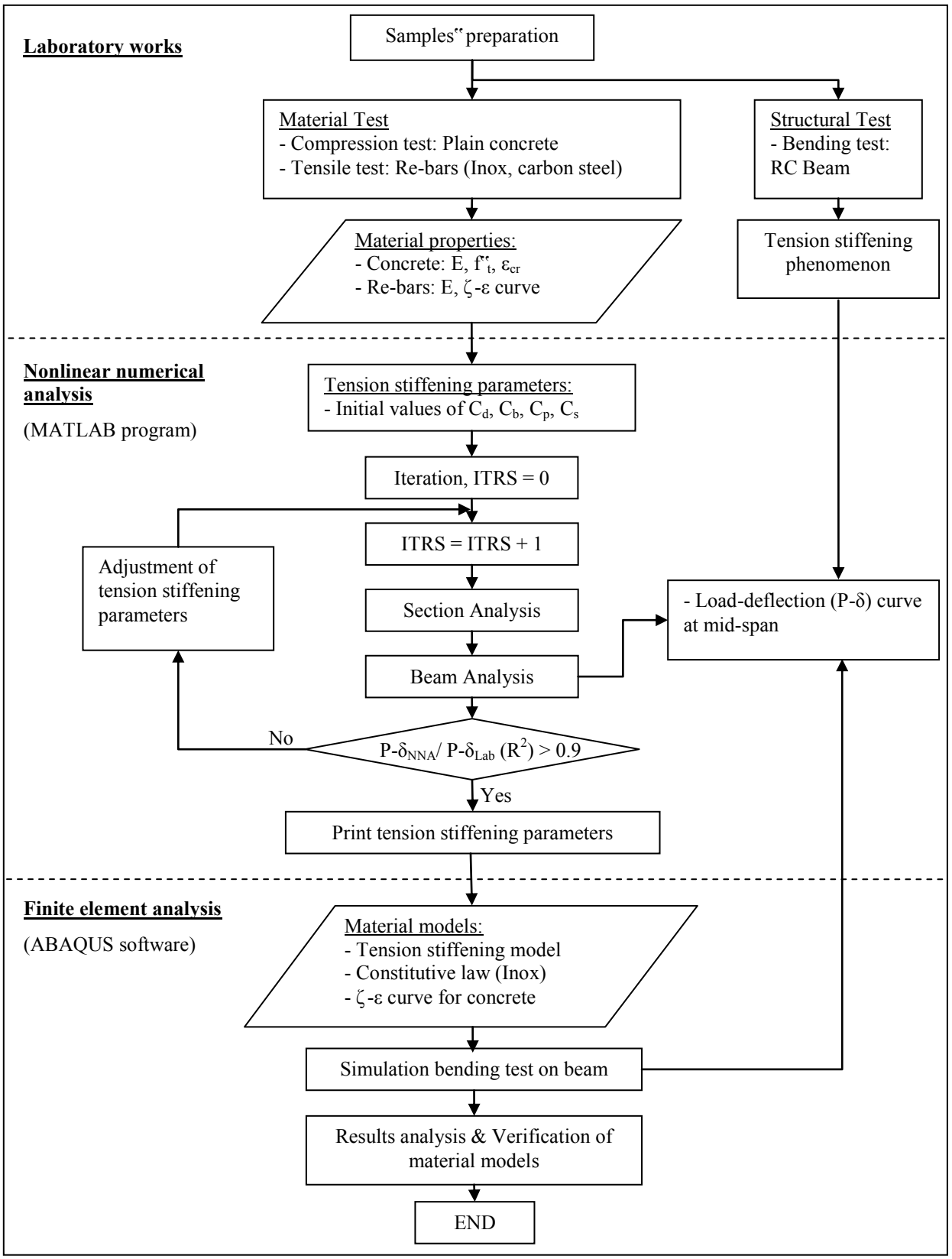

Fig. 3.13. Process to develop the interaction model for inoxydable steel in composite concrete

3. 5 Laboratory Investigation

As mentioned, the possibility of observing tension stiffening phenomenon in a concrete structure subjected to bending is investigated. A similar concept of sample preparation with study conducted by Reference [9] is applied. A series of strain gauges are attached to the austenitic steel bar in tension zone to record changes in stress when load is applied. These changes are analyzed and observed closely, particularly during the phase before and after cracking. LVDT is placed at the center of the beam to record the central deflection.

3.5. 1 Samples and Settings

Fig. 3.14 shows the dimension of the reinforced concrete beam sample used in this study. Two austenitic steel 20mm in diameter is used as the reinforcing bars in tension zone, and two carbon steel 8mm in diameter is used in compression zone. For this test, only austenitic-hot steel is use. Ten shear links formed from 6mm mild steel bars were provided at 70mm and 120mm from each ends for shear reinforcement in the shear spans. The beams were tested on simply supported condition with a clear span of 2.9m and loaded symmetrically and monotically. Concrete used for the beam sample has compressive strength, f_{ck} of 50 MPa, and Young‟s Modulus of 37,565 MPa. The mechanical properties of this concrete sample are discussed in Section 3.3.1.

As for the settings to study the tension stiffening behavior, a series of strain gauges are attached along the austenitic steel bars. Since the strain gauges were attached on the bar surface, the quantity has to be limited to minimize surface interferences. Therefore an effective number of strain gauges and the right position to place it have to be estimated prior. For this, a moment distribution diagram of the simply supported beam is used to predict the internal stress distribution as shown in Fig. 3.15. It can be observed that the stress distribution will increase between point A-B and will be identical to D-C. A total of six strain gauges were used and placed along the reinforcement bar at the position as shown in Fig. 3.15(b). It is marked as J1, J2, J3, J4, J5, and J6.

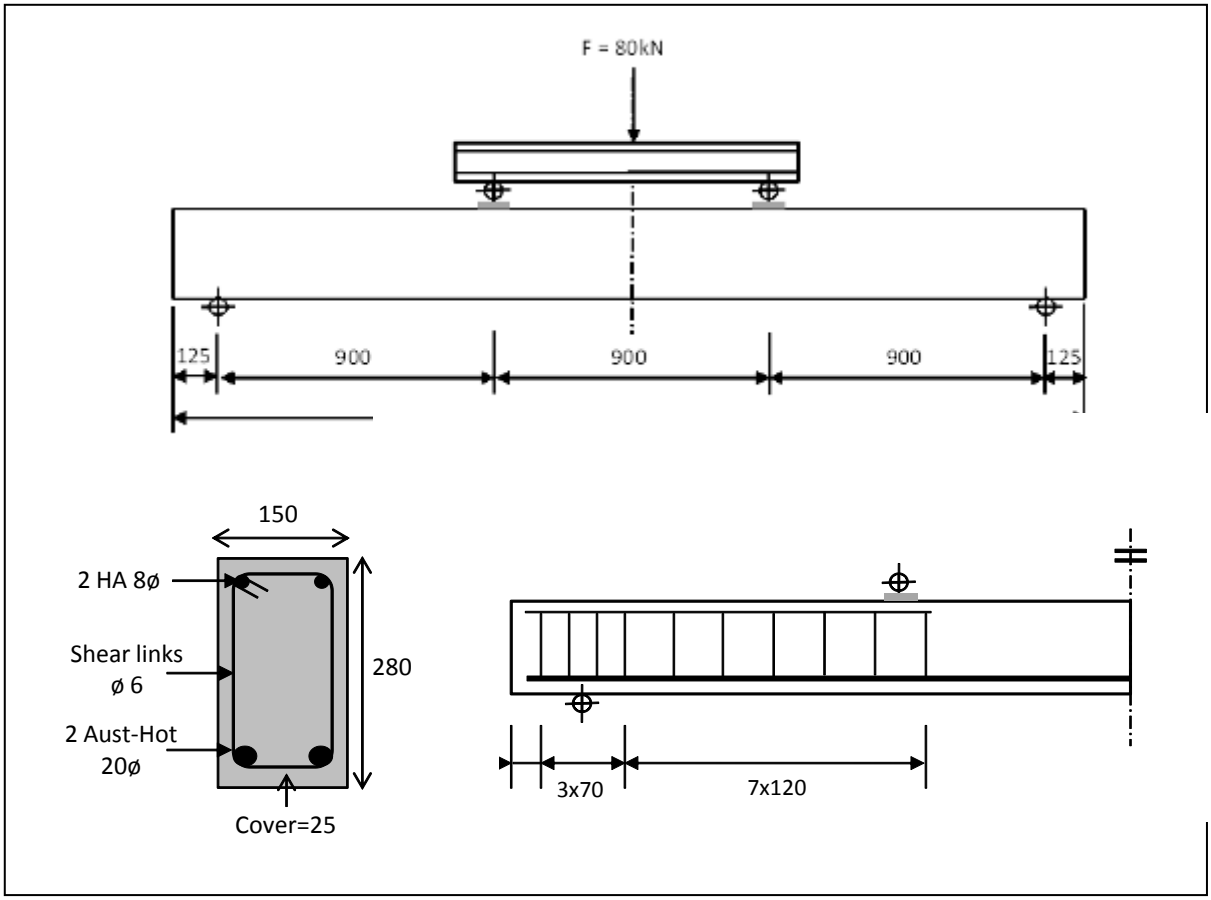

Fig. 3.14. Dimension of the RC beam as per constructed and tested in laboratory (units are in millimeter)

Fig. 3.16(a) shows the detail arrangement made on the strain gauges position. It is alternately positioned between the two bars to minimize the surface interferences and at the same time permit the changes in strain to be recorded in a close distances along the bar. Strain gauges marked as J2, J4, and J6 were placed along Bar 1, while J1, J3, and J5 were placed along Bar 2. When observed on the side view of the beam; Fig. 3.16(b), these alternately positioned strain gauges will develop a series of strain gauges closely distanced with each other along the beam member. The strain pattern can then be observed at different distance and load history. Fig. 3.17 shows the strain gauges attached on the reinforcing bars and the cable arrangement.

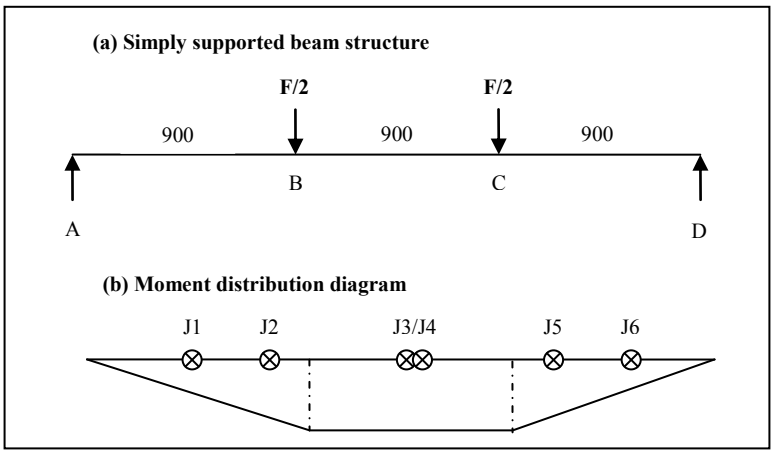

Fig. 3.15. Determination of strain gauges position based on the prediction of internal stress distribution using (a) structure of the simply supported beam, (b) and the theoretical moment distribution diagram

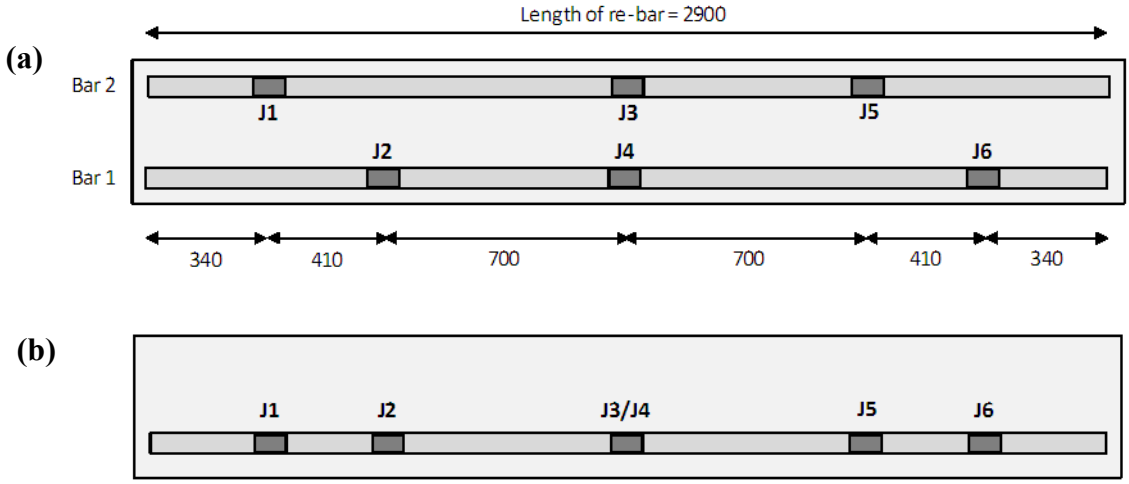

Fig. 3.16. Detailing position for each strain gauges along the re-bar: (a) Position on both re-bars as per plan view, (b) Side view of the RC beam showing the continuous position of the gauges

Fig. 3.17. Strain gauges on the reinforcing bars

3.5. 2 Tension Stiffening Phenomenon

Bending test is conducted to the simply supported beam. Load is applied symmetrically and monotonically in two points up to 80kN; before exceeding its yield limit.

Displacement is recorded in the center of the beam using LVDT. A load-displacement curve is then plotted as shown in Fig. 3.18.

Central deflection of the beam is 6.9mm for 80kN total load. Three tangential lines are drawn on the curve as shown in Fig. 3.18 (a). A smooth line of the three parts is shown in Fig. 3.18 (b). These three lines could give best fit to the original curve. Line I is a tangent between point A and B, line II for point B and C, and line III is for the curve between point C and D. Fig. 3.18 (b) shows the three phases; pre-cracking, crack development stage, and post-cracking. From the curve, crack starts at 27.5kN. During the experimental work, cracks were visible at 31kN of applied load. In bending loading case, this first cracking stage is also referred to as the limit of proportionality for the concrete [42].

Tension stiffening phenomenon is observed with the increase of strain recorded along the reinforcement bars when load is applied. Based on the discussion made in Section 2.4.1, tension stiffening can be viewed as an increase in stress on the reinforcement bar when cracks start to form due to the inability of concrete to resist tensile stress. Analyzing the readings of strain gauges attached to the bars, the stress curve is plotted for the applied load (Fig. 3.19). For all six strain gauges, an increase of readings is recorded between 27 and 44 kN of applied load. These increments can be viewed in two phases as shown in Fig. 3.19. Taking J4 as example, a linear increase is recorded between 0 kN to 27 kN, followed by a higher increase of stress between 27 kN to 80 kN. This sudden increase in strain and therefore the stress, shows the tension stiffening phenomenon as could be observed in direct tension test. All strain gauges show the same increment pattern for the same range of load. This is when cracks are forming in the concrete beam.

J4 shows the highest reading (370 MPa) followed by J3 (320 MPa) for 80 kN of the applied load. This is due to their position in the center of the beam when deflection is maximum and cracks tend to form in the center prior to other parts of the beam.. This is followed by J2 and J5, in which both reading shows close resemblance. J6 and J1 show the lowest reading. This proves the assumption that internal stress distribution will be identical for the two gauges if their position is identical from each end, as shown in Fig. 3.15. Readings from the strain gauges compared well with the theoretical assumption. These readings show the tension stiffening behavior of the beam sample.

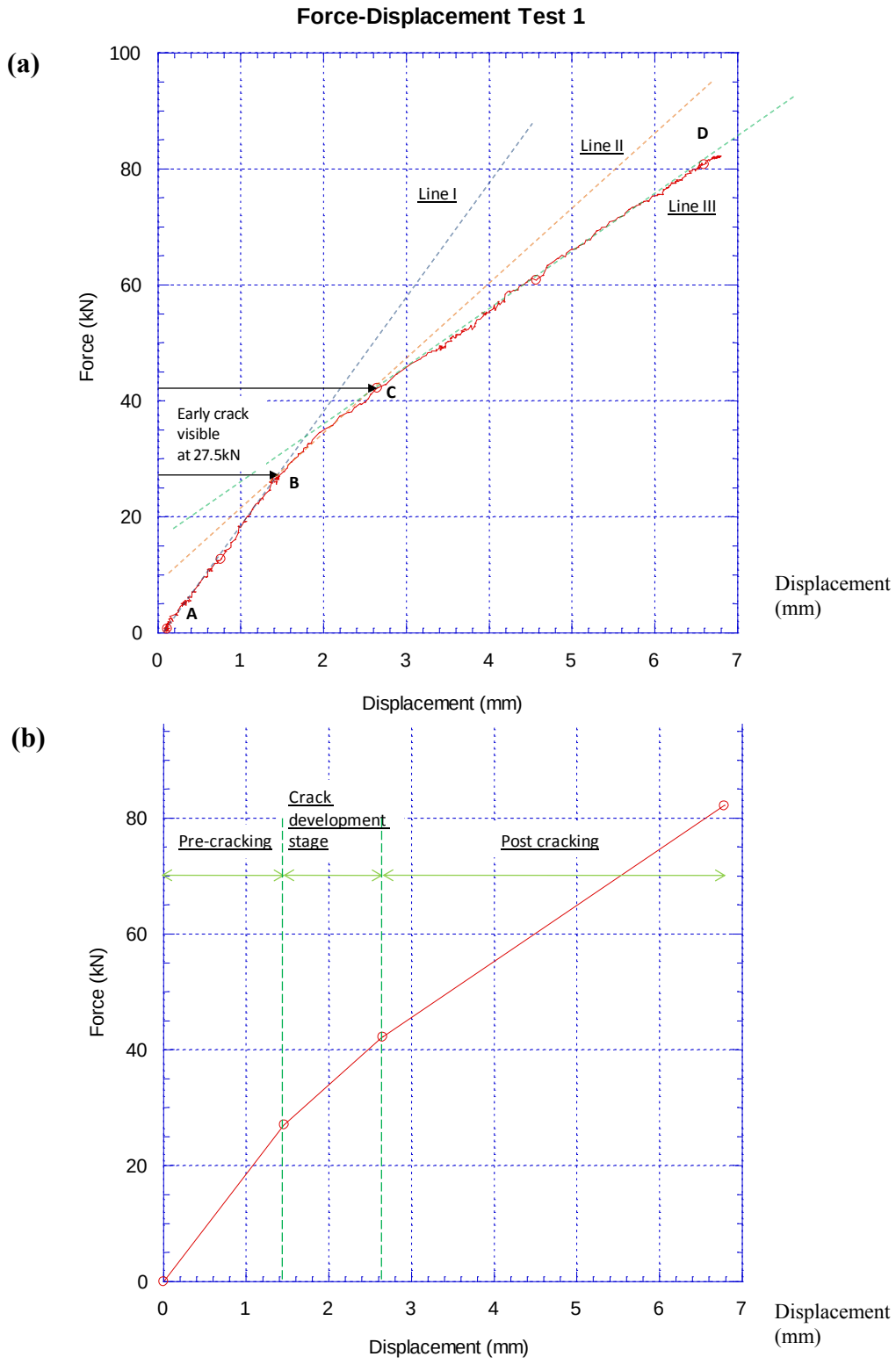

Fig. 3.18. Load-displacement curve for the concrete beam reinforced with inoxydable steel (a) Directly plotted from bending test, (b) Refinement of the experimental curve

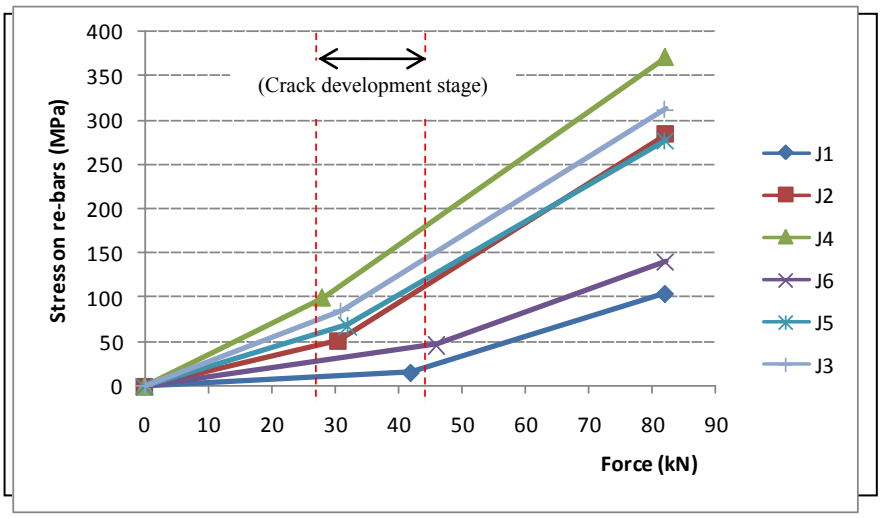

Fig. 3.19. Stress in each strain gauges for the applied force

Fig. 3.20 shows the strain pattern plotted along the reinforcement bar to investigate the strain distribution for the simply supported beam when load is applied. It can be observed that strain increases identically from both ends and maximum values are recorded in the center of the beam. When 30 kN load is applied, increase in strain is higher. Formation of cracks and deflection at the center gives higher values in the strain. This observation correlates well when compared to the findings from direct tension test conducted in Reference [9]. When strain pattern is plotted along the reinforcement bar, higher strain increase is observed at the crack position.

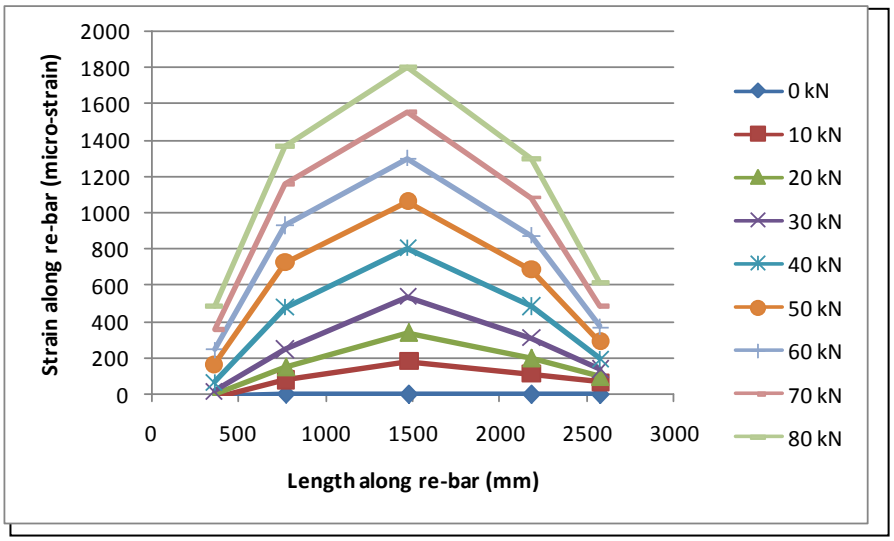

Fig. 3.20. Strain pattern along the reinforcement bar recorded during laboratory test

Tension stiffening phenomenon is also investigated in another different RC beam sample; reinforced with austenitic-cold (AC) steel. Results on this sample are recorded from the first crack until failure. Eight strain gauges are attached on the reinforcement bars. The position of each strain gauge is determined based on the same concept discussed for AH beam sample, shown in Fig. 3.15. Arrangement made along the AC rebars is shown in Fig. 3.21.

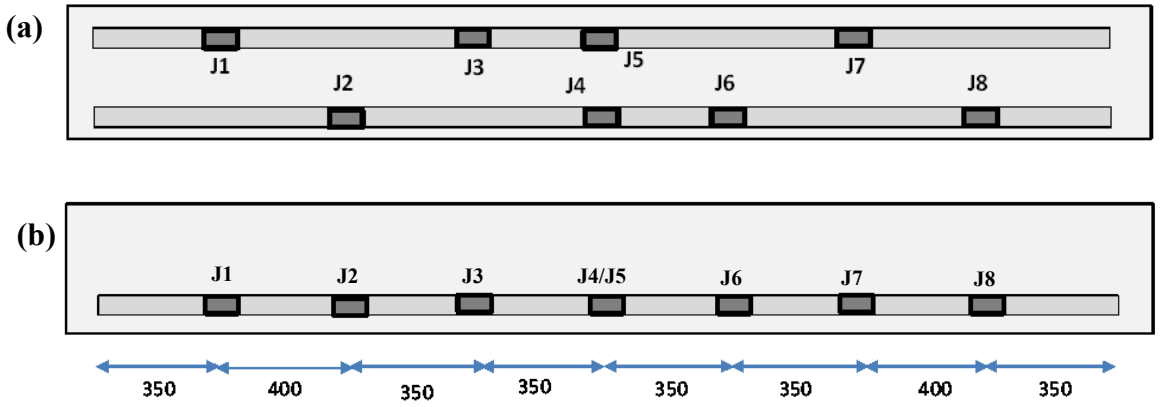

Fig. 3.21. Beam reinforced with AC; detailing position for each strain gauges along the re-bar: (a) Position on both re-bars as per plan view, (b) Side view of the RC beam showing the continuous position of the gauges

Changes recorded in the strain gauges are observed in three phases; pre-cracking, cracking phase, and post-cracking. Force-displacement curve for the premier cracking of the beam sample is plotted and the three phases are marked based on the same approach used in the austenitic-hot sample as shown in Fig. 3.18. Referring to Fig. 3.22, cracking phase starts between 30kN to 45kN applied load. These points are marked in the figure as K and L respectively for further reference. The austenitic-cold beam sample is then subjected to bending until rupture. The force-displacement curve for the entire load is shown in Fig. 3.23. Based on the same approach used in marking the different cracking phase of the beam sample, the hardening phase of the beam is marked with two points on the curve; M and N. This phase is recorded between 110 to 130kN. These points (K, L, M, and N) are then referred in observing stress increase in the rebar when load is applied; the tension stiffening phenomenon.

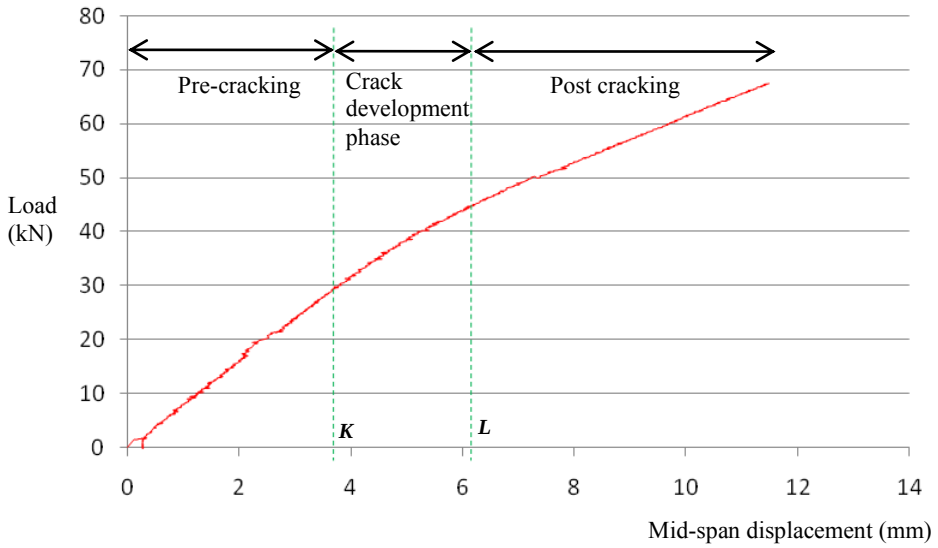

Fig. 3.22. Load-displacement curve (preliminary cracking) for the concrete beam reinforced with austenitic

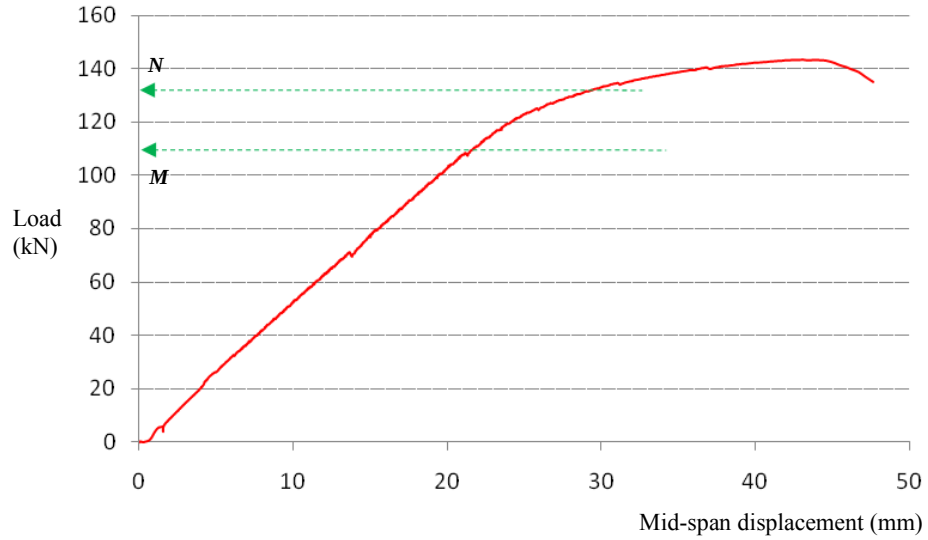

Fig. 3.23. Load-displacement curve (rupture) for the concrete beam reinforced with austenitic

Fig. 3.24 shows the stress changes recorded during loading until the beam sample ruptured. The four points K-L, and M-N are marked on the figure to signify the crack-development phase, and the hardening phase, respectively. It can be observed that a significant stress increase happens in both phases. Higher stress increase is recorded beyond point L; in the post-cracking phase. This is when bonding between concrete and rebar starts to wear off and concrete transfers stress to the reinforcement. Rapid increase in stress can then be observed in the hardening phase; between point M and N. At this stage, increase in

stress is resist by the reinforcement bars with less or no contribution from the surrounding concrete.

Strain gauges J4 and J5 recorded the highest reading due to its position in the middle of the span where maximum deflection occurs in the beam. Both strain gauges fail at 130kN (point N) due to deflection on the rebars. The other strain gauges have continuous reading until rupture. J1 and J8 have the lowest reading for their positions are near to the end support, thus have the least deflection in the beam. The stress increase (Fig. 3.25) due to loading recorded by the strain gauges shows the tension stiffening phenomenon in the AC beam sample.

Fig. 3.25 shows that comparable stress increases are recorded in each strain gauge during the cracking phase. This could signify the amount of bonding strength between the rebars and concrete as it is the same in each of the strain gauges position along the rebars. However, in the post-crack phase, the increment mounted in the middle span as the beam reaches its maximum deflection which shows failure in the rebar-concrete interaction and stress is now taken by the rebars alone. The amount decreases for strain gauges near the end supports.

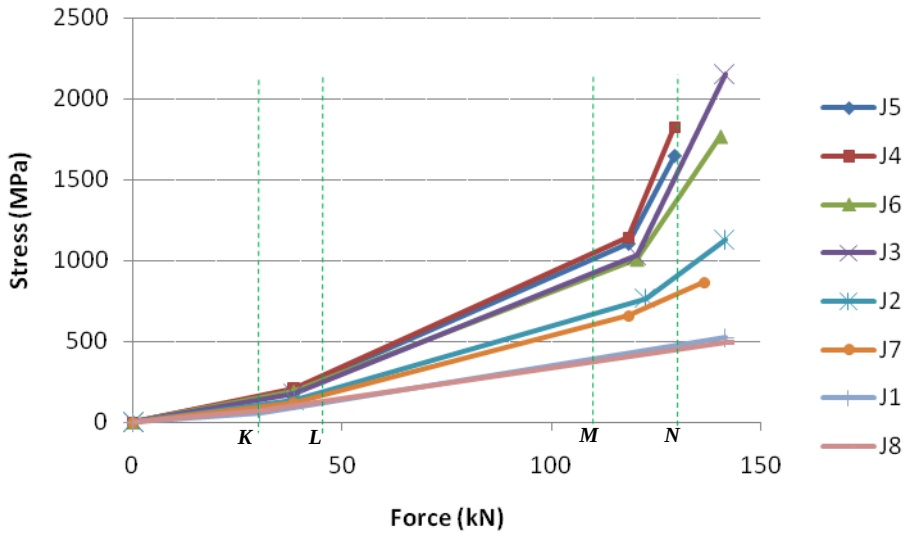

Fig. 3.24. Stress changes for the applied force (rupture)

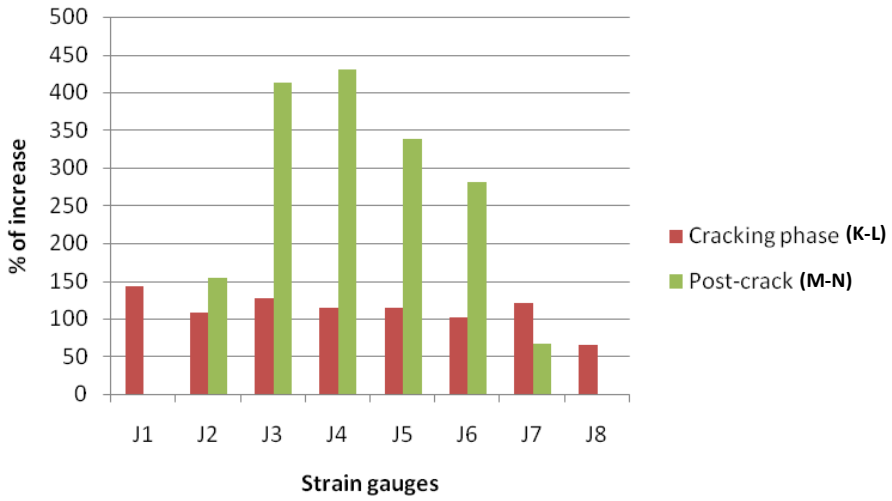

Fig. 3.25. Stress increase recorded in strain gauges

3. 6 Nonlinear Numerical Analysis (NNA)

After discussing the experimental approach and possibility of observing tension stiffening phenomenon in RC beam subjected to bending, method of developing the whole tension stiffening model using results obtained from the bending test will be discuss in this section. Parameters involved in defining the interaction properties between concrete and Inoxydable steel as reinforcing bars in structural element are determined through an inverse approach combining results from laboratory and NNA. Since tension stiffening models are adopted by smeared crack approach to simulate global response, the present approach rationally develops those parameters through direct matching of detailed nonlinear beam analysis and experimental global response. By comparing the load-deflection values obtained from the NNA with the results from laboratory test, tension stiffening model is chosen based on the closest resemblance between results from these two methods.

Tension stiffening model as suggested by Nayal and Rasheed, 2006 [30] is chosen to represent the interaction properties between inoxydable steel and concrete. This model has only a single set of stiffening parameters which applicable to the entire tension zone at all steps of the analysis. Due to its simplicity in simulating the post-cracking behavior, this model is used in this study. Fig. 3.26 shows the tension stiffening model, which depicts the main phenomena of primary and secondary cracking. This model involved four parameters; C_d, C_b, C_p, C_s together with the character of concrete; f'_t and ε_{cr} where

$$f_t = 0.3 f_{ck}^{\left(\frac{2}{3}\right)} \quad (3.21)$$

$$\varepsilon_{cr} = \frac{f_t}{E} \quad (3.22)$$

These concrete characters are determined based on a compression test conducted on the concrete sample used to prepare the concrete beam. These properties are discussed in Section 3.3.1. The four parameters are the one need to be determined through the inverse approach combining results from laboratory and NNA. Detail procedures are discussed in the following sub-sections.

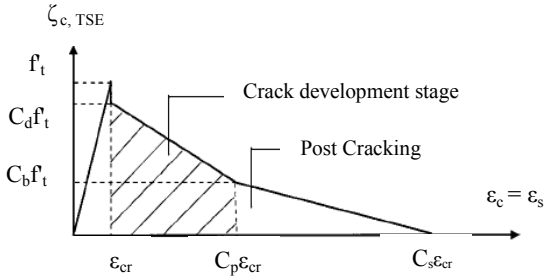

Fig. 3.26. Tension stiffening model used to represent interaction properties between Inoxydable steel and composite concrete.

3.6. 1 Method and Approach

In order to determine the four parameters in the tension stiffening model, NNA is conducted on the beam section to determine the load-deflection curve based on the section and beam properties. Laboratory sample of the concrete beam reinforced with austenitic-hot and the bending test results are used in this analysis. This analysis consists of two main stages; i) section analysis, ii) beam analysis. Beam properties shown in Fig. 3.14 are used in the section analysis and results of the laboratory test is used in the beam analysis phase. To analyze the beam section properties, cross-section of the beam is divided vertically into small layers through its total height as shown in Fig. 3.30. It is divided into 28 layers in which each layer is 10mm. Compression and tension zones of the section are identified, and strain at the center of each layer is then computed. Stress in each layer is evaluated using the corresponding material model. For beam analysis, beam is divided horizontally into small

sections as shown in Fig. 3.33. Beam is divided into 295 sections along its total length in which each section is 10mm long.

Fig. 3.27 shows the steps taken in conducting the NNA. In the beginning of the analysis, initial values of the tension stiffening parameters are introduced to the program together with the other properties of the RC beam obtained from laboratory samples. These include the materials and geometrical properties.

In the first iteration, section analysis will provide the properties detail for a particular section of the beam for each load increment. These properties will then be used in the beam analysis in order to determine load-deflection curve at mid-span of the beam. The load-deflection curve obtained from this NNA is then compared with the one obtained from laboratory work; bending test on the beam sample. The tension stiffening model applied in the section analysis is then corrected by changing the values of the four parameters; C_d, C_b, C_p, C_s so the load-deflection curve values from NNA resemble well with the laboratory results. The set of parameters which give the best-fit values with laboratory is selected as the tension stiffening model to represent the concrete beam reinforced with Inoxydable steel bars. These inversely estimated values give more reliable representation of interaction properties between the inox and composite concrete. This concept is visualized in Fig. 3.28.

If the coefficient of determination, R^2 between the two curves is more than 0.9, the values set of C_d, C_b, C_p, C_s will be chosen as the tension stiffening parameters for Inoxydable steel. Otherwise, second iteration will be conducted with a new set of parameters and the whole process will be repeated all over again.

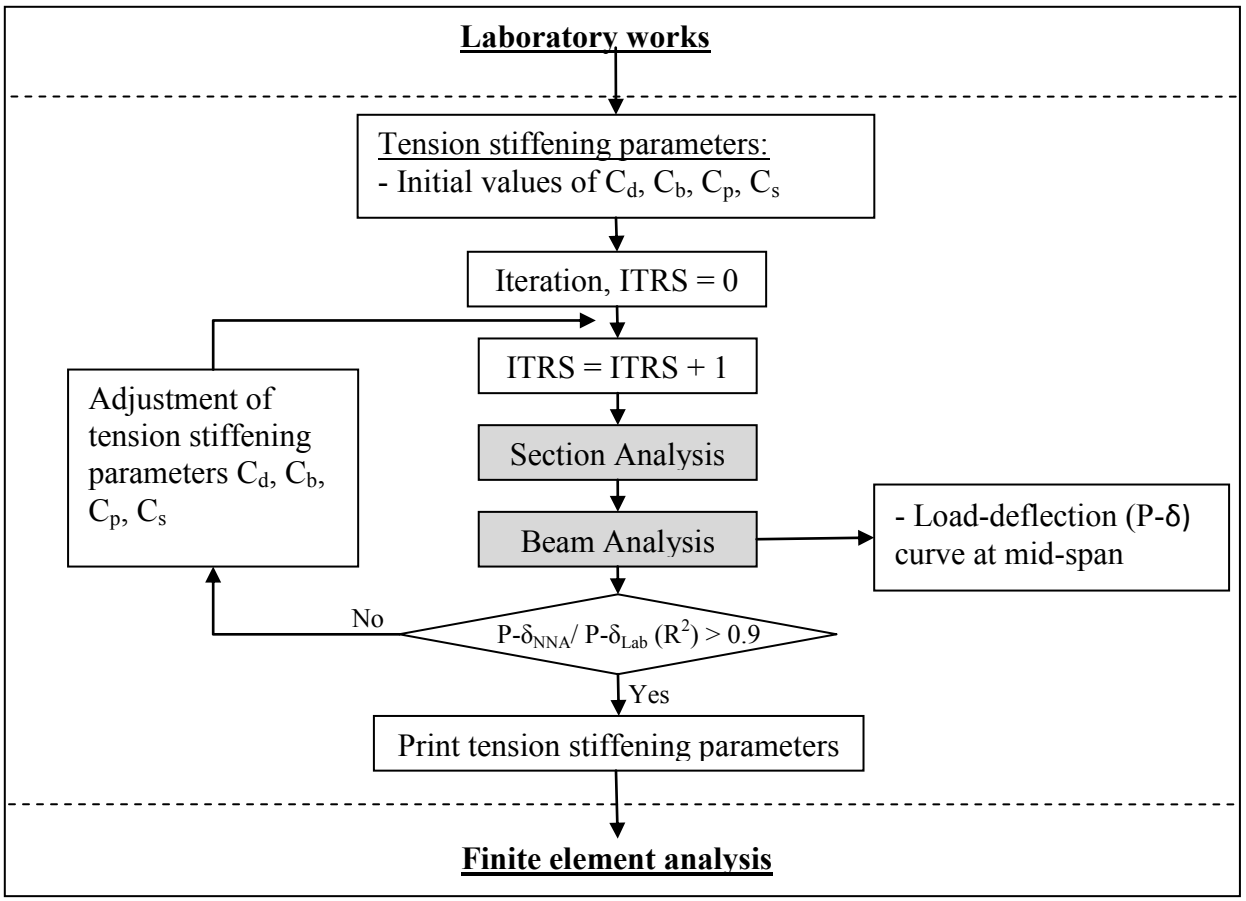

Fig. 3.27. Steps in the nonlinear numerical analysis

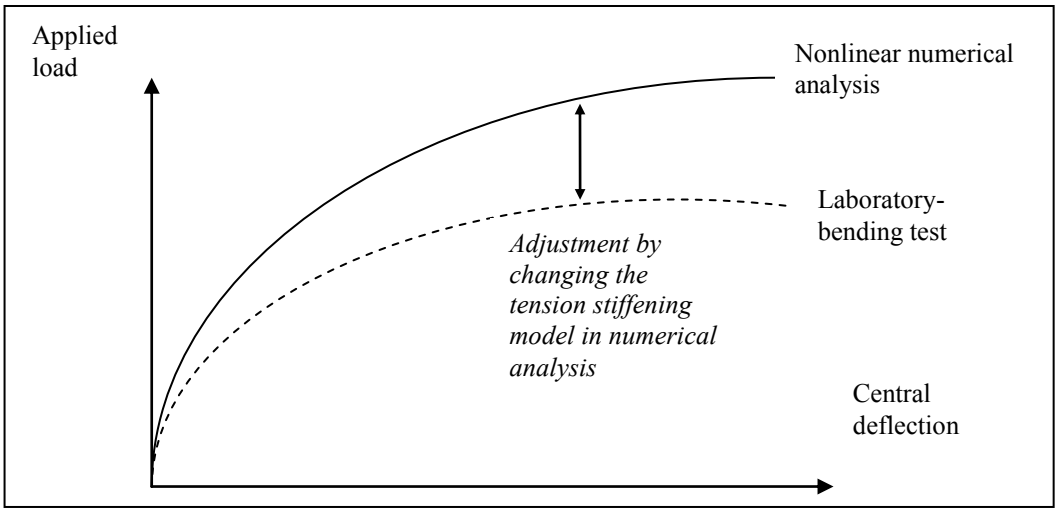

Fig. 3.28 The tension stiffening model is inversely develop by changing the parameters value used in section analysis so the central deflection obtained through NNA resemble the real laboratory results.

3.6. 2 Material Models

For concrete layers in compression zones, a fourth-degree polynomial model is chosen to represent the stress-strain relation;

$$\sigma_c = a_0 + a_1\varepsilon_c + a_2{\varepsilon_c}^2 + a_3{\varepsilon_c}^3 + a_4{\varepsilon_c}^4 \tag{3.23}$$

The above polynomials have been proposed on the basis of agreement with experimental work. They, moreover have distinct advantage of being directly integrable. The coefficients in Eq. 3.23 are defined by using the curve boundary condition based on concrete properties shown in Fig. 3.29;

$$\begin{Bmatrix} a_0 \\ a_1 \\ a_2 \\ a_3 \\ a_4 \end{Bmatrix} = \begin{bmatrix} 1 & 0 & 0 & 0 & 0 \\ 0 & 1 & 0 & 0 & 0 \\ 1 & \varepsilon_m & \varepsilon_m^2 & \varepsilon_m^3 & \varepsilon_m^4 \\ 0 & 1 & 2\varepsilon_m & 3\varepsilon_m^2 & 4\varepsilon_m^3 \\ 1 & 1 & 2C_u\varepsilon_m & 3(C_u\varepsilon_m)^2 & 4(C_u\varepsilon_m)^3 \end{bmatrix}^{-1} \begin{Bmatrix} 0 \\ E_{ci} \\ f_m \\ 0 \\ E_{cf} \end{Bmatrix} \tag{3.24}$$

where

$$f_m = k_c.f_{ck} \tag{3.25}$$

$k_c = 0.85$, 1.0 or > 1.0 according to some investigators. In this study k_c is taken as 1.0. As shown in Fig. 3.30, the slope of the descending line is evaluated by expressions suggested by Kent and Park [30] to include the effect of hoop confinement. The relation is extended horizontally when a stress of $0.2f_m$ is reached and it is terminated at a maximum confined compressive strain $C_c\epsilon_m$.

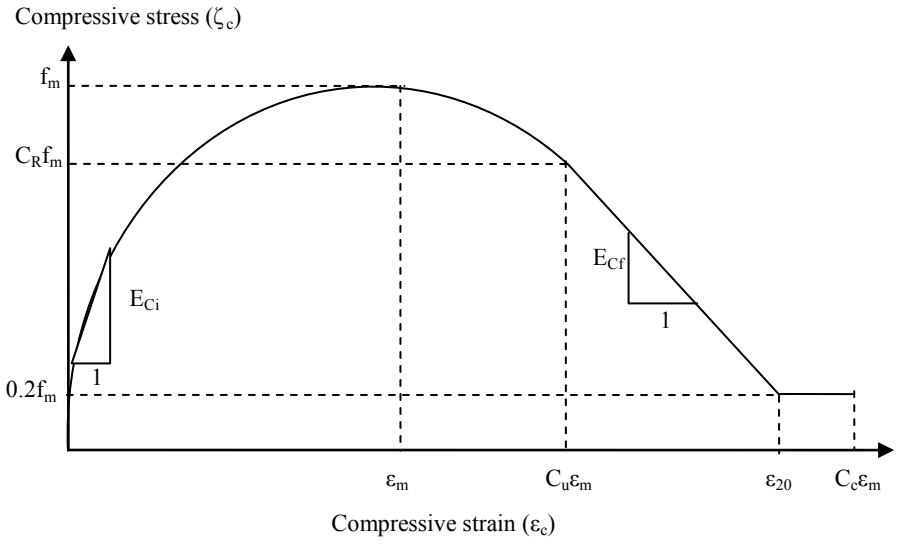

Fig. 3.29. Stress-strain relation for compressive concrete used in the analysis

For concrete in tension zone, the stress-strain relation of reinforced concrete suggested by Gilbert and Warner [30] (Fig. 2.7) is adopted to represent the tensile behavior combining tension softening, tension stiffening and local bond-slip effects. This relation is supported by experimental curve of plain concrete and compared well with test results on reinforced concrete slab conducted by the same authors. Furthermore, it is well suited to the present method of analysis. However in this study, the softening parameters are not changed according to the fiber location relative to the steel position, in which tension softening is ignored, but rather a continuous function is adopted over the whole tension zone. Fig. 3.26 shows the concrete stress-strain relation in tension used in the analysis. The four parameters C_d, C_b, C_p, and C_s are set to an initial trial values at the beginning of the analysis and inversely estimated from a combination of nonlinear analysis and experimental results.

For reinforcement bars, a bilinear relation is considered adequate for proper simulation of the actual stress-strain relation for reinforcing steel used in compression zone (carbon steel Grade 460) since the elastic-plastic behavior with or without introducing the strain hardening effect is easily simulated by controlling the slope of the second line. However, for tension zone where Inoxydable steel bars are used, a specific constitutive law developed in Section 3.2.3 (Eq. 3.17 and 3.18) is applied to represent the nonlinearity of this type of steel.

3.6. 3 Section Analysis

Increasing the loading (axial force and/or bending moment) applied to a section, causes the neutral axis depth, the strain and stress distributions, and the flexural and axial rigidities to vary in a nonlinear manner. Numbers of studies involving numerical techniques have therefore been conducted to tackle this situation. Bilinear and trilinear moment-curvature relations for flexural members are example of early and simple models. However, such models are incapable of tracing an accurate response for heavily reinforced sections, especially in presence of an axial force, Rasheed and Dinno, 1993 [43]. In this study, a nonlinear solution scheme is utilized within which direct and exact computations are made by performing closed-form integrations for nonlinear section properties. The section analysis

involved determination of overall effective or secant flexural rigidity (EIs) for the beam section. The strain profile is determined using the applied moment and the current value of the EIs about the inelastic centroid. The compression and tension zones of the section are identified. For each layer, strain is computed to evaluate the stress using the corresponding material model.

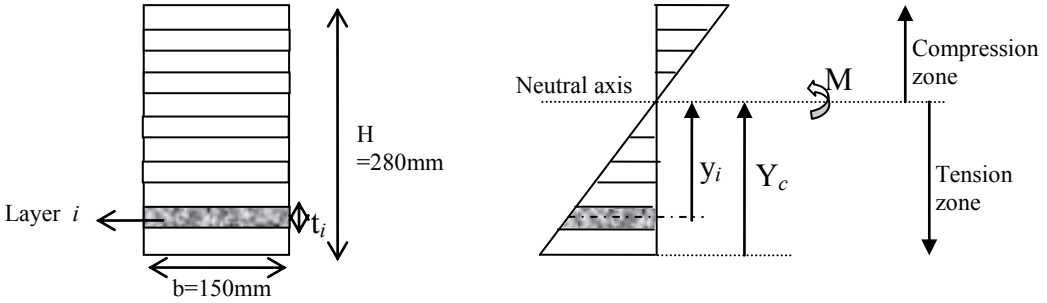

Fig. 3.30. Section analysis by finite layer approach

The overall effective or secant axial rigidity of the section (EA_s) is the summation of the individual layer areas times their corresponding secant modulus of elasticity:

$$EA_s = \sum_{i=1}^{NLR} E_{ci} B_{ci} t_{ci} + \sum_{j=1}^{N} \left(E_{rtj} - E_{ctj}\right) A_{rtj} + \sum_{k=1}^{M} (E_{rbk} - E_{cbk}) A_{rbk} \quad (3.26)$$

$$E_{ci} = \frac{\sigma_{ci}}{\varepsilon_{ci}} \quad (3.27)$$

$$E_{rtj} = \frac{\sigma_{rtj}}{\varepsilon_{rtj}} \quad (3.28)$$

$$E_{rbk} = \frac{\sigma_{rbk}}{\varepsilon_{rbk}} \quad (3.29)$$

Where

NLR = number of concrete layers in the section

N, M = numbers of the top and bottom reinforcement layers, respectively

E_{ci} = secant concrete modulus

B_{ci} = width of layer i

t_{ci} = thickness of layer i

E_{rtj} and E_{rbk}= secant moduli of elasticity of the top and bottom reinforcement layers

A_{rtj} and A_{rbk}= corresponding reinforcement areas

E_{ctj} and E_{cbk}= secant concrete moduli of elasticity at the level of the top and bottom reinforcement layers respectively

ε_{ci} , ε_{rtj} and ε_{rbk}= strain at the center of concrete layer *i*, top and bottom reinforcement layer *j* and *k* respectively

σ_{ci} , σ_{rtj} and σ_{rbk}= stress at the center of concrete layer *i*, top and bottom reinforcement layer *j* and *k* respectively corresponding to material models

The overall effective or secant flexural rigidity (EI_s) of the section is the flexural rigidity of each layer about the inelastic centroid (Y_c) summed up over the section depth. The inelastic centroid being the position about which the first moment of the axial rigidity (*EA*) vanishes (Fig. 3.30).

$$EI_s = \sum_{i=1}^{NLR} E_{ci}B_{ci}t_{ci}Y_i^2 + \sum_{j=1}^{N}\left(E_{rtj} - E_{ctj}\right)A_{rtj}\left(Y_{rtj}\right)^2 + \sum_{k=1}^{M}(E_{rbk} - EcbkArbkYrbk2 \quad (3.30)$$

where

Y_i= distance from the centroid of layer *i* to the section inelastic centroid

Y_{rtj} and Y_{rbk} = distance from the inelastic centroid to the centroid of the top and bottom reinforcement layers respectively.

The internal axial force (F_x) is given by;

$$F_s = \sum_{i=1}^{NLR} E_{ci}\varepsilon_{ci}B_{ci}t_{ci} + \sum_{j=1}^{N}\left(E_{rtj} - E_{ctj}\right)\varepsilon_{rtj}A_{rtj} + \sum_{k=1}^{M}(E_{rbk} - E_{cbk})\varepsilon_{rbk}A_{rbk} \quad (3.31)$$

The internal bending moment (M_{int}) about the inelastic centroid is represented by;

$$M_{int} = \sum_{i=1}^{NLR} E_{ci}\varepsilon_{ci}B_{ci}t_{ci}Y_i + \sum_{j=1}^{N}\left(E_{rtj} - E_{ctj}\right)\varepsilon_{rtj}A_{rtj}\left(Y_{rtj}\right) + \sum_{k=1}^{M}(E_{rbk} - EcbkerbkArbkYrbk \quad (3.32)$$

To develop an approach which lends itself to direct computation, the section is divided into two zones each of which is bounded by one of the extreme fibers and the neutral axis. According to the type of stress in any zone (tension or compression), it is further divided into regions having a certain stress-strain formula for each. The compression zone may include one or more of the following regions (Fig. 3.29):

Concrete: Region 1 $0 \le \varepsilon_c \le C_u\varepsilon_m$

Region 2 $C_u\varepsilon_m < \varepsilon_c \le \varepsilon_{20}$

Region 3 $\varepsilon_{20} < \varepsilon_c \le C_u\varepsilon_m$

Steel: Region 4 $0 \leq \varepsilon_{sc} \leq \varepsilon_y$

Region 5 $\varepsilon_y \leq \varepsilon_{sc} \leq \varepsilon_{su}$

The tension zone may also include one or more of the following regions:

Concrete: Region 1 $-\varepsilon_{cr} \leq \varepsilon_t \leq 0$

Region 2 $-C_p\varepsilon_{cr} \leq \varepsilon_t \leq -\varepsilon_{cr}$

Region 3 $-C_s\varepsilon_{cr} \leq \varepsilon_t \leq -C_p\varepsilon_{cr}$

Steel: Region 4 $-\varepsilon_y \leq \varepsilon_{st} \leq 0$

Region 5 $-\varepsilon_{su} \leq \varepsilon_{st} \leq -\varepsilon_y$

Explicit forms of the rigidities and the internal loadings for all the regions are derived by performing analytical integrations, as detailed in the following sub-section. By the summation of the region properties, the section properties are directly obtained.

$$EA_s = \sum_{i=1}^{2} \sum_{j=1}^{NRi} EA_{ij} \tag{3.33}$$

$$F_x = \sum_{i=1}^{2} \sum_{j=1}^{NRi} F_{x_{ij}} \tag{3.34}$$

$$EI_s = \sum_{i=1}^{2} \sum_{j=1}^{NRi} EI_{ij} \tag{3.35}$$

$$M_{int} = \sum_{i=1}^{2} \sum_{j=1}^{NRi} M_{c_{ij}} \tag{3.36}$$

where NRi is the number of regions per zone. The above equations; Eqs. (3.33)-(3.36) are detailed in Annex 8.1.

The effective section properties corresponding to any applied bending moment step, M, are evaluated as follows:

7. The instantaneous curvature is determined by dividing the applied moment by the most current value of the effective section flexural rigidity:

$$\phi = \frac{M}{EI_s} \tag{3.37}$$

8. The depth of the tension and the compression zones are defined using the most recent location of the inelastic centroid Y_c and the total height of the section H:

$$Y_{N1} = H - Y_c \tag{3.38}$$

$$Y_{N2} = Y_c \tag{3.39}$$

9. The section rigidities (EA_s, EI_s), internal axial force (F_x), and the bending moment (M_{int}) are calculated for the present strain distribution using Eqs. (3.26), (3.30)-(3.32).

10. The accuracy of the most recent inelastic centroid position is investigated using the criterion of vanishing the moment of axial rigidity about the current centroid (*ES*) at the correct position:

$$ES = \frac{F_x}{\phi} \tag{3.40}$$

A normalized convergence criterion is adopted with a certain tolerance limit depending on the level of accuracy required.

$$\frac{ES}{EA_s x Y_c} < S_{TOL} \implies Convergence\ achieved \tag{3.41}$$

Where S_{TOL} is the convergence tolerance of the section; taken as $5x10^{-7}$.

11. If Eq. (3.41) is satisfied, an equilibrium solution is reached, yielding the inelastic centroid position and the section properties for that step. Otherwise, steps 1-4 are repeated using the corrected inelastic centroid Y_c until convergence is achieved:

$$Y_{c(corrected)} = Y_{c(current)} + \frac{ES}{EA_s} \tag{3.42}$$

12. The analysis is stopped when a failure criterion is satisfied (F_{CON}). The failure criteria is implemented as rupture of reinforcement or crushing of concrete. Concrete crushing failure is defined at 0.003 compressive strain for unconfined compression and a higher value for confined concrete (the strain at which the compression stress of the descending branch reaches 0.2 f_c). Rupture failure occurs when the reinforcement reaches the ultimate rupture strain.

The above procedures are programmed using MATLAB to automate the section analysis for each load increment. Fig. 3.32 shows the flow chart of the program.

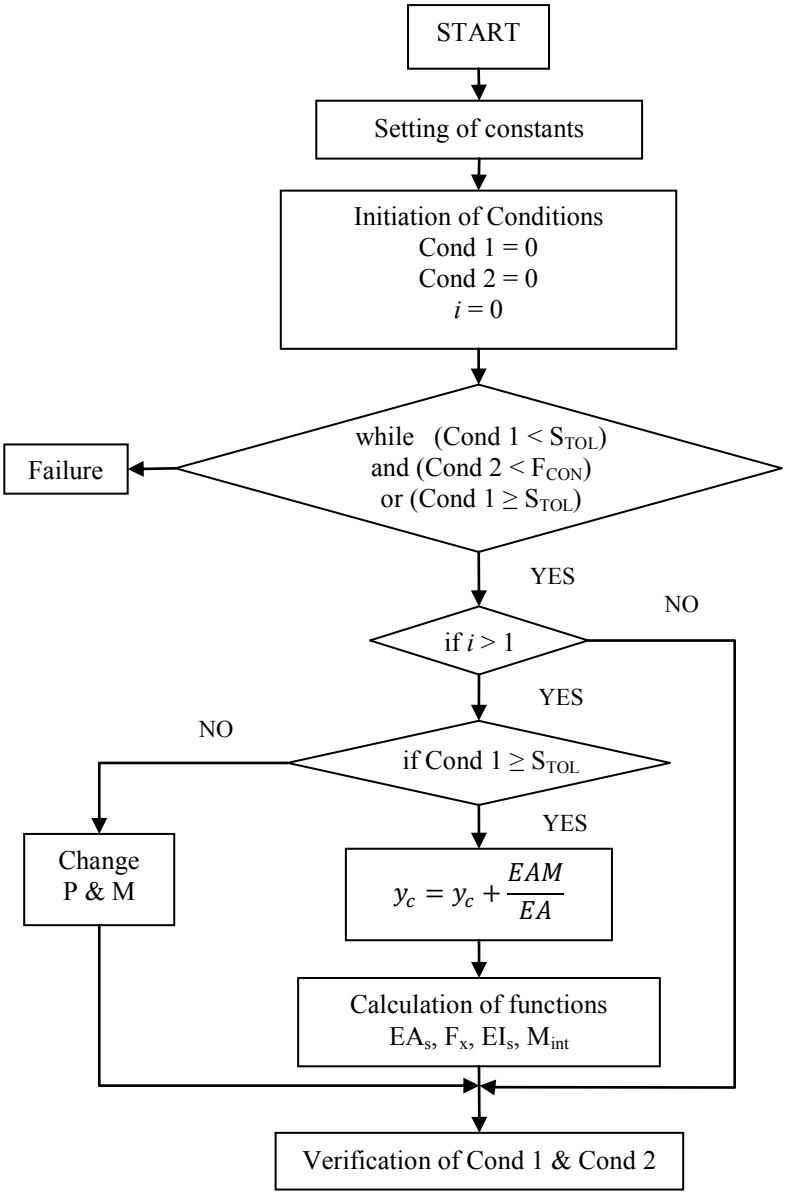

Fig. 3.32: Flow chart of the nonlinear numerical analysis programmed using MATLAB

3.6. 4 Beam Analysis

The nonlinear load-deflection solution of the beam is formulated using the moment area integration. Because the flexural rigidity reduces with an increase in moment, the stiffness of the beam is expected to vary along the span, in a nonlinear fashion, with the change in bending moment. This study is intended to consider an accurate stiffness distribution along the beam. This is accomplished by dividing the beam into a large number of segments and calculating the section flexural rigidity in the middle of each segment under

a certain load increment. The beam sample is divided into 295 segments; 10mm width for each segment (Fig. 3.33). The mid-span deflection is obtained by performing numerical integration of the moment of curvature distribution along half the span about the support point. The numerical integration is performed as a summation of the analytical integration contribution of each segment. This is expressed for the four-point bending case as:

$$\Delta_{midspan} = \int_0^{L/2} x\varphi(x)dx \tag{3.43}$$

$$= \sum_{i=1}^{N_s} \frac{P}{2EI_{si}} \left[\frac{X_{i+0.5}^3 - X_{i-0.5}^3}{3}\right] + \frac{PL_a}{2EI_{si}} \frac{\left[\left(\frac{L}{2}\right)^2 - (L_a)^2\right]}{2} \tag{3.44}$$

where N_s=number of segments along the beam shear span; P=total load applied on the beam; $X_{i-0.5}$=distance from the support point to the beginning of segment i; $X_{i+0.5}$=distance from the support point to the end of the segment i; L_a=shear span of the beam, and EI_{si}=flexural rigidity of segment i (Fig. 3.34).

The mid-span deflection is then plotted and compared to the curve obtained from laboratory test, as illustrated in Fig. 3.28. The tension stiffening model applied in the section analysis is then corrected by changing the values of the four parameters; C_d, C_b, C_p, C_s so the load-deflection curve values from NNA resemble well with the laboratory results. The set of parameters which give the best-fit values with laboratory is selected as the tension stiffening model to represent the concrete beam reinforced with Inoxydable steel bars. These inversely estimated values give more reliable representation of interaction properties between the inox and composite concrete.

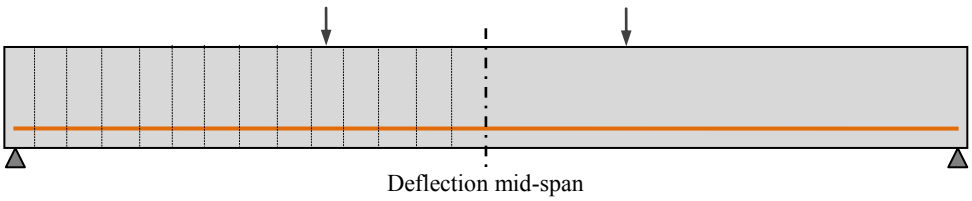

Fig. 3.33. Numerical analysis: Beam is divided into a large number of sections to determine the central deflection. Each section is analyzed to get stress, strain, and section rigidities for every increment of load

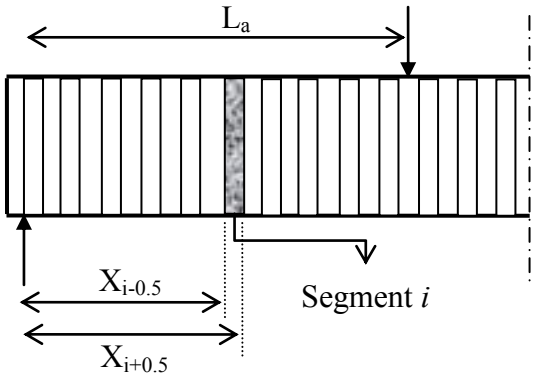

Fig. 3.34. Vertical segment of the beam analysis

3.6. 5 Tension Stiffening Model for Inoxydable Steel

Results obtained from the NNA are compared with laboratory findings in order to determine the tension stiffening model for inox. The beam sample constructed and tested under bending as been discussed in Section 3.5.1 is used in the analysis. Mechanical and geometrical properties of the beam are applied as input to the program.

A series of analyses are conducted to determine the tension stiffening parameters that correlate well with the real behavior of the RC beam as per laboratory findings. Table 3.3 shows the four sets of trial on selecting the values of C_d, C_b, C_p, C_s. Based on the section properties obtained from NNA, and load-deflection values from beam analysis, comparison with laboratory results gives value of 0.9, 0.5, 5 and 13 for C_d, C_b, C_p, C_s, respectively. The load-deflection curve from NNA using these tension stiffening parameters are compared with laboratory curve in Fig. 3.35. Good correlation can be observed from these two curves. Fig. 3.36 shows the final tension stiffening model develop for composite concrete beam reinforced with inoxydable steel from austenitic type. This model is useful to represent the interaction behavior between these two materials in any finite element modeling.

Table 3.3: Investigation of tension stiffening parameters

Parameter	Selecting C_d	Selecting C_b	Selecting C_p	Selecting C_s	Selected parameters
C_d	0.8,**0.9**,1	1.5	1.5	1.5	0.9
C_b	0.5	0.45, **0.5**, 1	0.8	0.8	0.5
C_p	4	4	4, **5**, 6	4	5
C_s	40	40	40	5, 10, **13**, 20	13

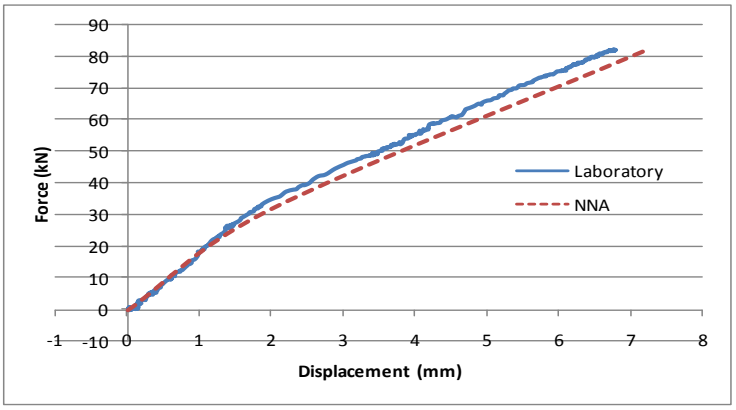

Fig. 3.35. Force displacement curve from laboratory results compared to the nonlinear numerical analysis

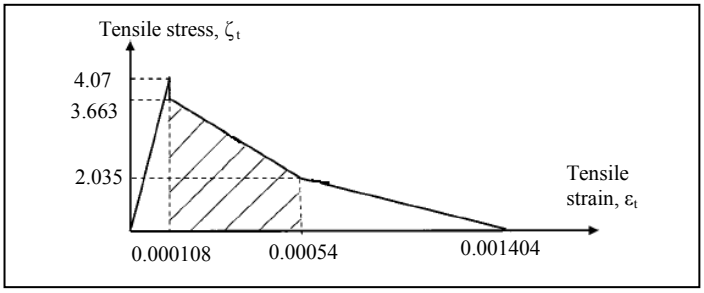

Fig. 3.36. Tension stiffening model for beam reinforced with inoxydable steel bars

3.6. 6 Comparison with Carbon Steel

According to a study conducted by Nayal and Rasheed, 2006 [30], selected values for tension stiffening parameters for concrete beam reinforced with carbon steel are 0.8, 0.45, 4, and 10 for Cd, Cb, Cp, and Cs respectively. Fig. 3.37 shows the tension stiffening model for inoxydable steel as compared to the standard carbon steel.

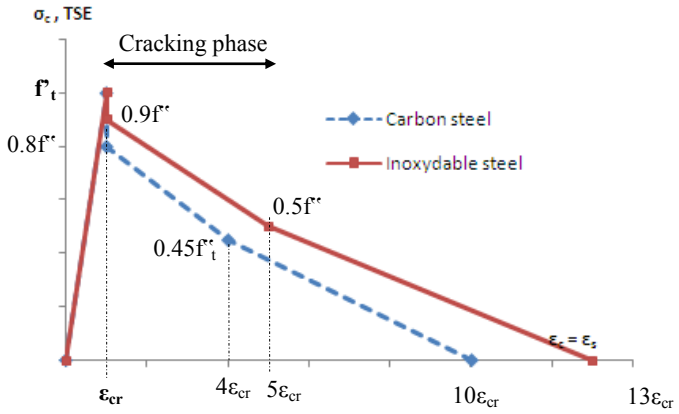

Fig. 3.37. Comparison of tension stiffening model for concrete beam reinforced with carbon steel and inoxydable steel

Referring to Fig. 3.37. it can be observed that concrete beam reinforced with inoxydable steel has higher tension stiffening effect than the one reinforced with standard carbon steel. In the cracking phase, the tension stiffening with inoxydable steel increases 50 percent as compared to standard steel.

The approach selected in this study is able to determine parameters involved in developing the tension stiffening model. Based on the inverse method, a more reliable result could be generated. This tension stiffening model could be used further in any numerical simulation to represent the interaction properties between inoxydable steel and concrete in composite material.

3. 7 Finite Element Analysis

The finite element method in comparison with the most common analytical methods of concrete behavior is a powerful tool to study the behavior of the reinforced concrete composite beams. A general purpose finite element code, Abaqus Version 6.4, is utilized in this study. Abaqus includes a variety of routines that allows for the implementation of specific material models (concrete and steel), boundary conditions, and bond behavior. The interaction between the reinforcing steel and concrete is also considered. Abaqus/Standard

(STD) has been chosen to model the reinforced concrete beam as per built and tested in the laboratory. Analysis with Abaqus/STD represents the classical version of the general finite element software and uses tangential stiffness approach that is unconditionally stable [44]. For resolution of nonlinear problems, there are two principle methods available; the traditional Newton-Raphson method (Static General), and the Riks arc length method (Static Riks) [49]. The first method is applied in this study to verify the material model developed for the inoxydable steel and the interaction properties defined between the reinforcement bars and surrounding concrete.

3.7. 1 Modeling Strategies

Three-dimensional finite element analysis is conducted to examine the behavior of composite concrete structural elements internally reinforced with inoxydable steel. Concrete is modeled using 8-node 3-D solid elements while the internal reinforcement bars are modeled using 2-node embedded bar formulation in the concrete elements. Through this approach, the reinforcing bars are treated as integral parts of the concrete element to determine the total internal resisting forces that are directly added to those of concrete.

Beam is modeled as simply supported with two point loads at 1/3 of the span. The loads are distributed evenly in a constraint area to avoid localized damage in one point as shown in Fig. 3.38 (a). The loading‟s arrangement and the dimension of the beam model are as shown in Fig. 3.14. The positions of each strain gauges; J1, J2, J3, J4, J5, and J6 are marked precisely along the main reinforcement bar based on their actual position in beam sample of laboratory work (Fig. 3.16). History output results are generated on each position of the strain gauges to compare the values with the ones recorded during experimental work.

The model is then meshed into small elements so that each of the concrete elements contains re-bar. Little or no reinforcement in elements often introduces mesh sensitivity in the analysis results in the sense that the finite element prediction does not converge to a unique solution as the mesh is refined because mesh refinement leads to narrower crack bands. This problem typically occurs if only a few discrete cracks form in the structure, and mesh refinement does not result in formation of additional cracks. If cracks are evenly distributed;

in this case due to the effect of rebar, mesh sensitivity is less of a concern. In practical calculations for reinforced concrete, the mesh is usually such that each element contains rebars. The interaction between the rebars and the concrete tends to reduce the mesh sensitivity.

In order to select a suitable mesh size to be used, the model is meshed into different numbers of element; ranges between 60 and 400 elements. Effect of the element size is verified by comparing vertical displacement obtained from the FEM with the one from laboratory works; taking 80kN of applied load as bench mark (Fig. 3.39(a)). When the model is meshed into 396 elements as shown in Fig. 3.39(b), results obtained from FEM shows the best resemblance with laboratory works (Fig. 3.39(a)). The comparison is verified through load-displacement curve plotted between these two analyses as shown in Fig. 3.40. A good correlation can be observed; maximum displacement of 7mm obtained from FEM for 80kN applied load as compared to 6.8mm from laboratory work.

For the reinforcement bars, the model is developed with two austenitic steel 20mm in diameter in tension zone, two carbon steel 8mm in diameter in compression zone, and 10 shear links formed from 6mm mild steel bars were provided at 70mm and 120mm from each end for shear reinforcement in the shear spans. Austenitic-hot steel as tested in laboratory work is used for the tension rebar. Tensile test results and constitutive laws as mentioned in the previous section are applied in the material properties for the reinforcement bar so their nonlinear plastic response could be accurately simulated in the numerical model. The reinforcement bars are modeled as embedded element in the concrete as shown in Fig. 3.38 (b). These elements are superposed on the mesh of plain concrete elements. This modeling approach allows the concrete behavior to be considered independently of the rebar. The same modeling technique is applied by Nour et al., 2007 [49].

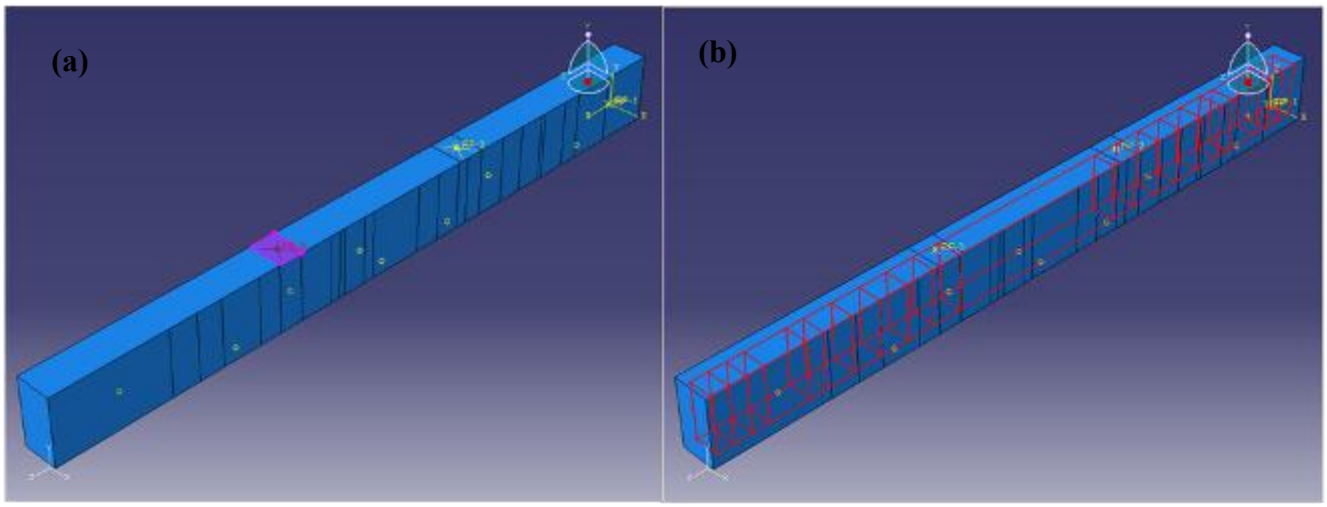

Fig. 3.38. Approaches in modeling the RC beam (a) Point load assigned and distributed uniformly in a constraint area to avoid local failure, (b) Re-bars and stirrups modeled as embedded in the concrete element

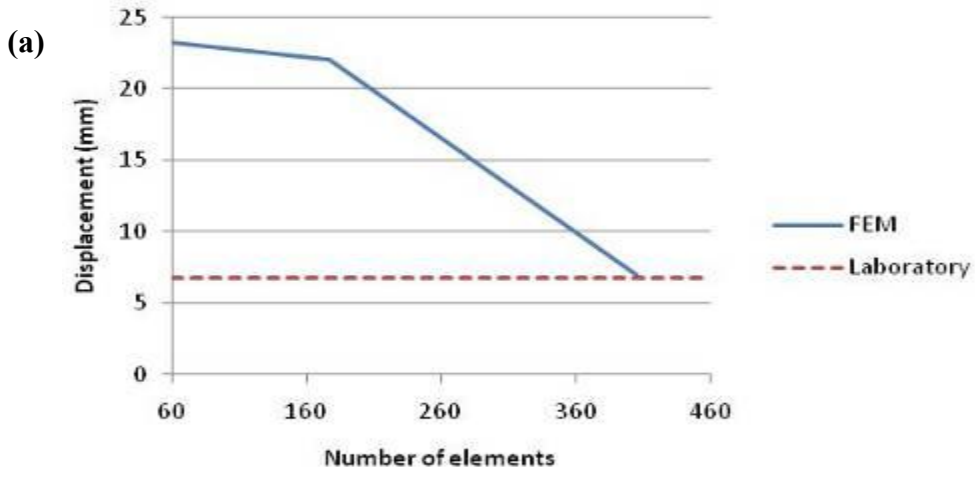

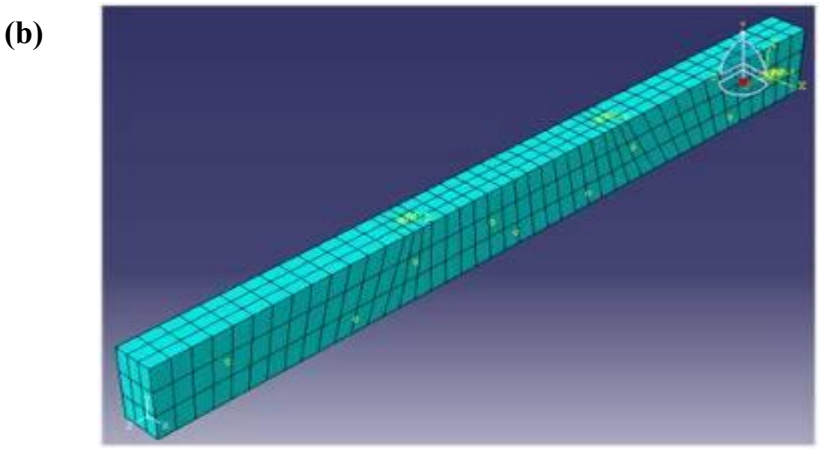

Fig. 3.39. Selection of suitable mesh size (a) Effect of mesh size on vertical displacement as compared to laboratory results for applied load of 80kN (b) mesh selected for the model

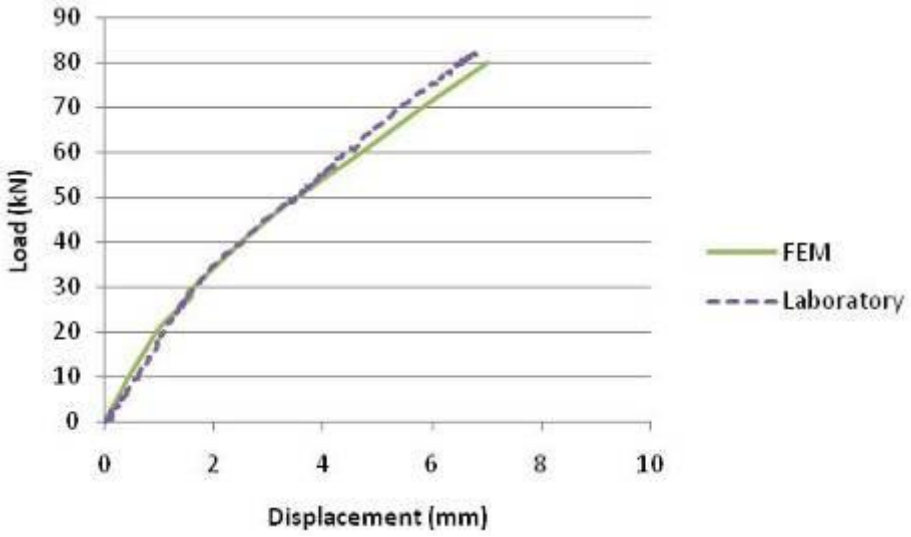

Fig. 3.40. Comparison of vertical displacement obtained from laboratory works and FEM

3.7. 2 Inelastic constitutive model for concrete

As mentioned above, the concrete behavior is considered independently of the rebar, so this section focuses on plain concrete model. The smeared crack model provided in Abaqus/STD for plain concrete is applied to the FEA model. Effects associated with the rebar/concrete interface, such as bond slip and dowel action, is considered by modifying some aspects of the plain concrete behavior; the use of tension stiffening to simulate load transfer across cracks through the rebar. This is discussed in the next section.

The concrete material model consists of an isotropically hardening yield surface, active when the stress is dominantly compressive, and an independent „„crack detection surface"""which determines if a point fails by cracking. The model is a smeared crack model, in the sense that it does not track individual „„macro"" cracks. This type of model assumes that cracks are uniformly distributed in the concrete mass. It applies the constitutive equations independently at each integration point of the finite element model to determine failure in concrete. The presence of cracks enters into these calculations by the way in which the cracks affect the stress and material stiffness associated with the integration point.

When the tensile strength criterion is exceeded, a micro-crack band perpendicular to the principal direction in tension develops. Material gradually loses its integrity, leading to the

degradation of material properties interpreted as tension damage. As in compression, tension damage evolution is described by means of a scalar parameter d, which represents the degradation of material properties due mainly to crack propagation. Thus, once the crack is initiated, the elastic modulus, E_c is reduced using the damaged material modulus E_d, defined as:

$$E_d = (1 - d)E_c \tag{3.45}$$

where d = 0 corresponds to undamaged material and d = 1 to completely damage material. The parameter d is estimated as proposed in [45].

The model uses the classical concepts of plasticity theory: a strain rate decomposition into elastic and inelastic strain rates, elasticity, yield, flow, and hardening.

The strain rate decomposition;

$$d\varepsilon = d\varepsilon^{el} + d\varepsilon_c^{pl} \tag{3.46}$$

where $d\varepsilon$ is the total mechanical strain rate, $d\varepsilon^{el}$ is the elastic strain rate which includes crack detection strains and $d\varepsilon_c^{pl}$ is the plastic strain rate associated with the "compression yield" surface.

The "compression yield" surface is

$$f_c = q - \sqrt{3}a_0 p - \sqrt{3}\tau_c = 0 \tag{3.47}$$

In uniaxial compression, $p = {}^{1}/_{3}\,\sigma_c$ and $q = \sigma_c$, where σ_c is the stress magnitude. a_0 is a constant, which is chosen from the ratio of the ultimate stress reached in biaxial compression to the ultimate stress reached in uniaxial compression; and τ_c is a hardening parameter obtain as;

$$\tau_c = \left(\frac{1}{\sqrt{3}} - \frac{a_0}{3}\right)\sigma_c \tag{3.48}$$

The model uses a "crack detection" plasticity surface in stress space to determine when cracking takes place and the orientation of the crack. Damaged elasticity is then used to describe the post-failure behavior of the concrete with open cracks. The basis of the post-cracked behavior is the brittle fracture concept. Assuming that the fracture energy required to form a unit area of crack surface (G_f) is a material property, this value is calculated from measuring the tensile stress as a function of the crack opening displacement, as;

$$G_f = \int \sigma_t \, du \tag{3.49}$$

The above described model has been successfully validated by different researchers [44]. It has proven to be capable to model the inelastic behavior of concrete and be used together with re-bars to model concrete reinforcement.

The effect from rebar/concrete interface is approximated by introducing the tension stiffening to the material model. This effect can be included in the numerical model either by modifying the stress-strain relationship of the reinforcing bar or the concrete [29]. Numbers of research have included this effect in the concrete model [25]-[30], [47]. In this study, tension stiffening effect is applied in the simulation by changing the material properties in concrete model rather than the reinforcement bars so that the constitutive law developed for inoxydable steel (as detailed in Section 3.2.3) can be used without any modification and the tension stiffening model developed in Section 3.6.5 (Fig. 3.36) can be applied directly to the numerical model.

3.7. 3 Comparison of experimental and numerical results

Based on the history output results generated at the position of each strain gauges modeled in the FEM; J1, J2, J3, J4, J5, and J6, a stress-strain curve is plotted. These results are verified by extracting the reinforcement bars frame from the composite model as shown in Fig. 3.42. As the developed model is symmetrical, and the position of strain gauges marked on the reinforcement bars are identical from both ends, stresses on the paired position; J3-J4, J2-J5, and J1-J6 resemble with each other as shown in Fig. 3.43. The sudden increase in stress; tension stiffening phenomenon is recorded at 22kN, earlier than the one recorded in laboratory; 27kN. J3 and J4 shows the highest values of stress throughout the loading process; 400MPa for 80kN load. This is due to their position at the center of the beam where maximum deflection occurred which leads to earlier formation of cracks. This is followed by J2 and J5 with 300MPa for the maximum load. J1 and J6 show the lowest stress; 150MPa for 80kN applied load.

Results from this numerical FEA are then compared with the readings on the strain gauges recorded in the experimental work, as shown in Fig. 3.45. Comparison is made between the paired strain gauges that provide similar readings due to their position along the bar. J4 and J3 are compared together in Fig. 3.45(a), comparison of J2 and J5 in Fig. 3.45(b), while J1 and J6 are compared in Fig. 3.45(c). In general, the result shows a good correlation

between the FEA and experimental results. Values from numerical analysis are slightly higher than the one obtained from laboratory work.

Stress values from FEA for J3 and J4 are 50MPa higher than the experimental work when the maximum load is applied. For J2 and J5, 25MPa difference in stress is observed for the 80kN load. J1 and J6 show a closer resemblance values in stress recorded through experimental and FEA.

The strain distribution patterns observed in the finite element modeling are similar with the experimental results. This can be seen by comparing Fig. 3.44 and Fig. 3.20, for the finite element model and strain gauges readings from laboratory work, respectively. By comparing these two figures, it can be observed that strain distribution at each end of the bar shows close resemblance between FEA and experimental. For the maximum load of 80kN, both ends of the re-bar have strain around 0.0006. This is where the J1 and J6 are located. For the location of J2 and J6, strain recorded in the experimental works is around 0.0014 as compared to FEA; 0.0016. However, the strain pattern in the center of the beam for FEA is higher than laboratory results; 0.0025 as compared to 0.0018.

The differences between FEA and experimental values could happen due to few reasons. The resemblance of FEA model to the actual behavior could be increased by taking into consideration the input parameter from density of reinforcement, the quality of the bond between the rebar and the concrete, the relative size of the concrete aggregate compared to the rebar diameter, and the mesh.

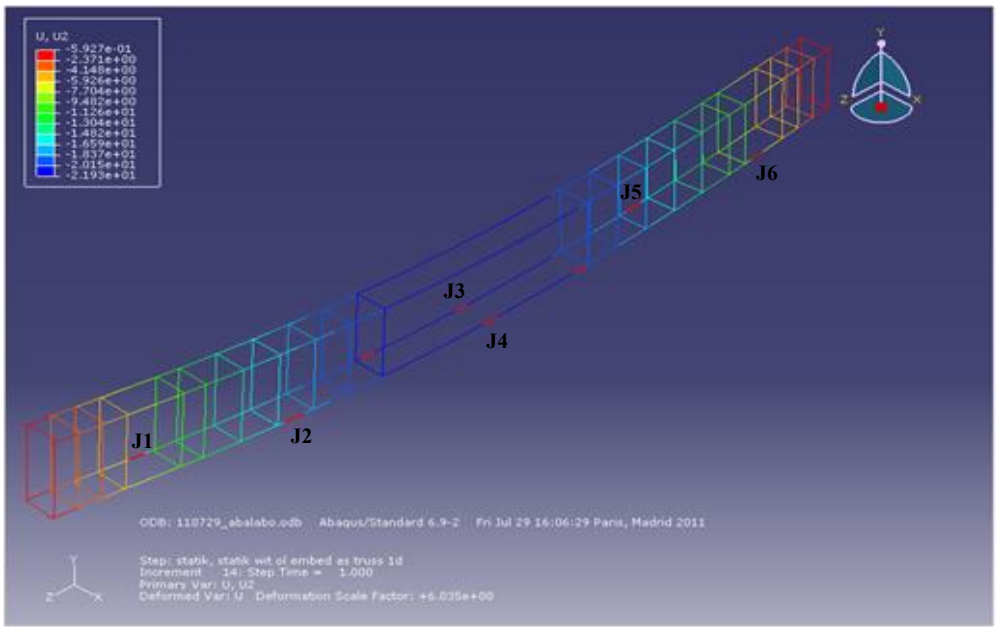

Fig. 3.42. History output results for each strain gauge J1, J2, J3, J4, J5, and J6 are verified by extracting the reinforcement bars frame from the composite model

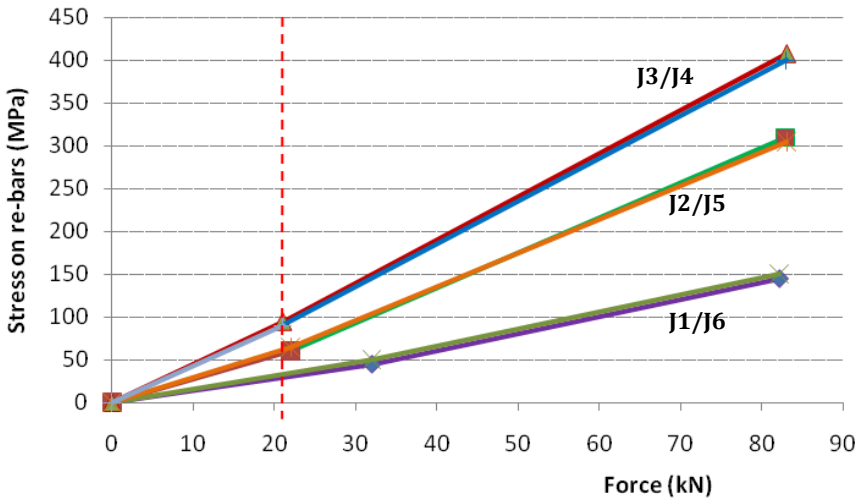

Fig. 3.43. Stress recorded at the position of each strain gauge for the applied force

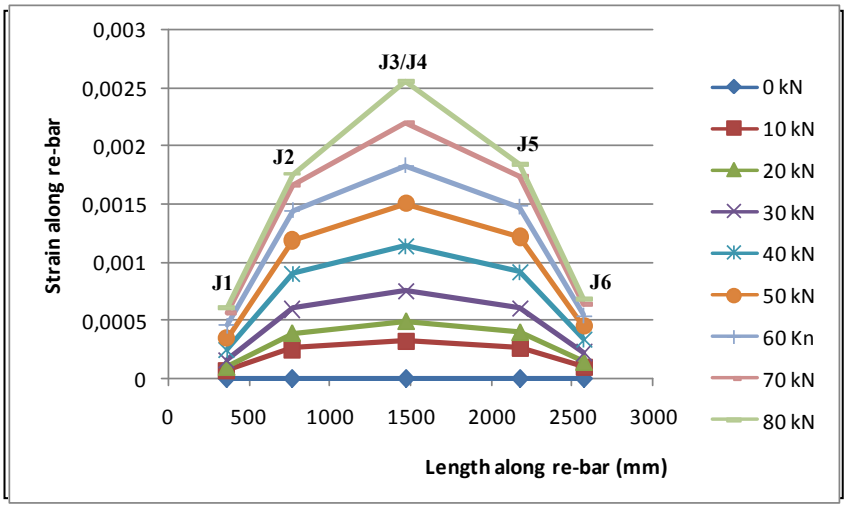

Fig. 3.44. Strain pattern along the reinforcement bar recorded through numerical analysis

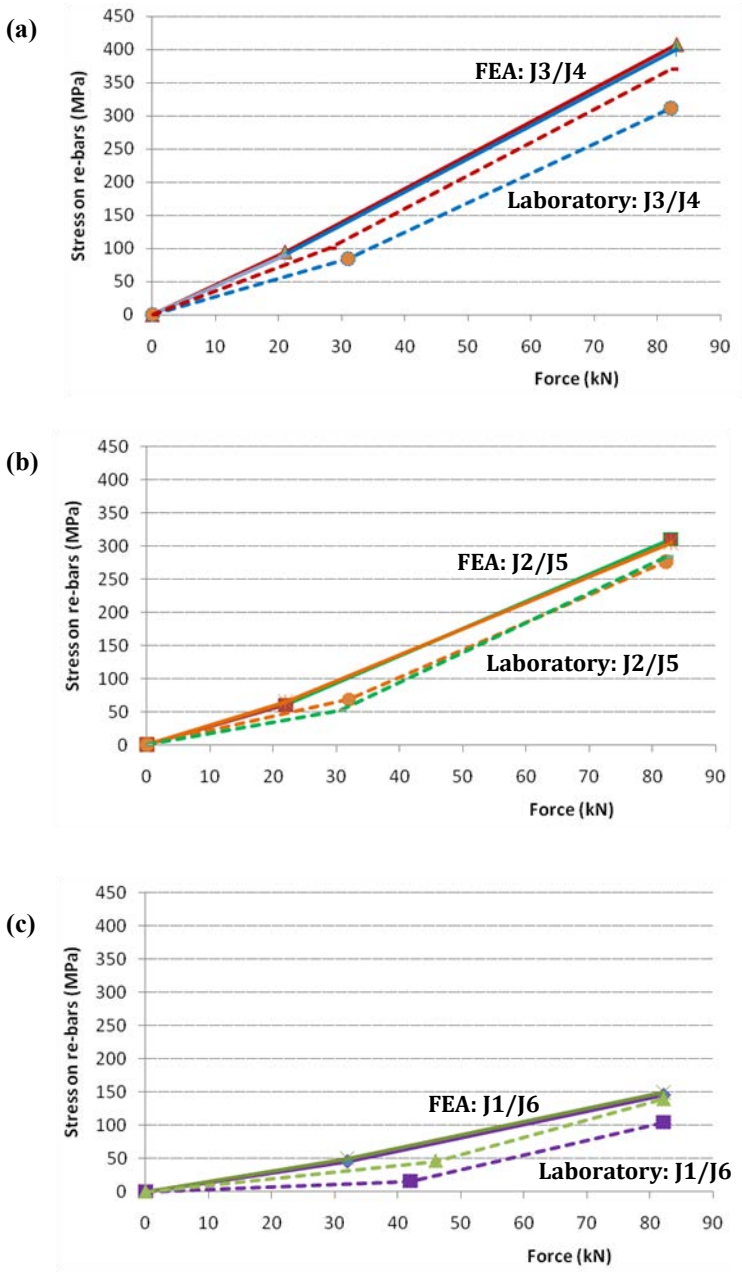

Fig. 3.45. Stress in each strain gauge for the applied force; comparison between laboratory results and numerical FEA (a) J3 and J4, (b) J2 and J5, and (c) J1 and J6.

3. 8 Tension Stiffening in Composite Concrete Reinforced with BFUP and Inox

In the previous section, approach to investigate the interaction behavior between inoxydable steel and concrete in composite beam is discussed. The approach (Fig. 3.46(a)) is able to observe the tension stiffening phenomenon and determine the interaction model for beam subjected to bending if the results are combined with nonlinear numerical analysis. In

terms of experimental setting, the approach is easier to set up and it consists of global experimental results which can be interpreted easily. In many references, tension stiffening is investigated through direct tension test (Fig. 3.46(b)), [8]-[12] which require additional setting for applying load and support to the sample. However, tension stiffening phenomenon is well observed in the direct tension test and results could be interpreted directly to determine the interaction model.

In this section, a new experimental approach is investigated to study the possibility of observing the tension stiffening phenomenon in composite concrete structure. This approach combined the concept of direct tension test and bending test (Fig. 3.46). A series of experimental settings are applied to determine a suitable concept which could observe the tension stiffening phenomenon.

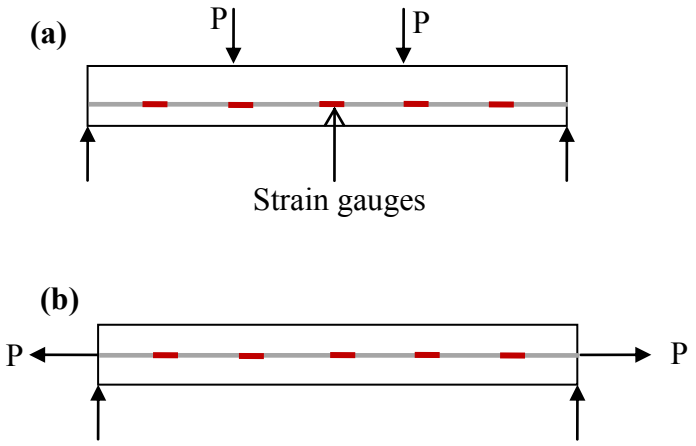

Fig. 3.46. Experimental setting to investigate tension stiffening (a) bending test, (b) direct tension test

In this combined approach (Fig. 3.47), two concrete blocks are reinforced with single reinforcement bar and joined together using steel plates. These steel plates are attached to the concrete surface and fixed to each other through pin connection which allows the concrete blocks to rotate when load is applied (Fig. 3.47 (a)). Deflection of the concrete blocks will cause the reinforcement bar to be pulled from the concrete surface (Fig. 3.47 (b)). Strain gauges are attached to the reinforcement bar to monitor changes when load is applied.

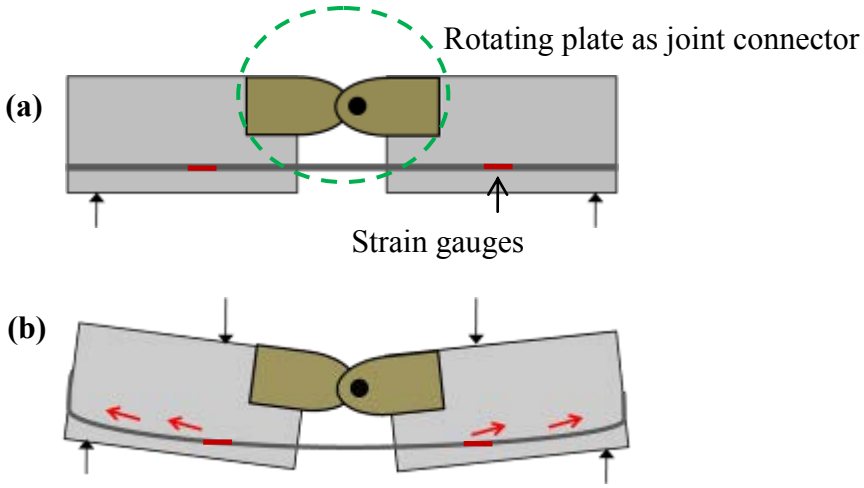

Fig. 3.47. Combined experimental concept to investigate tension stiffening phenomenon

The steel plate is attached to the concrete blocks through rod inserted in holes made in the concrete blocks. The holes made in the concrete block however weaken the area where connection is made with the steel plates (Fig. 3.48(a)). This has caused shear failure in the connection area when load is applied (Fig. 3.48(b)). To overcome this problem, Ultra-high performance fibre-reinforced concrete, UHPFRC (*Béton Fibré à Ultra-hautes Performance*), BFUP is used to increase the strength of concrete in the connection area. The concrete block is develop using two types of concrete; standard concrete (50 MPa) and BFUP as shown in Fig. 3.49 (a).

Fig. 3.48. Shear failure in the area of plate connector

The concrete height is 70mm; higher than h_{eff}. According to EC2, h_{eff} is the effective height to consider for steel-concrete interaction. Height of BFUP is 80mm; enough for the connection part (70mm).

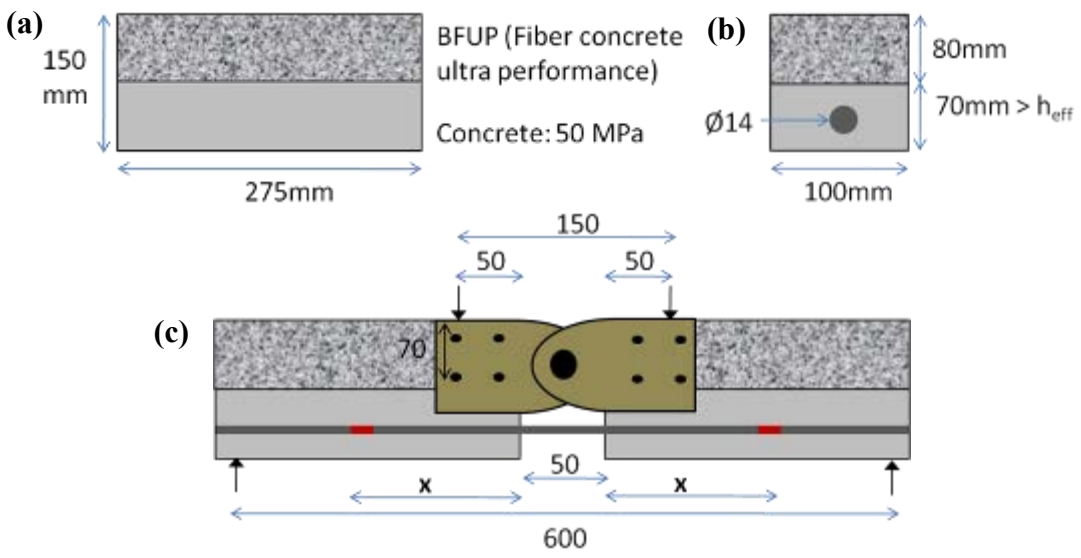

Fig. 3.49. Detailing of the test sample

A specially fabricated mould is used to prepare the concrete sample (Fig. 3.50(a)). It consists of two identical mould fixed in the position using steel frame. The concrete blocks are then separated in the middle (Fig. 3.50(b)). Standard concrete used to fill 70mm height of the mould and BFUP fills the rest of 80mm height as shown in Fig. 3.50(c) and (d) respectively. The whole sample is cured for 28 days before testing.

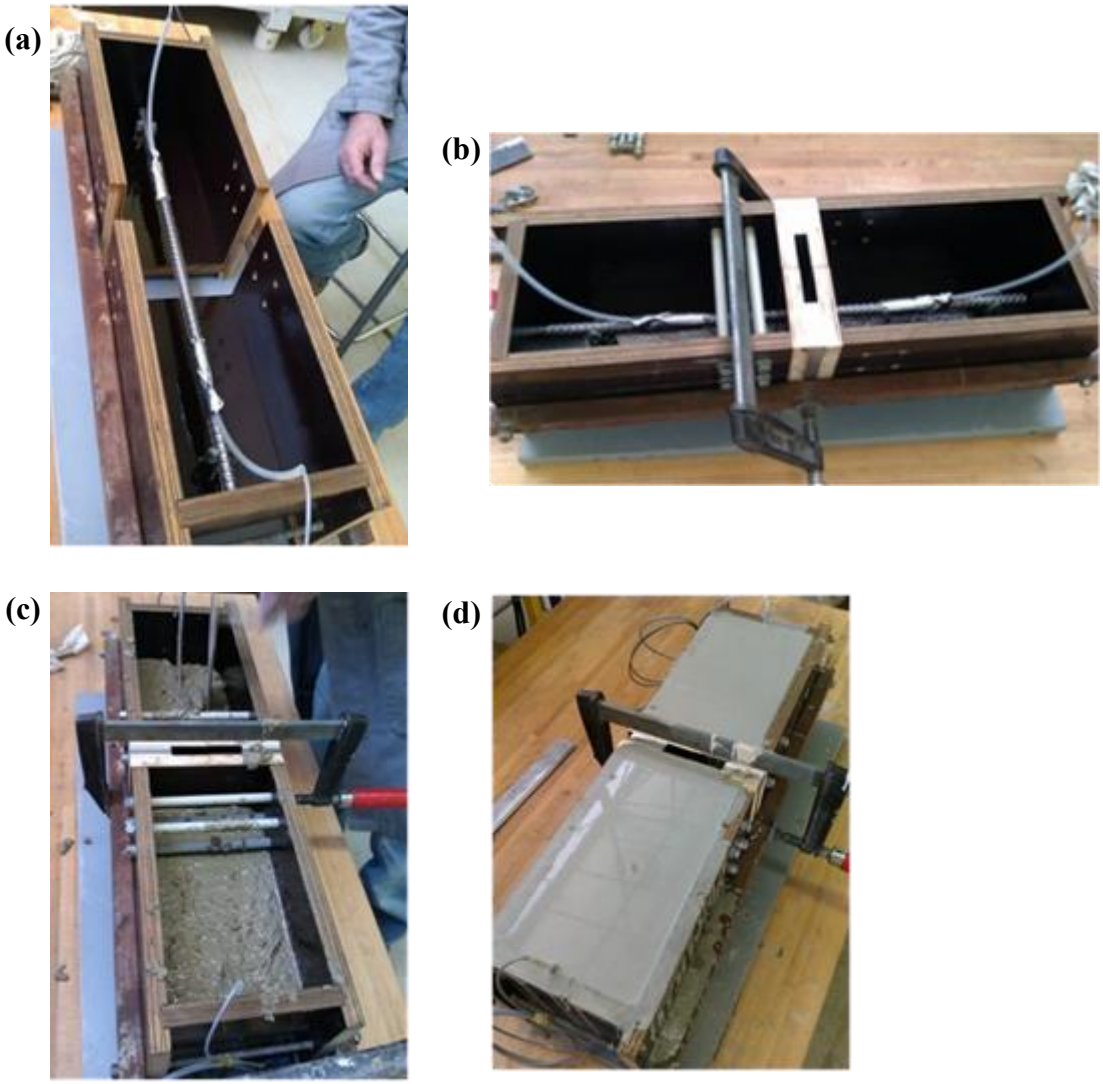

Fig. 3.50. Preparation of the composite concrete sample; (a) two identical mould fixed using steel frame (b) mould separated in the middle before concreting, (c) concreting of the sample with standard concrete (d) BFUP covers the height of the steel plate connector

Fig. 3.51 shows the procedure of fixing the steel plate connector to join the concrete blocks. All steel rods (Fig. 3.51(a)) and steel plates used for the connection are fixed on the sample after 28 days; when the concrete samples are ready to be tested. The connection system allows rotation between the concrete blocks when load is applied to the system. Fig. 3.52. (a) shows the prepared sample ready to be tested. Sample is placed on a bending test machine Fig. 3.52. (b) in a position shown in Fig. 3.49(c).

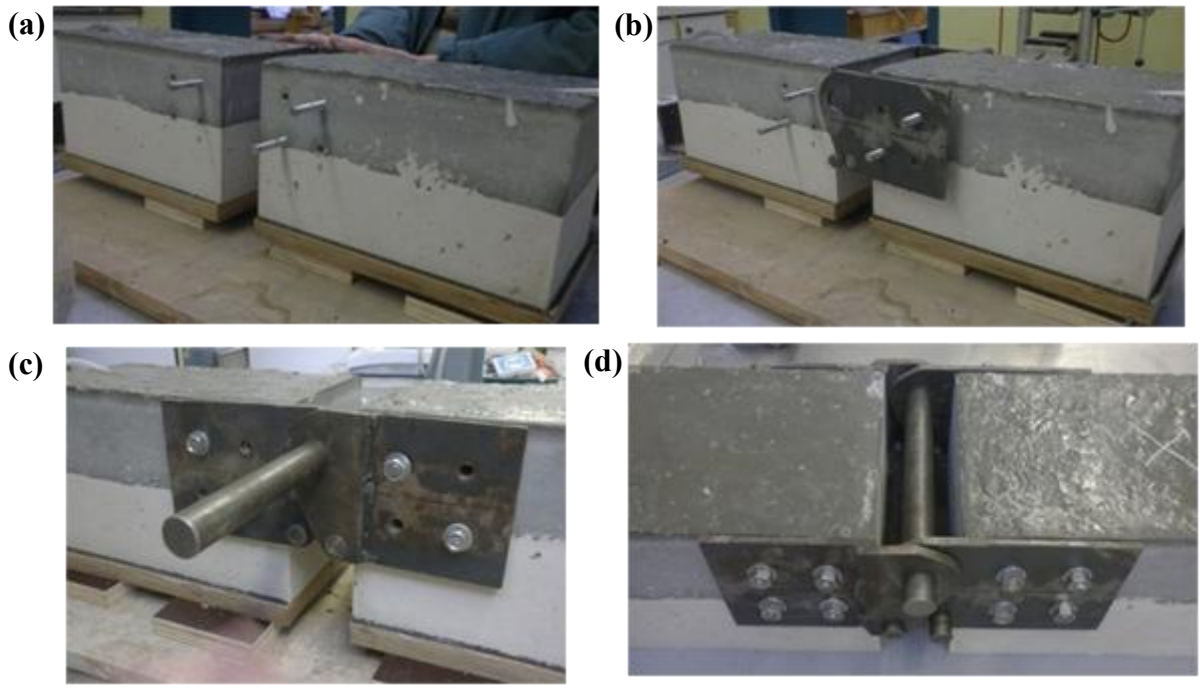

Fig. 3.51. Fixing plate connector within the concrete blocks; connection system to allow rotation between the concrete blocks (a) steel rods to fix the steel plates, (b) steel plate to hold the concrete block, (c) steel rod used to join the two parts of the concrete blocks, (d) pin joint allows rotation during loading

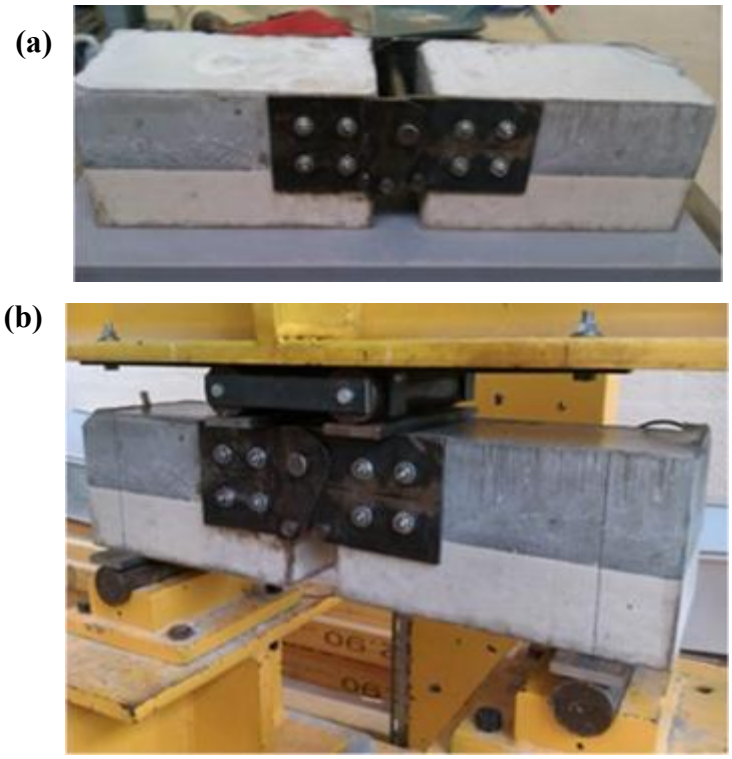

Fig. 3.52. (a) The prepared sample ready to be tested, (b) Setting on the bending test machine

When the above sample is tested under bending (Fig. 3.53 (a)), a problem occurs in the attached boundary of standard concrete and BFUP surface. At 60kN of applied load, cracks start to initiate, but the two types of concrete separated from each other (Fig. 3.53 (b)). Readings recorded from strain gauges are verified to observed changes during loading.

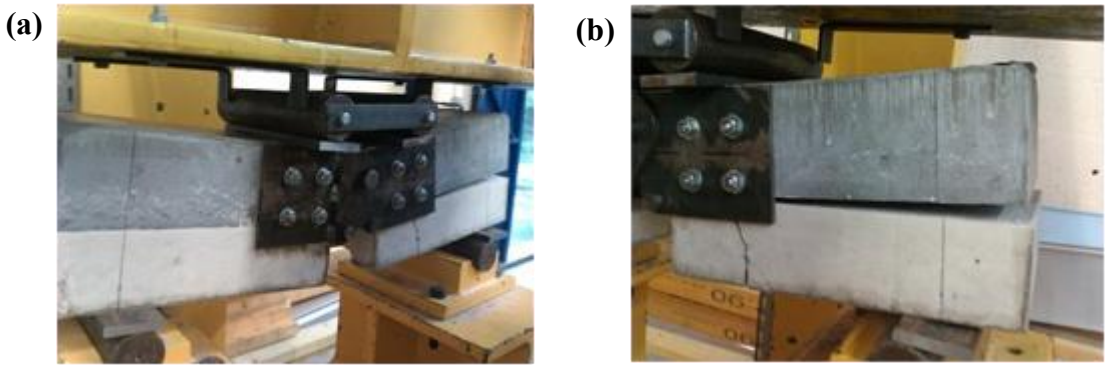

Fig. 3.53. Problem in the sample: (a) Rotated block caused slides between the two type of concrete (b) interaction failure between standard concrete and BFUP

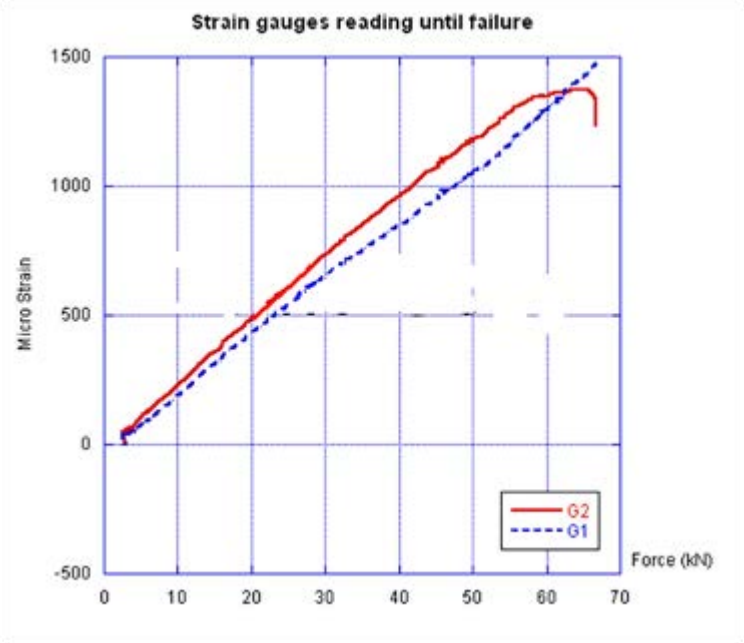

Fig. 3.54. Reading on strain gauges for the applied load

To overcome the surface failure problem between the two types of concrete, the connection between the surface boundaries is enhanced. This is done by doing the concreting of BFUP directly after the standard concrete. The wet surface enhanced the connection. To ensure a better connection, dowels are placed vertically in the standard concrete after pouring

it in the mould. When the BFUP is placed on top of it, the small nails react as a reinforcement that joins the two surfaces.

In order to have more deflection in the sample, surface traction is decrease. To lessen traction in the sample, part of the rebar is covered as shown in Fig. 3.55. Half the reinforcement bar is covered, so one concrete block will consists of a reinforcement bar with adherence to the surrounding concrete, and the other block will not have adherence in the reinforcement bar surface (Fig. 3.56).

However, problem occurs when this type of sample is tested. Big displacement occurred when load is applied (Fig. 3.57(a)). There is no visible crack in the concrete block (Fig. 3.57(b)). It shows that covering the reinforcement bar surface is not suitable for the setting. On the other hand, the surface between BFUP and standard concrete shows no failure (Fig. 3.57(b)).

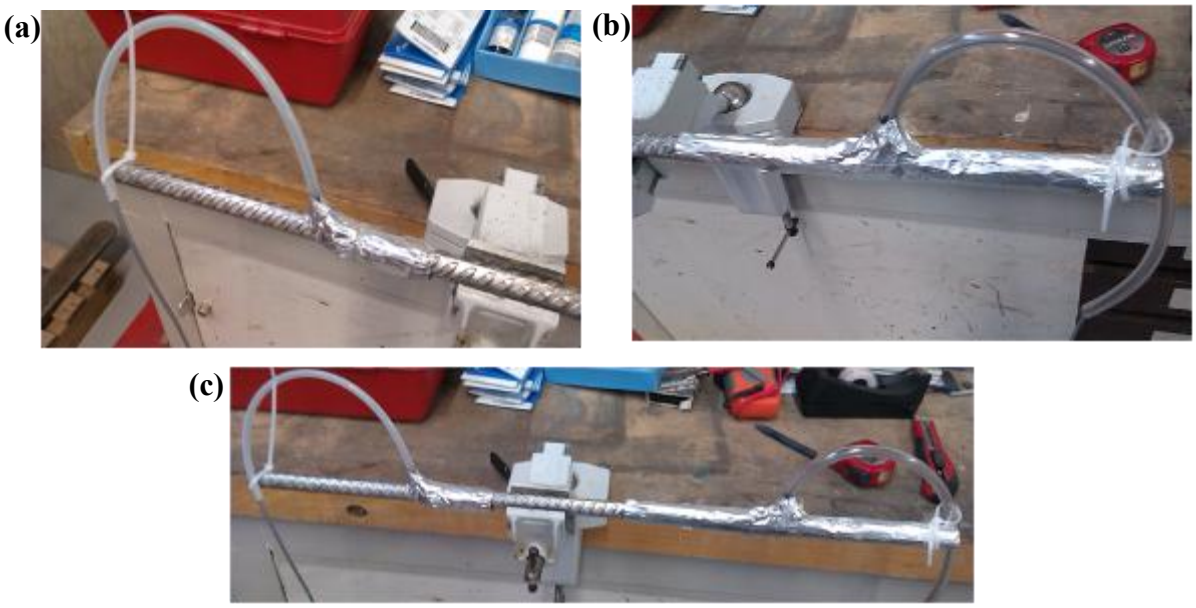

Fig. 3.55. Preparation of reinforcement bar: (a) non-covered side, (b) covered side, (c) the prepared bar for test sample

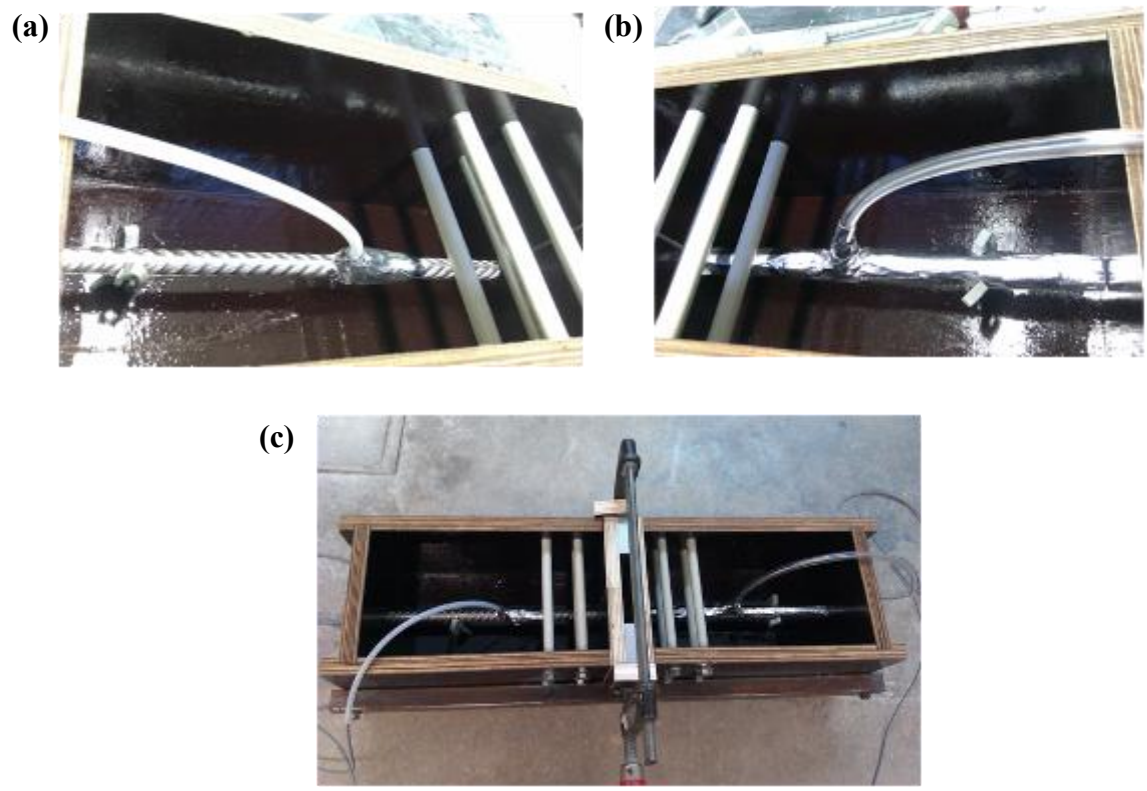

Fig. 3.56. Preparation of the mould: (a) non-covered side, (b) covered side, (c) the prepared mould for concreting

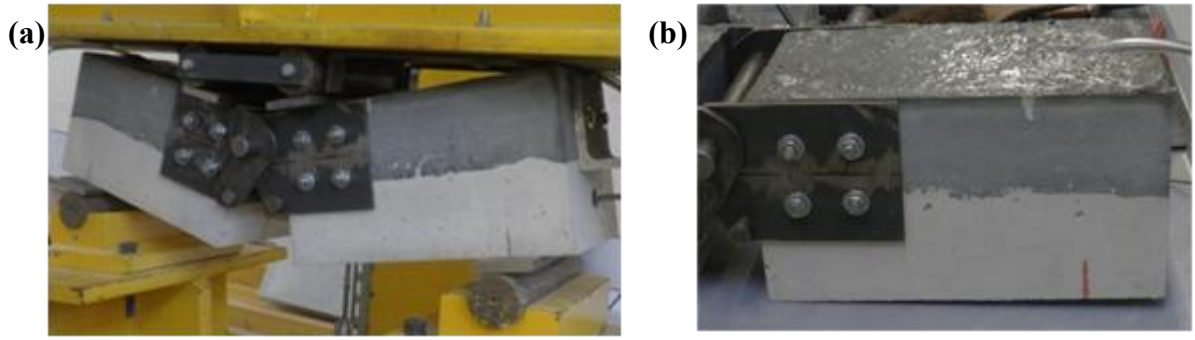

Fig. 3.57. Problem in sample (a) Excessive slide of the sample, (b) no crack on sample

Another sample is prepared; reinforcement bar is not covered to have full traction along the surface. Interaction between BFUP and standard concrete used before is applied as it can prevent surface failure. For this approach, two types of sample are prepared which has different distance of strain gauges from the concrete edge;

i) Sample-80 : x = 80mm (two units)

ii) Sample-140: x=140mm

where x is the distance of the strain gauges as shown in Fig. 3.49.

When subjected to bending load, this setting shows a good behavior. The steel plate rotated and visible cracks are initiated before the sample fails (Fig. 3.58). Readings from strain gauges attached to the reinforcement bar are analyzed.

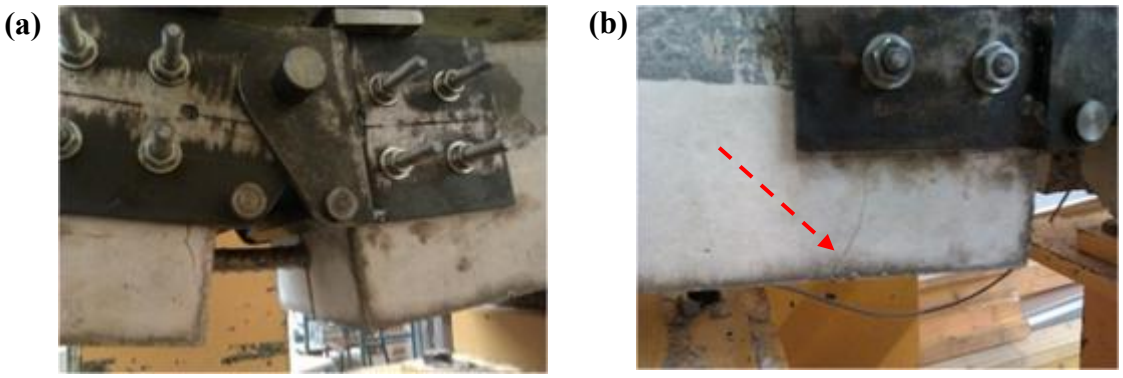

Fig. 3.58. Success setting (a) Steel plate rotated when load is applied, (b) visible crack appear before failure

As discussed in previous sections, bonding between reinforcement bars in composite concrete permits the surrounding concrete to resists some amount of stress during the initiation of crack. The amount of stress that can be resisted by concrete due to the bar-concrete bond shows the tension stiffening effects. This amount reduces as the interaction wear-off and finally fails. In other words, as the bond reduces, the stress will be transfer to reinforcement bars. This basically will increase the amount of stress in the rebar. This concept is applied in this laboratory work; tension stiffening viewed as the increase of stress in the reinforcement bars during the cracking phase. Results from the bending test are used to illustrate this increase as shown in Fig. 3.59-3.61. In each curve, a significant increase in stress can be observed during the cracking phase. This increase is summarizes in Table 3.4 for all of the samples.

When the strain gauge is positioned 80mm away from the edge (Sample-80a and 80b), an initial cracking point is recorded at 25kN as shown in Fig. 3.59 and Fig. 3.60. The cracking phase continues for the additional 20kN applied load; until 45kN. When readings are taken at 140mm distance from the edge (Sample-140), cracking is detected between 50kN to 70kN applied load as shown in Fig. 3.61. This cracking force is similar to the other two samples; Sample-80a and 80b. Within this cracking phase, for each sample, an average stress increase is recorded up to 100% compared to the pre-cracking phase as shown in Table 3.4. It

can be observed that strain gauge J2 has higher values of stress increase in each of the three samples. The differences between readings on J1 and J2 could be due to the early detected crack in the position of J2.

Table 3.4: Increase in stress during the cracking phase for all samples

Sample	Strain gauge	Strain gauge distance from edge	Stress increase (%)
Sample 80a	J1	80mm	88
	J2	80mm	143
Sample 80b	J1	80mm	76
	J2	80mm	122
Sample 140	J1	140mm	64
	J2	140mm	164

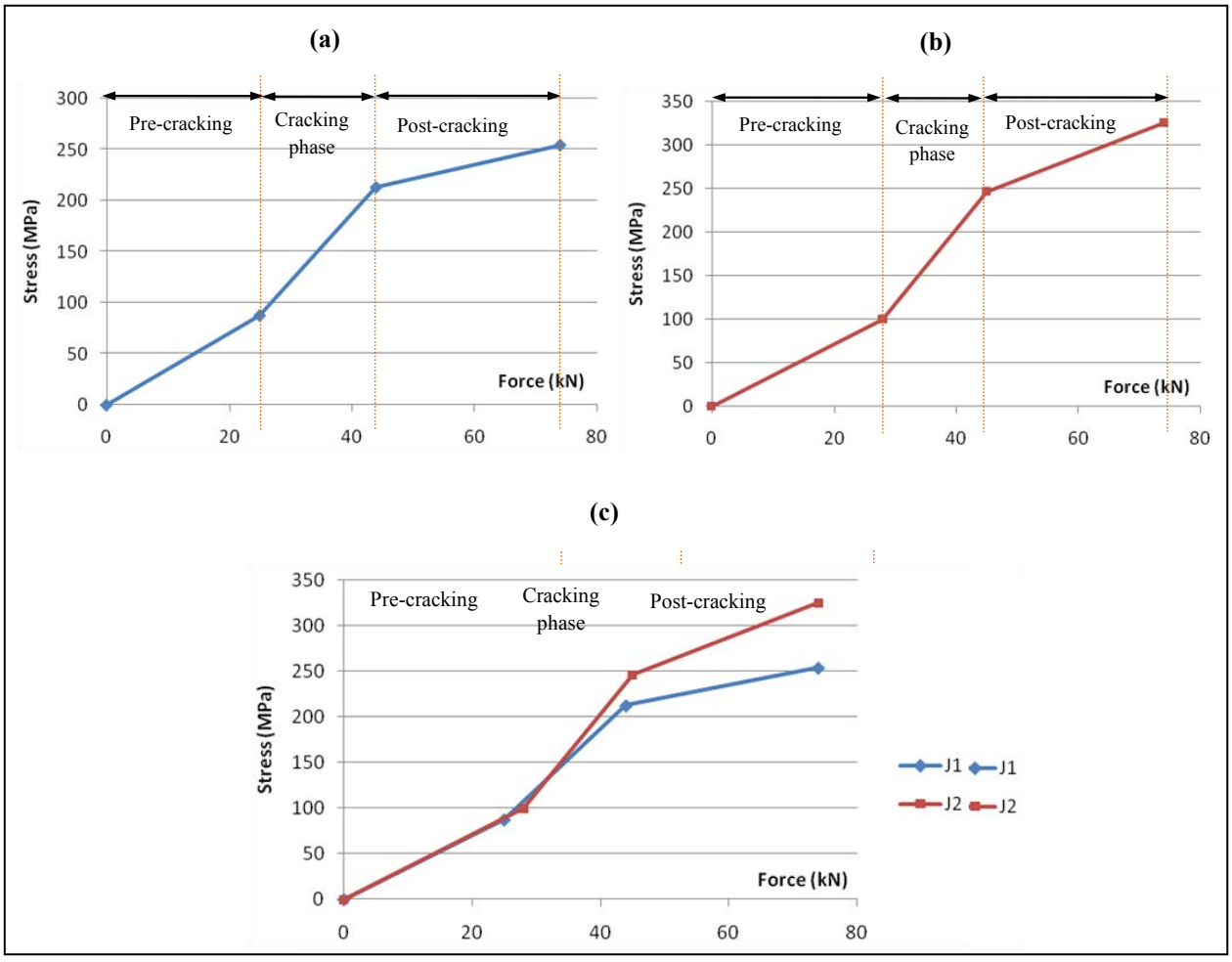

Fig. 3.59. Tension stiffening phenomenon in Sample 80a: a) Strain gauge J1, b) Strain gauge J2, c) comparison of J1 and J2

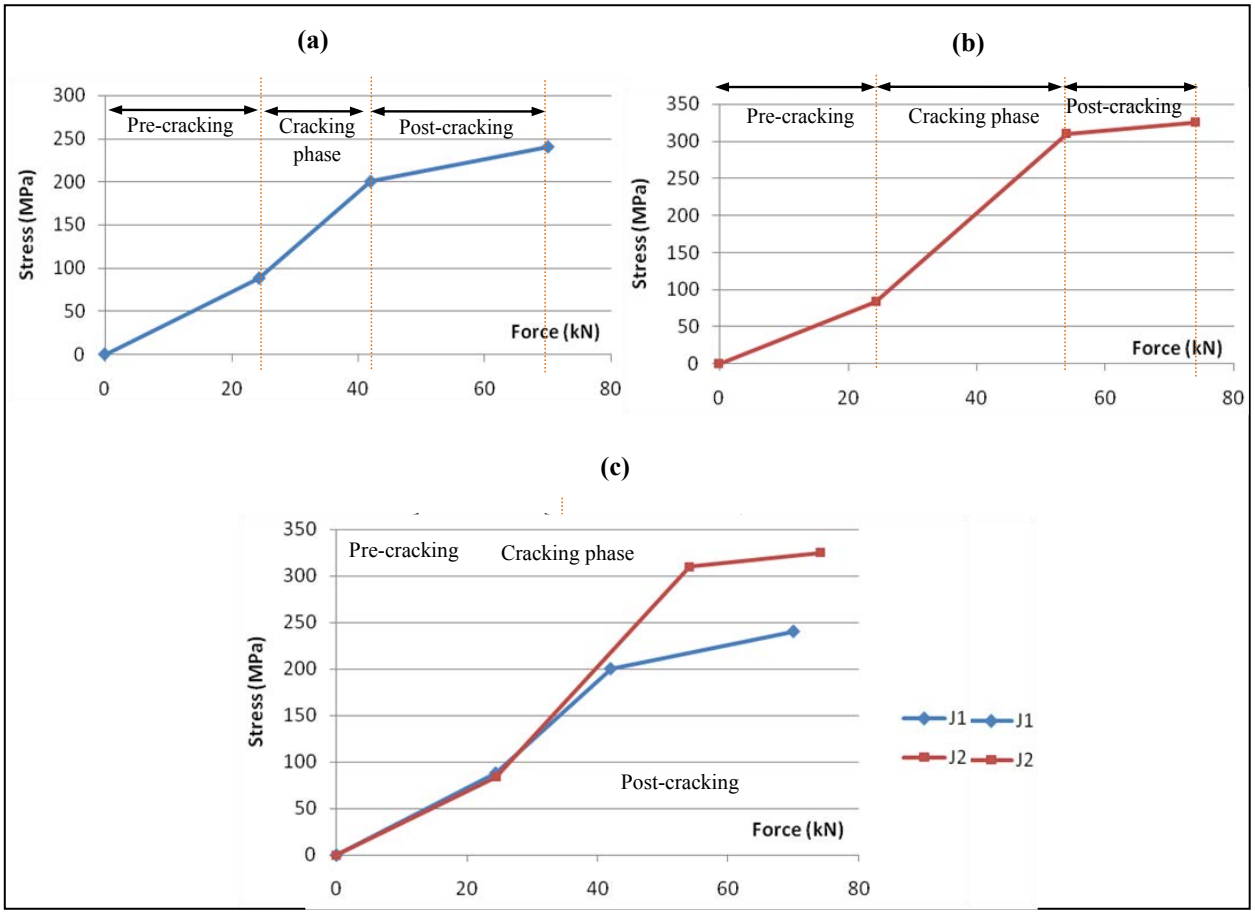

Fig. 3.60. Tension stiffening phenomenon in Sample 80b: a) Strain gauge J1, b) Strain gauge J2, c) comparison of J1 and J2

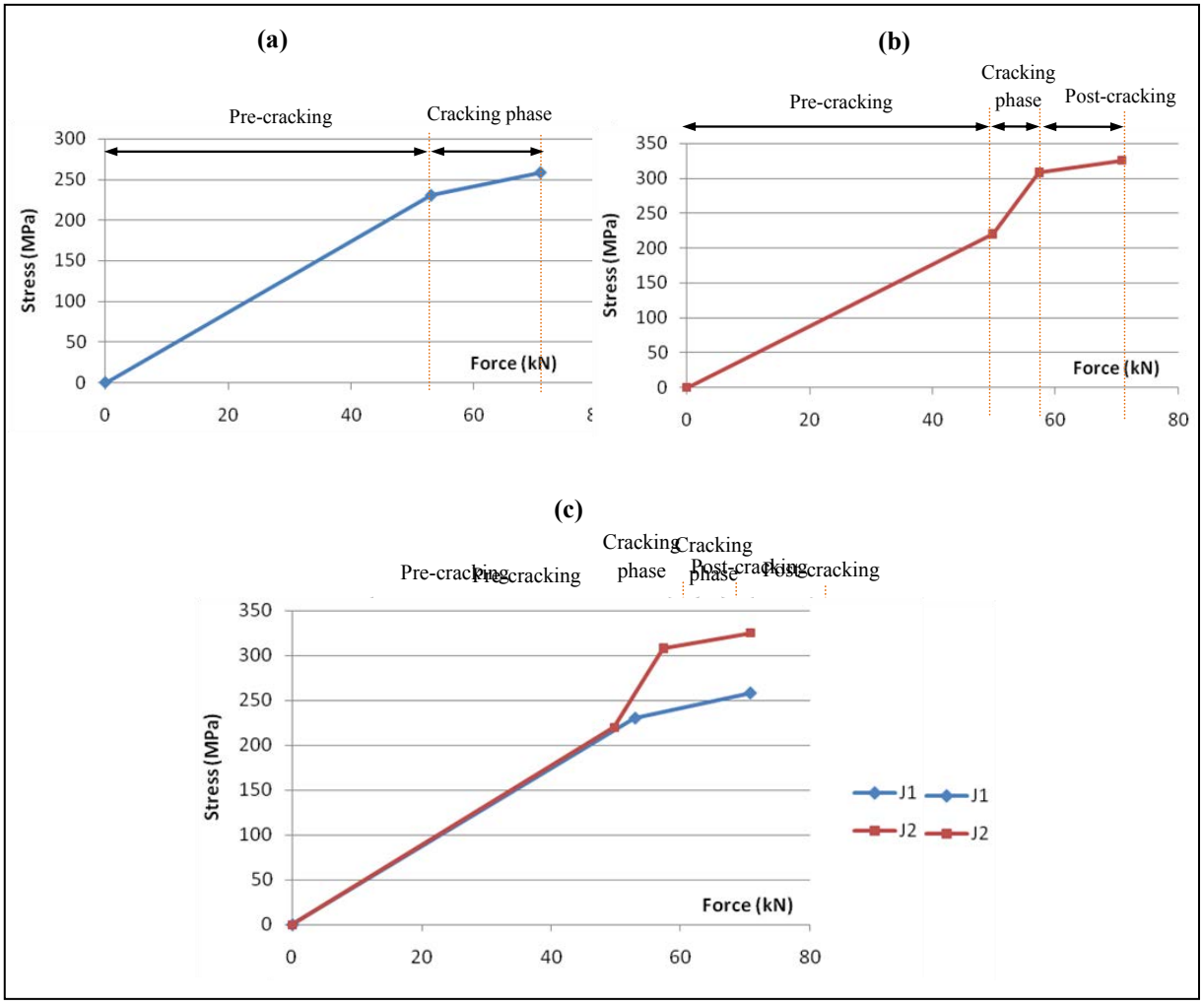

Fig. 3.61. Tension stiffening phenomenon in Sample 140: a) Strain gauge J1, b) Strain gauge J2, c) comparison of J1 and J2

3. 9 Remarks and Conclusions

In this chapter, the behavior of inoxydable steel and their interaction properties between the steel and the concrete is investigated. The behavior of a bare steel bar is not the same as that of a bar embedded in concrete. The grip allows the concrete between cracks to resist tensile forces, thereby reducing the average level of stress in the reinforcement steel bars. The consideration of this effect required experimental work and numerical analysis to determine the parameters that describe the transfer of part of the tensile stress in steel bars to concrete. A new constitutive law has been developed specifically for the inoxydable steel bars. This law is integrated into a nonlinear modeling approach of reinforced concrete

elements based on discretization in horizontal layers for the analyzed section and a vertical discretization for the overall analysis. This approach is able to determine the tension stiffening parameters of the concrete. These parameters are identified using an inverse method by comparing experimental results and those from the numerical calculation. The comparison between experimental results and the prediction of the model, implemented in Abaqus, shows a very good correlation.

Chapter 4

4. Inoxydable Steel in Structural Elements

In this chapter, the effect of inoxydable steel in structural elements is presented. Nowadays, inoxydable steel is utilized in construction generally as a secondary element. Despite their potential behavior, the application in a structural element is limited. Apart from learning the behavior of this type of steel as been discussed in Chapter 3, this study also investigates the effect of using inoxydable steel to the structural response. First, their effect when used as reinforcement bars in concrete beams are verified. The RC beam is subjected to cyclic load and bending up to rupture. Their effect to the overall performance of a structural frame are then discussed. Comparisons are made to similar frame model reinforced with standard construction steel bars.

The effect of inoxydable steel on structural responses is investigated under seismic actions. Prior to the seismic analysis, free-vibration analysis is conducted to determine the structural response when no external load is applied. This analysis gives the mode shapes of the structure and natural frequency of each frame model. To determine the response under seismic load, two types of analysis are conducted; nonlinear push over analysis, and time history analysis. Displacement control is applied in the push over analysis in which the performance of the different frame models are investigate when seismic excitation is applied by a horizontal load imposed to the structure in a pre-defined increments. Time history analysis is conducted using a nonlinear real time seismic excitation. The development of plastic hinges and base shear of the structure under different magnitude of seismic load is then compared.

4. 1 Reinforced Concrete Beam

In order to determine the effects of inoxydable steel when used as reinforcement bars in concrete beam, three types of RC beams are constructed and tested in the laboratory. Fig. 4.1 shows the dimension specification and loading arrangement. The beams are all identical except for the type of reinforcement bars used in tension zone. Table 4.1 shows the type of beam and rebar used.

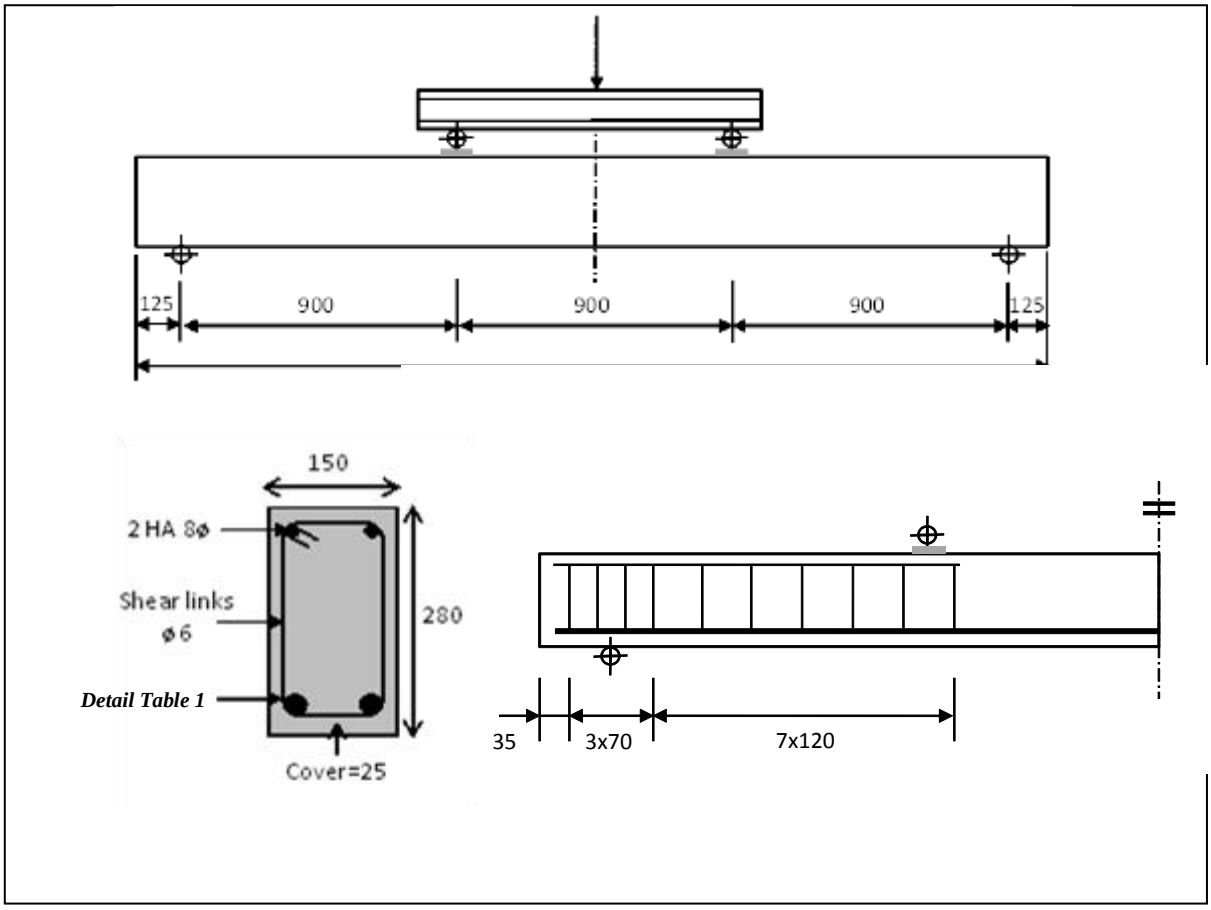

Fig. 4. 1 Dimensions and loading arrangement for the RC beam (units are in millimeter)

Table 4. 1 Type of beam and reinforcement bars used in tension zone

Beam type	Steel type	Number of rebars	Diameter of rebars (mm)
Beam 1	Austenitic-hot (AH)	2	20
Beam 2	Austenitic-cold (AC)	2	14
Beam 3	Carbon steel (CS)	2	20

The beam samples are conserved for 28 days before subjecting it to tests. Fig. 4.2 shows the load-displacement curve when the beam is subjected to cyclic load; three cycles of loading and unloading. Beam 1; reinforced with austenitic-hot (20mm diameter) is subjected to 100kN of load with 0.00225 Hz of frequency. The beam sample shows an elastic response (Fig. 4.2(a)). When Beam 2; reinforced with austenitic-cold (14mm diameter) is subjected to 120kN of load with 0.00172 Hz of frequency, the beam sample reduces its elastic capability in the first load cycle (Fig. 4.2(b)). Beam reinforced with carbon steel-20mm diameter; Beam 3 shows an elastic behavior when subjected to 90kN of load with 0.00271 Hz of frequency (Fig. 4.2(c)).

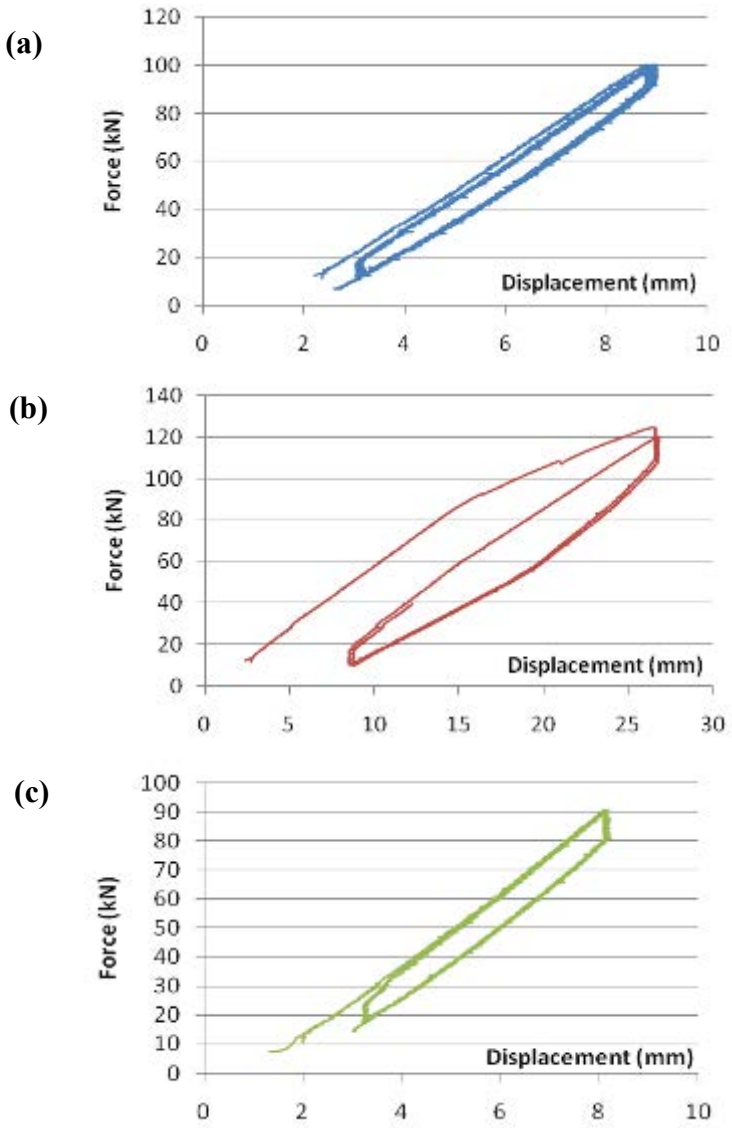

Fig. 4. 2 Laboratory results: Force-displacement curve for the concrete beam subjected to cyclic load (a) Beam 1, (b) Beam 2, (c) Beam 3.

Beam reinforced with austenitic-cold and carbon steel (Beam 2 and 3) are then subjected to bending until rupture. The force-displacement curve obtained from laboratory test is shown in Fig. 4.3. Comparing the two types of beam, Beam 2 and Beam 3 has 2.05 and 1.61 ductility ratio respectively. This shows the concrete beam reinforced with inoxydable steel (AC) is more ductile than the one reinforced with carbon steel. Beam 1 is only subjected to 160kN of load, due to the potential development of shear failure at the beam support.

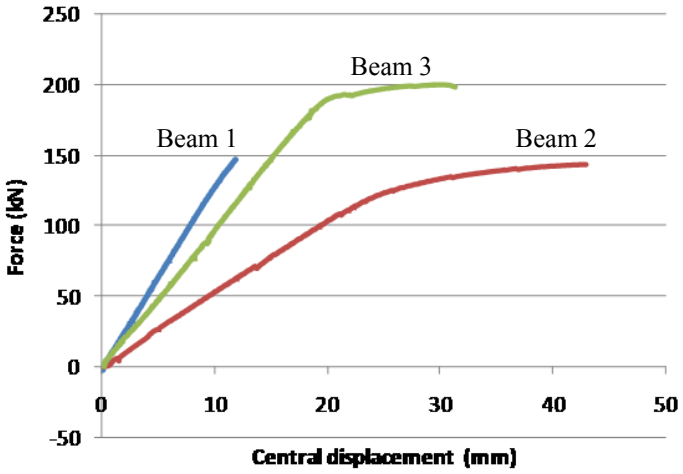

Fig. 4. 3 Laboratory results: Force-displacement curve for three types of concrete beam

As described above, Beam 2 is reinforced with austenitic-cold of 14mm diameter in size, while the other two beams are reinforced with 20mm diameter of re-bars. This is due to the unavailability of austenitic-cold steel sample in 20mm diameter. In order to have a similar comparison between the three types of reinforcement bars, a computer simulation is conducted for the same material properties and geometries, only that Beam 2 is reinforced with AC of 20mm diameter. The three RC beams are then subjected to an incremental load until failure. Fig. 4.4 shows the load-displacement curve obtained from the finite element analysis. Method of analysis and strategies are similar with the one mentioned in Section 3.7. Beam reinforced with austenitic-cold (Beam 2) shows the highest resistance followed by the one reinforced with austenitic-hot (Beam 1). In terms of ductility, beam sample with AH has the highest ductility. It can be observed that concrete beam reinforced with inoxydable steel has better performance than the standard carbon steel in both resistance and ductility.

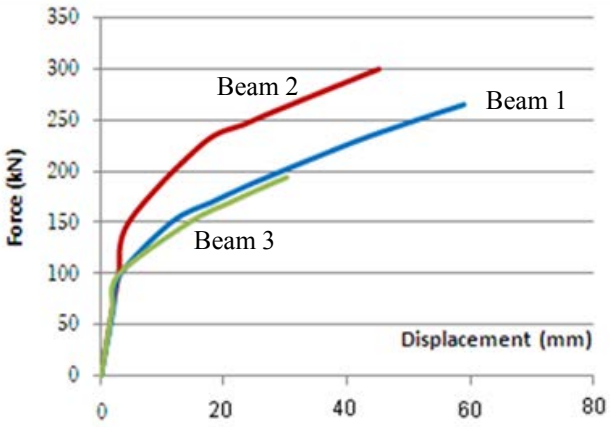

Fig. 4. 4 Finite element analysis results: Force-displacement curve for three types of concrete beam

4. 2 Reinforced Concrete Frame

Effects of inoxydable steel on structural response under seismic load are investigated. Two types of structural model are analyzed. These frame models were constructed based on same dimension but different arrangement of reinforcement bar types. The models consist of the following types:

i) Model 1: Reinforcement bars are from standard carbon steel, Grade-460

ii) Model 2: Reinforcement bars are from inoxydable steel; austenitic-hot used in beam section, austenitic-cold used in column section.

Austenitic-hot is proposed to be applied in the beam section due to its higher ductility but lower strength compared to austenitic-cold. While austenitic-cold is used in the column section due to its higher strength but lower ductility compared to austenitic-hot. This arrangement will give the effect of strong-column, weak-beam to the overall structure, thus lead failure to occur in the beam section instead of the column.

Fig. 4.5 shows the analysis conducted on the models and results that could be generated. These analyses can be used to enhance design and capacity of building structure by manipulating the benefit of inoxydable steel.

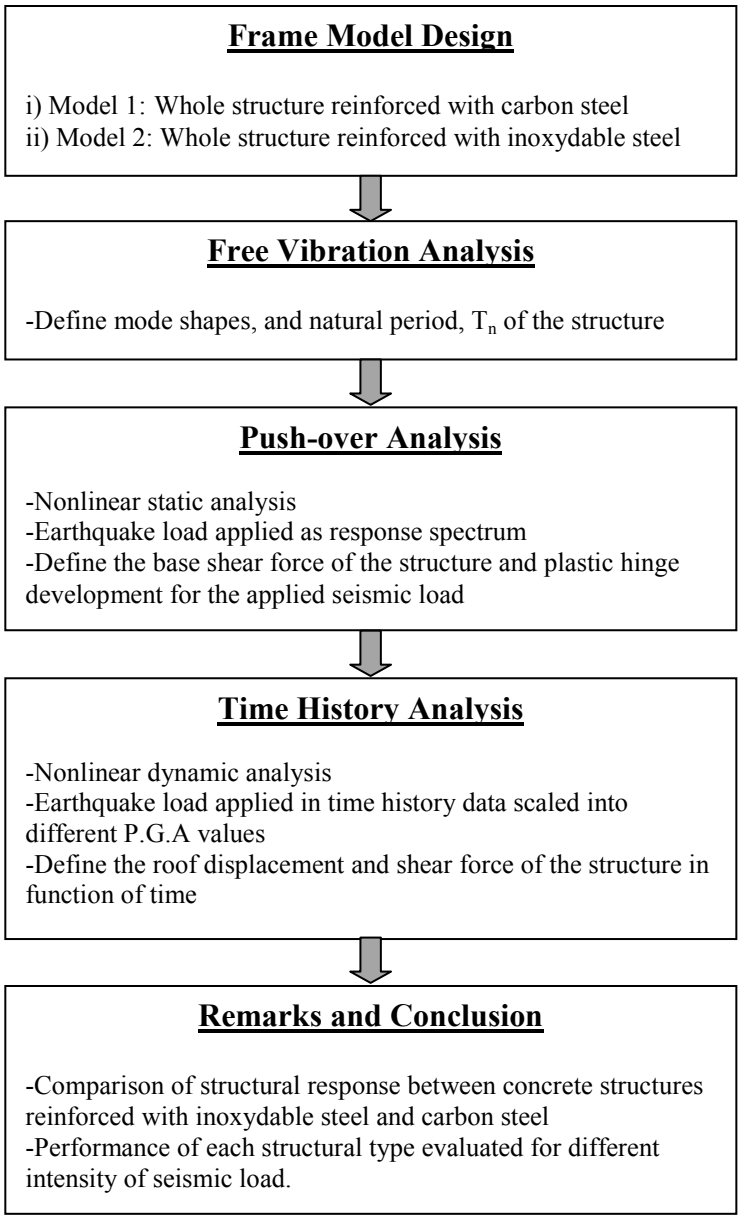

Fig. 4. 5 Overall RC frame analysis procedures conducted using SAP2000 software

Figure 4.6 shows the plan view of the building and the selected interior frame to be modeled. The building frame consists of four bays of 4m length. It has seven stories with 2.38m height each. Fig. 4.7 shows the column dimensions and reinforcement bars detail used in column section. Fig. 4.8 shows the arrangement and dimensions of beam. Detailing of reinforcement bars are listed in Table 4.2. The frame structure is modeled and analyzed in SAP2000 software.

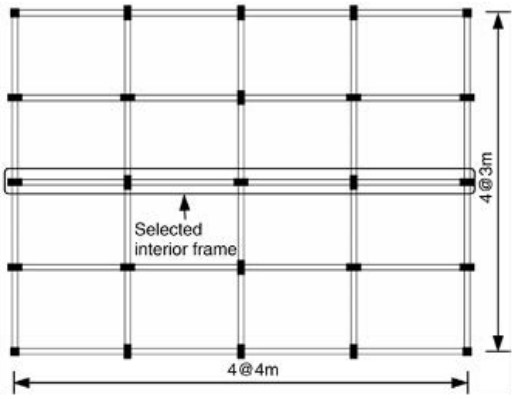

Fig. 4. 6 Plan view of the building

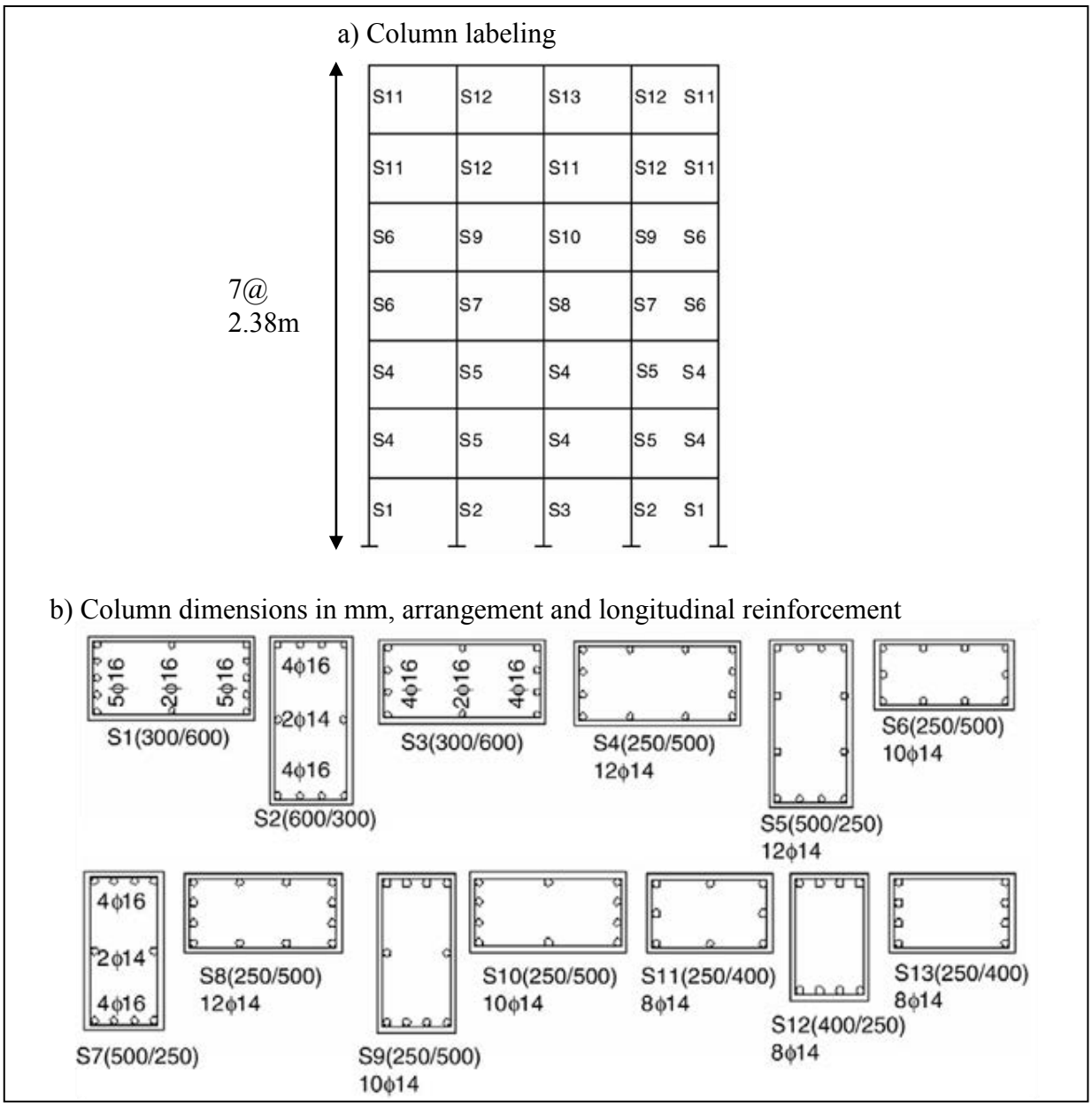

Fig. 4. 7 Column dimension and reinforcement bar properties

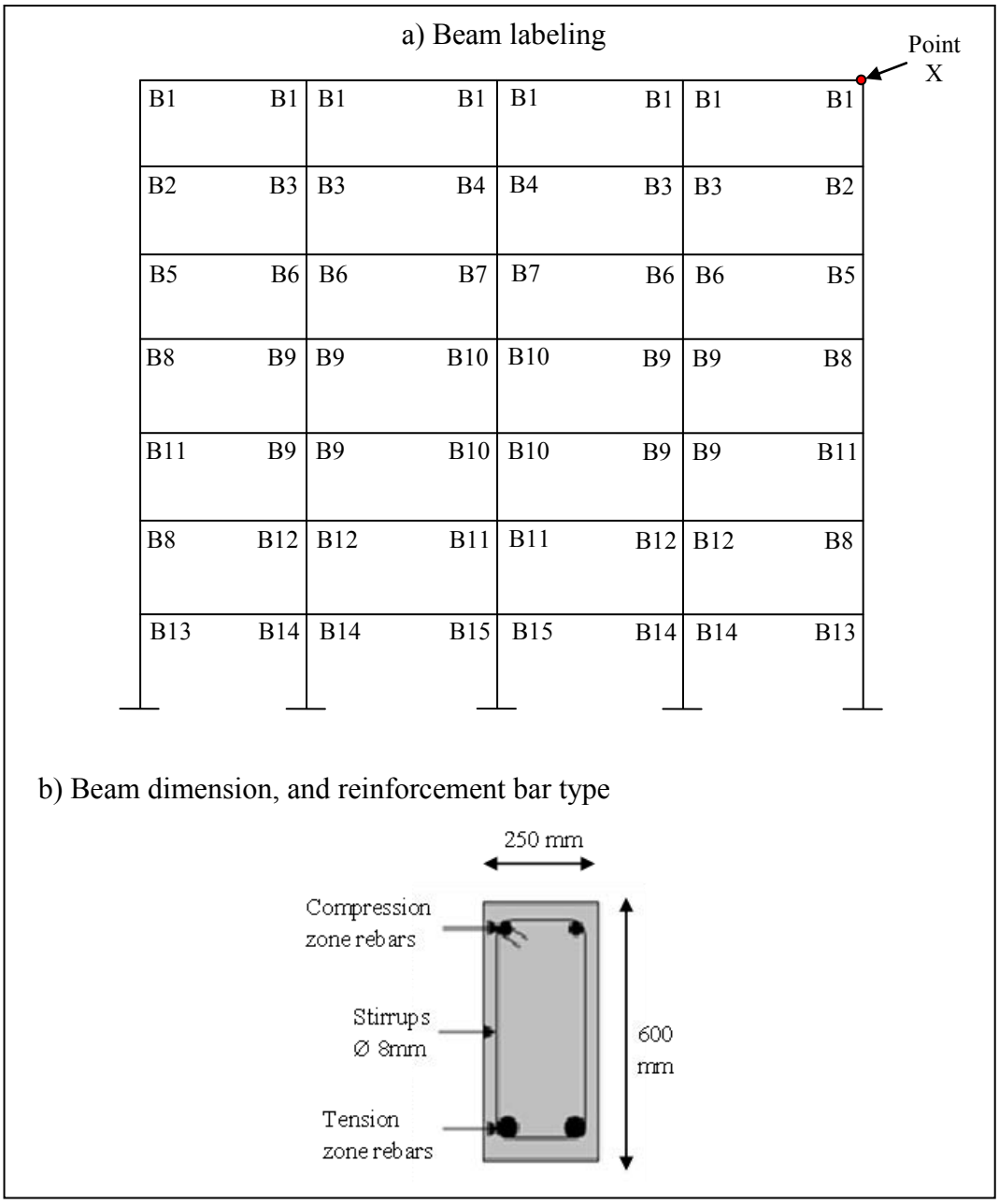

Fig. 4. 8 Beam labeling and dimension used in modeling analysis

Table 4. 2 Detailing of reinforcement bars

Beam section	Compression zone	Tension zone
B1	2 Ø 16mm	3 Ø 12mm
B2	2 Ø 25mm	3 Ø 12mm
B3	2 Ø 20mm	3 Ø 12mm
B4	3 Ø 20mm	3 Ø 12mm
B5	4 Ø 20mm	3 Ø 16mm
B6	4 Ø 16mm	3 Ø 12mm
B7	3 Ø 20mm	3 Ø 16mm
B8	3 Ø 25mm	4 Ø 16mm
B9	3 Ø 20mm	4 Ø 12mm
B10	4 Ø 20mm	2 Ø 20mm
B11	3 Ø 25mm	2 Ø 20mm
B12	2 Ø 25mm	4 Ø 16mm
B13	3 Ø 28mm	3 Ø 20mm
B14	2 Ø 25mm	2 Ø 20mm
B15	3 Ø 25mm	3 Ø 20mm

4.2. 1 Free Vibration Analysis

Free vibration analysis is conducted to determine the structural response of the RC frames without external load excitation. The structure moves with its own frequency. From this analysis, the natural period of the structural frame and the mode shapes are examined. The first five mode shapes are considered in the analysis.

The first five mode shapes of the structural frame are shown in Fig. 4.9. Structural frame reinforced with carbon steel is compared with inoxydable steel. It can be observed that the mode shapes for these two models are almost identical with each other. Table 4.3 shows the natural period for the two models. As for the mode shape, natural period for these models are similar. Reinforced concrete frame with carbon steel has slightly higher natural period than inoxydable steel for the first two mode shapes.

Mode shapes	Frame reinforced with carbon steel	Frame reinforced with inoxydable steel
1	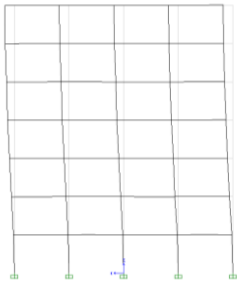	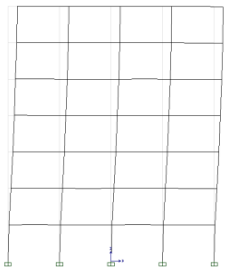
2	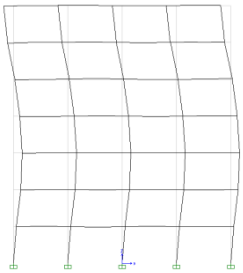	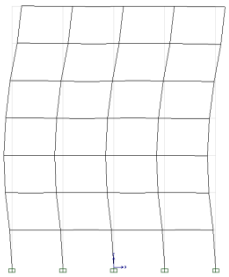
3	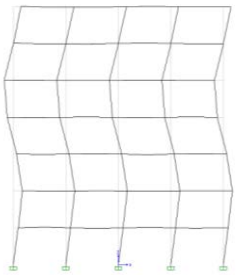	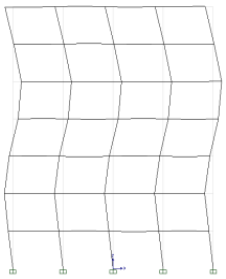
4	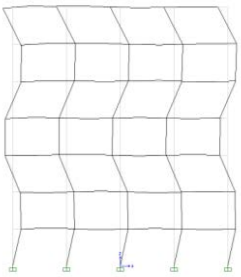	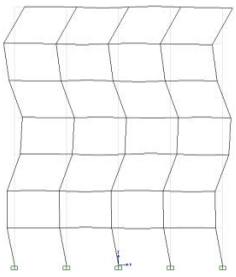
5	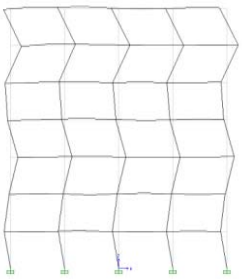	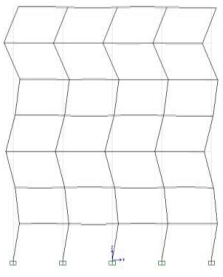

Fig. 4. 9 First five mode shapes of structural frame reinforced with inoxydable and carbon steel

Table 4. 3 Natural period for building frame reinforced with inox and carbon steel

Mode shape	Inox frame (sec)	Carbon steel frame (sec)
1	0.30499	0.30888
2	0.10764	0.10791
3	0.06426	0.06357
4	0.04595	0.04456
5	0.03807	0.03705

4.2. 2 Nonlinear Push-Over Analysis

In order to determine the structural response of the RC frame, a nonlinear static push-over analysis is conducted. This analysis can be done through a displacement control or force control basis; in which the first is used in this study. Displacement is set to 0.2m at the top corner node of the frame; point X (see Fig. 4.8). Relative displacement of this node is then plotted against base shear force as shown in Fig. 4.10. Inoxydable steel is compared with carbon steel. It can be observed that for the same displacement on the control point, base shear force for the structural frame reinforced with inoxydable steel is two times higher than the one reinforced with carbon steel. In other words, it takes twice the amount of force to cause the same displacement in the frame reinforced with inox. Structural frame with inoxydable steel has higher resistance than carbon steel.

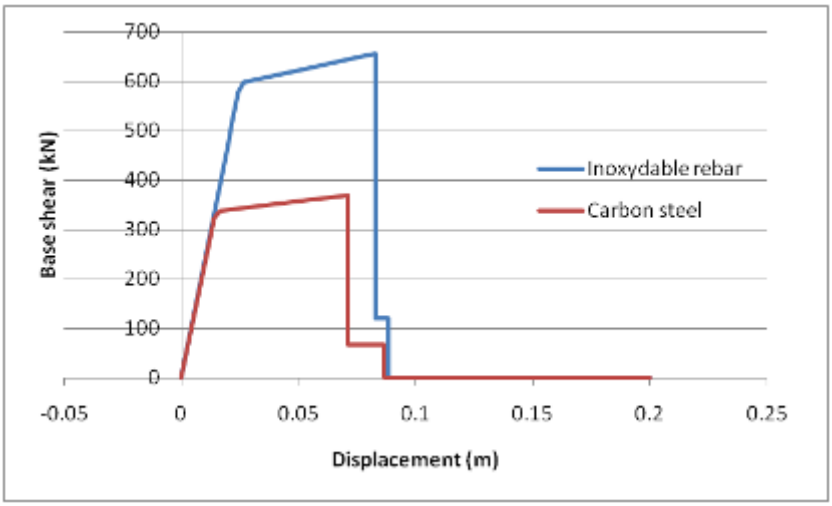

Fig. 4. 10 Comparison of base shear force for structural frame reinforced with inoxydable and carbon steel

Plastic hinge development for both types of frame model is also verified in this analysis. Detail results are shown in Table 4.3 and 4.4 for inoxydable steel and carbon steel respectively. According to FEMA 356 [34], the push-over curve used to define the force deformation behavior of the hinge can be represented in five points; labeled as A, B, C, D and E (Figure 4.11). A is unloaded component (origin), B is effective yield point, C is ultimate capacity line, D is residual strength, and E is total failure. Line AB is linear response begins, BC is strain hardening, CD is strength degradation, and line DE is strength reduced. Three points labeled as IO, LS and CP are used to define the acceptance criteria for the hinge. IO is immediate occupancy, LS is life safety, while CP is collapse prevention. This indication is used to interpret results from the push over analysis.

Comparing the analysis curve shown in Fig. 4.10 and the deformation criteria in Fig. 4.11, frame with inoxydable steel shows longer AB and CD line, but shorter DE. These shows the inox frame has higher limit of linear response and strength degradation, with lower reduction in strength. Fig. 4.12 shows the plastic hinge development sequence for inox frame.

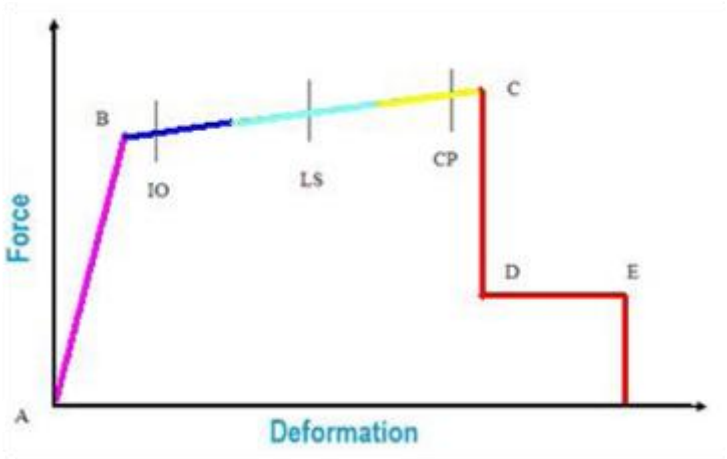

Fig. 4. 11 The force deformation criteria for hinges [34]

Table 4. 4 Push over analysis results for structural frame reinforced with inoxydable steel

Displacement m	Base Force KN	A to B	B to IO	IO to LS	LS to CP	CP to C	C to D	D to E	Beyond E	Total
-0.000023	0	182	0	0	0	0	0	0	0	182
0.019977	474.376	182	0	0	0	0	0	0	0	182
0.021648	514.003	181	1	0	0	0	0	0	0	182
0.024548	579.107	172	10	0	0	0	0	0	0	182
0.026781	599.187	169	13	0	0	0	0	0	0	182
0.050458	623.276	166	6	10	0	0	0	0	0	182
0.075861	648.944	162	10	0	10	0	0	0	0	182
0.082844	655.916	159	13	0	8	0	2	0	0	182
0.082846	119.766	159	13	0	0	0	0	10	0	182
0.088392	119.783	159	13	0	0	0	0	8	2	182
0.088394	104.128	159	13	0	0	0	0	6	4	182
0.088396	88.603	159	13	0	0	0	0	3	7	182
0.088398	0.094	159	13	0	0	0	0	0	10	182
0.108398	0.156	159	13	0	0	0	0	0	10	182
0.128398	0.217	159	13	0	0	0	0	0	10	182
0.148398	0.278	159	13	0	0	0	0	0	10	182
0.168398	0.339	159	13	0	0	0	0	0	10	182

Table 4. 5 Push over analysis results for structural frame reinforced with carbon steel

Displacement m	**Base Force** KN	**A to B**	**B to IO**	**IO to LS**	**LS to CP**	**CP to C**	**C to D**	**D to E**	**Beyond E**	**Total**
0.000014	0	182	0	0	0	0	0	0	0	182
0.01197	277.823	180	2	0	0	0	0	0	0	182
0.014083	322.105	176	6	0	0	0	0	0	0	182
0.015239	332.034	171	11	0	0	0	0	0	0	182
0.017002	337.798	170	12	0	0	0	0	0	0	182
0.051273	357.793	168	4	10	0	0	0	0	0	182
0.071273	369.445	168	4	0	8	0	2	0	0	182
0.071275	67.399	168	4	0	0	0	0	10	0	182
0.086773	67.446	168	4	0	0	0	0	3	7	182
0.086775	0.11	168	4	0	0	0	0	0	10	182
0.106775	0.171	168	4	0	0	0	0	0	10	182
0.126775	0.232	168	4	0	0	0	0	0	10	182
0.146775	0.293	168	4	0	0	0	0	0	10	182
0.166775	0.354	168	4	0	0	0	0	0	10	182
0.186775	0.415	168	4	0	0	0	0	0	10	182
0.200014	0.455	168	4	0	0	0	0	0	10	182

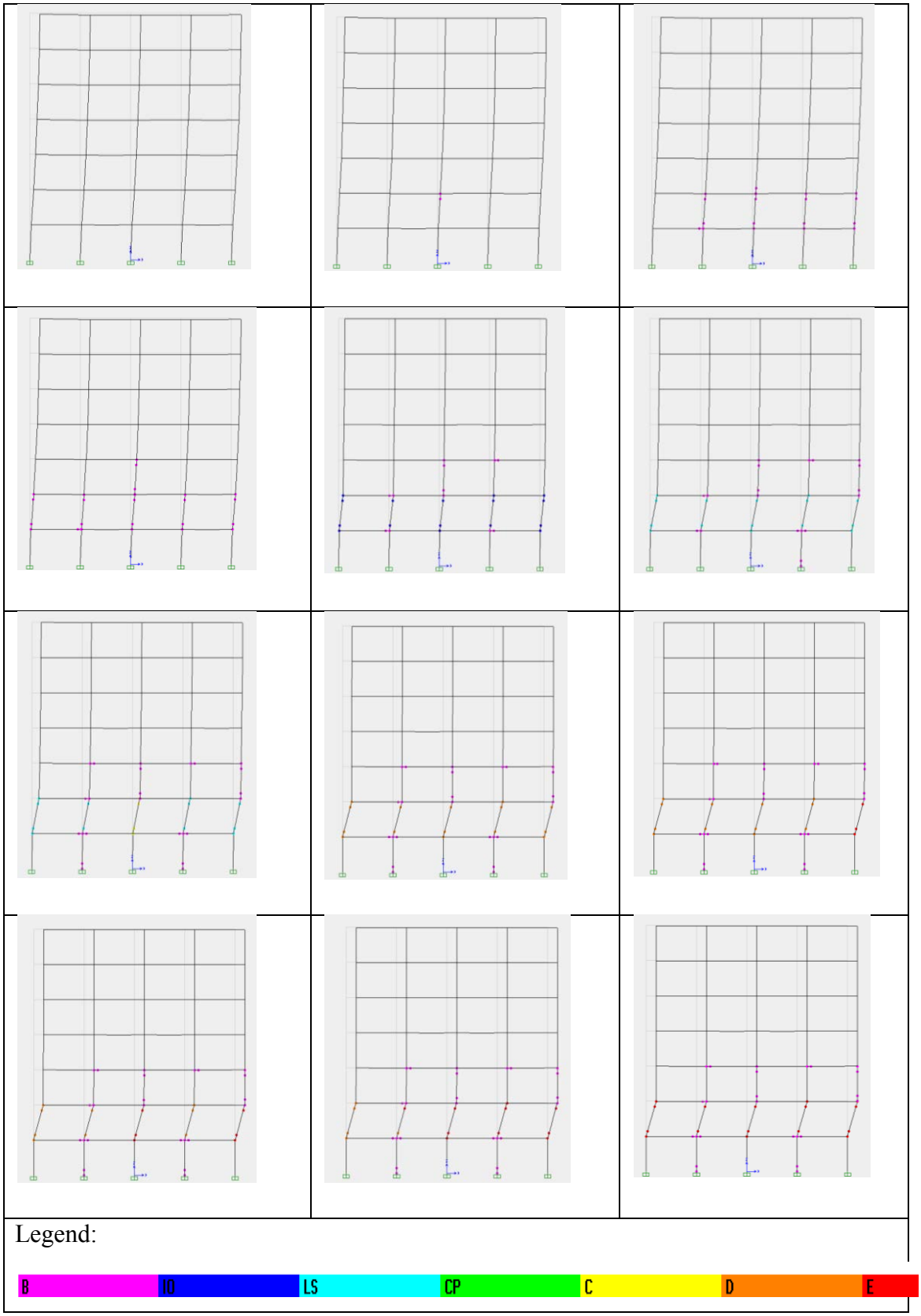

Fig. 4. 12 Sequence of plastic hinge development; nonlinear static pushover analysis for inox frame

4.2. 3 Time History Analysis

Time history analysis is conducted to determine response of the RC frames when seismic load is applied as a nonlinear frequency based horizontal load. For this type of analysis, an earthquake time history recorded on the Kuala Lumpur International Airport (KLIA), Malaysia is used as an input load as shown in Fig. 4.13. This earthquake excitation is based on the real condition of the selected site. Peak ground acceleration (P.G.A) is 0.04g, and the duration of the excitation is 23 second. For each frame model type, the analysis is conducted based on three load cases consisting different P.G.A values; 0.1g, 0.3g, and 0.5g to determine the frame behavior under different intensity of earthquake. The earthquake data is scaled up to 0.1g, 0.3g, and 0.5g, respectively. Performance of both frame models; frame with inox and frame with carbon steel is then compared based on the roof-displacement and based shear in function of time for each P.G.A values.

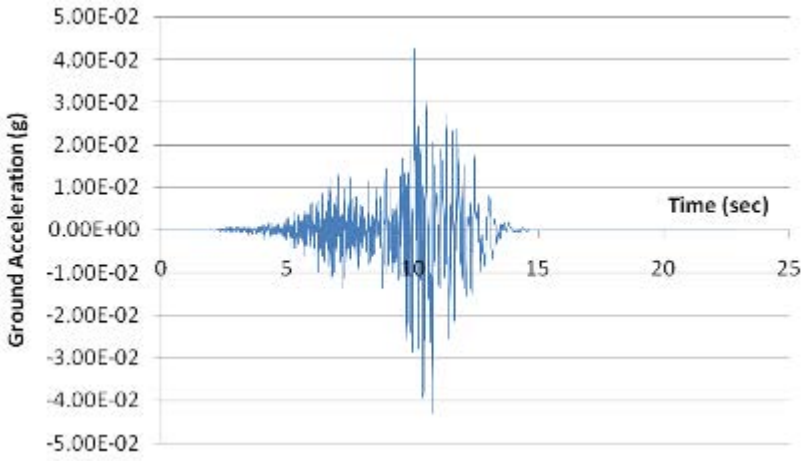

Fig. 4. 13 Earthquake time history used in the analysis; site KLIA, Malaysia

Fig. 4.14 shows the roof displacement pattern at frame nodes. Maximum displacement recorded between the 12 to 12.5 seconds. Table 4.6 shows the displacement for both inox frame and carbon steel frame for each P.G.A value. Comparison between the two models can be observed visually in Fig. 4.15. Frame model reinforced with carbon steel has higher displacement in every load case. The differences with displacement for inox frame increase as the P.G.A value increases.

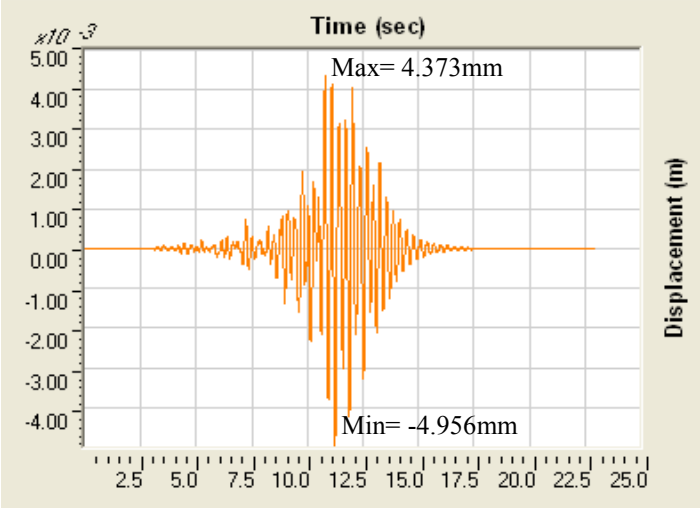

Fig. 4. 14 Roof displacement pattern at frame nodes

Table 4. 6 Roof displacement under different P.G.A for RC frame with inoxydable and carbon steel

P.G.A	Frame reinforced with inoxydable steel		Frame reinforced with carbon steel	
	Min (m)	Max (m)	Min (m)	Max (m)
0.1g	-4.456E-03	4.373E-03	-4.979E-03	4.462E-03
0.3g	-1.387E-02	1.312E-02	-1.548E-02	1.339E-02
0.5g	-2.078E-02	2.186E-02	-2.689E-02	2.231E-02

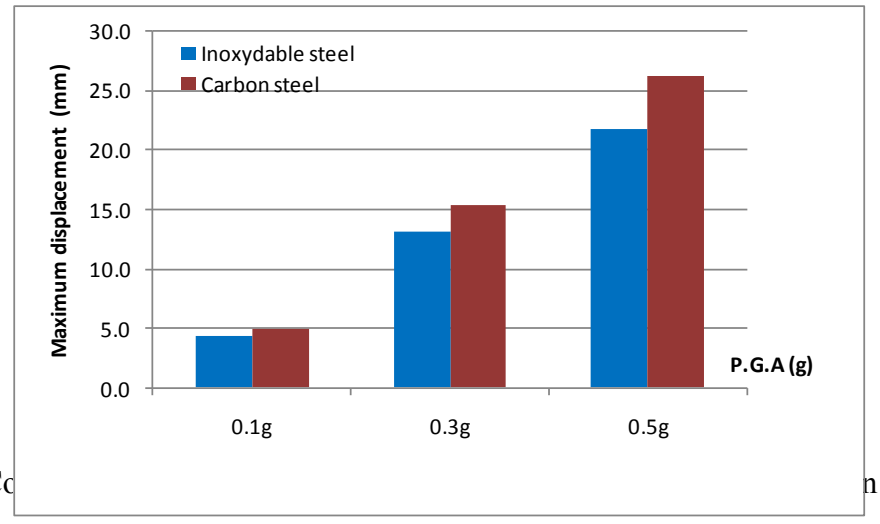

Fig. 4. 15 Co n steel

Fig. 4.16 shows the base shear pattern when the frame models are subjected to seismic load. Maximum base shear happens at the maximum excitation; between the 12 to 12.5 seconds. Table 4.7 shows the shear force for both inox frame and carbon steel frame for each P.G.A value. Comparison between the two models can be observed visually in Fig. 4.17. Frame model reinforced with carbon steel has higher base shear force in every load case. The differences with the one recorded in inox frame is less significant in low P.G.A value but increases as the P.G.A increase.

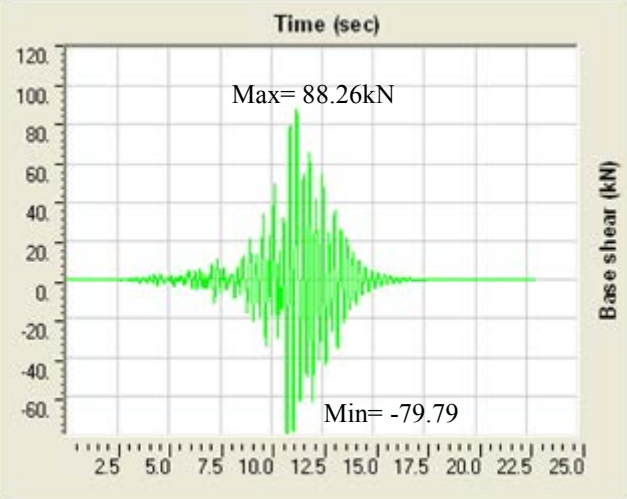

Fig. 4. 16 Base shear pattern at the support of the frame

Table 4. 7 Base shear under different P.G.A for RC frame with inoxydable and carbon steel

P.G.A	Frame reinforced with inoxydable steel		Frame reinforced with carbon steel	
	Min (kN)	Max (kN)	Min (kN)	Max (kN)
0.1g	-7.979E+01	8.026E+01	-8.012E+01	8.868E+01
0.3g	-2.393E+02	2.548E+02	-2.403E+02	2.660E+02
0.5g	-3.989E+02	4.013E+02	-4.006E+02	4.433E+02

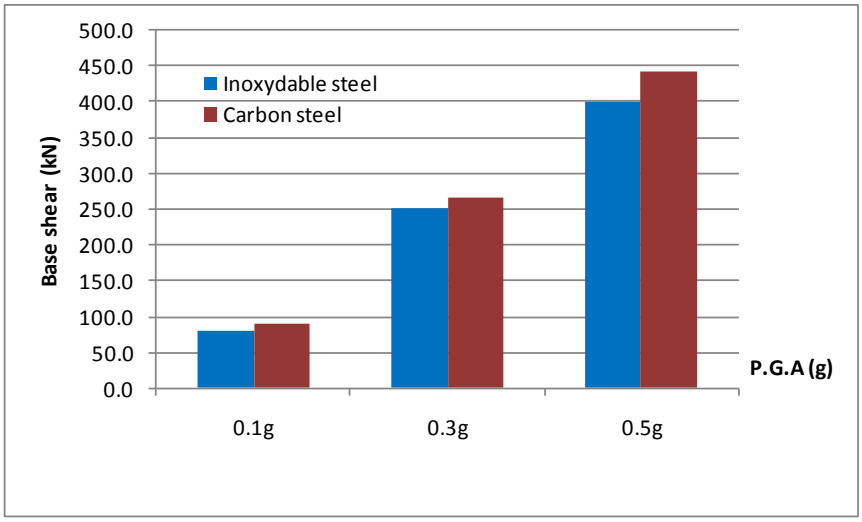

Fig. 4. 17 Comparison of maximum base shear between inox and carbon steel

4. 3 Remarks and Conclusion

In this chapter, the effect of inoxydable steel in structural responses is evaluated and compared with the traditional carbon steel. Evaluation is made on three types of composite concrete beam reinforced with different types of steel bars; austenitic-hot, austenitic-cold, and carbon steel. Each beam sample is subjected to cyclic load and bending up to failure. Beam models are constructed and tested in laboratory, and through computer simulation using Abaqus software. This chapter presented the structural response of RC frame subjected to seismic load. Free vibration analysis is conducted followed by nonlinear push-over analysis and time history analysis to verify the performance of two frame model types; the one reinforced with inoxydable steel, and reinforced with carbon steel. All analysis is simulated using SAP2000 software. Results obtained and discussed in this chapter show that RC beams and frames have better structural response when are reinforced with inoxydable steel.

5. Conclusions and Recommendations

In this PhD dissertation, a thorough study is conducted to investigate the behavior of composite concrete elements reinforced with inoxydable steel. The performance of these steels in structural elements like beams and the effect of using this type of steel to the structural frame is investigated and compared with standard carbon steel. Inoxydable steel type austenitic in annealed and cold worked states are chosen to be studied further due to their wide application in the construction field compared to the other types of inox. The behavior of a bare steel bar is not the same as that of a bar embedded in concrete. This study, therefore, focuses on two aspects in developing the material models; the behavior of the steel bar alone, and the interaction properties in composite concrete. Major work in this dissertation involved the development of these material models, followed by the study of their effect in the structural concrete elements subjected to static loading and dynamic load (seismic excitation).

In studying the behavior of inox as steel bar alone (Objective 1), it can be concluded that Inoxydable steel has lower elastic limit as compared to their yield point and ultimate tensile strength. Both austenitic-hot and austenitic-cold has lower Young‟s modulus compared to standard carbon steel, but it has higher yield strength and ultimate strength. In terms of ductility in the Inoxydable steel, a general decrease in ductility ratio could be observed with the increase in proof stress. Austenitic-hot has higher ductility ratio but lower strength compared to austenitic-cold which has higher strength but lower ductility ratio. When compared to carbon steel, both austenitic type steel are more ductile and exhibit a pronounced strain hardening capability.

In developing the constitutive law for inoxydable steel, the Ramberg-Osgood approach could be used. However, modification of the formula to determine sharpness of the stress-strain curve is needed. This is due to the lower proportional limit and extended strain hardening capability of inox. A new constitutive law has been developed specifically for the inoxydable steel bars and verification with laboratory findings show a good correlation between both, the experimental and analytical values. Modification of parameters in this

study is able to represent the nonlinear behavior of inox type austenitic before and after the yielding point.

In composite concrete, the grip with reinforcement steel bars allows the concrete between cracks to resist tensile forces, thereby reducing the average level of stress in the rebars. The consideration of this effect in developing the interaction properties between inox and concrete lead to a new proposition of experimental and numerical methodology in order to determine the parameters that describe the transfer of part of the tensile stress in steel bars to concrete. In the second part of this study; behavior of Inoxydable steel as reinforcement bars in composite concrete (Objective 2), determination of the interaction properties between inox and concrete through the proposed laboratory setting is able to monitor tension stiffening phenomenon in RC beam subjected to bending. Position of strain gauges could determine the tension stiffening amount from first crack formation until rupture. This approach is easier to set up and loading condition (bending) is more likely in beam structure as compare to the direct uniaxial tension test. However, extra efforts are needed in analyzing the test results and developing tension stiffening model. In this study, the bending test results are combined with nonlinear numerical analysis results to develop the tension stiffening model for Inoxydable steel type austenitic-hot.

In this approach, the developed constitutive law for inox is integrated into the nonlinear modeling approach of reinforced concrete elements based on discretization in horizontal layers for the analysis section and a vertical discretization for the overall analysis. The parameters are identified using an inverse method by comparing experimental results and those from the numerical calculations. Comparison between experimental results and the prediction of the model implemented in Abaqus shows a very good correlation. Compared to standard carbon steel, inox has 50% higher of tension stiffening.

The effect of inoxydable steel on structural responses is then investigated in RC beams and frames when subjected to static and dynamic load respectively (Objective 3). The RC beam samples are loaded under bending until rupture, while the RC frame is subjected to seismic loads. Results from laboratory work and computer simulations using SAP2000 show better structural response in composite structure reinforced with inoxydable steel compared to the standard carbon steel. Concrete beam reinforced with austenitic-hot has higher ductility, and the one reinforced with austenitic-cold has higher strength. Under seismic load, RC

frame with inox has lower roof-displacement and base shear force compare to carbon steel. The differences are more significant for higher peak ground acceleration values.

Recommendations

In this study, the interaction properties between inoxydable steel and concrete are not investigated through direct tension test due to some limitations in the laboratory settings. Series of strain gauges attached to the reinforcement bar surface could influence the bonding with surrounding concrete. Tension stiffening parameters are determined in concrete beam reinforced with austenitic-hot only. Only one type of reinforcement bar arrangement is used to verify the performance of inoxydable steel in RC frame.

Further development could enhance the findings obtained in this study and could be done in the following aspects;

- Direct determination of the tension stiffening parameters through a uniaxial tension test could be done and compared with the findings obtained in this study.
- Different approach of attaching the strain gauges on reinforcement bars should be investigated to maximize surface contact with surrounding concrete.
- Apply the same test procedures on RC beam with standard carbon steel and compare the tension stiffening results.
- Tension stiffening parameters for the composite concrete reinforced with the Ultra-high performance fiber-reinforced concrete, UHPFRC and inox could be determine based on the inverse method proposed herein.
- Different arrangement in the position of inoxydable steel in RC frame should be investigate to determine the most effective performance.
- Experimental investigation to determine the strong-column, weak-beam effect in concrete frame reinforced with inoxydable steel.

6. References

[1] Leslie Aitchison and William I. Pumphrey, A study of the properties of steels and the principles governing their selection for engineering applications, 1st ed. London: Macdonald & Evans LTD, 1953.

[2] Kouhi, J., Talja, A., Salmi, P., and Ala-Outinen, T. (2000). Current R&D Work on the Use of Stainless Steel in Construction in Finland. *Journal of Constructional Steel Research.* Vol. 54, 31–50.

[3] F. Velasco , G. Blanco, A. Bautista, M.A. Martínez, (2009), Effect of welding on local mechanical properties of stainless steels for concrete structures using universal hardness tests, *Construction and Building Materials*; 23: 1883–1891.

[4] A. Bautista, G. Blanco, F. Velasco, M.A. Martınez, (2007), Corrosion performance of welded stainless steels reinforcements in simulated pore solutions, *Construction and Building Materials*; 21: 1267–1276.

[5] A. Bouchaïr, J. Averseng, A. Abidelah, (2008), Analysis of the behavior of stainless steel bolted connections, *Journal of Constructional Steel Research*; 7(9): 1-11.

[6] Goitseone Malumbela, Mark Alexander, Pilate Moyo, (2010),Variation of steel loss and its effect on the ultimate flexural capacity of RC beams corroded and repaired under load, *Construction and Building Materials*; 24: 1051–1059.

[7] Anis, M. A., Farid, B.J., and Al-Janabi, A. I. M. (1990). Stress-Strain Relationship for Concrete in Compression Madel of Local Materials. *JKAU: Eng. Sci.* Vol. 2, l83-l94.

[8] B. Winkler, G. Hofstetter, and H. Lehar, (2004), Application of a constitutive model for concrete to the analysis of a precast segmental tunnel lining, *Int. J. Numer. Anal. Meth Geomech*.; 28: 797-819.

[9] H. Sooriyaarachchi, K. Pilakoutas, and E. Byars, Tension stiffening behavior of GFRP-reinforced concrete, *7th International Symposium on Fiber Reinforced Polymer Reinforcement for Reinforced Concrete Structures* (FRPRCS-7), November 6-10, 2005, Kansas City, Missouri.

[10] Peter H. Bischoff and Richard Paixao, (2004), Tension stiffening and cracking of concrete reinforced with glass fiber reinforced polymer (GFRP) bars, *Can. J. Civ. Eng.*; 31: 579-588.

[11] Yuichi Sato and Frank J. Vecchio, (2003), Tension stiffening and crack formation in reinforced concrete members with fiber-reinforced polymer sheets, *Journal of Structural Engineering*; 129 (6): 717-724.

[12] Chang-Koon Choi and Sung-Hoon Cheung, (1994), Tension stiffening model for planar reinforced concrete members, *Computers & Structures*; 59(1): 179-190.

[13] Ellobod, E. (2007). Nonlinear Behavior of Concrete-Filled Stainless Steel Stiffened Slender Tube Columns. *Thin-Walled Structures.* Vol. 45, 259–273.

[14] Chen, J. and Young, B. (2006). Stress–strain Curves for Stainless Steel at Elevated Temperatures. *Engineering Structures.* Vol. 28, 229–239.

[15] Delarbre, D. and Montmitonnet, P. (1999). Experimental and Numerical Study of the Ironing of Stainless Steel Cups. *Journal of Materials Processing Technology.* Vol. 91, 95–104.

[16] El Bartali, A., Aubin, V., and Degallaix, S. (2009). Surface Observation and Measurement Techniques to Study the Fatigue Damage Micromechanisms in a Duplex Stainless Steel. *International Journal of Fatigue.* Vol. 10, 1-7.

[17] Makkouk, R., Bourgeois, N., Serri, J., Bolle, B., Martiny, M., Teaca, M., and Ferron, G. (2008). Experimental and Theoretical Analysis of the Limits to Ductility of Type 304 Stainless Steel Sheet. *European Journal of Mechanics A/Solids.* Vol. 27, 181–194.

[18] Theofanous, M., Chan, T. M., and Gardner, L. (2009). Structural Response of Stainless Steel Oval Hollow Section Compression Members. *Engineering Structures.* Vol. 31, 922-934.

[19] Abdella, K. (2009). Explicit Full-Range Stress Strain Relations for Stainless Steel at High Temperatures. *Journal of Constructional Steel Research.* Vol. 65, 794-800.

[20] Velasco, F., Blanco, G., Bautista, A., and Martínez, M. A. (2009). Effect of Welding on Local Mechanical Properties of Stainless Steels for Concrete Structures Using Universal Hardness Tests. *Construction and Building Materials.* Vol. 23, 1883–1891.

[21] Gardner, L. and Baddoo, N. R. (2006). Fire Testing and Design of Stainless Steel Structures. *Journal of Constructional Steel Research.* Vol. 62, 532–543.

[22] Apostolopoulos, C. A., and Michalopoulos, D. (2007). Mechanical Properties of Reinforcing Steel and Fatigue Behavior in Corrosive Environment. *JMEPEG.* Vol 16, 559–566.

[23] Gu, P., Elliott, S., Beaudoin, J. J., and Arsenault, B. (1996). Corrosion Resistance of Stainless Steel in Chloride Contaminated Concrete. *Cement and Concrete Research.* Vol. 26:8, 1151-1156.

[24] Choi, J. H. (2008). Seismic Retrofit of Reinforced Concrete Circular Columns Using Stainless Steel Wire Mesh Composite. *Can. J. Civ. Eng.* Vol. 35, 140-147.

[25] B. Tighiouart, B. Benmokrane, D. Gao, (1998), Investigation of bond in concrete member with fibre reinforced polymer (FRP) bars, *Construction and Building Materials*; 12: 453-462.

[26] EN 1992-1-1. Eurocode 2 - Design of concrete structures, Part 1.1, General rules and rules for buildings. CEN; 2003.

[27] Choi, C. K. and Cheung S. H. (1996). Tension Stiffening Model for Planar Reinforced Concrete Members. *Computer and Structures.* Vol. 59:1, 179-190.

[28] Steven W.F. Tsang, Louis Y.L. Chu, (2011), An experimental study of the Tension Stiffening effect on the structural stiffness of Reinforced Concrete Cantilevered Balcony Structures using resonant frequency measurement approach, *Construction and Building Materials*; 25: 2690–2699.

[29] Ying-Wu Zhou and Yu-Fei Wu, (2011), General model for constitutive relationships of concrete and its composite structures, *Composite Structures*; 08(022): 1-13.

[30] Rim Nayal and Hayder A. Rasheed, (2006), Tension stiffening model for concrete beams reinforced with steel and FRP bars, *Journal of Materials in Civil Engineering*; 18(6): 831-841.

[31] Chopra, A. K. (2001) Dynamics of Structure, Theory and Applications to Earthquake Engineering 2nd edition. New Jersey, Prentice Hall.

[32] Pinho, R., Casarotti, C. and Antoniou, S. A., (2007). Comparison of Single-run Pushover Analysis Techniques for Seismic Assessment of Bridges. *Journal of Earthquake Engineering and Structural Dynamics.* Volume 36, 1347 –1362.

[33] Applied Technology Council. (1996). *Seismic Evaluation and Retrofit of Concrete Building.* California. ATC40.

[34] Federal Emergency Management Agency. (2000). *Prestandard and Commentary for the Seismic Rehabilitation of Buildings.* Washington, U.*S.A.* FEMA-356.

[35] Kawashima, K. (2006). *Seismic Damage of Bridges in Past Earthquake.* Presentation of Lecture Note Chapter 6. Tokyo Institute of Technology, Japan.

[36] Parke, G. and Hewson, N. (2008). *ICE Manual of Bridge Engineering*. Institution of Civil Engineer. Thomas Telford. London. UK.

[37] Federal Emergency Management Agency. (2000). *Recommended Seismic Design Criteria for New Steel Moment- Frame Buildings.* U.S.A. FEMA-350.

[38] International Code Council. *Uniform Building Code 1997: Structural Design Requirement (Division 5 – Soil Profile Type).* California. UBC1997.

[39] Samuel, K. G. (2006). Dependence of Strength and Ductility Ratios in Austenitic Stainless Steels. *International Journal of Pressure Vessels and Piping.* Vol. 83, 474–476.

[40] Kim JR Rasmussen, Full-range stress-strain curves for stainless steel alloys, Research Report No. R811, Department of Civil Engineering, The University of Sidney, 2001.

[41] Walter Ramberg and William R. Osgood, (1943), Description of stress-strain curves by three parameters, Technical Note No. 902, NASA Scientific and Technical Information Facility, Washington: NASA.

[42] Chote Soranakom and Barzin Mobasher, (2008), Correlation of tensile and flexural responses of strain softening and strain hardening cement composites, *Cement & Concrete Composites*; 30: 465–477.

[43] Garion, C., Skoczen´, B., and Sgobba, S. (2006). Constitutive Modelling and Identification of Parameters of the Plastic Strain-Induced Martensitic Transformation in 316L Stainless Steel at Cryogenic Temperatures. *International Journal of Plasticity*. Vol. 22, 1234–1264.

[44] Abaqus Analysis User"s Manual, Version 6.4. U.S.A: ABAQUS, Inc., 2003.

[45] Crisfield, M.A., and Wills, J., (1989), Analysis of R/C panels using different concrete models, *Journal of Engineering Mechanics*; 115: 578-597

[46] CEB-FIP. Model Code 1990, Bulletin d"Information. Comité Euro-International du Béton (CEB): Lausanne.

[47] Meiswinkel R, Rahm H. Modeling tension stiffening in RC structures regarding non-linear design analyses, *Proceedings ECCM 1999*, European Conference on Computational Mechanics, Munich, Germany, August 31-Sept. 3, 1999.

[48] EN 10002-1. British Standard - Metallic materials Tensile testing, Part 1, Method of test at ambient temperature. CEN; 2001.

[49] Ali Nour, Bruno Massicotte, Emre Yildiz, and Viacheslav Koval, (2007), Finite element modeling of concrete structures reinforced with internal and external fibre-reinforced polymers, *Can. J. Civ. Eng.*; 34: 340-354.

[50] Abdelhafid Bouzaiene and Bruno Massicotte, (1997), Hypoelastic tridimensional model for nonproportional loading of plain concrete, *Journal of Engineering Mechanics;* 123(11): 1111-1119.

[51] EN 1993-1-1. Eurocode 3 – Design of steel structures, Part 1.1, General rules. CEN; 2002.

[52] Rachid, Y.R., (1968), Ultimate strength analysis of reinforced concrete pressure vessels, *Nuclear Engineering and Design*; 7: 334-355.

[53] Becque, J. and Rasmussen, K. J.R. (2009). Experimental Investigation of the Interaction of Local and Overall Buckling of Stainless Steel I-Columns. *Journal Of Structural Engineering.* Vol. 10, 1340-1348.

[54] Beeby, A.W. and Scott, R.H. (2006). Mechanisms of Long-Term Decay of Tension Stiffening. *Magazine of Concrete Research.* Vol. 58:5, 255-266.

[55] Bischoff, P.H. and Paixao, R. (2004). Tension Stiffening and Cracking of Concrete Reinforced with Glass Fiber Reinforced Polymer (GFRP) Bars. *Can. J. Civ. Eng.* Vol. 31, 579–588.

[56] Bouchou, A. and Delobelle, P. (1996). Behaviour and Modelization of a 17-12 SPH Stainless Steel Under Cyclic, Unidirectional and Bidirectional Anisothermal Loadings. *Nuclear Engineering and Design.* Vol. 162, 21-45.

[57] Dabaon, M. A., El-Boghdadi, M. H., and Hassanein, M. F. (2009). Experimental Investigation on Concrete-Filled Stainless Steel Stiffened Tubular Stub Columns. *Engineering Structures.* Vol. 31, 300-307.

[58] Delobelle, P. and Bouchou, A. (1996). Behavior and Modeling of a 17-12 SPH Stainless Steel Under Cyclic, Uni and Bidirectional, Anisothermal Loadings. Part II: Modeling. *International Journal of Plasticity.* Vol. 12:3, 311-341.

[59] Di Sarno, L., Elnashai, A. S., and Nethercot, D. A. (2003). Seismic Performance Assessment of Stainless Steel Frames. *Journal of Constructional Steel Research.* Vol. 59, 1289–1319.

[60] Di Sarno, L., Elnashai, A. S., and Nethercot, D. A. (2006). Seismic Retrofitting of Framed Structures with Stainless Steel. Journal *of Constructional Steel Research.* Vol. 62, 93–104.

[61] Fardoun, F., Pola´k, J., and Degallaix, S. (1997). Internal and Effective Stress Analysis in Stainless Steels Using the Statistical Approach Method. *Materials Science and Engineering*. Vol. A234-236, 456-458.

[62] Feng, R. and Young, B. (2009). Behaviour of Concrete-Filled Stainless Steel Tubular X-Joints Subjected to Compression. *Thin-Walled Structures.* Vol. 47, 365-374.

[63] Fischer, G. and Li V.C. (2002). Influence of Matrix Ductility on Tension-Stiffening Behavior of Steel Reinforced Engineered Cementitious Composites (ECC). *ACI Structural Journal.* Vol. 99, 1-65.

[64] Inel, M. and Ozmen, H. B. (2006). Effects of Plastic Hinge Properties in Nonlinear Analysis of Reinforced Concrete Buildings. *Engineering Structures.* Vol. 28, 1494–1502.

[65] Lee K. J., Chun, M. S., Kim, M. H., and Lee, J. M. (2009). A New Constitutive Model of Austenitic Stainless Steel For Cryogenic Applications. *Computational Materials Science.* Vol. 46, 1152–1162.

[66] Macdonald, M., Rhodes, J., and Kotelko, M. (2007). Stainless Steel Stub Columns Subject to Combined Bending and Axial Loading. *Thin-Walled Structures.* Vol. 45, 893–897.

[67] Mortezaei, A. and Kheyroddin, A. (2008). Nonlinear Analysis of RC Flanged Shear Walls Considering Tension-Stiffening Effect. *Journal of Applied Sciences.* Vol. 8:3, 394-406.

[68] Mo, Y. L. and Han, R. H. (1996). Cyclic Load Tests on Prestressed Concrete Model Frames. *Engineering Structures.* Vol. 18:4, 311-320.

[69] Noh, S.Y. (2009). Tension Stiffening Model for Numerical Analysis of RC Structures by Using Bon-Slip Relationship. *Journal of Advanced Concrete Technology.* Vol. 7:1, 61-78.

[70] Nour, A., Massicotte, B., Yildiz, E., and Koval, V. (2007). Finite Element Modelling of Concrete Structures Reinforced with Internal and External Fibre-Reinforced Polymers. *Can. J. Civ. Eng.* Vol. 34, 340-354.

[71] Pola´k, J., Fardoun, F., and Degallaix, S. (2001). Analysis of the Hysteresis Loop in Stainless Steels I. Austenitic and Ferritic Steels. *Materials Science and Engineering.* Vol. A297, 144–153.

[72] Pola´k, J., Fardoun, F., and Degallaix, S. (2001). Analysis of the Hysteresis Loop in Stainless Steels II. Austenitic–Ferritic Duplex Steel and the Effect of Nitrogen. *Materials Science and Engineering.* Vol. A297, 154–161.

[73] Real, R. and Mirambell, E. (2005). Flexural Behaviour of Stainless Steel Beams. *Engineering Structures.* Vol. 27, 1465–1475.

[74] Salem, H., Hauke, B., and Maekawa, K. (1999). Fracture of Concrete Cover-its Effect on Tension Stiffening and Modelling. *Journal of Materials, Conc. Struct.* Vol. 42, 295-307.

[75] Sato, Y. and Vecchio, F.J. (2003). Tension Stiffening and Crack Formation in Reinforced Concrete Members with Fiber Reinforced Polymer Sheets. *ASCE.* Vol. 129:6, 717.

[76] Stramandinoli, R. S. B. and La Rovere, H. L. (2008). An Efficient Tension-Stiffening Model for Nonlinear Analysis of Reinforced Concrete Members. *Engineering Structures*. Vol. 30, 2069–2080.

[77] Tavassoli, A. A. (1995). Assessment of Austenitic Stainless Steels. *Fusion Engineering and Design.* Vol. 29, 371-390.

[78] Verderma, G.M., Fabbrocino, G, and Manfredi, G. (2008). Seismic Response of R.C. Columns with Smooth Reinforcement. Part II: Cyclic Tests. *Engineering Structures.* Vol. 30, 2289–2300.

[79] Weng, C. C., Yin, Y. L., Wang, J. C., and Liang, C. Y. (2008). Seismic Cyclic Loading Test of SRC Columns Confined with 5-Spirals. *Science in China Press.* Vol. 51:5, 529-555.

[80] Wu, H.Q. and Gilbert, R.I. (2009). Modeling Short-Term Tension Stiffening in Reinforced Concrete Prisms using a Continuum-Based Finite Element Model. *Engineering Structures.* Vol. 31, 2380-2391.

[81] Xu, Q. and Hayhurst, D. R. (2003). The Evaluation of High-Stress Creep Ductility for 316 Stainless Steel at 550 8C by Extrapolation of Constitutive Equations Derived for Lower Stress Levels. *International Journal of Pressure Vessels and Piping.* Vol. 80, 689–694.

[82] Yen Lei Voo, Behzad Nematollahi, Abu Bakar Bin Mohamed Said, Balamurugan A Gopal, and Tet Shun Yee (2012). Application of Ultra-High Performance Fiber Reinforced Concrete – The Malaysia Perspective. *International Journal of Sustainable Construction Engineering & Technology.* Vol 3(1).

[83] A. Kamen, E. Denarie´, H. Sadouki, E. Bruhwiler (2009). UHPFRC Tensile Creep at Early Age. *Materials and Structures* 42:113–122.

[84] Acker, P., and Behloul, M., „Ductal® Technology: A Large Spectrum of Properties, A Wide Range of Applications", FIB Symposium, Avignon, France, April 2004.

Publications involving thesis work

[1] S. Alih, A. Khelil, (2011), Behavior of Inoxydable Steel and their Performance as Reinforcement Bars in Concrete Beam: Experimental and Nonlinear Finite Element Analysis, *Construction and Building Materials*, **37**, 481-492.

[2] S. Alih, A. Khelil, (2012), Tension Stiffening Parameter in Composite Concrete Reinforced with Inoxydable Steel: Laboratory and Finite Element Analysis, *World Academy of Science, Engineering and Technology,* **62**, 535-540.

[3] S. Alih, A. Khelil, (2012), Developing Tension Stiffening Model for Concrete Beam Reinforced with Inoxydable Steel through Inverse Method, submitted in *Composite Structure.*

[4] S. Alih, A. Khelil, (2012), Determination of Tension Stiffening Phenomenon in Composite Concrete Reinforced with Inoxydable Steel and Ultra-high performance fibre-reinforced concrete, UHPFRC, submitted in *Composite Structure.*

[5] S. Alih, A. Khelil, (2012), Performance of Inoxydable Steel in Composite Concrete Structure Subjected to Seismic Load, submitted in *Construction and Building Materials.*

[6] S. Alih, A. Khelil, (2012), Developing Tension Stiffening Model for Concrete Beam Reinforced with Inoxydable Steel through Inverse Method, *XXX^{e} Rencontres AUGC-IBPSA Chambéry,* Savoie, France.

[7] S. Alih, H. Fares, A. Khelil, (2012), Effet de Raidissement en Traction du Béton avec des Armatures Inox, *Treizième édition des Journées scientifiques du Regroupement Francophone pour la Recherche et la Formation sur le Béton (RF)^{2}B,* Lyon, France.

7. List of Abbreviation and Symbols

Abbreviation / Symbol	Description	References: Section/ Fig./ Table/ Eq. (Page)
Inox	Inoxydable steel	Sect. 1. (5-6)
AH	Inoxydable steel from austenitic type in annealed form	
AC	Inoxydable steel from austenitic type in cold form	
CS	Standard carbon steel, f_y 460	
FVA	Free vibration analysis	Sect. 2.5.1 (29)
POA	Push over analysis	Sect. 2.5.2 (30)
THA	Time history analysis	Sect. 2.5.3 (35)
BFUP	*Béton fibré à ultra-hautes performance*	Sect. 3.3.2 (52)
UHPRFC	Ultra-high performance reinforced fiber concrete	
FRP	Fiber reinforced polymer	Sect. 3.4 (54)
RC	Reinforced concrete	
NNA	Nonlinear numerical analysis	Sect. 3.6 (67)
FEA	Finite element analysis	Sect. 3.7 (81)
FEM	Finite element model	
°C	Degree Celsius	Sect. 2.1 (13)
Mo	Molybdenum	Sect. 2.3 (20-24)
Cr	Chromium	
Ni	Nickel	
N	Nitrogen	
C	Carbon	
Si	Silicon	
Mn	Manganese	
Cu	Copper	
Ti	Titanium	
Nb	Niobium	
Al	Aluminium	
Co	Cobalt	
V	Vanadium	
S	Sulphur	
Ce	Cerium	
REM	Rare earth metals	

σ_S	steel stress of the reinforced concrete member	Eq. 2.2, Fig. 2.5 (24)
$\sigma_{S,II}$	stress of bare steel at a given strain	
$\sigma_{S,TSE}$	stress difference between the steel stress σ_S of the reinforced concrete member and the stress $\sigma_{S,II}$ of bare steel at a given strain	
$\sigma_{C,TSE}$	concrete stress equivalent to $\sigma_{S,TSE}$	Eq. 2.1 (24)
ρ_{eff}	Effective reinforcement ratio	Eq. 2.3 (24)
$A_{c,eff}$	Effective zone of concrete around the re-bars	Fig. 2.6 (24-25)
A_s	Sectional area of the steel	
$h_{c,ef}$	Height of the effective zone of concrete around rebar	
h	Total height of beam cross section	
d	Distance of the outer beam section to the center gravity of rebar layers	
x	Distance of the outer beam section to neutral axis of the beam cross section	
IO	Structural performance based on POA; Immediate occupancy	Fig. 2.10, 2.12-2.13 (31-33)
LS	Structural performance based on POA; Life safety	
CP	Structural performance based on POA; Collapse prevention	
C	Structural performance based on POA; Collapse	
NSP	Nonlinear static procedure	Sect. 2.5.2 (33)
ATC	Applied Technology Council	Sect. 2.5.2 (34)
SDOF	Single degree of freedom	
E	Modulus of elasticity	Table 3.2 (42)
fy	Yield strength	
ε_y	Yield strain	
ε_u	Ultimate tensile strain	Sect. 3.2.1 (44)
σ_u	Ultimate tensile strength	
E_0	Young‟s modulus	Eq. 3.1
$\sigma_{0.2}$	0.2% proof stress	Eq. 3.2
n	Parameter which determines the sharpness of stress-strain curve	Eq. 3.3
ε	Tensile strain	Eq. 3.1
σ	Tensile stress	

p	Corresponding plastic strain	Sect. 3.2.1 (44)
σ_p	Proof stress	
$\bar{\varepsilon}$	Transformed strain for tensile stress higher than 0.2% proof stress	Eq. 3.6, Fig. 3.5(b)
$\bar{\sigma}$	Transformed stress for tensile stress higher than 0.2% proof stress	Eq. 3.7, Fig. 3.5(b)
$E_{0.2}$	Initial modulus to the curve for tensile stress higher than 0.2% proof stress	Eq. 3.8
e	Non-dimensional proof stress	
$\bar{\sigma}_u$	Transformed ultimate tensile strength	Eq. 3.9, Fig. 3.5(b)
$\bar{\varepsilon}_{u_p}$	Transformed ultimate plastic strain	Eq. 3.10, Fig. 3.5(b)
m	Exponent dependent on the ultimate tensile strength in relation to the 0.2% proof stress	Eq. 3.12 (46)
R^2	Coefficient of determination	Sect. 3.2.2 (47)
ITRS	Iteration	Fig. 3.13 (55)
Ø	Diameter of reinforcement bars	Fig. 3.14 (57)
J1, J2, … Jn	Numbering used to identify strain gauges attached to the reinforcement bars	Fig. 3.15-3.16 (58)
P	Axial load applied in bending test	Fig. 3.18 (61)
δ	Maximum vertical displacement in the middle span of RC beam in bending test	
f_t	Tensile strength of concrete in direct tension	Eq. 3.21 (68)
f_{ck}	Ultimate compressive strength of concrete	
ε_{cr}	Homogenized cracking tensile strain	Eq. 3.22 (68)
C_d, C_b, C_p, C_s	Tension stiffening parameters	Fig. 3.26 (68)
σ_c	Compressive stress of concrete	Eq. 3.23 (71)
ε_c	Compressive strain of concrete	
f_m	Strength of concrete in flexural compression	Eq. 3.25 (71)
k_c	Parameter value at 0.85, 1.0 or > 1.0 according to some investigators. In this study k_c is taken as 1.0	
NLR	Number of concrete layers in the section	Sect. 3.6.3 (73-75)
N	Numbers of the top reinforcement layers	
M	Numbers of the bottom reinforcement layers	
E_{ci}	Secant concrete modulus	Eq. 3.27
B_{ci}	Width of layer *i*	

t_{ci}	Thickness of layer *i*	Sect. 3.6.3 (73-75)
E_{rtj}	Secant moduli of elasticity of the top reinforcement layers	Eq. 3.28
E_{rbk}	Secant moduli of elasticity of the bottom reinforcement layers	Eq. 3.29
A_{rtj}	Reinforcement areas of the top reinforcement layers	
A_{rbk}	Reinforcement areas of the bottom reinforcement layers	
E_{ctj}	Secant concrete moduli of elasticity at the level of the top reinforcement layers	
E_{cbk}	Secant concrete moduli of elasticity at the level of the bottom reinforcement layers	
ε_{ci}	Strain at the center of concrete layer *i*	
ε_{rtj}	Strain at the center of top reinforcement layer, *j*	
ε_{rbk}	Strain at the center of bottom reinforcement layer, *k*	
σ_{ci}	Stress at the center of concrete layer *i* corresponding to material models	
σ_{rtj}	Stress at the center of top reinforcement layer, *j* corresponding to material models	
σ_{rbk}	Stress at the center of bottom reinforcement layer, *k* corresponding to material models	
EA_s	Secant axial rigidity of the beam section	Eq. 3.26
EI_s	Secant flexural rigidity of the beam section	Eq. 3.30
Y_c	Inelastic centroid	
Y_i	distance from the centroid of layer *i* to the section inelastic centroid	
Y_{rtj}	Distance from the inelastic centroid to the centroid of the top reinforcement layers	
Y_{rbk}	Distance from the inelastic centroid to the centroid of the bottom reinforcement layers	
F_x	Internal axial force	Eq. 3.31
M_{int}	Internal bending moment	Eq. 3.32
ϕ	Instantaneous curvature	Eq. 3.37
ES	Moment of axial rigidity about the current centroid	Eq. 3.40
S_{TOL}	Convergence tolerance of the section	Eq. 3.41, Fig. 3.32

F_{CON}	Failure criterion to stop the analysis	Fig. 3.32 (77)
$\Delta_{midspan}$	mid-span deflection	Eq. 3.43 (78)
N_s	Number of segments along the beam shear span	Eq. 3.44 (78)
$X_{i-0.5}$	Distance from the support point to the beginning of segment *i*	
$X_{i+0.5}$	Distance from the support point to the end of the segment *i*	
L_a	Shear span of the beam	
EI_{si}	Flexural rigidity of segment *i*	
E_d	Damaged material modulus	Eq. 3.45 (86)
$d\varepsilon$	Total mechanical strain rate	Eq. 3.46 (86)
$d\varepsilon^{el}$	Elastic strain rate which includes crack detection strains	
$d\varepsilon_c^{pl}$	Plastic strain rate associated with the "compression yield" surface	
τ_c	hardening parameter	Eq. 3.47-3.48 (86)
G_f	Fracture energy required to form a unit area of crack surface	Eq. 3.49 (86)
P.G.A	Peak ground acceleration	Sect. 4.2.3 (120)

8. Annex

8.1 Analytical Procedures in NNA

The section properties are the submission of concrete, and reinforcing bars in tension and compression zones. Eq. (3.26) can then be written as

$$EA_s = EA_{concrete} + EA_{re-bar\ compression} + EA_{re-bar\ tension}$$

$$\therefore\ EA_s = B.\sum_{i=1}^{N_R} S_{i1} + \sum_{i=1}^{N}(E_{sti} - E_{cti})\,A_{sti} + \sum_{j=1}^{M}\left(E_{sbj} - E_{cbj}\right)A_{sbj} \quad \text{(A.1)}$$

The same goes with Eq. (2)-(4) for EI_s, F_x, and M_{int}. It can therefore be written as;

$$EI_s = B.\sum_{i=1}^{N_R}(S_{i3} + 2Y_0S_{i2} + Y_0^2S_{i1}) + \sum_{i=1}^{N}(E_{sti} - E_{cti})A_{sti}.(H + Y_N - Y_{sti} - Y_0)^2 + j{=}1MEsbj{-}EcbjAsbj.YN{-}Ysbj{-}Y02 \quad \text{(A.2)}$$

$$F_x = B.\varphi\sum_{i=1}^{N_R} S_{i2} + \sum_{i=1}^{N}(E_{sti} - E_{cti})\,\varepsilon_{sti}A_{sti} + \sum_{j=1}^{M}\left(E_{sbj} - E_{cbj}\right)\varepsilon_{sbj}A_{sbj} \quad \text{(A.3)}$$

$$M_{int} = B.\varphi\sum_{i=1}^{N_R}(S_{i3} + 2Y_0S_{i2}) + \sum_{i=1}^{N}(E_{sti} - E_{cti})\varepsilon_{sti}A_{sti}.(H + Y_N - Y_{sti} - Y_0) + j{=}1MEsbj{-}EcbjεsbjAsbj.YN{-}Ysbj{-}Y0 \quad \text{(A.4)}$$

S_{i1} to S_{i3} in the equations above are depends on concrete region involved in the compression (i = 1,2,3 for Region 1 to 3 respectively) or tension zone (i = 4,5,6 for Region 4 to 6 respectively). Each region is detailed as follows;

i) Compression zone:

Region 1: $0 \le \varepsilon_c \le C_u\varepsilon_m$

$$S_{11} = y_{c1}\sum_{i=1}^{4}\frac{a_i}{i}\,(\varphi y_{c1})^{i-1}$$

$$S_{12} = y_{c1}^2\sum_{i=1}^{4}\frac{a_i}{i+1}\,(\varphi y_{c1})^{i-1}$$

$$S_{13} = y_{c1}^3 \sum_{i=1}^{4} \frac{a_i}{i+2} (\varphi y_{c1})^{i-1}$$

Where, $y_{c1} = H + Y_n$ or $\frac{C_u \varepsilon_m}{\varphi}$ (whichever is less)

Region 2: $C_u \varepsilon_m \leq \varepsilon_c \leq \varepsilon_{20}$

$$C_1 = \frac{C_R f_m - C_u \varepsilon_m E_{cf}}{\phi}$$

$$S_{21} = E_{cf}(y_{c2} - y_{cu}) + C_1 \ln \frac{y_{c2}}{y_{cu}}$$

$$S_{22} = E_{cf} \frac{(y_{c2}^2 - y_{cu}^2)}{2} + C_1(y_{c2} - y_{cu})$$

$$S_{23} = E_{cf} \frac{(y_{c2}^3 - y_{cu}^3)}{3} + C_1 \frac{(y_{c2}^2 - y_{cu}^2)}{2}$$

Where, $y_{c2} = H + Y_N$ or $\frac{\varepsilon_{20}}{\phi}$ (whichever is less)

$$y_{cu} = \frac{C_u \varepsilon_m}{\phi}$$

Region 3: $\varepsilon_{20} < \varepsilon_c \leq C_c \varepsilon_m$

$$C_2 = \frac{0.2 f_m}{\phi}$$

$$S_{31} = C_2 \ln \frac{y_{c3}}{y_{20}}$$

$$S_{32} = C_2(y_{c3} - y_{20})$$

$$S_{33} = C_2 \frac{(y_{c3}^2 - y_{20}^2)}{2}$$

Where, $y_{c3} = H + Y_N$ or $\frac{C_c \varepsilon_m}{\phi}$ (whichever is less)

$$y_{20} = \frac{\varepsilon_{20}}{\phi}$$

ii) Tension zone:

Region 4: $-\varepsilon_{cr} \leq \varepsilon_t \leq 0$

$$S_{41} = \frac{f_t}{\varepsilon_{cr}} . y_{t1}$$

$$S_{42} = \frac{f_t}{\varepsilon_{cr}} . \frac{y_{t1}^2}{2}$$

$$S_{42} = \frac{f_t}{\varepsilon_{cr}} . \frac{y_{t1}^3}{3}$$

Where, $y_{t1} = Y_n$ or $\frac{\varepsilon_{cr}}{\varphi}$ (whichever is less)

Region 5: $-C_p\varepsilon_{cr} \leq \varepsilon_t \leq -\varepsilon_{cr}$

$$T_1 = \frac{C_d}{C_p - 1}\frac{f_t}{\varepsilon_{cr}}$$

$$T_2 = C_p - \frac{C_b}{C_d}$$

$$T_3 = 1 - \frac{C_b}{C_d}$$

$$S_{51} = T_1 . \left[T_2 y_{cr} \ln\frac{y_{t2}}{y_{cr}} - T_3(y_{t2} - y_{cr})\right]$$

$$S_{52} = T_1 . \left[T_2 y_{cr}(y_{t2} - y_{cr}) - T_3 . \frac{y_{t2}^2 - y_{cr}^2}{2}\right]$$

$$S_{53} = T_1 . \left[T_2 y_{cr}\frac{y_{t2}^2 - y_{cr}^2}{2} - T_3 . \frac{y_{t3}^3 - y_{cr}^3}{3}\right]$$

Where, $y_{t2} = Y_n$ or $\frac{C_p\varepsilon_{cr}}{\varphi}$ (whichever is less)

$y_{cr} = \frac{\varepsilon_{cr}}{\varphi}$

Region 6: $-C_s\varepsilon_{cr} \leq \varepsilon_t \leq -C_p\varepsilon_{cr}$

$$T_4 = \frac{C_b}{C_s - C_p}\frac{f_t}{\varepsilon_{cr}}$$

$$S_{61} = T_4 . \left[C_s y_{cr} \ln\frac{y_{t3}}{y_{cp}} - (y_{t3} - y_{cp})\right]$$

$$S_{62} = T_4 . \left[C_s y_{cr}(y_{t3} - y_{cp}) - \frac{y_{t3}^2 - y_{cp}^2}{2}\right]$$

$$S_{63} = T_4 . \left[C_s y_{cr}\frac{y_{t3}^2 - y_{cp}^2}{2} - \frac{y_{t3}^3 - y_{cp}^3}{3}\right]$$

Where, $y_{t3} = Y_n$ or $\frac{C_s\varepsilon_{cr}}{\varphi}$ (whichever is less)

$y_{cp} = \frac{C_p\varepsilon_{cr}}{\varphi}$

For concrete section in Eq. (A.1) and Eq. (A.2), the equation used can be detailed as below;

i) Concrete in compression

$$\sigma_c = a_0 + a_1\varepsilon_c + a_2{\varepsilon_c}^2 + a_3{\varepsilon_c}^3 + a_4{\varepsilon_c}^4$$

Where, $\begin{Bmatrix} a_0 \\ a_1 \\ a_2 \\ a_3 \\ a_4 \end{Bmatrix} = \begin{bmatrix} 1 & 0 & 0 & 0 & 0 \\ 0 & 1 & 0 & 0 & 0 \\ 1 & \varepsilon_m & \varepsilon_m^2 & \varepsilon_m^3 & \varepsilon_m^4 \\ 0 & 1 & 2\varepsilon_m & 3\varepsilon_m^2 & 4\varepsilon_m^3 \\ 1 & 1 & 2C_u\varepsilon_m & 3(C_u\varepsilon_m)^2 & 4(C_u\varepsilon_m)^3 \end{bmatrix}^{-1} \begin{Bmatrix} 0 \\ E_{ci} \\ f_m \\ 0 \\ E_{cf} \end{Bmatrix}$

Since boundary condition $a_0 = 0$,

$$\sigma_c = a_1\varepsilon_c + a_2{\varepsilon_c}^2 + a_3{\varepsilon_c}^3 + a_4{\varepsilon_c}^4$$

Effective elasticity modulus of each layer;

$$E(Y) = \frac{\sigma(Y)}{\varepsilon(Y)}$$

$$\therefore\ E_c(Y) = \frac{\sigma_c(Y)}{\varepsilon_c(Y)}$$

$$= \frac{a_1\varepsilon_c + a_2{\varepsilon_c}^2 + a_3{\varepsilon_c}^3 + a_4{\varepsilon_c}^4}{\varepsilon_c}$$

$$= a_1 + a_2\varepsilon_c + a_3{\varepsilon_c}^2 + a_4{\varepsilon_c}^3 \qquad \text{(A.5)}$$

Eq. (A.5) is used further in determining the integral of EA, EI, F_x, and M_c. Taking Region 1 as example, equations involved can be derived as follows;

Height of section in compression in Region 1 = y_{c1}

$$y_{c1} = H + Y_N$$

$$= \frac{\varepsilon_1}{\varphi}$$

$$\therefore \varepsilon_c = y_{c1}.\varphi$$

This will be used along with $E_c(Y)$

a) For S11

From Eq. (3.33),

$$EA = \sum_{i=1}^{2} \sum_{j=1}^{NRj} EA_{ij}$$

i=zones; compression or tension, j=regions for each zone

EA for concrete in compression zone; Region 1 (EA_{11})

$$EA = \int E_c\,(y).B.dy$$

$$= \int [a_1 + a_2\varepsilon(y) + a_3\varepsilon^2(y) + a_4\varepsilon^3(y)].B.dy$$

$$= \int [a_1 + a_2(\varphi.y_{c1}) + a_3(\varphi.y_{c1})^2 + a_4(\varphi.y_{c1})^3]\,.B.dy_{c1}$$

$$= \left[\frac{a_1 y_{c1}}{1} + \frac{a_2.\varphi.{y_{c1}}^2}{2} + \frac{a_3.\varphi^2.{y_{c1}}^3}{3} + \frac{a_4.\varphi^3.{y_{c1}}^4}{4}\right].B$$

$$= B.y_{c1}\left[\frac{a_1}{1} + \frac{a_2}{2}(\varphi.y_{c1}) + \frac{a_3}{3}(\varphi^2.{y_{c1}}^2) + \frac{a_4}{4}(\varphi^3.{y_{c1}}^3)\right]$$

$$= B.y_{c1}\left[\frac{a_1}{1} + \frac{a_2}{2}(\varphi.y_{c1}) + \frac{a_3}{3}(\varphi.y_{c1})^2 + \frac{a_4}{4}(\varphi.y_{c1})^3\right]$$

$$= B.y_{c1}\sum_{i=1}^{4} \frac{a_i}{i}(\varphi.y_{c1})^{i-1}$$

$$S_{11} = y_{c1}\sum_{i=1}^{4} \frac{a_i}{i}(\varphi.y_{c1})^{i-1}$$

b) For S12

From the equation of internal axial force, Fx;

$$F_x = \sum_{i=1}^{2} \sum_{j=1}^{Nrj} F_{x_{ij}}$$

F_x for concrete in compression zone (i=1), Region 1(j=1);

$$F_x = \int \sigma(y).B.dy$$

$$= \int [a_1\varepsilon(y) + a_2\varepsilon^2(y) + a_3\varepsilon^3(y) + a_4\varepsilon^4(y)]\,.B.dy$$

$$= \int [a_1(\varphi.y_{c1}) + a_2(\varphi.y_{c1})^2 + a_3(\varphi.y_{c1})^3 + a_4(\varphi.y_{c1})^4]\,.B.dy_{c1}$$

$$= \left[\frac{a_1.\varphi.{y_{c1}}^2}{2} + \frac{a_2.\varphi^2.{y_{c1}}^3}{3} + \frac{a_3.\varphi^3.{y_{c1}}^4}{4} + \frac{a_4.\varphi^4.{y_{c1}}^5}{5}\right].B$$

$$= B.\varphi.{y_{c1}}^2\left[\frac{a_1}{2} + \frac{a_2}{3}(\varphi.y_{c1}) + \frac{a_3}{4}(\varphi^2.{y_{c1}}^2) + \frac{a_4}{5}(\varphi^3.{y_{c1}}^3)\right]$$

$$= B.\varphi.{y_{c1}}^2\left[\frac{a_1}{2} + \frac{a_2}{3}(\varphi.y_{c1}) + \frac{a_3}{4}(\varphi.y_{c1})^2 + \frac{a_4}{5}(\varphi.y_{c1})^3\right]$$

$$= B.\varphi.{y_{c1}}^2\sum_{i=1}^{4}\frac{a_i}{i+1}(\varphi.y_{c1})^{i-1}$$

$$S_{12} = {y_{c1}}^2\sum_{i=1}^{4}\frac{a_i}{i+1}(\varphi.y_{c1})^{i-1}$$

c) <u>For S13</u>

EI is the overall effective elasticity modulus times moment of inertia about the inelastic centroid (Yc).

For concrete, $EI = \int E(y).B.(y-y_0)^2.dy$

$$= \int [E(y).B.(y^2 - 2y.y_0 + {y_0}^2)]dy$$

$$= \int [E(y).B.y^2 - E(y).B.2y.y_0 + E(y).B.{y_0}^2]\,dy$$

$$= \int [E(y).y^2 - E(y).2y.y_0 + E(y).{y_0}^2]B.dy$$

$$\int E(y).y^2.dy = \int [a_1 + a_2\varepsilon(y) + a_3\varepsilon^2(y) + a_4\varepsilon^3(y)].y^2.dy$$

$$= \int [a_1 + a_2(\varphi.y_{c1}) + a_3(\varphi.y_{c1})^2 + a_4(\varphi.y_{c1})^3].{y_{c1}}^2.dy_{c1}$$

$$= \int [a_1.{y_{c1}}^2 + a_2.\varphi.{y_{c1}}^3 + a_3.\varphi^2.{y_{c1}}^4 + a_4.\varphi^3.{y_{c1}}^5].dy_{c1}$$

$$= \left[\frac{a_1.{y_{c1}}^3}{3} + \frac{a_2.\varphi.{y_{c1}}^4}{4} + \frac{a_3.\varphi^2.{y_{c1}}^5}{5} + \frac{a_4.\varphi^3.{y_{c1}}^6}{6}\right].B$$

$$= {y_{c1}}^3\left[\frac{a_1}{3} + \frac{a_2}{4}(\varphi.y_{c1}) + \frac{a_3}{5}(\varphi^2.{y_{c1}}^2) + \frac{a_4}{6}(\varphi^3.{y_{c1}}^3)\right]$$

$$= {y_{c1}}^3\left[\frac{a_1}{3} + \frac{a_2}{4}(\varphi.y_{c1}) + \frac{a_3}{5}(\varphi.y_{c1})^2 + \frac{a_4}{6}(\varphi.y_{c1})^3\right]$$

$$= {y_{c1}}^3 \sum_{i=1}^{4} \frac{a_i}{i+2} (\varphi . y_{c1})^{i-1}$$

$$S_{13} = {y_{c1}}^3 \sum_{i=1}^{4} \frac{a_i}{i+2} (\varphi . y_{c1})^{i-1}$$

d) For EI

From $EI = \int [E(y).y^2 - E(y).2y.y_0 + E(y).{y_0}^2]B.dy$

It has been derived that $\int E(y).y^2\, dy = S_{13}$

$$\int E(y).y\, dy = \int [a_1 + a_2\varepsilon(y) + a_3\varepsilon^2(y) + a_4\varepsilon^3(y)]\, y\, .dy$$

$$= \int [a_1 + a_2(\varphi . y_{c1}) + a_3(\varphi . y_{c1})^2 + a_4(\varphi . y_{c1})^3]\ y_{c1}.dy_{c1}$$

$$= \int [a_1 . y_{c1} + a_2 . \varphi . {y_{c1}}^2 + a_3 . \varphi^2 . {y_{c1}}^3 + a_4 . \varphi^3 . {y_{c1}}^4] . dy_{c1}$$

$$= \left[\frac{a_1 . {y_{c1}}^2}{2} + \frac{a_2 . \varphi . {y_{c1}}^3}{3} + \frac{a_3 . \varphi^2 . {y_{c1}}^4}{4} + \frac{a_4 . \varphi^3 . {y_{c1}}^5}{5}\right]$$

$$= {y_{c1}}^2 \left[\frac{a_1}{2} + \frac{a_2}{3}(\varphi . y_{c1}) + \frac{a_3}{4}(\varphi^2 . {y_{c1}}^2) + \frac{a_4}{5}(\varphi^3 . {y_{c1}}^3)\right]$$

$$= {y_{c1}}^2 \left[\frac{a_1}{2} + \frac{a_2}{3}(\varphi . y_{c1}) + \frac{a_3}{4}(\varphi . y_{c1})^2 + \frac{a_4}{5}(\varphi . y_{c1})^3\right]$$

$$= {y_{c1}}^2 \sum_{i=1}^{4} \frac{a_i}{i+1} (\varphi . y_{c1})^{i-1}$$

$$= S_{12}$$

As been driven, $\int E(y)\, dy = S_{11}$

Therefore, for Region 1, $EI = \int [E(y).y^2 - E(y).2y.y_0 + E(y).{y_0}^2]B.dy$

$$= [S_{13} - 2y_0 . S_{12} + {y_0}^2 . S_{11}]B$$

∴ For the whole concrete regions in the section; as in Eq. (A.2) is

$$EI_c = B. \sum_{i=1}^{N_R} [S_{i3} - 2y_0 . S_{i2} + {y_0}^2 . S_{i1}]$$

8.2 Code developed using MATLAB

```
clear all;clc

%PROGRAM TO DEVELOP SECTION ANALYSIS

%Step 1: Input material and geometric properties
tc=14;
trb=10;
trt=4;
Bc=150;
H=280;
Hc = 280;
x=84.3;
psi=pi;
drb=20;
drt=8;
Arb=314.2;
Art=50.3;
Econ=37565;
Erb=200000;
Ert=210000;
fyrb=480;
fyrt=430;
STOL=5E-5;
FTOL=5E-4;
epscr=0.000108;
ft=4.07;
Cd=1.5;
Cb=0.8;
Cp=6;
Cs=40.0;
```

```
epsm=0.002;
Cu=1.5;
a1=1;
a2=1;
a3=1;
a4=1;
AAA=[a1 a2 a3 a4];

%STEP 2: calculating initial condition; Constants
%2.1 Inelastic centroid, yc
yc=Hc-x;

%2.2 Axial rigidity, EA
EA=(Econ*Hc*Bc)+(Erb*2*Arb)+(Ert*2*Art);

%2.3 Flexural rigidity, EI
EI=Econ*((Bc*yc*(2/3*yc))+(Bc*(Hc-yc)*(2/3*(Hc-
yc))))+((Erb*2*Arb)*(yc-31-drb/2))+((Ert*2*Art)*(Hc-yc-31-
drb/2));



P = 40000;
M = 36E6;


%STEP 3: Initiation of conditions

cond1 = 0;
cond2 = 0;

EEEA = [];
EEEI = [];
FFFx = [];
```

```
MMMC = [];
YYYn = [];
YYYc = yc;
EEEAS = [];
iiii = 0;


%STEP 4: Enter the boucles

while (cond1 < STOL && cond2 < FTOL) || (cond1 >= STOL)

    if cond1>= STOL
    iiii = iiii+1;
    if iiii > 1
    yc = YYYc(iiii-1)+EAM/EA;
    YYYc = [YYYc yc];
    else
        P = input('input value of P :')
        M = input('input value of M :')
    end

    end



    %STEP 6: Calculate moment effective about the inelastic
centroid, Mo
Yg=Hc/2;
Mo=M+P*(Yg-yc);


%STEP 7: Calculate section curvature, si and axial strain,
epsilon zero
si=Mo/EI;
```

```
eps0=P/EA;

%-------------------------------------------------------------

%Equations needed to get new section properties

%Compression zone
%Region 1:
yc1=Cu*epsm/si;

S11=0;
S12=0;
S13=0;

for i=1:1:4

 var1=(AAA(i)/i)*((si*yc1)^(i-1));
 var2=(AAA(i)/(i+1))*((si*yc1)^(i-1));
 var3=(AAA(i)/(i+2))*((si*yc1)^(i-1));

 S11=S11+var1;
 S12=S12+var2;
 S13=S13+var3;
end

S11=yc1*S11;
S12=(yc1^2)*S12;
S13=(yc1^3)*S13;


%Tension zone
%Region 4:
yt1=epscr/si;
```

```
S41=(ft/epscr)*yt1;
S42=(ft/epscr)*((yt1^2)/2);
S43=(ft/epscr)*((yt1^3)/3);

%Region 5:
T1=(Cd/(Cp-1))*(ft/epscr);
T2=Cp-(Cb/Cd);
T3=1-(Cb/Cd);

yt2=(Cp*epscr)/si;
ycr=epscr/si;
yt3=(Cs*epscr)/si;

S51=T1*(T2*ycr*log10(yt2/ycr)-T3*(yt2-ycr));
S52=T1*(T2*ycr*(yt2-ycr)-T3*((yt2^2-ycr^2)/2));
S53=T1*(T2*ycr*((yt2^2-ycr^2)/2)-T3*((yt3^3-ycr^3)/3));

%Region 6:
T4=(Cb/(Cs-Cp))*(ft/epscr);

ycp=(Cp*epscr)/si;

S61=T4*(Cs*ycr*log10(yt3/ycp)-(yt3-ycp));
S62=T4*(Cs*ycr*(yt3-ycp)-((yt3^2-ycp^2)/2));
S63=T4*(Cs*ycr*((yt3^2-ycp^2)/2)-((yt3^3-ycp^3)/3));



%Steel bars
%Bottom bar

sigrb = P /(psi*((drb/2)^2));

if sigrb< fyrb
```

```
   epsrb =sigrb/Erb;

else

   epsrb=(sigrb-474)/1187;
end


%Bottom top

sigrt=P/(psi*((drt/2)^2));

if sigrt < fyrt
    epsrt =sigrt/Ert;
else
    epsrt=(sigrt-423)/1160;
end

%-------------------------------------------------------------

%STEP 8: Calculate new section properties
%8.1 Neutral axis position, Yn
Yo=eps0/si;
Yn=Yo-yc;

%8.2 Secant Axial rigidity, EAs
%Concrete layers

EAcon=Bc*(S11+S41+S51+S61);

%Bottom rebar layers
EArb =(Erb - Econ)*(0.5*psi*((drb/2)^2));

%Top rebar layers
```

```
EArt = (Erb-Econ)*(0.5*psi*((drt/2)^2));

%EAs for whole section
EAs=EAcon+EArb+EArt;

%8.3 Secant flexural rigidity, EIs
%Concrete layers
EIcon = [];

EEIcon=Bc*((S13+(2*Yo*S12)+(Yo^2*S11))+(S43+(2*Yo*S42)+(Yo^2*S
41))+(S53+(2*Yo*S52)+(Yo^2*S51))+(S63+(2*Yo*S62)+(Yo^2*S61)));

%Bottom rebar layers
Yb1=36;
Yb2=46;

    EIrb1=(Erb-Econ)*(0.5*psi*((drb/2)^2))*((Yn-Yb1-Yo)^2);
    EIrb2=(Erb-Econ)*(0.5*psi*((drb/2)^2))*((Yn-Yb2-Yo)^2);

%Top rebar layers
Yt1=33;
Yt2=37;

     EIrt1=(Erb-Econ)*(0.5*psi*((drt/2)^2))*((H+Yn-Yt1-Yo)^2);
     EIrt2=(Erb-Econ)*(0.5*psi*((drt/2)^2))*((H+Yn-Yt2-Yo)^2);

%EIs for whole section
EIs=EEIcon+EIrb1+EIrb2+EIrt1+EIrt2


%8.4 Internal axial force, Fx
%Concrete layers
    Fcon=Bc*si*(S12+S42+S52+S62);
```

```
%Bottom rebar layers
    Frb=(Erb-Econ)*epsrb*(0.5*psi*((drb/2)^2));

%Top rebar layers

     Frt=(Erb-Econ)*epsrt*(0.5*psi*((drt/2)^2));

%Fx for whole section
Fx=Fcon+Frb+Frt;



%8.5 Internal bending moment, Mc
%Concrete layers

Mcon=Bc*si*((S13+2*Yo*S12)+(S43+2*Yo*S42)+(S53+2*Yo*S52)+(S63+
2*Yo*S62));

%Bottom rebar layers
Yb1=36;
Yb2=46;

    Mrb1=(Erb-Econ)*epsrb*(0.5*psi*((drb/2)^2))*(Yn-Yb1-Yo);
    Mrb2=(Erb-Econ)*epsrb*(0.5*psi*((drb/2)^2))*(Yn-Yb2-Yo);

    %Top rebar layers
Yt1=33;
Yt2=37;

     Mrt1=(Erb-Econ)*epsrt*(0.5*psi*((drt/2)^2))*(H+Yn-Yt1-
Yo);
     Mrt2=(Erb-Econ)*epsrt*(0.5*psi*((drt/2)^2))*(H+Yn-Yt2-
Yo);

%Mint for whole section
```

```
Mc=Mcon+Mrb1+Mrb2+Mrt1+Mrt2;


%STEP 9: Moment of the axial rigidity about inelastic centroid
EAM=(Fx-(eps0*EAs))/si;
Mg=Mc-(Fx*(Yg-yc));




%STEP 10: Calculate the condition again

cond1 = EAM/(EAs*yc);
cond2 = max(abs((M-Mc)/M),abs((P-Fx)/P));

EEEA = [EEEA EA];
EEEAS = [EEEAS EAs];
EEEI = [EEEI EI];
FFFX = [FFFx Fx];
MMMc = [MMMC Mc];
YYYn = [YYYn Yn]
EIcon = [EIcon EEIcon];
end


disp('failure of the section')
```

Abstract

This thesis focus on studying the behavior of composite concrete reinforced with inoxydable steel. The behavior of a bare steel bar is not the same as that of a bar embedded in concrete. The grip allows the concrete between cracks to resist tensile forces, thereby reducing the average level of stress in the reinforcement steel bars. The consideration of this effect required an experimental and numerical methodology to determine the parameters that describe the transfer of part of the tensile stress in steel bars to concrete. A new constitutive law has been specifically developed for the inoxydable steel bars. This law is integrated into a nonlinear modeling approach of reinforced concrete elements based on discretization in horizontal layers for the analysis section and a vertical discretization for the overall analysis. This approach is able to determine the tension stiffening parameters of the concrete. These parameters are identified using an inverse method by comparing experimental results and those from the numerical calculation. The comparison between experimental results and the prediction of the model implemented in Abaqus shows a very good correlation. Finally, the effect of inoxydable steel on structural responses under seismic actions is presented. Three models are designed and analyzed based on the seismic capacity taking into account the structural ductility of the inoxydable steel.

Résumé

Les travaux effectu s dans cette thèse portent sur l' tude du comportement des l m ents en béton armé avec de l'acier inoxydable. Le comportement d'une barre d'acier seule n'est pas le même que celui d'une barre enrob e de b ton. L'adh rence permet au b ton situ entre les fissures de r sister à des efforts de traction, r duisant ainsi le niveau moyen d'effort dans l'acier. La consid ration de cet effet a n cessit la mise en place d'une m thodologie exp rimentale et num rique afin de d terminer les paramètres de transfert d'une partie des efforts de traction de l'acier vers le b ton. Une nouvelle loi de comportement spécifique pour les barres en acier inoxydable a été développée. Cette loi est intégrée dans une approche de modélisation non lin aire du comportement d' l m ents en b ton arm selon une discr tisation par couches horizontales pour l'analyse en section et une discrétisation verticale pour l'analyse globale. Cette approche permet de d terminer les paramètres du modèle de raidissement en traction du béton. Ces paramètres sont identifiés grâce à la méthode inverse par comparaison entre les résultats expérimentaux et ceux issus du calcul numérique. La comparaison entre les résultats expérimentaux et la prédiction du modèle impl m ent dans Abaqus d montre une très bonne concordance. Enfin, l'effet de l'acier inox sur les réponses structurales sous actions sismiques est présenté. Trois modèles sont conçus et analysés vis-à-vis de la capacité sismique en tenant compte de la ductilité structurale apportée par les armatures inox.